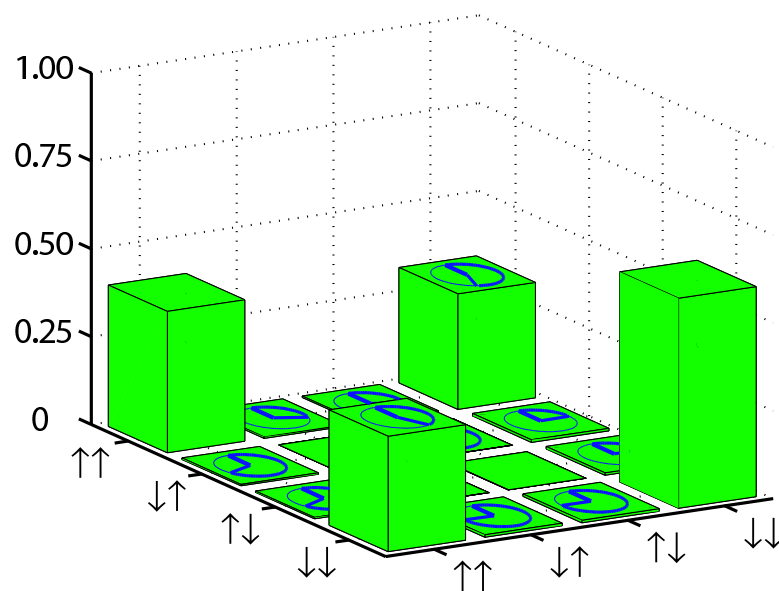

Entanglement of Two Trapped-Ion Spin Qubits

A thesis submitted for the degree of
Doctor of Philosophy



Jonathan Home

Hilary Term
2006

Linacre College
Oxford

Abstract

Entanglement of two trapped-ion spin qubits.
A thesis submitted for the degree of Doctor of Philosophy
Hilary Term 2006

Jonathan Home
Linacre College, Oxford

This thesis describes experimental and theoretical work aimed at development of an ion trap quantum information processor. The experimental work is concerned with the control and manipulation of quantum states of one and two $^{40}\text{Ca}^+$ ions, and includes the implementation of a two-qubit logic gate between two trapped ions. Tomography was used to obtain elements of the density matrix, from which we can deduce that a maximally entangled state of the ions' spin was created with 83% fidelity.

In order to implement the quantum logic gate, the ion-light interaction needs to be well understood, and a high level of control over the spin and motional states is required. The experimental work described in this thesis represents advances in both these areas. We have demonstrated ground state cooling, preparation of superpositions of Fock and coherent states of motion, and measured the lowest heating rate and longest motional coherence times observed in an ion trap. We have also experimentally studied spin decoherence in the context of qubit memory and logic gate infidelity.

A single trapped ion was used to thoroughly investigate the state-dependent force used for the two-ion logic gate. These experiments created the largest mesoscopic superpositions of motional states yet observed in an ion trap. The motion was entangled with the spin of the ion, creating states analogous to those considered in the “Schrödinger’s” cat thought experiment. The measured coherence times for these states were an order of magnitude longer than those reported elsewhere.

The theoretical work included in this thesis is a study of the design of ion traps optimised for fast separation of trapped ions. We provide insights into the important characteristics of the trapping potential during separation, and compare a range of electrode geometries. Ion separation is a key issue in scaling up ion trap quantum information processor experiments.

Acknowledgements

I wish to thank Prof. Andrew Steane, who supervised this work, and provided inspiration, enthusiasm, support, fish and chips, and many fun arguments/discussions covering much of the subject matter. Thanks to Dr. David Lucas for answering lots of questions, his knowledge of the experiment, and the high-endurance overnight sessions in the lab. I would also like to thank Prof. Derek Stacey for his support, and the fastidious attention to the details which we had all missed.

In addition, thanks to the Oxford ion trappers past and present; Dr. Matthew McDonnell, Dr. John-Patrick Stacey, Dr. Nick Thomas and Dr. Simon Webster, plus Ben Keitch, Gergely Imreh and David Schwer. In particular Matt, for his long hours in the lab and technical wizardry. Also to Graham Quelch and Rob Harris for their practical knowledge and ideas.

I must also thank all of the friends I've had during my many years in Oxford. I hope you guys had as much fun as I did. In particular, thanks go to John James, Stephen Otim and Paul Njoroge for helping me through a difficult period in the first year of my DPhil.

Thanks to my family, especially my parents, for providing me with all the chances I've had in life, for my continuing education, and for challenging me to explain what I do.

Last, but in no way least, thanks to Yuki for being so loving and supportive, both in Oxford, and at a distance of 6600 miles.

Contents

Abstract	i
Acknowledgements	ii
1 Introduction	1
1.1 Background	2
1.2 Thesis Layout	5
2 Experimental Details.	7
2.1 Trapping and Loading Ions	7
2.1.1 The electrodes.	7
2.1.2 Trapping fields and ion frequencies.	8
2.1.3 Compensation of stray d.c. electric fields.	9
2.1.4 Loading Ions	9
2.2 The $^{40}\text{Ca}^+$ ion.	9
2.2.1 Magnetic fields.	10
2.3 Laser Systems.	11
2.3.1 Frequency stabilisation and control.	12
2.3.2 Switching	12
2.3.3 Pulse generation.	13
2.4 Laser use in a typical experiment.	13
2.4.1 Cooling and population preparation.	14
2.4.2 Coherent Manipulations	15
2.4.3 Read-out	16
3 Coherent interaction of light with a trapped ion.	18
3.1 The Hamiltonian for a trapped ion	18
3.2 Interaction with two optical light fields.	19
3.2.1 Motional effects - the Lamb-Dicke regime.	20
3.2.2 Spin-flip transitions.	21
3.2.3 The oscillating dipole force	22
4 Cooling, Heating and Fock States.	23
4.1 Cooling and Temperature Diagnosis	23
4.1.1 Cooling methods.	23
4.1.2 Temperature Diagnosis.	25
4.1.3 Experimental results.	27
4.2 Heating rates.	29

4.3	Fock states of motion	32
5	Coherence Measurements.	41
5.1	Measurement of spin coherence	42
5.1.1	Decoherence.	43
5.1.2	Experimental results	44
5.2	Measurement of motional coherence	47
5.3	Coherence during quantum manipulations	50
5.3.1	Photon Scattering.	50
6	Coherent Manipulation of Two Trapped Ions.	54
6.1	Interaction of two trapped ions with light	54
6.1.1	Modes of oscillation	54
6.1.2	Interaction with light.	55
6.1.3	Sideband transitions	55
6.2	Cooling and Temperature diagnostics.	56
6.2.1	Cooling two ions.	56
6.2.2	Temperature Diagnosis.	56
6.3	Carrier transitions with two ions.	57
7	Spin-Dependent Forces and Schrödinger’s Cat.	62
7.1	Introduction to coherent states	63
7.2	The forced harmonic oscillator.	63
7.2.1	The oscillating force.	64
7.3	Laser-ion interaction	69
7.3.1	Travelling-standing wave	69
7.3.2	State-dependent force	70
7.3.3	Light shifts	70
7.4	Creation of “Schrödinger’s Cat” states	75
7.4.1	Effect of initial temperature on the observed signal.	76
7.5	Experimental results	77
7.5.1	Discussion	82
7.5.2	Coherence of Schrödinger’s Cat states.	83
7.6	Conclusions	84
8	Spin state tomography.	89
8.1	Tomography	89
8.1.1	Equal rotations applied to qubits	90
8.1.2	Available information.	90
8.1.3	Indistinguishability of $\uparrow\downarrow$ and $\downarrow\uparrow$	91
8.2	Maximum likelihood estimation	92
8.3	Experimental method.	92
8.3.1	Setting the correct pulse length.	93
8.3.2	Determination of experimental rotation angle.	94
8.4	Application to easily prepared states.	94

9 Entanglement of spin qubits.	104
9.1 Implementation.	106
9.2 State-dependent force on two ions.	106
9.2.1 Stretch mode excitation	107
9.2.2 Off-resonant COM mode excitation	108
9.3 Experimental diagnostics.	109
9.3.1 Setting the correct ion separation.	109
9.3.2 Extracting the fidelity from experimental data.	110
9.3.3 Cancellation of single qubit rotations	112
9.4 Experimental results.	113
9.4.1 Measurement of Entanglement	118
9.5 Contributions to infidelity	119
9.6 Conclusions	120
10 Segmented Trap Design.	121
11 Conclusion	123
11.1 Future plans and improvements.	125
A Adiabatic elimination of the upper level	127
B Wavefunction for two ions driven on a motional sideband	129
C Electrode configurations for fast separation of trapped ions.	130

Chapter 1

Introduction

This thesis concerns the controlled manipulation of entanglement in systems of one and two trapped ions, and a study of trap designs optimised for fast separation of ions. This work is part of a longer term project which aims to realise quantum information processing in an ion trap.

The field of quantum information processing is well established theoretically. It has already provided many insights into the relationship between physics and information, and into the nature of entanglement. This work has resulted in a wealth of fascinating proposals for experiments which might be performed with a quantum information processing device, e.g. quantum error correction, quantum algorithms, teleportation, simulation of quantum systems and studies of entanglement.

The experimental realisation of these proposals represents a major challenge. One of the most promising technologies in this area involves small numbers of ions trapped in free space by electric fields. At present, experiments performed at the National Institute of Standards and Technology, Boulder, USA and the University of Innsbruck, Austria have demonstrated many of the basic requirements for quantum information processing with trapped ions.

The issues which currently limit ion trap experiments to small scale demonstrations are

1. Instability of the ions themselves due to ambient fluctuations of their environment.
2. Instability of the laser fields used for gate implementation.
3. Individual control and addressing of ions.
4. The ability to move information around the processor.

We wish to contribute new ideas to this field. The experiments described in this thesis have explored the issues of stability of the ions themselves, and the interaction between the $^{40}\text{Ca}^+$ ions and the Raman laser fields used for gates. Scaling up of ion trap systems will require technological advances e.g. in the design and fabrication of multiple trap arrays, and a deep understanding of the physical mechanisms involved. Contributions to both of these issues are made in the work described here.

1.1 Background

Entangled states of 2 or more particles exhibit correlations between individual particles which have no classical analogue. Entanglement lies at the heart of quantum mechanics, and the control and manipulation of entangled states is fundamental to recent ideas in information processing, communications and metrology. Investigation of large scale entangled states may also provide insights into the problem of measurement in quantum mechanics, and elucidate the link between classical and quantum mechanics.

One example of the proposed use of entangled states is quantum information processing. This field is concerned with the use of quantum mechanical systems to process information. Ideas for a universal quantum simulator which could simulate the physical behaviour of any other were proposed by R. Feynman [1, 2]. Any such quantum simulator could also be viewed as a universal computer, since any computer must be a physical system. Feynman noted that such a processor could compute certain problems more efficiently than any classical computer. These ideas were developed further by D. Deutsch [3], who laid down a simple set of specifications for a universal quantum processor.

In the network model proposed by D. Deutsch [3], the processor relies on the control and manipulation of an array of two state quantum systems (qubits), which by their quantum nature can exist in superpositions of states. Deutsch realized that any quantum system could be simulated using a restricted set of simple operations between qubits (up to 4-qubit logic gates). Later it was proved that one and two-qubit gates were sufficient [4, 5]. Quantum algorithms make use of entangled qubits which can be individually addressed and coherently controlled to compute a problem. Measurement of the states of the individual qubits provides the output. Progress in the field was stimulated by the development of algorithms for certain problems which require resources which scale polynomially with the size of the problem using a quantum processor, whereas the scaling is exponential for a classical computer. An important example is the algorithm devised by P. Shor for finding prime factors of a large number [6]. Another important algorithm which gives a significant speed up over a classical processor is the algorithm devised by L. Grover [7] for searching for an element in an unordered list. The property of quantum systems which is crucial to the speed up over classical computation is, arguably, entanglement [8, 9, 10].

A major obstacle to realisation of a quantum information processor is that the qubits interact in an uncontrolled manner with each other and their environment. This “decoheres” the quantum state, and leads to a loss of stored information, thus the algorithm will fail.

The use of quantum error correction (QEC) allows us to protect quantum information against irreversible errors [11, 12]. It works by encoding the logical information from one qubit into several entangled qubits. After a period in which errors might have occurred, an appropriately chosen measurement is performed on a subset of the qubits, revealing the presence and nature of errors, but not the logical information. The measurement projects the qubits onto a particular subspace, and indicates which unitary operation to perform on the logical qubit in order to correct its state.

Development of a large scale quantum information processor requires generation of entanglement between many individual quantum systems (the qubits), and the ability to control and measure each qubit individually. This remains a major technical goal which is the focus of much research worldwide. The basic elements of a quantum computer were specified by Deutsch. This opened the way to more detailed discussion of the experimental requirements. Many of the issues were helpfully summarised by D. DiVincenzo [13], who

set out the following list of requirements.

1. A scalable physical system with well characterised qubits.
2. The ability to initialise the state of the qubits to a simple fiducial state, eg. $|000\dots\rangle$.
3. Long relevant decoherence times, much longer than the gate operation time.
4. A “universal” set of quantum gates.
5. A qubit-specific measurement capacity.

In addition to the above, the issues of scalability and stability of the device add the following

6. The ability to transport information around the processor (this is analogous to the job of the wires in a classical processor).
7. The ability to re-initialise the state of the qubits in real time (required for QEC).
8. High gate precision.

Schemes for quantum information processing have been proposed in many candidate technologies, including nuclear magnetic resonance (NMR) [14], trapped ions [15, 16], photons [17], and the quantised flux and charge of superconductors in Josephson junction circuits [18]. NMR has been used to demonstrate quantum algorithms [19, 20], but uses an ensemble approach which lacks scalability [21, 22].

Deterministic entanglement and logic gates between individual qubits have only been achieved with trapped ions [23, 24, 25], neutral atoms [26], Josephson junctions [27] and superconducting charge qubits [28].

Ion traps are at present among the most advanced of the proposed technologies. A string of ions trapped in free space forms a qubit register. Two internal states of the ion are used as the qubit. The ions interact via the Coulomb interaction, which allows the implementation of logic gates between qubits.

The state of each ion can be initialised by optical pumping. Internal state coherence times of up to 15 s [29] have been measured, which is much longer than the typical gate time ($\leq 150 \mu\text{s}$). A universal set of one and two qubit gates is available using laser radiation. Finally, the use of electron “shelving” allows qubits to be read out reliably and individually.

The issue of scalability and transport of information in an ion trap system is the focus of much research in the ion trap community. As the length of a string of ions trapped in a single harmonic well increases, the spectral density of normal modes increases, which makes gates between ions increasingly hard to implement with high fidelity. A number of methods to get around this problem have been proposed. The most promising of these seems to be moving the ions around an array of traps [30, 31]. Other proposals include transferring information between ions using photonic qubits which are coupled to the ions using a high finesse cavity [32].

Experimental demonstrations of elements required for quantum information processing have been led by the groups at NIST, Boulder using hyperfine states in the ground state of Be^+ ions, and at the Institute for Quantum Optics in Innsbruck, using levels in the $S_{1/2}$ and $D_{5/2}$ levels of $^{40}\text{Ca}^+$.

The NIST group demonstrated some of the basic elements of the J. I. Cirac and P. Zoller C-NOT gate [15] in the same year that it was proposed [33], and followed this by deterministic entanglement of four ions [24] using the gate proposal of A. Sørensen and K. Mølmer [34]. In 2003, the group demonstrated a new form of controlled-phase gate with 97% fidelity [23]. In these experiments all ions were illuminated together.

In order to individually address ions the NIST group has taken two approaches. In the first, the ions are illuminated together, and the ions are differentially addressed using the intensity or phase profile of the laser beams [35]. Subsequent work has involved separating ions into two traps. Initial experiments on moving and separating ions were performed in 2002 [36], and ions were subsequently separated as part of a demonstration of quantum state teleportation [37].

The entangled states created by the phase gate demonstrated by this group are those required for quantum-error correction. In 2004 they demonstrated a single round of quantum error correction using an entangled state of three ions [38]. This experiment used both the laser beam profile and separation of ions to individually manipulate the states of the ions. The phase gate has been used to produce a “Schrödinger’s cat” state ($|000000\rangle + |111111\rangle$) of 6 trapped ion qubits in a single trap [39].

The Innsbruck group implemented the original Cirac-Zoller gate proposal in 2003 [25]. The Innsbruck experiment makes use of the 729 nm quadrupole transition in Calcium. They individually address ions in a string using a tightly focussed laser beam, allowing them to perform a universal set of logic operations. This has allowed them to perform a full tomography of the state of their ions [40]. The Innsbruck group also performed quantum state teleportation in 2004 [41]. Subsequent improvements in precision has led to the production and tomography of “W” entangled states of up to eight ions [42].

In 2005 deterministic entanglement of ions was also achieved by the ion trap groups at the University of Oxford using a $^{40}\text{Ca}^+$ ground state qubit (see chapter 9) and the University of Michigan using two hyperfine states in the ground level of $^{111}\text{Cd}^+$ as the qubit [43].

Simple quantum algorithms have been carried out in the NIST, Innsbruck and Michigan groups. These include implementation of the Deutsch-Josza algorithm with a single ion [44], a simple form of the Grover search algorithm with two ions [45], and the implementation of the semi-classical quantum Fourier transform [46], which forms an important part of the Shor factorisation algorithm.

Separation of ions in a trap without considerable heating remains a technical difficulty. Two-qubit gates which rely on the ion being in the Lamb-Dicke regime are yet to be implemented after separation of two ions. Sympathetic cooling of the ions using another ion species may well be required, and demonstrations have been done at NIST using Hg^+ to cool Be^+ , and at the University of Michigan, where Cd^{113} was used to cool Cd^{111} . Multiple traps and small scale traps required for implementation of the Kielpinski proposal [31] have been experimentally investigated by both the NIST and Michigan groups [47, 48].

In order to implement quantum information processing, the qubit states will need to be extremely robust against decoherence, and logic operations must be implemented with extremely high fidelity. In most of the experiments described above, the primary form of decoherence of quantum memory is magnetic field fluctuations. Internal states with an energy splitting which is much less sensitive to these fluctuations are being investigated with a view to use as a qubit. One approach is to use hyperfine ground states on a “clock” transition $M_F = 0 \rightarrow M_F = 0$, where the energy splitting is a second order effect in the applied field. One such transition is found in $^{43}\text{Ca}^+$, and a coherence time of 0.9(2) s

was recently observed in the Oxford group using this transition. Subsequent tests have revealed that this may be limited by synthesiser stability rather than decoherence of the quantum state of the ion. Transitions with second order sensitivity to the magnetic field are also available at intermediate field strengths. An example is found in Be^+ , and was used to achieve coherence times up to $15(2)$ s by the NIST group [29]. The two-qubit gate performed by the Michigan group [43] used a qubit based on a “clock” transition.

Single photon scattering during gate operations is a fundamental source of gate infidelity. Recent experiments performed at NIST, Boulder indicate that for gates which utilise Raman transitions between states in ground hyperfine levels, the majority of photons scattered do not cause spin state decoherence, so long as the detuning of each Raman beam from the single photon resonance is larger than the fine structure splitting of the upper level [49].

In addition to quantum information processing experiments, the NIST group has also performed an interesting study of the decoherence of quantum systems and the exploration of the transition between classical and quantum behaviour. In 1996 they created superpositions of motional states of a single ion which are analogous to Schrödinger’s cat states [50]. These were used to study decoherence by applying phase and amplitude damping to superpositions of coherent and Fock states of motion [51]. The Michigan group has also studied Schrödinger cat states more recently [52]. Both studies are closely related to the results presented in chapter 7 of this thesis.

1.2 Thesis Layout

This thesis describes work done as part of the long term development of an ion trap information processor in Oxford. The experiments described are all concerned with the preparation, characterisation and control of the spin and motion of one and two ions. The short term goal of these experiments was implementation of a universal 2-qubit logic gate, and deterministic entanglement of the spin states of two ions. A detailed study of the physical mechanism which was used to implement the gate was performed using a single ion. These experiments produced entangled states of the spin and motion which are interesting in their own right.

Chapter 2 describes the experimental apparatus and methods used for Doppler cooling, initialisation, coherent manipulations and readout of the ions.

A brief introduction to the interaction between the laser fields and a single ion is given in chapter 3. A theoretical derivation of the Hamiltonian for this interaction is given for two light fields with a difference frequency tuned close to resonance with spin flip transitions, and close to resonance with the vibrational frequency of the ion. The effect of ion motion on the interaction strength is also considered. Solutions of Schrödinger’s equation are given for an ion in the Lamb-Dicke regime.

Chapter 4 describes a study of the cooling of a single ion to the ground state of motion using Doppler cooling plus two methods of sideband cooling. This builds upon earlier work described in the thesis of Dr. S. Webster [53]. A measurement of the heating rate of the ion from the ground state is described and compared to values measured by other ion trap groups. The final part describes the creation of Fock states of motion of a single ion by the application of sideband pulses to an ion in the ground state.

The work in chapter 5 is concerned with characterisation of decoherence of the quantum states of a single trapped ion. A brief description of the sources of decoherence of the spin and motional degrees of freedom is given. The spin coherence time is measured

using a Ramsey separated pulse sequence. A similar method is used to study the motional coherence time of a single ion in our trap. The final parts of the chapter describe experiments which measure decoherence during interaction between the ion and the Raman light fields. This leads to infidelity during logic operations. A study of the photon scattering rate is included.

Chapter 6 gives an introduction to cooling and manipulation of the quantum states of two trapped ions. The methods used for cooling and temperature diagnosis of two ions are described and experimental results are given. The second part of this chapter describes Rabi flopping experiments with two ions. The results allow us to deduce the relative intensity of the light at each ion. A method for equalising the illumination of the ions is described.

Chapter 7 describes the generation of Schrödinger's cat like states, entangled states of the spin and motional degrees of freedom. These states are generated by application of a spin-state dependent optical dipole force. The polarisation components of the light field used to create the force also cause shifts in the energies of the two qubit states. These are discussed and used to diagnose laser intensity. The state-dependent force on the ion allows us to create superpositions of mesoscopic states of motion. A measurement of the coherence time of these states is described.

In chapter 8, a method for partial tomography of the spin states of two trapped ions is given. Currently our experiment is restricted to performing the same rotation to both ions, and the readout method cannot distinguish $|\uparrow\downarrow\rangle$ from $|\downarrow\uparrow\rangle$. This restricts the information which can be obtained from the tomography. The partial tomography is experimentally demonstrated by application to states created by single qubit rotations.

Chapter 9 describes the experimental demonstration of entanglement of two spin qubits. A diagnostic experiment for setting the correct ion separation is described. In initial experiments, the method used was the same as that used by Leibfried et. al. [23]. However the light shift effects described in chapter 7 made entanglement difficult to achieve by this method, and reduced the fidelity with which the desired state was created. Further experiments were performed with a pulse sequence which cancelled the light shift. This allowed a simple diagnostic experiment to be used to optimise the force on the ion, resulting in a higher fidelity. The tomography method described in chapter 8 was used to reconstruct the density matrix of the entangled state. Sources of infidelity are discussed, and future improvements suggested.

Chapter 10 is a study of the design of electrode structures optimised for fast separation of ions in a single trap into two separated traps. These ideas are important in the context of scaling up the ion trap system to a large processor. The study includes a discussion of the issues surrounding trap design, which is applied to a large range of potential electrode configurations. The effect of imperfections in trap fabrication is also quantified.

Chapter 11 concludes.

Chapter 2

Experimental Details.

This chapter gives an overview of the apparatus used in the experiments described throughout the rest of this thesis. It introduces in turn the trap itself, the Calcium ion and qubit states, the laser systems used to address transitions, and the methods by which the experiment is controlled. The final section describes the various stages of a typical experimental sequence.

2.1 Trapping and Loading Ions

2.1.1 The electrodes.

Our trap is a linear Paul trap, which confines ions using a combination of static and oscillatory electric fields. The electrode geometry is shown in figure 2.1. An alternating voltage is applied to the four r.f. electrodes, producing an oscillating quadrupole which confines ions in the x, y plane. Axial confinement is provided by two d.c. endcap electrodes.

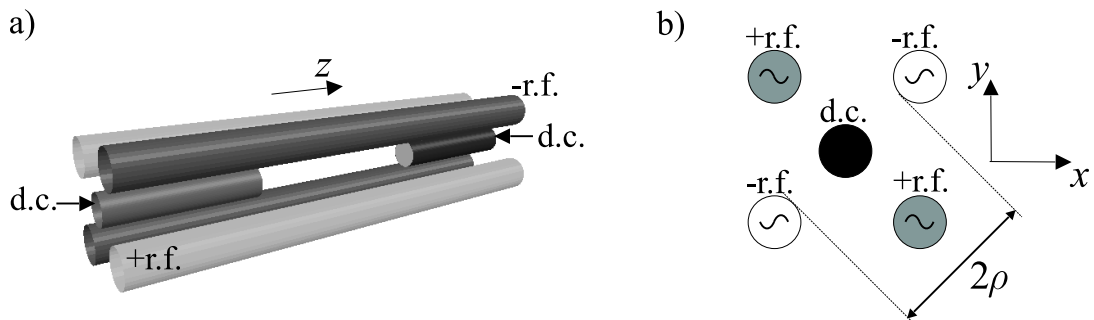


Figure 2.1: a) A perspective view and b) a cross-section view of the r.f. and d.c. electrodes of our trap. Diagonally opposite pairs of r.f. electrodes have the same voltage applied. Voltages on the two pairs of r.f. electrodes are 180° out of phase. The voltages on the two d.c. end-cap electrodes are controlled separately. The shortest distance between the ions and any electrode surface is $\rho = 1.22$ mm.

To provide the radial confinement, voltages of $V_0 \cos(\Omega t)$ are applied to diagonally opposite pairs of r.f. electrodes, with one pair 180° out of phase with the other. The distance from the centre of the trap to the r.f. electrode surface is $\rho = 1.22$ mm.

Confinement in the z direction is provided by positive voltages U_{EC1} and U_{EC2} applied to the two d.c. end-cap electrodes, which are positioned on the axis of the trap with ends at $\pm r_z = 3.6$ mm. Trap centre is taken to be at $z = 0$. These voltages are provided by two channels of an EMCO octo-channel supply. Each channel of this system converts a d.c. input voltage of 0-5 V into a proportional high voltage output. The voltage which can be applied to the end-cap electrodes is limited by the breakdown voltage of the vacuum feedthrough at $U \simeq 700$ V.

2.1.2 Trapping fields and ion frequencies.

For a perfectly built trap with voltage U applied to both end-cap electrodes, the potential near the centre of the trap is of the form

$$V(x, y, z) = \frac{\eta_{dc}U}{r_z^2} \left(z^2 - \frac{x^2 + y^2}{2} \right) + \frac{\eta_{rf}V_0}{\rho^2} \cos(\Omega_{rf}t)(x^2 - y^2) \quad (2.1)$$

where η_{dc} and η_{rf} are parameters which account for shielding effects due to the trap geometry. For our trap, these parameters have been measured to be $\eta_{dc} = 0.10(3)$ and $\eta_{rf} = 1.1(2)$ [54].

The potential along the z axis consists solely of the d.c. term. The axial ion motion is thus simple harmonic motion with frequency

$$\omega_z = \sqrt{\frac{2e\eta_{dc}U}{Mr_z^2}} \quad (2.2)$$

where M is the mass of the calcium ion.

The motion of ions in the radial directions can be calculated by transforming the equation of motion into the Mathieu form [55, 56] with Mathieu parameters

$$q_x = \frac{4e\eta_{rf}V_0}{M\Omega_{rf}^2\rho^2}, \quad a_x = -\frac{4e\eta_{dc}U}{M\Omega_{rf}^2r_z^2} \quad (2.3)$$

The solutions to the Mathieu equation can be found using the Floquet theorem. For the trap parameters used in our experiment, $|a_x| \ll q_x^2 \ll 1$, so a satisfactory approximate solution can be obtained using the pseudopotential model [55, 57].

$$x(t) \simeq x_0 \cos\left(\frac{\beta\Omega_{rf}}{2}\right) \left(1 + \frac{q_x}{2} \cos(\Omega_{rf}t)\right) \quad (2.4)$$

where x_0 is set by the initial conditions and

$$\beta = \sqrt{\frac{q_x^2}{2} - a_x} \quad (2.5)$$

The trajectory described by equation 2.4 involves oscillations at the secular frequency $\omega_r = \beta\Omega_{rf}/2$ superposed with a fast oscillation at frequency Ω_{rf} , which is called micromotion. The amplitude of the micromotion is smaller than the secular motion by the factor $q_x/2$. The micromotion oscillation is in phase with the driving fields, hence the ion does not exchange energy with them.

The maximum end cap voltage of 700 V limits the axial trap frequency to $\omega_z \leq 2\pi \times 812$ kHz. The centre of the trap can be moved along the z -axis by adjusting the relative voltage on the d.c. electrodes.

The r.f. voltage is generated by a Colpitts oscillator circuit, which oscillates at a frequency of 6.3 MHz when connected to the trap. This circuit generates a maximum voltage of $V_0 \simeq 120$ V. We typically work at $V_0 \simeq 91$ V to reduce the amount of electrical noise on the electrodes. Using this voltage on the r.f. electrodes means that the radial secular frequencies are 722 kHz when the axial frequency is 800 kHz and 850 kHz when the axial trap frequency is 500 kHz.

The ion frequencies can be measured by scanning the frequency of an oscillating “tickle” voltage applied to one of the d.c. trap electrodes. The ions are continuously Doppler cooled, and the fluorescence is observed on a CCD camera. When the tickle frequency is resonant with the secular motion, the motion of the ion is resonantly excited, which can be seen on the camera. This method determines the secular frequency to < 1 kHz. In order to measure axial frequency, the tickle voltage is applied to one of the end-cap electrodes. In order to measure the radial frequency, it must be applied to one of the d.c. compensation electrodes, which are parallel to the r.f. electrodes but are positioned at a radius of 5.94 mm [54].

2.1.3 Compensation of stray d.c. electric fields.

Stray electric fields in one of the radial directions move the equilibrium position of the ion away from the axis of the trap. A stray field $\underline{E} = E\hat{x}$ displaces the ion along the x axis, and the ion experiences an oscillating field in the y direction. This oscillating field produces an increase in the micromotion component along y . If the ion is interacting with light which has wavevector component along y , then in the rest frame of the ion, the light has a modulated Doppler shift at the frequency of the micromotion. The response of the ion changes with the Doppler shift, so by looking for correlations between the arrival time of photons scattered from the ion and the r.f. drive voltage, the presence of micromotion can be detected. The method used is described in detail in the thesis of Dr. J. P. Stacey [58]. The stray electric fields are then nulled by applying d.c. voltages to two of the four “compensation” electrodes.

2.1.4 Loading Ions

Ions are loaded into our trap by a two photon photo-ionisation method, the details of which can be found in [59]. The method uses two lasers at 423 nm and 389 nm which intersect at 90° with a beam of calcium atoms effusing from an oven. The oven consists of a metal tube containing solid calcium. A d.c. current is passed through the walls of the oven and heats it up, causing sublimation of the calcium. A small hole in the side of the metal tube allows any gaseous calcium to effuse. 423 nm laser light excites the $^1S_0 \rightarrow ^1P_1$ transition in the calcium atoms. 389 nm light then excites population from this state into the continuum. This creates charged ions which can then become trapped.

2.2 The $^{40}\text{Ca}^+$ ion.

The lowest energy levels in the $^{40}\text{Ca}^+$ ion are shown with the linewidths and branching ratios for transitions between them in figure 2.2. In our experiments the two spin states of the $4S_{1/2}$ level are used as the qubit. A field of $\simeq 1.5$ Gauss is applied in order to separate these states in energy by $\simeq h \times 4.2$ MHz. We define $|\downarrow\rangle$ to be the state which has the lower energy. Doppler cooling, sub-Doppler cooling and fluorescence detection are all

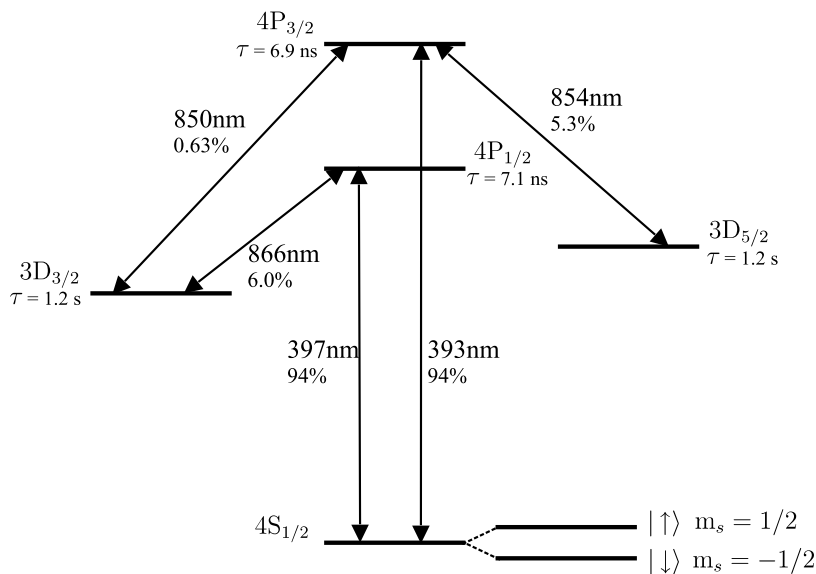


Figure 2.2: The lowest energy levels of the $^{40}\text{Ca}^+$ ion and the transitions between them. The energies are not shown to scale. A d.c. magnetic field is applied to the ion, which splits up the energies of the Zeeman sub-levels of each level. This is only shown in the case of the ground state. Throughout this thesis I use the convention that the spin state having the lowest energy is spin down, and the higher energy state is spin up.

performed by illuminating the ion with 397 nm laser light. An intense 866 nm laser is used to repump population which decays from the $4P_{1/2}$ level into the $3D_{3/2}$ level. The 393 nm, 854 nm and 850 nm lasers are all used to read out the spin-state of the ion.

2.2.1 Magnetic fields.

The d.c. magnetic fields in our trap are provided by 3 pairs of coils which pass d.c. current. The coils are arranged such that the direction of the field can be completely controlled by adjusting the relative current passing through them.

During the loading process, a large current is passed through the oven, which heats up. Experimentally we find that this causes a shift in the magnetic field at the position of the ion, and the field continues to drift after the oven current has been turned off. This can be observed by magnetic resonance as follows. The ion is prepared in the spin state $|\downarrow\rangle$, then an oscillating magnetic field is applied, which drives Rabi oscillations between the two qubit states. The spin state of the ion is subsequently measured. For a fixed pulse duration and frequency, the experiment is repeated 500 times, and the fraction of times that the ion is measured to be spin up is recorded. The frequency of the oscillating magnetic field pulse is then changed, and the experiment is repeated. For pulse durations less than π/Ω , where Ω is the Rabi frequency of the radiation-ion interaction, the maximum population in spin up will occur when the oscillating magnetic field is resonant with the qubit transition. The magnetic field is then found using $B = hf_0/2\mu_B$, where f_0 is the magnetic resonance frequency.

The results of a series of these scans taken while the oven was on and for the two hours after turning the oven off is shown in figure 2.3. From the figure, we can see that turning

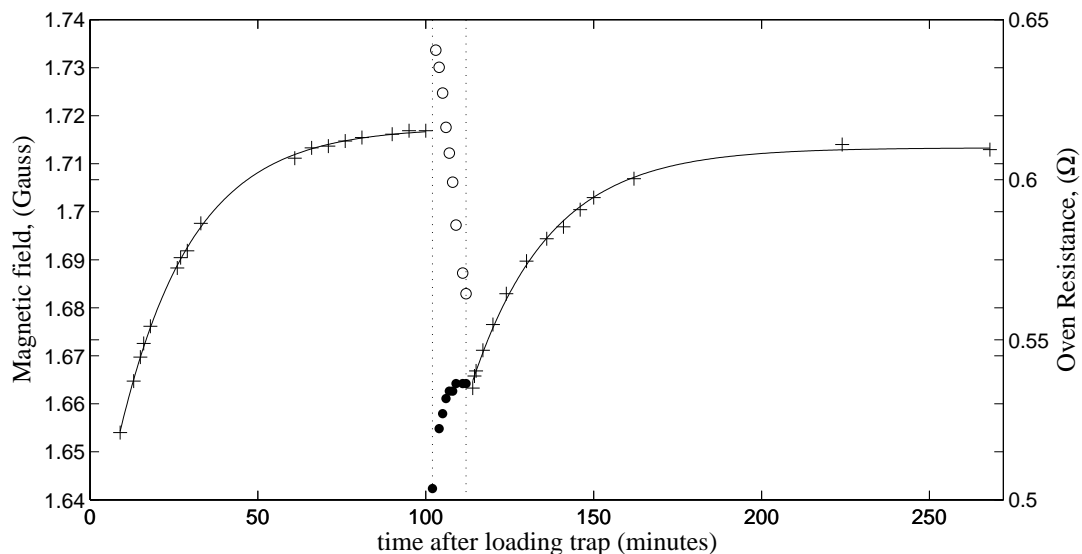


Figure 2.3: The magnetic field deduced from the frequency separation of the Zeeman sub-levels of the ground state plotted as a function of time after loading the trap (which is when the oven was turned off). Data taken with the oven turned off are represented by +, and data taken with the oven turned on by \circ . The oven was turned on at $t = 100$ minutes and off again at $t = 114$ minutes. The oven current was monitored while the oven was turned on, which gives a measurement of the resistance (filled circles). The oven resistance gives an indication of the temperature of the oven. Both sets of data taken with the oven turned off are fitted with exponential decay curves, which have decay times of 22 minutes and 23 minutes for the earlier and later data sets respectively.

on the oven produces a sudden shift of the magnetic field at the ion of $\simeq 15$ mG. Turning the oven off produces a similar shift but with the opposite sign. This implies that the current through the oven creates a magnetic field at the ion of $\simeq 15$ mG.

During the 10 minute period when the oven is on, the field also drifts by 50 mG. After the oven is switched off, the field exponentially drifts back to close to the value it was at before the oven was switched on with a time constant of around 23 minutes. These drifts are possibly due to magnetisation of materials in the walls of the vacuum can or the walls of the oven itself.

A typical experiment involving cooling to the ground state and coherent manipulations of the ion's spin requires the frequency splitting of the spin states to be stable to within 10 kHz, and for some experiments to within 1 kHz. 10 kHz corresponds to a magnetic field of 3.6 mG. It can be seen from the figure that due to the drifting magnetic field experiments requiring < 3.6 mG drift cannot be performed for ~ 120 minutes after loading the trap.

2.3 Laser Systems.

Table 2.1 gives a summary of the laser systems used for the $^{40}\text{Ca}^+$ experiments presented in the rest of the thesis. Full details can be found in the theses of J. P. Stacey [58], M. J. McDonnell, [60], C. J. Donald [54] and D. Stevens [61]. Here I present a brief

overview. All the laser systems are extended cavity diode lasers except for the 397nm “slave” laser which is used to drive Raman transitions. The “slave” laser is a further diode laser, but its frequency is controlled through injection locking by the “master” laser. The external cavities are used in the Littrow configuration, i.e. the first order light from a grating at one end of the cavity is directed back into the diode. Zeroth order light is used as the output of the laser. The laser wavelength is crudely controlled by adjusting the temperature of the diode, and the angle of the grating. Finer adjustment can be achieved by changing the current through the diode or the length of the external cavity. In our laser systems this is done by applying a voltage to a piezo-electric crystal on the back of the grating.

wavelength	Diode Power	Reference cavity width	Lock type	Lock width	Extinction ratio
(nm)	(mW)	(MHz)		(MHz)	$I_{\text{off}}/I_{\text{on}}$
397	30	110	side		$< 10^{-6}$
397 “master”	5	n/a	n/a	n/a	n/a
397 “slave”	30	n/a	n/a	n/a	10^{-3}
866	50	15	side		
393	5	2.9	PDH	1.5	10^{-6}
850	150	15	side	1.5	
854	50	n/a	n/a	n/a	

Table 2.1: Laser systems used in experimental work. The 854 laser is not locked to a cavity. The third column gives the FWHM of the transmission of an optical reference cavity to which the laser is locked by an electric servo. The type of lock used is either to the side of a cavity fringe, or a Pound-Drever-Hall [62] system. The extinction ratio is defined as the ratio of intensities of light arriving at the ion when the beam is switched off by one or more AOMs to when it is switched on.

2.3.1 Frequency stabilisation and control.

For some of our laser systems, we require high frequency stability. In order to achieve this these lasers are locked to high-finesse reference cavities. The important characteristics of the cavities are the reflectivity R of the mirrors and the length L . The length of the cavity defines the free-spectral range $c/2L$, which is the frequency difference between adjacent longitudinal cavity modes. For some of our cavities the cavity length can be adjusted to change the transmission frequency.

The 397 nm laser is locked to a 250 mm fixed-length home made confocal cavity. The 393 nm, 866 nm and 850 nm lasers are locked to scannable commercial cavities built at the National Physical Laboratory. The method we use for reading out the spin state of the ion uses a two-photon resonance driven by 393 nm and 850 nm laser beams. This resonance is sensitive to their linewidth, hence for the 393 nm laser a Pound-Drever-Hall [62] method is used. All the other lasers are locked to the side of a cavity fringe.

2.3.2 Switching

The laser beams are switched on and off using Acousto-Optic Modulators (AOMs). These work by passing an acoustic wave through a crystal. This modulates the refractive index

of the crystal, which results in Bragg diffraction of light passing through it. The first order beam is used for the experiment. The extinction of the AOMs is imperfect. On a single pass, the ratio of the intensity following the first order beam path when the AOM is switched on to that when it is switched off is typically $\simeq 1000$. For light which is resonant with transitions from the ground state better extinction is required, hence at least one of the AOMs in these beams is used in double pass.

2.3.3 Pulse generation.

The pulse sequences are generated by a laser control unit (LCU) designed by B. Keitch [63]. The LCU unit has 16 input channels plus a clock input, and generates TTL pulses on 16 output channels which can drive loads of input impedance $\geq 50 \Omega$. In a typical experiment, a pulse sequence is programmed into the computer. This is then written to a hardware timing card which controls the input to the LCU. The card had a time resolution of $0.2 \mu\text{s}$ for all the experiments except those described in chapters 8 and 9, which used an upgraded card with a time resolution of $0.1 \mu\text{s}$. The TTL pulses drive switches on synthesizers which power the AOMs or the r.f. output to the field coil. The minimum time between pulses generated by the control unit is limited by the time taken for the computer to write to the IC hardware timing card. During this time the gated input to the LCU is off, hence all the clocked digital outputs are also turned off. This “dead” time is $13.2 \mu\text{s}$ in all experiments except those in chapters 8 and 9, for which the dead time is $6 \mu\text{s}$. Some of the outputs from the LCU are not synchronized with the clock, hence output on these channels will change as soon as instructions are written to the timing card. This is useful for ensuring some laser pulses switch on in the correct sequence (eg. so that the 850 nm laser turns on before the 393 nm laser during the readout sequence).

2.4 Laser use in a typical experiment.

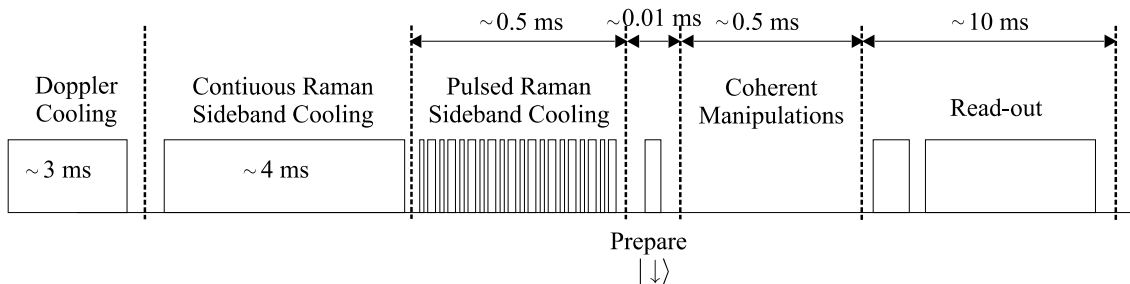


Figure 2.4: A typical experimental sequence, not drawn to scale. An indication of the duration of each part of the sequence is given. The coherent manipulations section is left blank as sequences of Raman pulses in this period of the experiment are the focus of most of the rest of this thesis.

A typical sequence of pulses used in one run of an experiment is shown in figure 2.4. A given sequence is repeated a large number ($500 \rightarrow 1000$) of times, which allows us to deduce the populations of the ground spin states at the end of the sequence. The experiment starts with Doppler cooling of the ion, then has two periods of sub-Doppler cooling. The spin state of all of the ions is then set to $|\downarrow\rangle$ by optical pumping, and subsequently coherent

manipulations are carried out. The final stage of the experiment is read-out of the spin state of the ion. This is described in section 2.4.3.

The directions of the laser beams with respect to the trap axis (z) are shown in figure 2.5. Three laser beams are not shown as their directions are out of the plane of the diagram. These are the photo-ionisation lasers and the vertical 397 nm beam which is used for compensation of stray horizontal fields (see section 2.1.3).

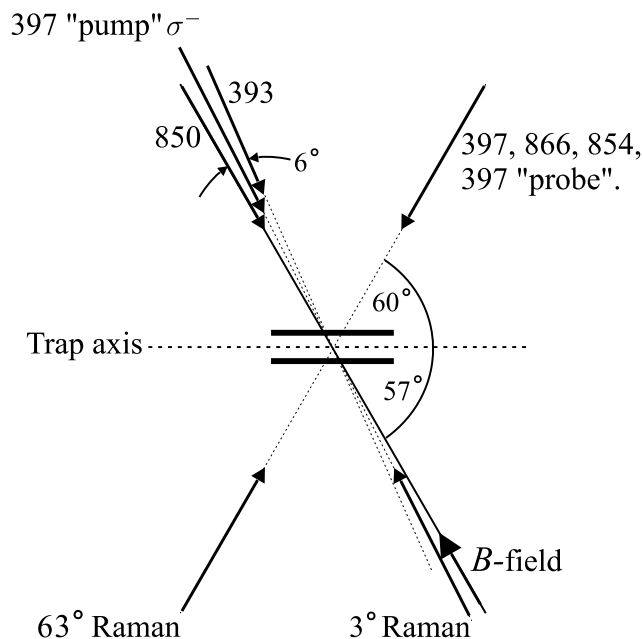


Figure 2.5: Directions of the laser beams with respect to the trap axis. The 850 nm is aligned along the magnetic field, with the 397 nm ‘‘pump’’ beam at 3° and the 393 nm at 6° to this direction. The two Raman beams are at 3° and 63° to the magnetic field.

2.4.1 Cooling and population preparation.

The 397 nm transition is used for cooling the ion and for population preparation. Doppler cooling is implemented with a linearly polarised 397 nm beam propagating at 60° to the trap axis with the 866 nm laser, linearly polarised in the vertical direction, serving to repump population out of $D_{5/2}$ level. This allows all three modes of motion of the ion to be cooled. The Doppler limit temperature is $\simeq 540 \mu\text{K}$ for this transition, which is equivalent to $\bar{n} = 20$ in the 500 kHz trap and $\bar{n} = 10$ in the 800 kHz trap. We don’t expect to reach the Doppler limit temperature after Doppler cooling as the Zeeman splitting of the ground state means that the transition is effectively broadened. We expect the temperature of the ion after Doppler cooling to be $\sim 1 \text{ mK}$.

The second stage of cooling is continuous Raman sideband cooling, implemented by two laser beams which are red-detuned 130 MHz from the 397 nm transition. The low intensity ‘‘probe’’ beam enters the trap coincident with the Doppler cooling beam, while the high intensity σ^- polarised ‘‘pump’’ beam is aligned at 3° to the magnetic field.

The quantum state $|\downarrow\rangle$ is used as the initial state of the ions in all the experiments presented throughout this thesis. The state is prepared by pulsing on the pump beam for

long enough to ensure that the population has been optically pumped into this state. Due to the relative sizes of the Clebsch-Gordon co-efficients for decay from the $P_{1/2}$ levels, on average 3 photons are required to prepare the $|\downarrow\rangle$ state.

2.4.2 Coherent Manipulations

Coherent manipulations of the ion's spin state are performed using either an oscillating magnetic field or by driving a Raman transition.

The oscillating magnetic field is provided by a 40 turn coil of 1 mm thick copper wire which sits on the top window of the vacuum system. The coil has a conical geometry with an opening angle of 30° , in order that it doesn't block the photoionisation and 397 nm vertical micromotion compensation laser beams. It has two layers which are 2 mm apart, spaced in order to reduce resistance due to proximity effects [64]. The coil forms part of a resonant circuit, which when placed on the trap has a Q of $\simeq 34$. A variable capacitor attached in series with the coil allows the resonant frequency to be tuned over a range of ~ 500 kHz around a centre frequency of 4.5 MHz.

Raman transitions are driven using a pair of laser beams derived from the slave laser of a master-slave system. The beams are detuned by $\simeq 30$ GHz from resonance with the 397 nm $^2S_{1/2} \rightarrow ^2P_{1/2}$ transition. The choice of detuning was made based on a previous study of photon scattering using a blue diode laser [54], in which increased photon scattering due to amplified spontaneous emission was observed when the laser is detuned from resonance by multiples of 60 GHz.

The master-slave system is a commercial Toptica system and was set up by Dr. Matthew McDonnell. A full description is given in his thesis [60]. The optical layout was set up by Dr. Simon Webster – further details can be found in his thesis [53]. The two beams enter the trap at 60° to one another, and to the trap axis. The beam aligned at 3° to the magnetic field is vertically polarised, which means that the intensity of the π polarisation component is less than 0.6% of the intensity in each circular polarisation component.

The beam at 63° to the magnetic field is linearly polarised with its axis of polarisation at an angle β to the vertical. Choosing a primed frame with the z' axis pointing along the direction of the beam, y' axis vertical and the x' axis in the plane of the trap axis and the laser beams, the electric field is

$$\mathbf{E}_{63} = |\mathbf{E}_{63}| [\sin(\beta)\hat{\mathbf{x}}' + \cos(\beta)\hat{\mathbf{y}}'] \cos(\omega_2 t + \phi_2) \quad (2.6)$$

where $|\mathbf{E}_{63}|$ is the amplitude of the electric field, ω_2 is the frequency of the laser beam and ϕ_2 is its phase. This frame can be projected onto the axis defined by the magnetic field. Defining an unprimed frame with z the opposite direction to the B-field, y vertical and x perpendicular to both, the electric field is given by

$$\mathbf{E}_{63} = |\mathbf{E}_{63}| [\sin(\beta) \cos(63^\circ)\hat{\mathbf{x}} + \cos(\beta)\hat{\mathbf{y}} - \sin(\beta) \sin(63^\circ)\hat{\mathbf{z}}] \cos(\omega_2 t + \phi_2) \quad (2.7)$$

This field can be decomposed into σ^+ , σ^- and π components using $\mathbf{E}_{\sigma^\pm} = (\mathbf{E}_x \pm i\mathbf{E}_y)/\sqrt{2}$,

$\mathbf{E}_\pi = \mathbf{E}_z$, which gives

$$\mathbf{E}_{63}^{\sigma^+} = \frac{1}{\sqrt{2}} |\mathbf{E}_{63}| [\cos(63^\circ) \sin(\beta) \hat{\mathbf{x}} + i \cos(\beta) \hat{\mathbf{y}}] = \sqrt{I_{\sigma^+}} e^{i\Phi} \quad (2.8)$$

$$\mathbf{E}_{63}^{\sigma^-} = \frac{1}{\sqrt{2}} |\mathbf{E}_{63}| [\cos(63^\circ) \sin(\beta) \hat{\mathbf{x}} - i \cos(\beta) \hat{\mathbf{y}}] = \sqrt{I_{\sigma^-}} e^{-i\Phi} \quad (2.9)$$

$$\mathbf{E}_{63}^\pi = -|\mathbf{E}_{63}| \sin(63^\circ) \sin(\beta) \hat{\mathbf{z}} = \sqrt{I_\pi} \quad (2.10)$$

$$(2.11)$$

where the phase Φ is given by

$$\Phi = \arctan \left[\frac{1}{\cos(63^\circ) \tan(\beta)} \right] \quad (2.12)$$

and the intensities of the three components are

$$I_\pi = I_{63} \sin^2(63^\circ) \sin^2 \beta \quad (2.13)$$

$$I_{\sigma^\pm} = \frac{1}{2} I_{63} [\cos^2(63^\circ) \sin^2 \beta + \cos^2 \beta] \quad (2.14)$$

In most of the experiments presented in this thesis $\beta = 45^\circ$ ¹, hence the intensities of the polarisation components are $I_\pi = 0.40 I_{63}$, $I_{\sigma^\pm} = 0.30 I_{63}$ and the phase $\Phi = 1.14$ radians.

The relative frequency of the 3° beam and the 63° beam is controlled by the relative frequencies of the AOMs which they pass through. The frequency of the 63° beam AOM is fixed. Changes to the difference frequency of the two beams are implemented by changing the driving frequency of the 3° beam AOM. This also causes the deflection angle of the beam through the AOM to change. For this reason, the centre of the AOM is imaged onto the ions [53]. The final lens before the trap is mounted on a $x - y - z$ translation stage to allow fine adjustment of the beam position.

2.4.3 Read-out

The read-out of the quantum state of the ions at the end of the experiment was devised by Dr. M. McDonnell, and the details can be found in his thesis [60]. It is performed in two stages. In the first, a σ^+ polarised 393 laser is used to transfer population from the $|\uparrow\rangle$ state via $P_{3/2}$ into the $D_{5/2}$ ‘‘shelf’’ level, so called because when the fluorescence lasers (397 nm and 866 nm) are on, population in this state does not interact with the light. Population transfer out of the $|\downarrow\rangle$ state is inhibited by a dark resonance created by the 393 nm and 850 nm lasers.

The branching ratios for decay from the $P_{3/2}$ level to the $S_{1/2}$, $D_{5/2}$ and $D_{3/2}$ levels are 94%, 5.3% and 0.63%. In order to transfer population from $|\uparrow\rangle$ into the shelf, the ion must on average absorb ~ 20 photons. This means that by the time the ion reaches its final state, 13% of the population will have been repumped by 866 nm light. On average, half of this amount will be repumped into the wrong ground state, which places a limit on the fraction of population making the transfer from $|\uparrow\rangle \rightarrow D_{5/2}$ at $\sim 94\%$. The readout efficiency is further limited by the linewidth and power of the 393 nm and 850 nm lasers [60, 65].

¹Subsequently we have found that this value is incorrect due to modification of the state of polarisation caused by a mirror placed after the $\lambda/2$ plate in the 63° beam path. See the results section of chapter 7 for details.

After the population transfer pulse has been applied, the 397 nm and 866 nm lasers are turned on, and the fluorescence level is recorded using collection optics and a photomultiplier tube (PMT). A typical count rate is around 10 ms^{-1} per ion.

The experimental sequence is repeated a large number of times (typically 500), and the fraction of times that the ion produces fluorescence above a set threshold is recorded. This gives values for the probability of fluorescence $P(f)$.

The imperfect readout efficiency does not prevent us learning full information about the spin state of the ion, given that can find the probabilities of fluorescence are for an ion in each of the two spin states by repeating the experiment a large number of times². Let $p = P(f|\downarrow)$ probability that an ion prepared in the $|\downarrow\rangle$ state produces fluorescence, and $q = P(s|\uparrow)$ be the probability that an ion prepared in the $|\uparrow\rangle$ state is shelved. These probabilities can be determined by repeatedly preparing the ion in the state $|\downarrow\rangle$, and reading out the state of the ion, then repeating the same procedure with the ion prepared in the state $|\uparrow\rangle$.

The probabilities that the ion is shelved (or fluorescing) given that it had a probability of $P(\uparrow)$ of being spin up, and a probability $P(\downarrow)$ of being spin down, are given by

$$\begin{pmatrix} P(s) \\ P(f) \end{pmatrix} = \begin{pmatrix} q & 1-p \\ 1-q & p \end{pmatrix} \begin{pmatrix} P(\uparrow) \\ P(\downarrow) \end{pmatrix} \quad (2.15)$$

In order to deduce the spin state at the end of the experiment from the fluorescence probability, we must invert this to obtain

$$\begin{pmatrix} P(\uparrow) \\ P(\downarrow) \end{pmatrix} = \frac{1}{p+q-1} \begin{pmatrix} p & p-1 \\ q-1 & q \end{pmatrix} \begin{pmatrix} P(s) \\ P(f) \end{pmatrix} \quad (2.16)$$

For an experiment involving two ions, an extra threshold is set, which allows us to distinguish between fluorescence from both ions and fluorescence from only one ion. The probability that both ions fluoresce given that the state prior to readout was $|\downarrow\downarrow\rangle$ is $P(ff|\downarrow\downarrow) = p^2$. The probability that both are shelved given that the state prior to readout was $|\uparrow\uparrow\rangle$ is $P(ss|\uparrow\uparrow) = q^2$. These values can be obtained by the same method as for a single ion. The populations of the states can be deduced from the probabilities $P(ss)$, $P(sf)$, $P(fs)$ and $P(ff)$ by taking the outer product of the matrix in equation 2.16 with itself. In our experiment, we have no way of deducing which of the two ions are fluorescing, hence the size of this matrix reduces from 4×4 to 3×3 , and we have

$$\begin{pmatrix} P(\uparrow\uparrow) \\ P(\uparrow\downarrow + \downarrow\uparrow) \\ P(\downarrow\downarrow) \end{pmatrix} = \frac{1}{(p+q-1)^2} \begin{pmatrix} p^2 & p(p-1) & (1-p)^2 \\ 2p(q-1) & 2pq-p-q+1 & 2q(p-1) \\ (q-1)^2 & (q-1)q & q^2 \end{pmatrix} \begin{pmatrix} P(ss) \\ P(sf+fs) \\ P(ff) \end{pmatrix} \quad (2.17)$$

where $P(sf+fs)$ is the probability that one ion only fluoresces and $P(\uparrow\downarrow + \downarrow\uparrow)$ is the probability of finding the ions in either $|\uparrow\downarrow\rangle$ or $|\downarrow\uparrow\rangle$ if a direct measurement of the spins could be made.

²More advanced quantum information experiments such as teleportation and error correction require operations conditional on a measurement made within a single shot of the experiment. In this case imperfect readout would become a problem. High fidelity single shot readout of ions was used in the demonstrations of teleportation carried out at NIST, Boulder and the University of Innsbruck [37, 41], and the error-correction experiment carried out at NIST [38].

Chapter 3

Coherent interaction of light with a trapped ion.

This chapter introduces the basic physics of the interaction between the Raman laser beams and a trapped ion. For simplicity, a single ion is considered. The generalisation to two trapped ions is discussed in later chapters.

3.1 The Hamiltonian for a trapped ion

The Hamiltonian for a single ion in a harmonic trap can be written as a sum of motional and internal parts. In order to describe the interaction of the Raman beams with the ion the simplest approach is to describe an atom with three electronic energy levels E_1 , E_2 , E_3 , as shown in figure 3.1. The energy of the lowest level is taken to be the zero of energy ($E_1 = 0$). The energy difference between level 3 and level 2 is much larger than the energy separation of the lower two levels. The Hamiltonian for the internal energy of the ion is then

$$\hat{H}_S = E_2 |e_2\rangle \langle e_2| + E_3 |e_3\rangle \langle e_3| \quad (3.1)$$

where $|e_i\rangle$ is the electronic state of the i th level.

The difference wavevector of the Raman laser beams is aligned along the axis of the trap, hence we consider solely the axial motion, for which the harmonic approximation is very accurate. The position of the ion is given by \underline{r} . The Hamiltonian for the motion of the ion along the axis is

$$\hat{H}_z = \hbar\omega_z(\hat{a}^\dagger\hat{a} + 1/2) \quad (3.2)$$

where ω_z is the vibrational frequency of the axial mode given by equation 2.2, and \hat{a}^\dagger and \hat{a} are the creation and annihilation operators of the ion's vibrational mode. The position of the ion relative to its equilibrium position is given by $z = z_0(\hat{a} + \hat{a}^\dagger)$, where $z_0 = \sqrt{\hbar/2M_{Ca}\omega_z}$ is the r.m.s. size of the ground state wavefunction.

The eigenstates of the motional Hamiltonian are the harmonic oscillator Fock states, which are labelled by the quantum number n , and have energy $\hbar\omega_z(n + 1/2)$. The Fock states will be written in the form $|n\rangle$ throughout the rest of this thesis.

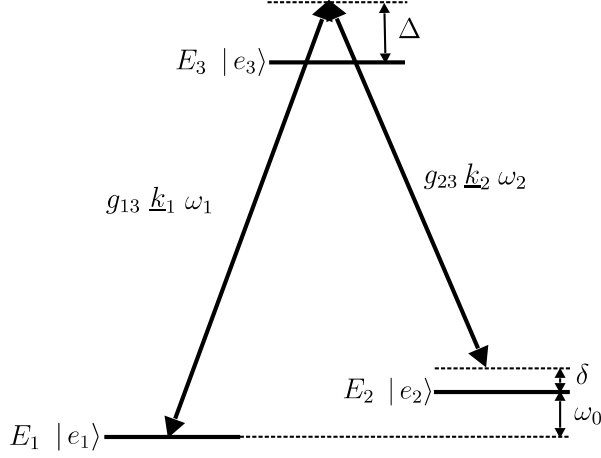


Figure 3.1: The electronic energy levels for a three-level atom. In the text, the energy of the state $|e_1\rangle$ is taken to be zero. The energies of the other levels are given as E_2 and E_3 which are measured relative to E_1 . Radiation of frequency ω_1 and wavevector \underline{k}_1 interacts with the atom, coupling the states $|e_1\rangle$ and $|e_3\rangle$ with strength g_{13} . Radiation of frequency ω_2 and wavevector \underline{k}_2 interacts with the atom, coupling the states $|e_2\rangle$ and $|e_3\rangle$ with strength g_{23} .

3.2 Interaction with two optical light fields.

Coherent manipulations of the spin-qubit and motional states of the ion are driven by stimulated Raman transitions using two high intensity laser beams detuned by $\Delta = 2\pi \times 30$ GHz from the $397 \text{ nm } ^2\text{S}_{1/2} \rightarrow ^2\text{P}_{1/2}$ transition. The parameters which describe the laser beams are shown in figure 3.1. The difference frequency of the two beams is $\omega = \omega_1 - \omega_2 = \delta + \omega_0$, where $\delta \ll \omega_0 \ll \Delta$. The coupling strength between the dipole moment of the ion and the light fields is given by g_{ik} , where levels i and k are the levels coupled by the light.

In the approximation that the light field oscillating at frequency ω_1 (ω_2) only couples $|e_1\rangle$ ($|e_2\rangle$) to $|e_3\rangle$, the interaction Hamiltonian between the two light fields and the three-level ion is

$$\hat{H}_I = \hbar g_{13} \cos(\underline{k}_1 \cdot \underline{r} - \omega_1 t + \phi_1) |e_1\rangle \langle e_3| + \hbar g_{23} \cos(\underline{k}_2 \cdot \underline{r} - \omega_2 t + \phi_2) |e_2\rangle \langle e_3| + \text{h.c.} \quad (3.3)$$

where $g_{13} = g_{31}^* = \langle e_1 | \underline{r} \cdot \underline{\epsilon}_1 | e_3 \rangle \zeta_1 / \hbar$ gives the strength of coupling between the light and the atom. A similar expression holds for g_{23} and g_{32}^* . $\underline{\epsilon}_1$ and ζ_1 are the polarisation direction and magnitude of the optical field which oscillates at ω_1 . It is convenient to work in the interaction picture with respect to the spin Hamiltonian \hat{H}_S and make the rotating wave approximation with respect to the optical frequencies, which gives

$$\hat{H}'_I = \frac{\hbar g_{13}}{2} e^{i(\underline{k}_1 \cdot \underline{r} - \Delta t + \phi_1)} |e_1\rangle \langle e_3| + \frac{\hbar g_{23}}{2} e^{i(\underline{k}_2 \cdot \underline{r} - (\Delta - \delta)t + \phi_2)} |e_2\rangle \langle e_3| + \text{h.c.} \quad (3.4)$$

The laser powers and detunings used in our experiments satisfy the conditions $g, \delta \ll \Delta$, hence we can make the approximation that spontaneous emission from the upper level can be neglected, and this level can be “adiabatically eliminated”. This is described in

appendix A. The resulting Hamiltonian is

$$\begin{aligned} \hat{H}_I &= -\hbar \frac{|g_{13}|^2}{4\Delta} |e_1\rangle \langle e_1| - \hbar \frac{|g_{32}|^2}{4\Delta} |e_2\rangle \langle e_2| \\ &\quad - \frac{\hbar\Omega_R}{2} e^{i(\Delta\mathbf{k}\cdot\mathbf{r}-\delta t+\phi)} |e_1\rangle \langle e_2| - \frac{\hbar\Omega_R^*}{2} e^{-i(\Delta\mathbf{k}\cdot\mathbf{r}-\delta t+\phi)} |e_2\rangle \langle e_1| \end{aligned} \quad (3.5)$$

where $|g_{13}|^2/4\Delta$ and $|g_{32}|^2/4\Delta$ are the single beam light shifts of levels 1 and 2 and $\Omega_R = g_{13}g_{32}/2\Delta$ is the effective Rabi frequency which characterises the coupling between the two levels. $\phi = \phi_1 - \phi_2$ is the phase difference of the two light fields at the position of the ion. In experimental work, the laser polarisations are typically arranged so that the single beam light shifts are the same for each level. This means that the single beam light shifts only contribute to the global phase of the ion, hence these terms be dropped from the Hamiltonian. This has been done for all the work in the rest of this chapter.

3.2.1 Motional effects - the Lamb-Dicke regime.

In our experiments, the difference wavevector of the two light fields is aligned with the z axis of the trap. The wavevectors \mathbf{k}_1 and \mathbf{k}_2 differ in angle by θ , hence $\Delta\mathbf{k}\cdot\mathbf{r} = 2k \sin(\theta/2)z$, where $k = 2\pi/\lambda$ and λ is the wavelength of the optical radiation. It is convenient to introduce the dimensionless Lamb-Dicke parameter, defined as

$$\eta = \delta k z_0 = \sqrt{\frac{E_R}{\hbar\omega_z}} = 2k \sin(\theta/2) \sqrt{\frac{\hbar}{2M\omega_z}} \quad (3.6)$$

where E_R is the recoil energy of the ion. The Lamb-Dicke parameter gives the ratio of the extent of the ground state wavefunction of the ion to the wavelength of the light with which it is interacting. In order that each part of the wavefunction of the ion experiences the same phase of the light field, the extent of the wavefunction must be small compared to the wavelength of the light. Where this is the case, we say the ion is in the Lamb-Dicke regime. For an ion in the Fock state with vibrational quantum number n , the r.m.s. extent of the wavefunction is $z_0\sqrt{2n+1}$, hence this condition is met if $\eta^2(2n+1) \ll 1$.

The momentum imparted to the ion by the light leads to a modification of the Rabi frequency by a factor [30]

$$M_{n',n} = \langle n' | e^{i\eta(\hat{a}+\hat{a}^\dagger)} | n \rangle = (i\eta)^{|n-n'|} (n_{<}/n_{>}!)^{1/2} e^{-\eta^2/2} L_{n_{<}}^{|n-n'|}(\eta^2) \quad (3.7)$$

for a transition where the motional state changes from $|n\rangle$ to $|n'\rangle$, where $n_{>}$ ($n_{<}$) is the greater (lesser) of n' and n and the $L_{n_{<}}^{|n-n'|}(\eta^2)$ are generalized Laguerre polynomials of order $|n-n'|$. In the interaction picture of the harmonic oscillator Hamiltonian \hat{H}_z , this matrix element is

$$M_{n',n}^I = \langle n' | e^{i\eta(\hat{a}e^{i\omega_z t} + \hat{a}^\dagger e^{-i\omega_z t})} | n \rangle \quad (3.8)$$

which means that the Hamiltonian in equation 3.5 can be written

$$\hat{H}_I = -\frac{\hbar\Omega_R M_{n',n}^I}{2} e^{-i(\delta t-\phi)} |e_1, n'\rangle \langle e_2, n| + \text{h.c.} \quad (3.9)$$

In the Lamb-Dicke limit $M_{n',n}$ and $M_{n',n}^I$ can be further simplified by neglecting terms of order η^2 and higher, which simplifies the the Hamiltonian describing the interaction of the ion and the light to the form

$$\hat{H}_I = \frac{\hbar\Omega_R}{2} |e_1\rangle \langle e_2| \left(1 + i\eta(\hat{a}e^{i\omega_z t} + \hat{a}^\dagger e^{-i\omega_z t}) \right) e^{-i(\delta t-\phi)} + \text{h.c.} \quad (3.10)$$

3.2.2 Spin-flip transitions.

In this section, the above discussion is applied to the case in which the radiation drives transitions between different spin states of the ground state of a trapped ion. For simplicity, the ion is assumed to be in the Lamb-Dicke regime. The lower energy state $|e_1\rangle$ is taken to be $|\downarrow\rangle$ and the higher energy state $|e_2\rangle = |\uparrow\rangle$. The polarisation of the two light fields is arranged in order to drive transitions between the spin states.

When the difference frequency of the laser beams is tuned such that it is close to resonance with the frequency difference between the spin states of the ion $|\delta| \ll \omega_z$, the Hamiltonian in equation 3.10 can be written

$$\hat{H}_I \simeq \hat{H}_{\text{carrier}} = \frac{\hbar\Omega_R}{2} |\downarrow\rangle \langle\uparrow| e^{-i(\delta t - \phi)} + \text{h.c.} \quad (3.11)$$

where the rotating wave approximation with respect to the motional frequencies has now been applied. The Schrödinger equation can be solved analytically, and gives a unitary evolution operator

$$U(t, \delta) = \begin{pmatrix} e^{-i\frac{\delta t}{2}} \left[\cos\left(\frac{Xt}{2}\right) + i\frac{\delta}{X} \sin\left(\frac{Xt}{2}\right) \right] & -i\frac{\Omega_R}{X} e^{-i\frac{\delta t}{2} + i\phi} \sin\left(\frac{Xt}{2}\right) \\ -i\frac{\Omega_R}{X} e^{i\frac{\delta t}{2} - i\phi} \sin\left(\frac{Xt}{2}\right) & e^{i\frac{\delta t}{2}} \left[\cos\left(\frac{Xt}{2}\right) - i\frac{\delta}{X} \sin\left(\frac{Xt}{2}\right) \right] \end{pmatrix} \quad (3.12)$$

where $X = (\delta^2 + \Omega_R^2)^{1/2}$. On resonance this simplifies to

$$U(t) = \begin{pmatrix} \cos(\Omega_R t/2) & -ie^{i\phi} \sin(\Omega_R t/2) \\ -ie^{-i\phi} \sin(\Omega_R t/2) & \cos(\Omega_R t/2) \end{pmatrix} \quad (3.13)$$

This evolution operator describes rotations on the Bloch sphere representing the spin state of the ion. The spin state undergoes Rabi oscillations at frequency Ω_R . This type of transition is called a carrier transition. It changes the spin state of the ion but doesn't affect the motional state.

If the difference frequency of the two laser beams is tuned close to the blue motional sideband ($\delta = \omega_z + \epsilon$, where $|\epsilon| \ll |\delta|$), the resonant term in the Hamiltonian is

$$\hat{H}_I \simeq \hat{H}_{\text{bsb}} = i\hbar\eta\sqrt{n+1}\frac{\Omega_R}{2} |\downarrow, n\rangle \langle\uparrow, n+1| e^{-i(\epsilon t - \phi)} + \text{h.c.} \quad (3.14)$$

where $|\downarrow, n\rangle$ represents the spin-down state with vibrational quantum number n . The solution of the Schrödinger equation for this Hamiltonian is again Rabi flopping as given in equations 3.12 and 3.13 with Ω_R and ϕ replaced by $\eta\sqrt{n+1}\Omega_R$ and $\phi + \pi/2$ respectively, where n is the vibrational quantum number of the lowest level involved in the transition.

When the difference frequency of the two laser beams is tuned close to the red motional sideband ($\delta = -\omega_z + \epsilon$, where $|\epsilon| \ll |\delta|$), the resonant term in the Hamiltonian is

$$\hat{H}_I \simeq \hat{H}_{\text{rsb}} = i\hbar\eta\sqrt{n}\frac{\Omega_R}{2} |\downarrow, n\rangle \langle\uparrow, n-1| e^{-i(\epsilon t - \phi)} + \text{h.c.} \quad (3.15)$$

The solution of the Schrödinger equation for this case is again Rabi flopping, but with a flopping frequency $\eta\sqrt{n}\Omega_R$ and the same phase as for the blue-sideband transition.

In the treatment above, the off resonant terms (oscillating with frequency ω_z) were neglected. In the case of the carrier transition, this is a good approximation, as the extra terms are also reduced by factors of the Lamb-Dicke parameter. However in the case of

the sideband transitions, the “carrier” term is greater in amplitude than the resonant term by a factor $1/\eta$. For the blue sideband, this term is

$$\hat{H}_{\text{bsb}}^o = i\hbar \frac{\Omega_R}{2} e^{-i(\omega_z + \epsilon)t} |\downarrow, n\rangle \langle \uparrow, n| + \text{h.c.} \quad (3.16)$$

If $\Omega_R \ll \omega_z$, then the main effect of this extra term is to light shift the two levels involved by a factor $\Omega_R^2/4\omega_z$ [66]. The sign of this shift is such that the 1st blue sideband and 1st red sideband are both shifted closer to the carrier frequency by $\Omega_R^2/2\omega_z$.

If $\Omega_R \simeq \omega_z$, the ion makes transitions on both the sideband and the carrier, and the dynamics becomes more complicated. In most of the experimental work carried out throughout this thesis $\Omega_R \ll \omega_z$.

3.2.3 The oscillating dipole force

In addition to spin-flip transitions, we can also choose laser polarisation and frequency so that we do not affect the spin state, but do drive transitions between vibrational states. This is the case for the Schrödinger’s cat experiments of chapter 7 and the phase gate used to generate entanglement of the ions in chapter 9. The strength of interaction with each spin state depends on the exact choice of polarisation. In terms of the treatment given above, the electronic state $|e_1\rangle = |e_2\rangle = |m\rangle$, where $|m\rangle$ is the spin state of the ion. For these conditions, the Hamiltonian in equation 3.10 can be written

$$\hat{H}_I = \hbar \sum_{m=\uparrow, \downarrow} \left[\Omega_R^m \cos(\omega t - \phi_m) - \eta \Omega_R^m \sin(\omega t - \phi_m) (\hat{a} e^{i\omega_z t} + \hat{a}^\dagger e^{-i\omega_z t}) \right] |m\rangle \langle m| \quad (3.17)$$

where Ω_R^m is the effective Rabi frequency and ϕ_m the phase of the coupling between spin state $|m\rangle$ and the light field. The first term in this Hamiltonian is an oscillating light shift at frequency ω . The second term produces a light shift which varies with the position of the ion along the z -axis, hence gives rise to an oscillating force on the ion. This force is discussed in the context of single ion manipulation in chapter 7 and for two ions in chapter 9.

Chapter 4

Cooling, Heating and Fock States.

The experiments described in this chapter were concerned with optimising the cooling of a single ion to the ground state of motion, measurements of the heating rate and the production of Fock states of motion. The methods of cooling are described and discussed. When the ion is in the Lamb-Dicke regime it is relatively simple to measure its temperature by driving sideband transitions. This method is used to measure the heating rate of the ion, which is found to be the lowest measured in an ion trap up until now. By first preparing an ion in the ground state of motion, we can then prepare other Fock states of motion. This is described in the final section of this chapter.

4.1 Cooling and Temperature Diagnosis

4.1.1 Cooling methods.

The ion is cooled in three stages. The first stage is Doppler cooling [67]. This is implemented using a single linearly polarised 397 nm laser beam propagating at 60° to the trap axis, and an 866 nm repump laser to prevent optical pumping into the $D_{3/2}$ level. The Doppler limit temperature given by $T_D = \hbar\Gamma/2k_B$ gives the expected temperature for a trapped ion up to a numerical factor of order 1, depending on the direction and polarisation of the cooling beam [68]. For a calcium ion $T_D \simeq 540 \mu\text{K}$ for the 397 nm transition. This corresponds to a mean axial vibrational excitation of 14 for a single ion in an 800 kHz trap, and 23 for a single ion in a 500 kHz trap. In practice, there are a number of reasons why this Doppler limit temperature is not attained. Firstly, the ground and excited states are split by the magnetic field, which increases the effective linewidth of the transition. Secondly, the axis of the trap is at 60° to the cooling beam. The frictional cooling rate is thus reduced by a factor $1/\cos(60^\circ)^2 = 4$ compared to the recoil heating due to the spontaneous emission of photons, which results in a final temperature which is higher than T_D by a factor $\simeq 2$.

In addition, the 397 nm laser was operated at around one saturation intensity in the experiments presented in this chapter, in order to enhance the number of photons scattered during state detection. This also broadens the cooling transition, providing another reason why we would not expect the ion to be at the Doppler limit temperature after Doppler cooling. In the experiments performed with a 500 kHz trap in later chapters, the power of the Doppler laser was switched between the cooling pulse and the state detection pulse in order to reduce the temperature of the ion after this stage of cooling.

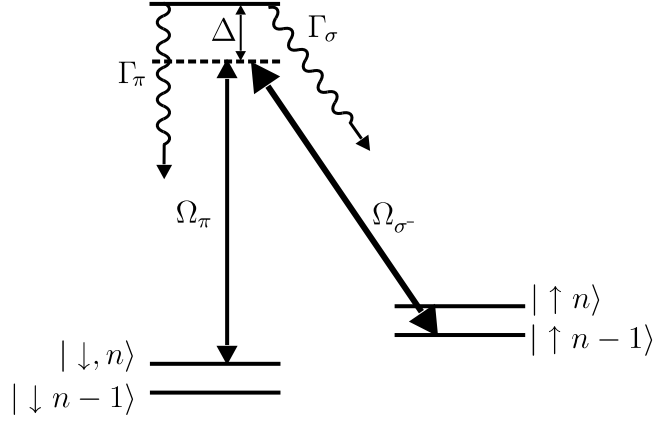


Figure 4.1: General scheme for continuous Raman cooling. The two 397 nm light fields are detuned by 130 MHz from the 397 nm transition. The frequency difference of the π and σ^- beams is set to resonance with the $|\downarrow, n\rangle \rightarrow |\uparrow, n-1\rangle$ transition. The intensities of the two beams are set such that typical values are $\Omega_{\sigma^-} = 2\pi \times 40$ MHz, $\Omega_{\pi} = 2\pi \times 8$ MHz and $\Delta = 2\pi \times 130$ MHz. $\Gamma = 2\pi \times 22$ MHz. The large difference between the Rabi frequencies for the σ^- and π light mean that the stimulated process is more likely when the ion is in the $|\downarrow\rangle$ state, whereas the spontaneous Raman process is more likely when the ion is in the $|\uparrow\rangle$ state. Since the stimulated process from $|\downarrow\rangle \rightarrow |\uparrow\rangle$ leads to a loss of one quantum of motional energy, on average the ion loses energy.

The second stage of cooling is continuous Raman sideband cooling. A thorough description of this method is given in the thesis of Dr. S. Webster [53]. The cooling uses two laser beams derived from the 397 nm laser. One of these beams (the “pump”) is σ^- polarised, and has a much higher intensity than the π polarised (“probe”) beam. Both beams are detuned 130 MHz to the red of the 397 nm transition. The difference frequency of the two beams is set close to the first red-sideband transition (after allowing for light shifts of the levels involved). The main driven processes and decays relevant to this cooling method are shown in figure 4.1. Consider an ion starting in the state $|\downarrow, n\rangle$. The two main possibilities are for it to make a stimulated Raman transition, which will transfer the ion into the state $|\uparrow, n-1\rangle$, or a spontaneous Raman transition, which is most likely to transfer the ion to the state $|\uparrow, n\rangle$. Once in the $|\uparrow, n-1\rangle$ state, the ion then undergoes either a stimulated Raman transition back into $|\downarrow, n\rangle$ or a spontaneous Raman transition into $|\downarrow, n-1\rangle$. The low power of the probe (π) beam means that the spontaneous process is negligible in the \downarrow to \uparrow transition, hence on average the ion loses ~ 1 vibrational quantum of energy per cycle. The above description ignores the effect of recoil heating, but this is small as long as $\omega_z \gg \omega_R$, where $\hbar\omega_R = \hbar^2 k^2 / 2M_{Ca}$ is the recoil energy of the ion. In an 800 kHz trap $\omega_z \simeq 25\omega_R$. After this stage of cooling we typically achieve a mean vibrational quantum number of $\bar{n} \simeq 0.4$ in a trap with a vibrational frequency of 800 kHz. The final temperature is limited by off resonant driving of the carrier and first blue sideband transitions.

The third stage of cooling is pulsed Raman sideband cooling, which is also described in detail in the thesis of Dr. S. Webster [53]. The essential idea is shown in figure 4.2. Consider an ion starting in the $|\downarrow, n\rangle$ state. A π pulse on the red sideband is performed using the Raman lasers, which coherently transfers the ion into $|\uparrow, n-1\rangle$ state. This is

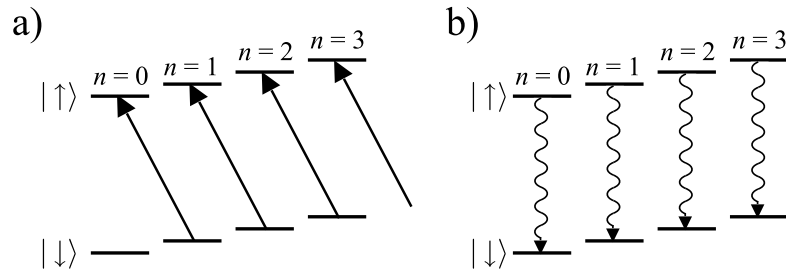


Figure 4.2: A single cycle of pulsed Raman sideband cooling. For each spin state, the ladder of motional states is shown from $n = 0$ to $n = 3$. a) a π pulse on the red-sideband transition, implemented using the Raman lasers. This reduces the vibrational quantum number of the ion by 1. b) repumping of the spin state. The mean change in n for the repumping step is close to zero. The net change in vibrational quantum per cycle is therefore one unless the ion is in the ground state. This cycle is repeated until the ion is in the ground state.

followed by a 397 nm σ^- pulse, which on average repumps the ion into $|\downarrow, n - 1\rangle$. Therefore the ion loses one vibrational quantum of energy each time these two pulses are applied (again ignoring the effect of recoil heating). This sequence is repeated until the ion is in the $|\downarrow, 0\rangle$ state, which is unaffected by both pulses. Since the time required for a π pulse on the sideband varies with n , the time of the sideband pulses is changed for each repetition. For cooling using N pulses of cooling, the π times are chosen such that the first pulses are π pulses for the red-sideband transition from level $n \simeq N \rightarrow N - 1$. The pulse lengths increase throughout the cooling until the final pulse is a π pulse for the $n = 1 \rightarrow 0$ transition.

It is reasonable to ask why pulsed Raman sideband cooling is not used directly after Doppler cooling. The explanation is that the matrix elements on the first sideband go to zero at a given n value. This happens at $n = 92$ for the 800 kHz trap and at $n = 56$ for the 500 kHz trap. If the ion starts at twice the Doppler limit temperature, then the fraction of population which gets trapped above the matrix element zero is 0.04 for the 800 kHz trap and 0.3 for the 500 kHz trap. Close to these zeros in the matrix element the sideband pulses for the pulsed cooling would have to be very long in order to cool the ion. This would reduce the cooling rate. The larger linewidth of the continuous cooling means that it can off resonantly drive the second red sideband, which can pump the ion to lower n for vibrational levels where the first sideband matrix element is small. This is implied by the observation that in the 500 kHz trap, the best overall cooling (continuous cooling plus pulsed cooling) is achieved by setting the relative detuning of the pump and probe beams red-detuned from the first red sideband for the continuous cooling.

Both methods of sub-Doppler cooling are limited by off-resonant driving of carrier and blue sideband transitions. The linewidth of the cooling transition is larger for the continuous Raman cooling for our parameter choices, so the temperatures achieved by this method are higher than for the pulsed Raman cooling.

4.1.2 Temperature Diagnosis.

If the ion is in the Lamb-Dicke regime, it is possible to diagnose its temperature using stimulated Raman transitions. The ion is first prepared in the spin down state and we

assume the motional state is an incoherent mixture of Fock states. After applying a pulse of time t_p resonant with the blue sideband, the probability of finding the ion in the spin up state is

$$P_b(\uparrow) = \frac{1}{2} \sum_{n=0}^{\infty} P(n)(1 - \cos(\Omega_{n,n+1}t_p)) \quad (4.1)$$

where $P(n)$ is the probability that it started in the Fock state with vibrational quantum number n , and $\Omega_{n,n+1} = \eta\sqrt{n+1}\Omega$. The probability of finding the ion in the spin up state after a pulse of length t_p on the red sideband is

$$P_r(\uparrow) = \frac{1}{2} \sum_{n=1}^{\infty} P(n)(1 - \cos(\Omega_{n,n-1}t_p)) \quad (4.2)$$

where $\Omega_{n,n-1} = \eta\sqrt{n}\Omega$. The ratio of these two probabilities is

$$R = \frac{\sum_{n=1}^{\infty} P(n)(1 - \cos(\Omega_{n,n-1}t_p))}{\sum_{n=0}^{\infty} P(n)(1 - \cos(\Omega_{n,n+1}t_p))} \quad (4.3)$$

If the probability distribution for finding the ion in the Fock state $|n\rangle$ is thermal, then the probabilities $P(n)$ are given by

$$P(n) = \frac{\bar{n}^n}{(\bar{n} + 1)^{n+1}} \quad (4.4)$$

where \bar{n} is the mean vibrational quantum number of the probability distribution. Substituting this form into equation 4.3 and re-labelling $n \rightarrow n + 1$ in the numerator enables us to write

$$R = \frac{\bar{n}}{\bar{n} + 1} \quad (4.5)$$

Inverting this expression gives

$$\bar{n} = \frac{R}{1 - R} \quad (4.6)$$

The mean vibrational quantum number is extracted experimentally using a fixed length probe pulse with the Raman laser beams. The ion is first cooled and prepared in $|\downarrow\rangle$. A probe pulse is then applied with duration t_p . This is repeated a large number (typically 500) times, and the fraction of times the ion is shelved is recorded. The difference frequency ω of the Raman beams producing the probe pulse is then changed and the experiment repeated. This is repeated for a range of ω around each of the sidebands. Example data is shown in figure 4.3.

The results from each sideband are jointly fitted with

$$\begin{aligned} P(f) &= b + a \left\{ \frac{\Omega^2}{2(\Omega^2 + \delta_b^2)} \left[1 - \cos \left((\Omega^2 + \delta_b^2)^{\frac{1}{2}} t_p \right) \right] \right. \\ &\quad \left. + \frac{R\Omega^2}{2(\Omega^2 + \delta_r^2)} \left[1 - \cos \left((\Omega^2 + \delta_r^2)^{\frac{1}{2}} t_p \right) \right] \right\} \end{aligned} \quad (4.7)$$

where b is the baseline, a is the amplitude of the blue sideband, R is the ratio of sideband heights, Ω is an effective Rabi frequency for the sideband transitions and $\delta_r = \omega - \omega_r$ and

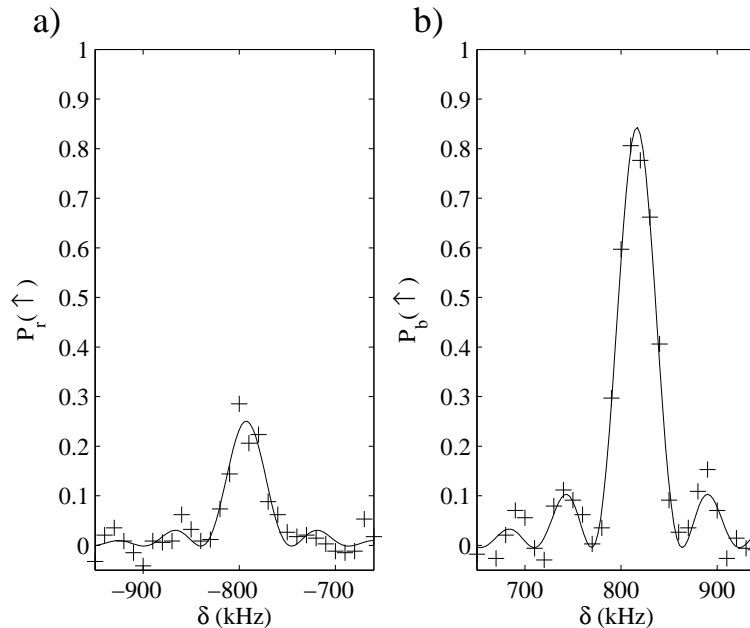


Figure 4.3: $P(\uparrow)$ as the difference frequency of a fixed length Raman probe pulse is scanned over a) the red sideband and b) the blue sideband in order to deduce the temperature of the ion. Each data point represents the average of 500 sequences. The data from a) and b) is jointly fitted with equation 4.7. The ratio of the sideband heights obtained from the fit is $R = 0.30$, which corresponds to $\bar{n} = 0.42$.

$\delta_b = \omega - \omega_b$ are the detunings of the difference frequency of the Raman laser beams from the resonant frequency of the red sideband ω_r and blue sideband ω_b respectively (This formula is strictly valid only for a Fock state but is a good approximation for a thermal state). In the fit, $b, a, R, \Omega, \omega_a$ and ω_b were allowed to float. An example of a fitted scan over the sidebands is shown in figure 4.3. Although in this example the population $P(f)$ has been converted into a spin population using equation 2.16, this is not necessary in order to perform the temperature measurement since these two quantities have a linear relationship and in order to deduce the temperature of the ion we take the ratio of the population change.

Diagnosis of cooling is made more difficult if the Rabi frequency is high, due to off resonant excitation of the carrier transition. This is illustrated by figure 4.4, where the off-resonant carrier excitation gives a similar transfer of population to that due to the red sideband pulse when the difference frequency of the Raman beams is resonant with the red sideband. In order to minimise this effect, the power in the cooling beam could be turned down, or the pulse time arranged so that the red sideband lies at a minimum of the response of the carrier.

4.1.3 Experimental results.

In order to optimise the cooling, we experimentally adjusted the cooling parameters, while observing the effect on ion temperature. As a quick diagnostic, a fixed length Raman probe pulse resonant with the red sideband was used. If the experimental adjustment reduced

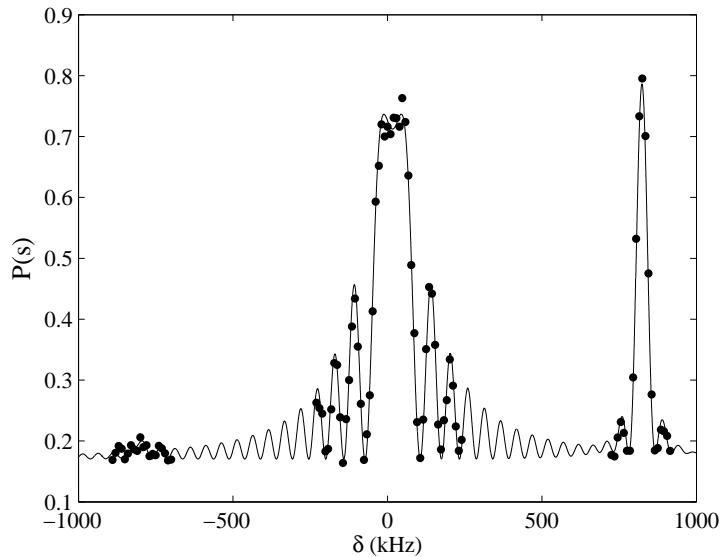


Figure 4.4: A scan over the carrier, red sideband and blue sideband. The mean vibrational quantum number is $\bar{n} = 0.03$. The fitted curve is a sum of three functions with the same form as equation 4.7. The Rabi frequency, readout levels, carrier frequency Ω_c , trap frequency ω_z and light shift of the sidebands relative to the carrier were floated. The figure illustrates the influence of off-resonant carrier excitations when the laser is tuned to the red-sideband transition.

the height of this sideband, the Raman probe pulse was switched to being resonant with the blue sideband, in order to check that the change was not due to factors which do not indicate better cooling e.g. a change in the readout levels.

Initially we optimised the continuous cooling by adjusting the relative frequency of the pump and probe beams in order to achieve the lowest temperature after this stage of cooling. The pulsed cooling was then introduced, and a similar method was used to optimise the frequency difference of the Raman laser beams. It was later found that by adjusting the frequency difference of the continuous cooling beams while observing the temperature after pulsed cooling, even lower values of \bar{n} could be obtained. This may be due to a non-thermal distribution of population. The optimal pump-probe detuning for continuous cooling may leave population trapped at n states where the first sideband transition rate is very low. The pulsed cooling is then not able to cool this population. In order to cool further, the continuous cooling must off resonantly excite the second red sideband, allowing this trapped population to move to lower n .

The results of temperature measurements taken over a period of three weeks are shown in figure 4.5. The cooling was fairly reliable over this period. The lowest vibrational quantum number for the continuous Raman sideband cooling is typically $\bar{n} \sim 0.4$. When the continuous sideband cooling method is working well, 5 pulses of pulsed Raman sideband cooling are enough to reach $\bar{n} \leq 0.08$, which indicates a $\geq 92\%$ ground state occupation. The lowest temperatures were obtained towards the end of the three weeks. The improvement is mainly due to empirical adjustment of the difference frequency of the continuous sideband cooling beams, although this did not have an observable effect on the temperature after the continuous cooling. One possible reason for such behaviour would be the

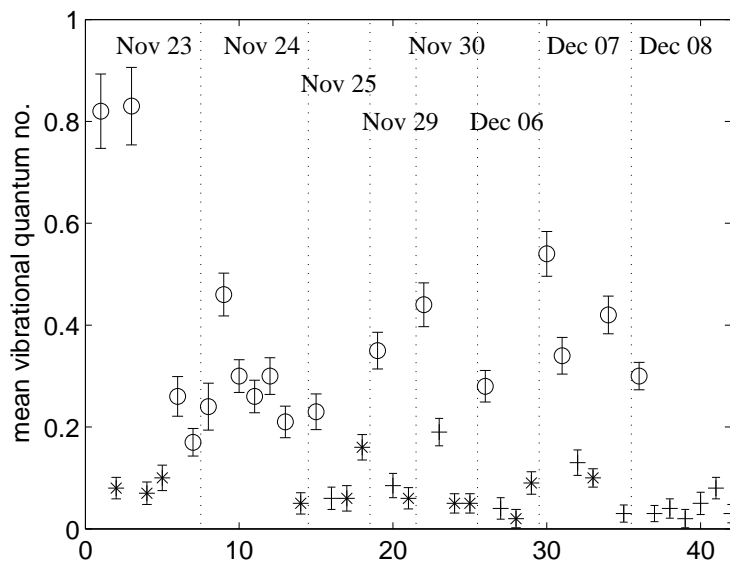


Figure 4.5: Temperature measurements taken over a three week period. The unfilled circles represent data taken after 4 ms of continuous Raman sideband cooling. The + represent data taken after continuous Raman sideband cooling and 5 cycles of pulsed sideband cooling, and the * represent data taken after continuous Raman sideband cooling and 10 cycles of pulsed sideband cooling.

population trapping discussed above.

4.2 Heating rates.

In order to carry out experiments in which we control motional states of the ion, we require that it does not heat up on the time scale of the experiment. The most likely cause of heating of the ion from the ground state is fluctuations in the electric field at the ion. This could be due to noisy supply voltages applied to the electrodes, Johnson noise from the resistance in the trap electrodes themselves or fluctuating patch potentials. Potential sources of patch potentials are materials adsorbed on the surfaces of the electrodes or randomly orientated domains at the electrode surfaces [69]. The heating rate for an ion of mass M in a trap of frequency $\omega_z/(2\pi)$ can be related to the electric field noise at the ion by

$$\dot{\bar{n}} = \frac{e^2 S_E(\omega_z)}{4M\hbar\omega_z} \quad (4.8)$$

where $S_E(\omega) = 2 \int_{-\infty}^{\infty} \langle E(t)E(t+\tau) \rangle e^{i\omega\tau} d\tau$ is the spectral density of electric field noise at the ion (units of $(V/m)^2 \text{Hz}^{-1}$) [69].

We studied the heating rate in our trap by cooling the ion to the ground state, inserting a delay, and then measuring the temperature. In order to discriminate between photon scattering (which would randomise the ion's spin state) and heating, a repump pulse of 397 σ^- light was inserted immediately before the temperature measurement pulse.

Two methods were used. The heating rates obtained in November were obtained by pausing for the delay time, then applying a red sideband probe pulse. The delay time was

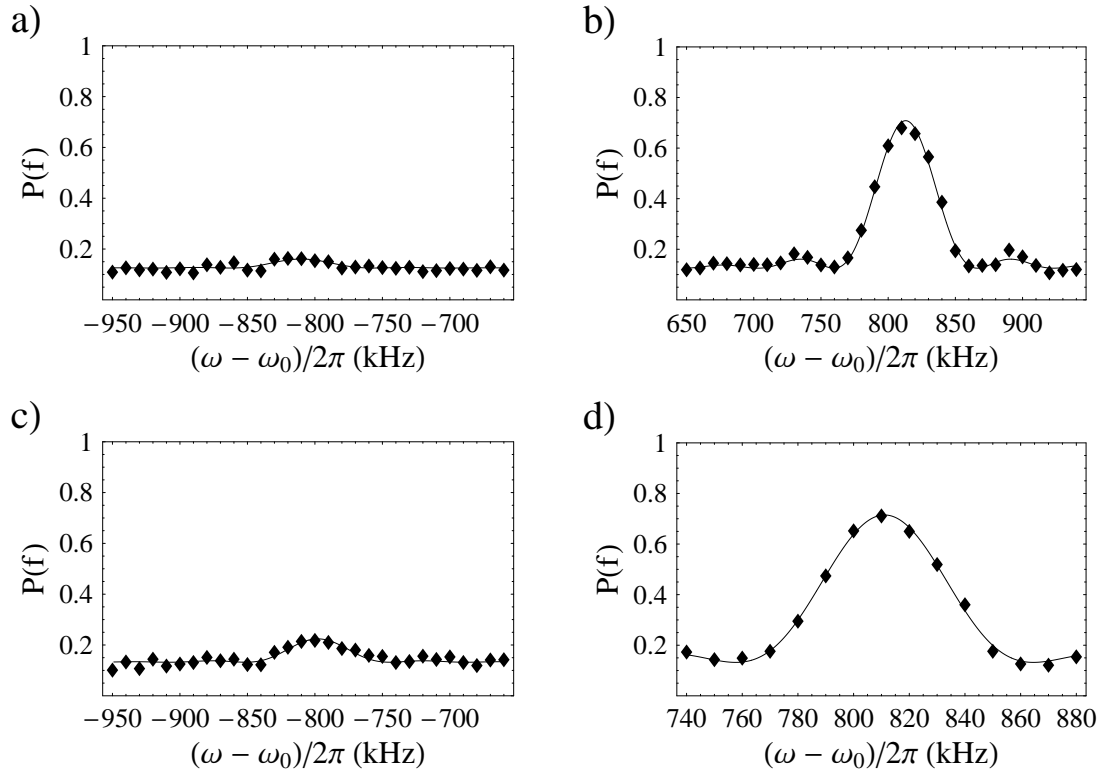


Figure 4.6: Example data from a scan of the red and blue sidebands with a delay of a), b) 0 ms and c), d) 50 ms between the population preparation pulse and the Raman probe. The difference frequency of the Raman laser beams is ω , and ω_0 is close to the resonant frequency of the carrier transition (ω_0 is set to the carrier transition frequency at the beginning of the experiments, but as the magnetic field drifts, the carrier transition frequency changes). b). The mean vibrational quantum number deduced for the 0 ms delay is 0.04(1) quanta, and for the 50 ms delay is 0.19(2) quanta. This gives a heating rate of $\bar{n} = 3.0(5)$ quanta s^{-1} . The heating rate corresponding to this data in figure 4.7 is 2.7(4) quanta s^{-1} (data point 28, 07 december 2005). This is because an additional scan with zero delay was carried out directly after the 50 ms delay data. This data gave $\bar{n} = 0.06(2)$ quanta. In order to calculate the heating rate the mean of the two values of \bar{n} using 0 ms delay was taken.

scanned from $0 \rightarrow 10$ ms. For each delay time, the sequence was run 500 times and the fraction of times the ion was shelved was obtained. This was converted into $P_{\text{rsb}}(\uparrow)$ using equation 2.16. This was repeated on the blue sideband. The ratio of populations on the red and blue sidebands was thus extracted for each delay time. These were converted into measurements of \bar{n} using equation 4.5. A straight line was fitted to results of the measured \bar{n} against delay time; the gradient of this line gives the heating rate. For delay times ≤ 10 ms this method is adequate, since the total time required to make measurements of the red and blue sidebands is ~ 20 minutes, for which time the magnetic field is generally quite stable.

In order to reduce the error on the heating rate measurements, we introduced longer delay times. For sequences of pulses longer than 20 ms, the experiments get much longer

due to the need to trigger them from the 50 Hz mains electricity supply. This means that the total time required to perform the heating rate experiment described in the previous paragraph would be $\sim 40 - 60$ minutes. Therefore it is necessary to protect against drift in the magnetic field. For this reason, the data obtained in October and December were obtained by scanning over the sidebands as described in section 4.1.2 for each delay time. An example of the data is shown in figure 4.6.

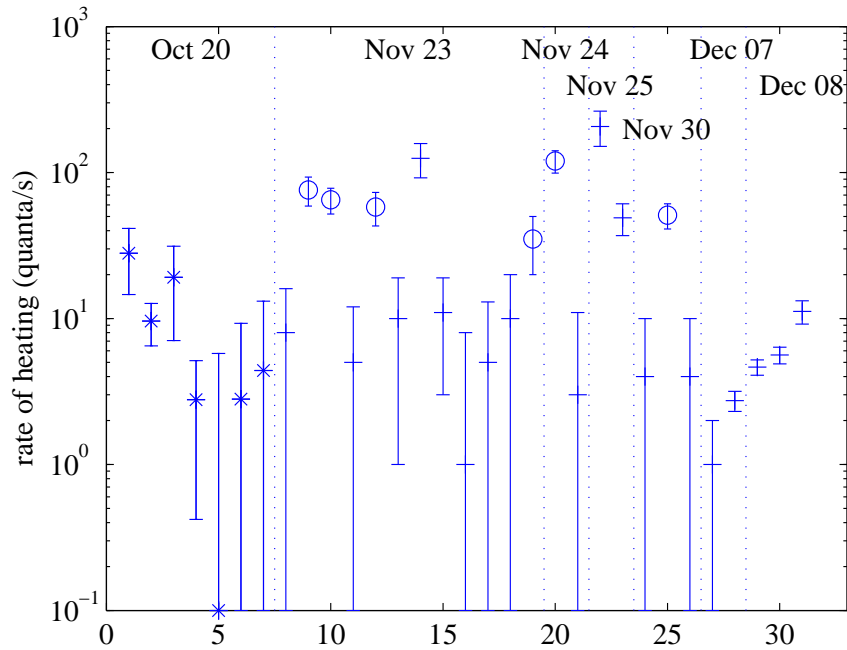


Figure 4.7: Heating rates obtained by inserting delays between the end of cooling and the temperature measurement. The data represented by + are the results of experiments performed in an 800 kHz trap, whereas the data represented by a \star are results of experiments performed in a 500 kHz trap. Data represented with a circle was taken with the 397 nm double pass Master AOM in order to study the effect of poor extinction of the 397 nm beam on the heating of the ion.

The results of heating rate measurements are shown in figure 4.7. The heating rate is mostly found to be < 10 quanta s^{-1} , which corresponds to a rate of change of temperature of < 0.38 mK s^{-1} .

The October data can be split into two parts. The first three points shown in figure 4.7 were taken during the day, and have a mean heating rate of 11 ± 3 quanta s^{-1} . Points 4–7 were taken in the evening, when the mean heating rate was found to be 2.5 ± 0.9 quanta s^{-1} or 2.9 ± 0.3 quanta s^{-1} depending on whether point 5 is included in the average. Point 5 exhibited a negative heating rate, which may be due to the anomalously high starting temperature which was measured.

The mean heating rate on the 7th of December was 2.5 ± 0.5 quanta s^{-1} . On the 8th of December the heating rate was measured with and without the “tickle” box attached to the end-cap electrode. Data points 29 and 30 were taken with the tickle box attached, and give a heating rate of 5.0 ± 0.4 quanta s^{-1} . After the tickle box was detached, the heating

rate was 11 ± 2 quanta s^{-1} . The lowest measured heating rate was 1.0 ± 1.0 quanta s^{-1} on the 7th of December.

On a few occasions in November heating rates much greater than 10 quanta s^{-1} were observed. This high heating rate does not seem to have impeded the cooling. When the heating rate of 200 quanta s^{-1} was recorded on the 25th of November the mean vibrational quantum number with no gap was $\bar{n} = 0.06$. These “anomalous” heating rates didn’t occur regularly enough for an investigation into their cause. If the three data measurements of $\bar{n} > 30$ are ignored, the mean heating rate for the November data is 5.5 ± 1.8 quanta s^{-1} .

Using equation 4.8 to convert the heating rate into a spectral density of electric field noise, the electric field noise at the ion for an ion in our trap which is heated at 2.5 quanta s^{-1} is $S_E(2\pi \times 812 \text{ kHz}) = 6.7 \times 10^{-14} \text{ (V/m)}^2 \text{ Hz}^{-1}$.

The heating rates and deduced spectral density of electric field noise in several ion trap systems in use worldwide are shown in figure 4.8. The heating rate in ion traps has been empirically observed to increase as $1/\rho^4$ [69, 71], where ρ is the shortest distance from the trap centre to the surface of an electrode. This dependence is consistent with a model of fluctuating patch potentials on the electrodes [69]. The heating rates we have measured and the deduced spectral density of electric field fluctuations at the ion are the lowest which have been measured. This is mainly due to the large scale of the trap compared to others.

We also looked for heating due to low level stray light. The heating rate measurement is a sensitive detector of stray light, since each photon scattered will heat the ion by $\sim \eta^2 = 0.04$ quanta. For this reason, the heating rate was studied with the double pass AOM in the Doppler, probe and pump beams turned on, meaning that each of these beams were now extinguished by a single pass AOM only. This heating rate was measured in November by sitting at the red and blue sideband frequencies as was described earlier in this section. The data from these measurements is represented by circles in figure 4.7. The mean value of the heating rate from these measurements is 60 ± 14 quanta s^{-1} .

A scattered photon imparts one recoil energy E_R to the ion, which can be written in terms of the Lamb-Dicke parameter as $E_R = \eta^2 \hbar \omega_z$. For a calcium ion in an 800 kHz trap, this corresponds to 0.04 vibrational quanta. In order to estimate the number of photons required to produce a heating rate of 60 quanta s^{-1} , we can therefore divide this heating rate by 0.04. This gives a rate of 1500 photons s^{-1} . This is probably an overestimate, since on occasions when the scattered photons mean that the ion ends up in the $|\uparrow\rangle$ state before the repump pulse, extra recoils of energy will be gained during repumping.

4.3 Fock states of motion

The ability to cool a trapped ion to the ground state is a useful initial step to enable us to prepare other quantum states of motion. In this section we consider the preparation of Fock states.

To create the Fock state $|1\rangle$ from an ion starting in $|0, \downarrow\rangle$, a π pulse is applied on the blue sideband. This transfers the ion into the state $|1, \uparrow\rangle$.

The Fock state $|2\rangle$ can be created by two methods. It could be done by driving the second sideband transition, transferring the ion from $|0, \downarrow\rangle \rightarrow |2, \uparrow\rangle$. This transition has strength $\simeq \eta^2 = 0.04$. In order to use fewer synthesisers and to minimise the time required to create the state, we chose to first drive the ion into $|1, \uparrow\rangle$ using a π pulse on the blue-sideband, then used a π pulse on the red sideband to put the ion in the state $|2, \downarrow\rangle$. Note

that due to the change in the matrix elements with n , these two π pulses must have different lengths.

Diagnosis of these states is performed by driving Rabi flopping on a motional sideband. The rate of flopping on the $n \rightarrow n+1$ sideband goes as $\Omega_{n,n+1} = (n+1)^{1/2} \eta L_n^1(\eta^2) \Omega_c$, hence a measurement of the flopping frequency gives us information about the motional state. The Fourier transform of the Rabi flopping gives an indication of the frequency components present. Population of vibrational levels other than the one which was prepared should show up in the Fourier transform due to the different Rabi flopping frequencies associated with different values of the motional matrix elements.

The experiment performed is to create a Fock state, then apply a pulse of length t on the $n \rightarrow n+1$ sideband. This sequence is repeated a large number of times for t between 0 and an upper limit which varied between $t_{\max} \sim 250 \mu\text{s}$ and $t_{\max} \sim 1.1 \text{ ms}$. The fraction of times the ion is shelved for each value of t was measured by repeating the experimental sequence 500 or 1000 times.

The data for $P(s)$ is fitted with

$$P(\uparrow) = B + A \frac{1}{2} \left[1 \pm e^{-\Gamma t^2} e^{-\gamma t} \cos(\Omega_{n,n+1} t) \right] \quad (4.9)$$

where A and B are the amplitude and baseline respectively, γ and Γ are phenomenological decay constants, and n is the number of the Fock state which was created prior to the variable length sideband pulse¹. The values of all these parameters were allowed to float. Next, in order to deduce the populations of the different Fock states from the data a Fourier transform was applied and the results were fitted with a single Voigt profile

$$V(\Omega) = B_v + A_v \text{Re} \left[\frac{i}{\pi} \int_{-\infty}^{\infty} \frac{e^{-x^2}}{\left(\frac{(\Omega - \Omega_v)}{g_L} + i \frac{g_L}{g_G \sqrt{\ln 2}} - x \right)} dx \right] \quad (4.10)$$

for which the amplitude A_v , baseline B_v , centre frequency Ω_v , and the widths of both the Lorentzian and Gaussian components (g_L and g_G respectively) were allowed to float. The raw data, Fourier transform of the data, fitted curves and the residuals from the Voigt profile fit to the Fourier transform are shown in figures 4.9 to 4.12.

The residuals from this fit were used to estimate an upper limit on the populations of the Fock states other than that which was supposed to be prepared. First the Rabi frequencies of sideband transitions for population starting in states with vibrational quantum numbers from $m = 0$ to $m = 4$ were calculated using the Rabi frequency obtained using the fit to the raw data and the relative sizes of the motional matrix elements (given by equation 3.7 in section 3.2.1). These frequencies are represented by vertical lines on figures 4.9 to 4.12 c). An estimate was then made of the maximum size r_m of the residuals at these frequencies. The populations of the states were then calculated from

$$P_m = \frac{r_m}{\text{Max}(V(\Omega)) + \sum_{m=0}^4 r_m} \quad (4.11)$$

where $V(\Omega)$ is the Voigt fit to the Fourier transform data. As the maximum size of the residuals was taken at each frequency, the values calculated should be the maximum probability for states other than the state which we attempted to prepare, and the minimum probability for the state which we attempted to prepare. A selection of the fitted param-

¹See chapter 5 for a discussion of Gaussian and exponential decay of coherence

eters are summarised in table 4.1, along with the probabilities P_m the ion having started in Fock states with vibrational quantum numbers from 0 to 4.

The Rabi frequencies for the fits to the raw data shown in figures 4.9 and 4.10 are $\Omega_{0,1} = 2\pi \times 26$ kHz and $\Omega_{1,2} = 2\pi \times 35.8$ kHz respectively. These both agree with the values obtained from fitting a Voigt profile to the Fourier transform of the data. The ratio of these two values is 1.38, which is close to the value of 1.39 predicted by the matrix elements. The population of the prepared vibrational state $n = 0$ is found from the data in figure 4.9 to be $P_0 > 0.92$, which is in agreement with the temperature measurement 0.04(3) made prior to the data being taken. The data shown in figure 4.10 indicates that the probability with which the Fock state $n = 1$ was prepared is found to be $P_1 > 0.93$. The amplitude of the oscillations in $P(s)$ are in agreement with both of these measurements.

The Rabi frequencies for the fits to the raw data shown in figures 4.11 and 4.12 are $\Omega_{1,2} = 2\pi \times 30.1$ kHz and $\Omega_{2,3} = 2\pi \times 33.2$ kHz respectively. These are not in agreement with the values of $\Omega_{v,1,2} = 2\pi \times 29.3$ kHz and $\Omega_{v,2,3} = 2\pi \times 34.2$ kHz respectively obtained from the Voigt fit to the Fourier transform of the data. The difference in the two fits may be due to the implicit assumptions made in fitting the data. Both fits were performed using a least-squares fit method. A fit to the raw data thus makes the assumption that noise affects only the value of $P(s)$ at a given time, but assumes that the frequency component is constant throughout. On the other hand a fit to the Fourier transform makes allowance for many frequency components. On the day when this data was taken, the Raman laser lost injection on a number of occasions. It is therefore possible that the injection mechanism was not working well, which might have lead to intensity fluctuations. The ratio of the fitted Rabi frequencies on the $n = 1 \rightarrow 2$ transition and the $n = 2 \rightarrow 3$ transition is 1.10 for the fit to the raw data and 1.17 for the fit to the Fourier transform. The value predicted by the matrix elements is 1.20.

The probability with which the desired Fock states were prepared is found to be $P_1 > 0.91$ and $P_2 > 0.88$. These values are both greater than the amplitude A_P of the oscillations in the probability $P(\uparrow)$ of finding the ion spin up. One explanation for the low oscillation amplitude of the $n = 1 \rightarrow 2$ transition is that the π pulse which created the state $|\uparrow, 1\rangle$ is

fig	n	$\Omega_{n,n+1}/2\pi$ (kHz)	$P(s \downarrow)$	$P(s \uparrow)$	A_P	$\Omega_v/2\pi$ (kHz)	P_0	P_1	P_2	P_3	P_4
4.9	0	26.0	0.2	0.75	0.98	26.0	0.92	0.04	0.02	0	0.02
4.10	1	35.8	0.2	0.74	0.93	36.0	0	0.93	0.06	0.01	0
4.11	1	30.1	0.09	0.74	0.68	29.3	0.02	0.91	0.04	0.04	0.00
4.12	2	33.2	0.13	0.82	0.81	34.2	0.06	0.01	0.88	0.00	0.05

Table 4.1: A selection of the fitted parameters from fits to the raw data and the Fourier transform of the data for sideband flopping on the $n \rightarrow n+1$ transition, for an ion prepared in the Fock state with vibrational quantum number n . The results shown in figures 4.9 and 4.10 were taken on a different day and used different laser intensity to those shown in figures 4.11 and 4.12. The fitted Rabi frequencies are $\Omega_{n,n+1}$ for the fit to the raw data using equation 4.9 and Ω_v for the fit to the Fourier transform of the data using equation 4.10. $P(s|\downarrow)$ and $P(s|\uparrow)$ are the measured readout levels. A_P is the amplitude of the oscillations in the raw data, given by $A_P = A/(P(s|\uparrow) - P(s|\downarrow))$. The populations P_m of the vibrational starting states were calculated from the residuals of the fit to the Fourier transform using the method described in the text.

imperfect. This would leave some population in the $|\downarrow, 0\rangle$ state which would not interact with the radiation on the red-sideband transition. If a perfect π pulse on the red sideband was subsequently used to prepare $|\downarrow, 2\rangle$ and the blue sideband transition was subsequently driven, some of this population would be expected to show up as population starting in $n = 0$. The probabilities deduced from the residuals of the fit to the Fourier transform indicate that up to 5% of the population may remain in $|\downarrow, 0\rangle$. If the red-sideband π pulse was imperfect, it is possible that we would be unable to detect the presence of this “missing” population. This is because the population remaining in $|\downarrow, 0\rangle$ and $|\uparrow, 1\rangle$ would be driven by the blue-sideband pulse between these two states. The observed spin state population would then depend on the coherence between these two states.

Additional factors which would reduce the contrast of the fringes are loss of injection for the Raman laser, and the radiation driving the blue sideband transition being detuned from resonance. However, a frequency scan of the difference frequency of the Raman beams over the blue sideband produced a peak contrast which was the same as the contrast observed in the flopping data, so the latter is unlikely.

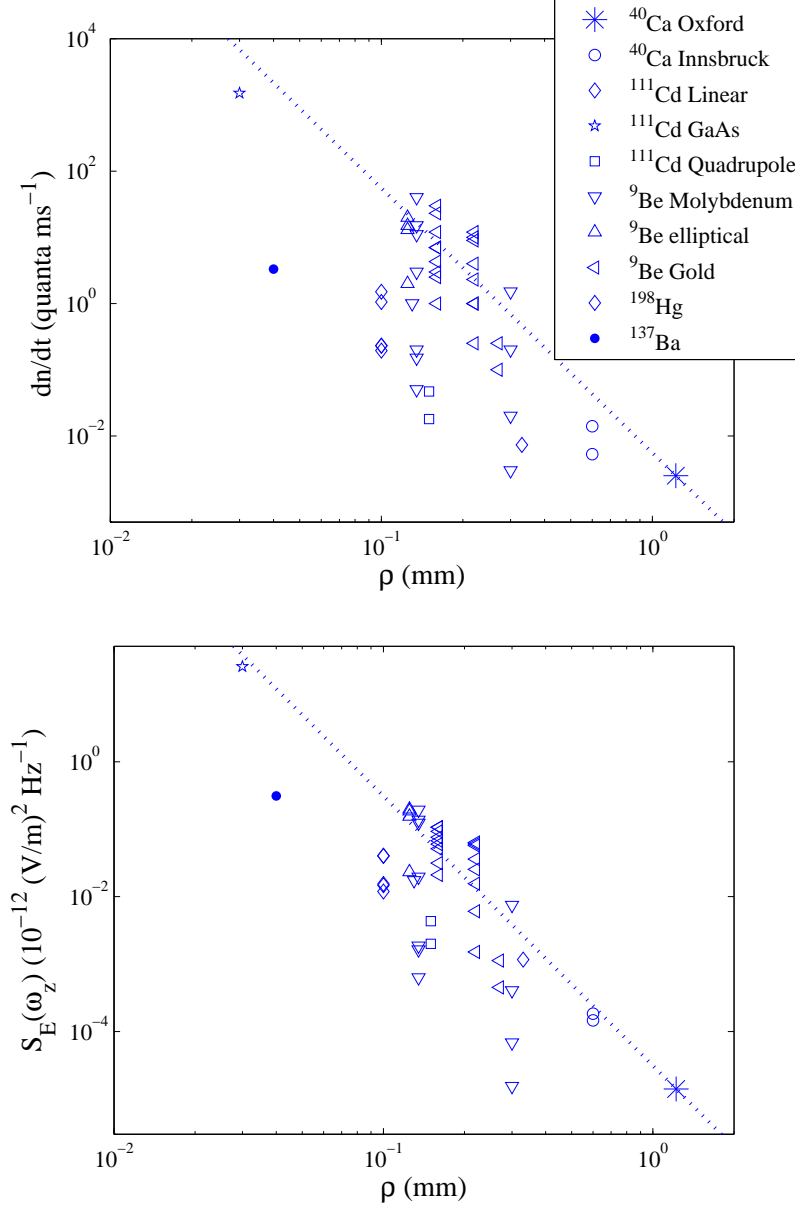


Figure 4.8: a) Observed heating rate against the smallest distance from the ion to an electrode surface in several ion trap systems. In addition to the measurements presented here are measurement results from experiments performed in Innsbruck using a $^{40}\text{Ca}^+$ ion [70], University of Michigan with a $^{111}\text{Cd}^+$ ion [71], NIST Boulder with both $^9\text{Be}^+$ [33, 69, 36] and $^{198}\text{Hg}^+$ [72] ions and at IBM San Jose with a $^{137}\text{Ba}^+$ ion [73]. The trap frequencies used in these experiments all lie between 812 kHz and 14 MHz. The dashed line is $y = (1.22 \text{ mm})^4 \dot{n}_{Ox} / \rho(\text{mm})^4$ where $\dot{n}_{Ox} = 2.5 \text{ quanta } s^{-1}$ is the heating rate measurement described above. This line gives an indication of the $1/\rho^4$ dependence of the heating rate on ρ which is predicted by a model of microscopic charged patches on the electrodes [69]. The spectral densities of electric field fluctuations at the ion are shown in b). These were deduced using equation 4.8 from the measured heating rates, along with the corresponding trap frequencies and masses of the ions. These data were collected by Prof. C. R. Monroe at the University of Michigan.

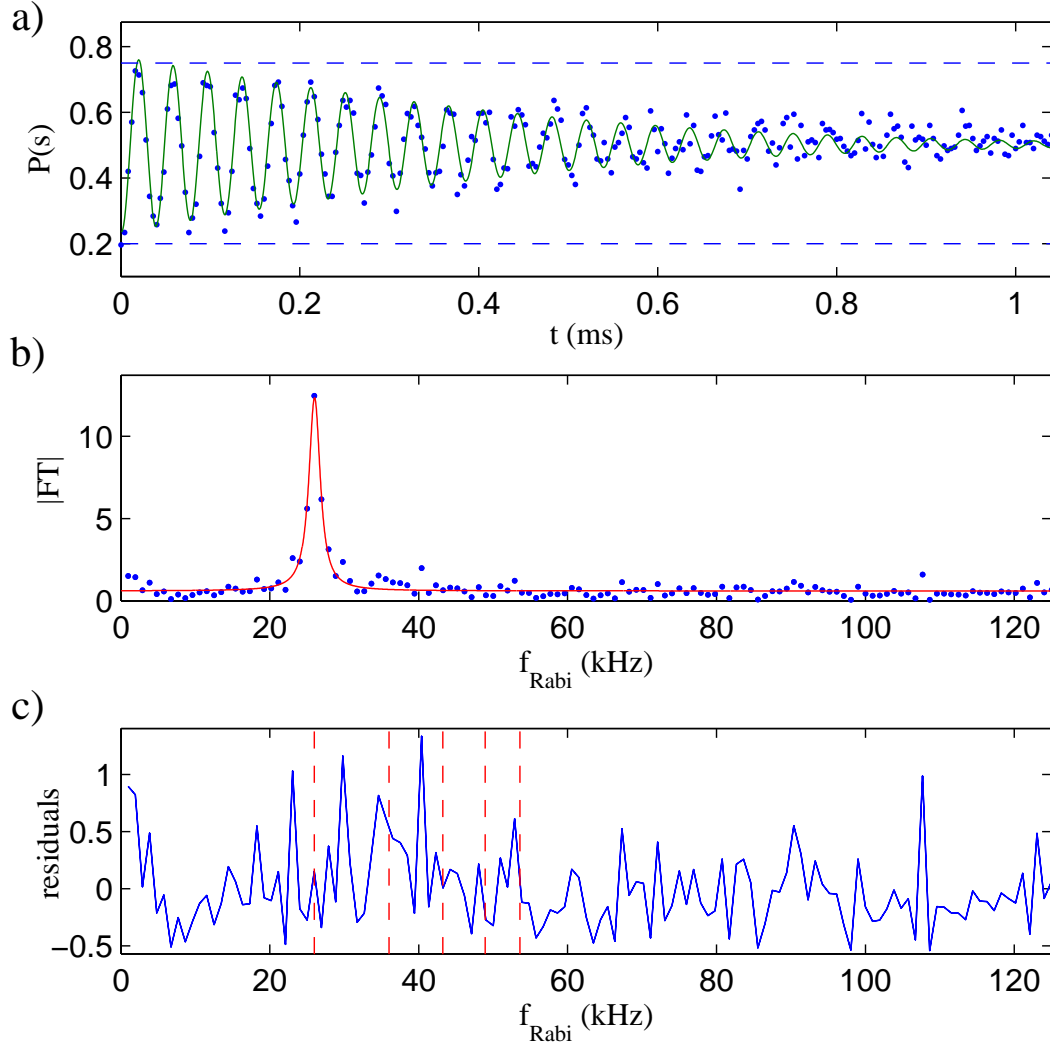


Figure 4.9: a) The variation of $P(s)$ for Rabi flopping on the blue sideband transition for an ion initially prepared in $|\downarrow, 0\rangle$. The solid curve is a fit to the data using equation 4.9. The readout levels $P(s|\uparrow)$ and $P(s|\downarrow)$ are indicated by horizontal dashed lines. b) shows the absolute value of the discrete Fourier transform of the data. The bulk of the population starts in $n = 0$, hence the maximum of the Fourier transform is at the blue-sideband frequency for population starting in this state. The Fourier transform is fitted with a Voigt profile (solid curve), for which the residuals are shown in c). The vertical dashed lines indicate the Rabi frequencies of the blue-sideband transitions for an ion starting in $m = 0$ to 4, calculated using the Rabi frequency of the $n = 0 \rightarrow 1$ transition from the fitted Voigt profile and the relative matrix elements given by equation 3.7. The size of the residuals at these frequencies allow us to put an upper limit on the populations of vibrational states other than that which we attempted to prepare.

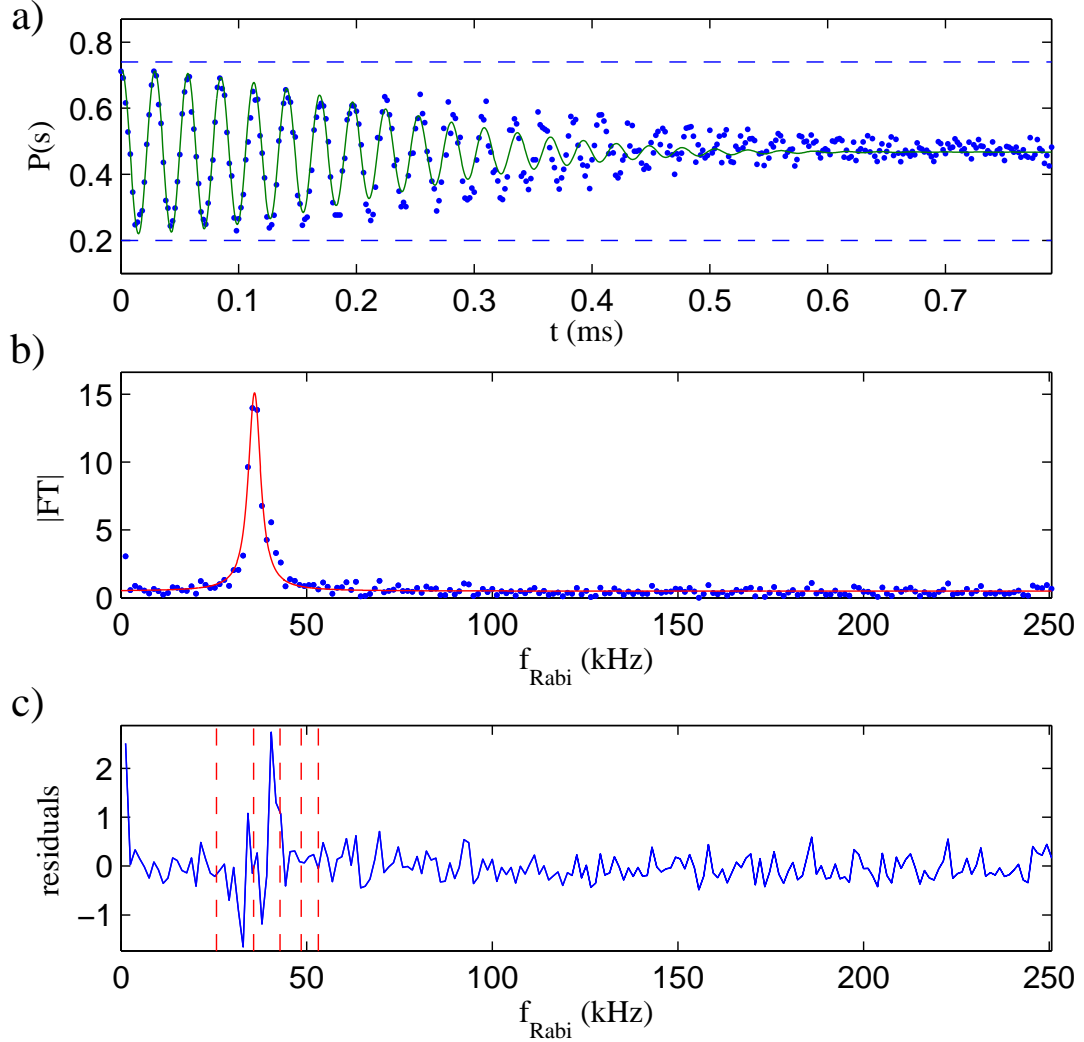


Figure 4.10: a) The variation of $P(s)$ for Rabi flopping on the red sideband transition for an ion initially prepared in $|\uparrow, 1\rangle$. The solid curve is a fit to the data using equation 4.9. The readout levels $P(s|\uparrow)$ and $P(s|\downarrow)$ are indicated by horizontal dashed lines. b) shows the absolute value of the discrete Fourier transform of the data. The bulk of the population starts in $n = 1$, hence the maximum of the Fourier transform is at the red-sideband frequency for population starting in this state. The Fourier transform is fitted with a Voigt profile (solid curve), for which the residuals are shown in c). The vertical dashed lines indicate the Rabi frequencies of the blue-sideband transitions for an ion starting in $m = 0$ to 4, calculated using the Rabi frequency of the $n = 1 \rightarrow 2$ transition from the fitted Voigt profile and the relative matrix elements given by equation 3.7. The size of the residuals at these frequencies allow us to put an upper limit on the populations of vibrational states other than that which we attempted to prepare.

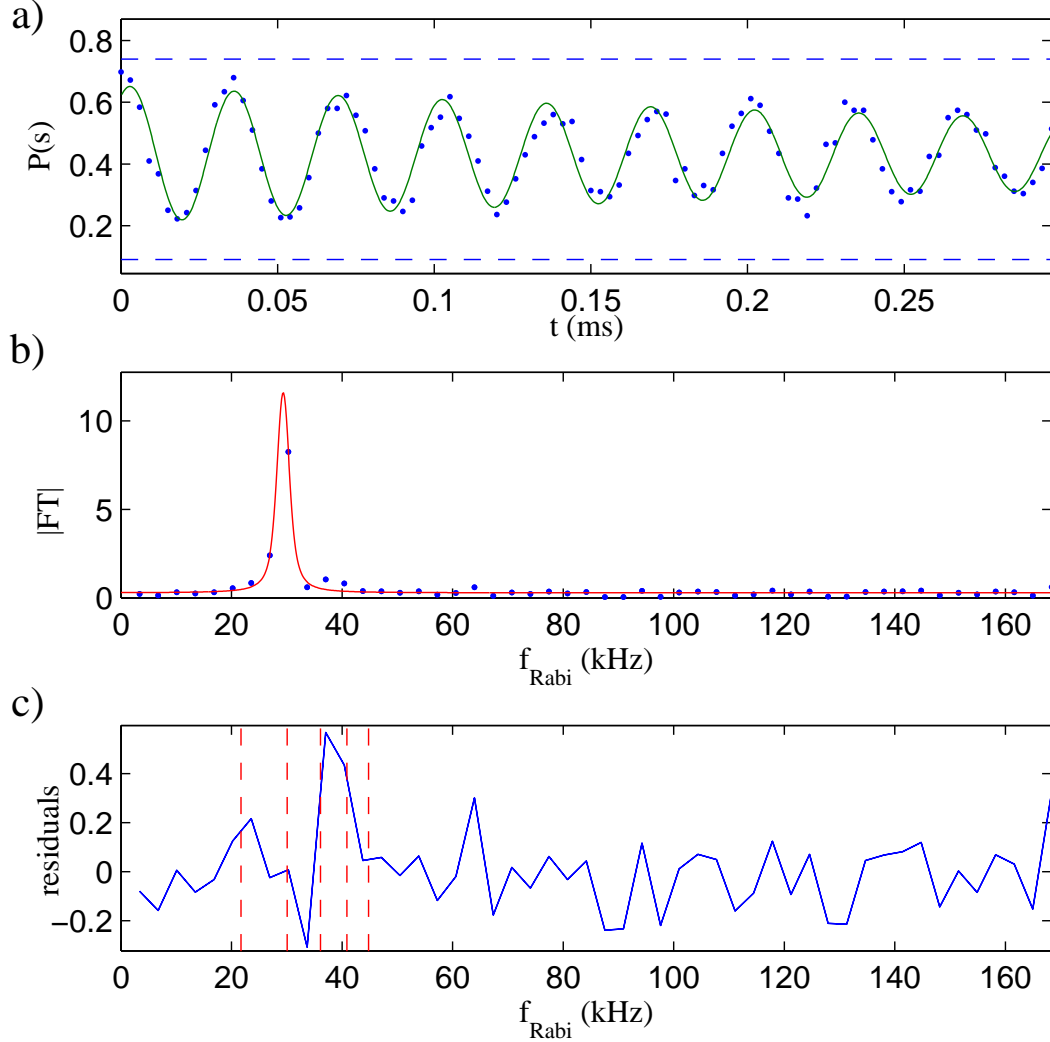


Figure 4.11: a) The variation of $P(s)$ for Rabi flopping on the red sideband transition for an ion initially prepared in $|\uparrow, 1\rangle$. The solid curve is a fit to the data using equation 4.9. The readout levels $P(s|\uparrow)$ and $P(s|\downarrow)$ are indicated by horizontal dashed lines. b) shows the absolute value of the discrete Fourier transform of the data. The bulk of the population starts in $n = 1$, hence the maximum of the Fourier transform is at the red-sideband frequency for population starting in this state. The Fourier transform is fitted with a Voigt profile (solid curve), for which the residuals are shown in c). The vertical dashed lines indicate the Rabi frequencies of the blue-sideband transitions for an ion starting in $m = 0$ to 4, calculated using the Rabi frequency of the $n = 1 \rightarrow 2$ transition from the fitted Voigt profile and the relative matrix elements given by equation 3.7. The size of the residuals at these frequencies allow us to put an upper limit on the populations of vibrational states other than that which we attempted to prepare.

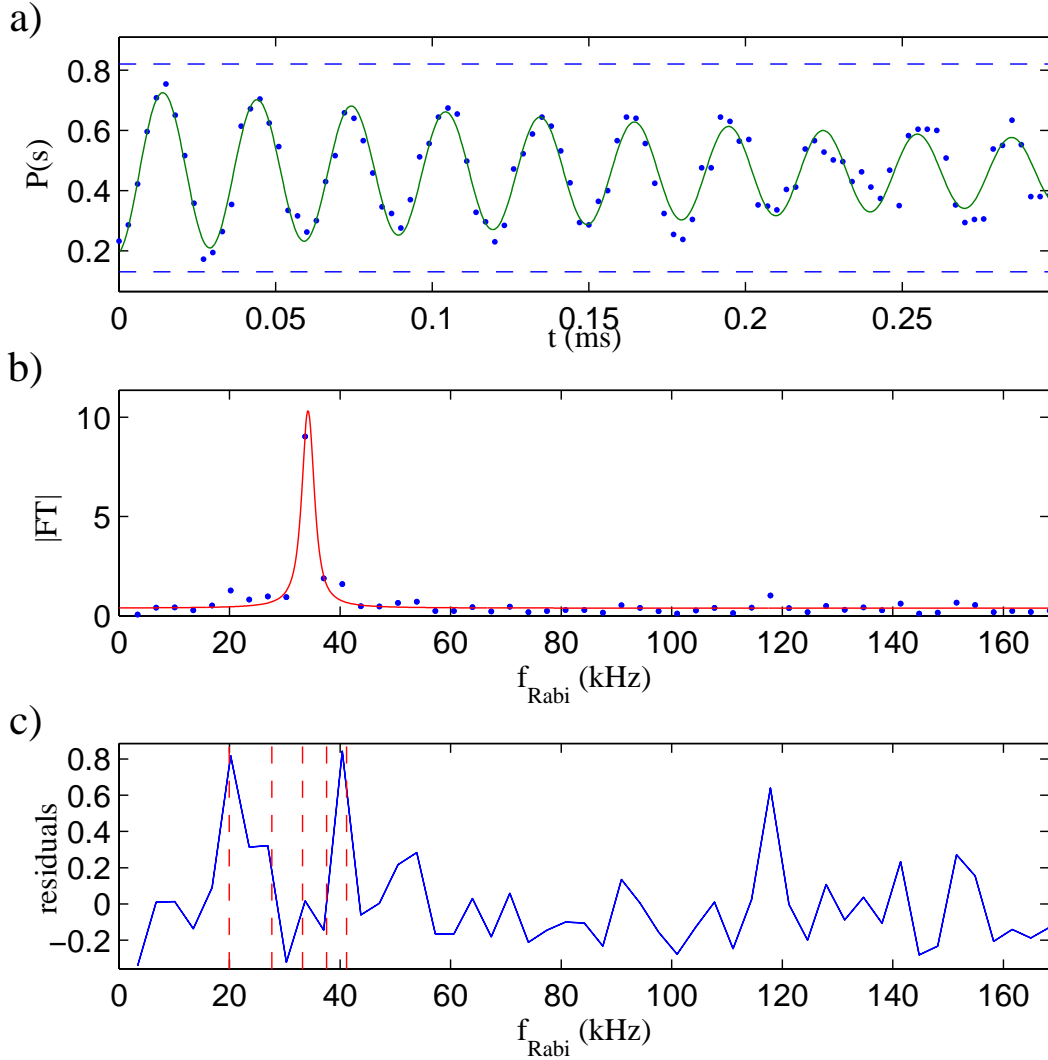


Figure 4.12: a) The variation of $P(s)$ for Rabi flopping on the blue sideband transition for an ion initially prepared in $|\downarrow, 2\rangle$. The solid curve is a fit to the data using equation 4.9. The readout levels $P(s|\uparrow)$ and $P(s|\downarrow)$ are indicated by horizontal dashed lines. b) shows the absolute value of the discrete Fourier transform of the data. The bulk of the population starts in $n = 1$, hence the maximum of the Fourier transform is at the blue-sideband frequency for population starting in this state. The Fourier transform is fitted with a Voigt profile (solid curve), for which the residuals are shown in c). The vertical dashed lines indicate the Rabi frequencies of the blue-sideband transitions for an ion starting in $m = 0$ to 4, calculated using the Rabi frequency of the $n = 2 \rightarrow 3$ transition from the fitted Voigt profile and the relative matrix elements given by equation 3.7. The size of the residuals at these frequencies allow us to put an upper limit on the populations of vibrational states other than that which we attempted to prepare.

Chapter 5

Coherence Measurements.

Any experiment which relies on coherent manipulation of the quantum states of ions is limited by the decoherence of the system due to its interaction with the environment. In order to implement quantum logic in a system of trapped ions, we are concerned with manipulations of the quantum state of both the spin and motion. A detailed discussion of the sources of decoherence in an ion trap system is given by Wineland et. al. [30]. It is useful to split the study of decoherence up into three categories. These are

1. Decoherence of the spin state of the ion. In a quantum computer, this represents decoherence of the qubit memory.
2. Decoherence of the ion motion. Coherence of the motional states is important during logic gates between ions, as will be seen in chapter 9.
3. Decoherence caused by non ideal applied fields which are responsible for logic operations. This reduces the fidelity of the logic gates, and hence the computation.

These will be discussed in order below.

1. A fundamental source of decoherence of the ion's spin state is radiative decay [30], which represents amplitude damping of the state. Since the energy difference between the two qubit levels in our experiment is small, the lifetime of the upper qubit level in a perfect vacuum is very long (10^{21} s) compared to the duration of even the longest experiments which we perform. In practice, this is much reduced, and is probably limited by stray light due to imperfect extinction of laser beams on the 397 nm and 393 nm transitions, which will lead to photon scattering.

In the absence of applied electric fields for logic operations, the primary source of decoherence of the spin state is fluctuations of the magnetic field amplitude. These cause damping of the phase relationship between the qubit states, and hence a loss of the coherence. The fluctuations can be split into two parts dependent on their timescale. Decoherence due to fluctuations which are slow compared to typical experiment times can be guarded against by inverting the spin states at regular intervals. On the other hand, fluctuations which occur on a timescale which is fast compared to that of a typical experimental are difficult to protect against.

The mains electricity supply oscillates at 50 Hz, which causes a large 50 Hz component of the magnetic field. This is protected against in all the experiments presented below by triggering the start of each experimental sequence at a given point in the 50 Hz cycle.

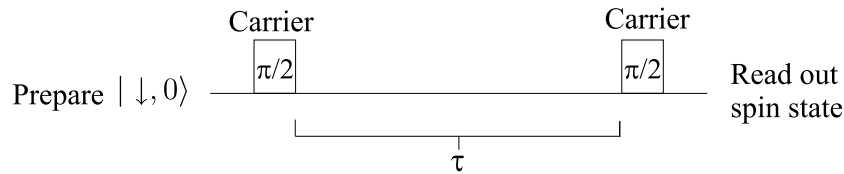


Figure 5.1: Pulse sequence used to measure the coherence time of the spin state of the ion. The spin dynamics throughout the sequence is described in the text. The first $\pi/2$ pulse defines the phase of the superposition of spin states. In order to observe Ramsey fringes, the phase of the second $\pi/2$ pulse relative to the phase difference between the two spin states of the ion must be varied. In the spin coherence measurements this was done by scanning the difference frequency of the Raman laser beams over a range of 100 kHz around the qubit resonance. The carrier flopping Rabi frequency used in the experiments was 42 kHz, hence the length of the $\pi/2$ pulses was $6 \mu\text{s}$.

2. Decoherence of the motional state is primarily due to the instability of the trapping electric fields. This is discussed in detail by Wineland et. al. [30] and an extensive experimental study is described by Turchette et. al. [51]. Two different mechanisms produce decoherence. If the trap frequency fluctuates, but the electric field at the ion remains zero, dephasing will occur between motional states of different energies. Fluctuations of trap parameters can also cause a fluctuating electric field at the ion. This will heat the ion, as well as causing dephasing between motional state superpositions. For superpositions where $\Delta n \sim 1$ (which are experimentally realised in this chapter), the heating rate and dephasing rates are of similar size [74].
3. In order to implement logic gates with trapped ions, we address the ion with laser light, as described in chapter 3. The control parameters of the light field are the optical phase, the polarisation, and the intensity. If any of these fluctuate, this will make the logic operations imperfect. The laser field will also off resonantly scatter photons on the $S_{1/2} \rightarrow P_{1/2}$ transition, which will decohere the internal state of the ion.

The first two sections of this chapter are concerned with studies of the coherence times of both the spin and motional degrees of freedom. The basic technique is first introduced in the context of measurements of the coherence of the spin state. This same method is later applied to measurement of the coherence of the motional state of the ion.

The final part of this chapter deals with measurements of decoherence due to the Raman laser beams. This includes a study of the rate of photon scattering from the off-resonant light fields.

5.1 Measurement of spin coherence

In order to illustrate the experimental method for measuring coherence times, we will first use the example of measurement of the spin coherence of the ion. It will be seen later that this method and the general treatment of decoherence used here apply equally well to measurements of motional coherence.

In order to measure the coherence time of the spin states of the ion we use the Ramsey separated pulse sequence shown in figure 5.1. The initial $\pi/2$ pulse puts the ion into an

equal superposition of the two spin states, with an initial phase defined by the phase of the light at the ion (this will be taken to be zero phase in this section). After a delay with possible decoherence the density matrix is

$$\rho = \frac{1}{2} \left[|\uparrow\rangle \langle \uparrow| + |\downarrow\rangle \langle \downarrow| + C e^{i\phi_a} |\downarrow\rangle \langle \uparrow| + C e^{-i\phi_a} |\uparrow\rangle \langle \downarrow| \right] \quad (5.1)$$

where C and ϕ_a are the magnitude and phase of the coherence between the two spin states. After a second $\pi/2$ pulse with phase ϕ_f is applied, the population elements of the density matrix element become,

$$P(\uparrow) = \frac{1}{2} (1 + C \cos(\phi_a - \phi_f)) \quad (5.2)$$

$$P(\downarrow) = \frac{1}{2} (1 - C \cos(\phi_a - \phi_f)) \quad (5.3)$$

The amplitude of the Ramsey fringes observed as the phase ϕ_f is varied therefore provides a measure of the magnitude of the coherence.

In order to observe Ramsey fringes, we must vary the phase of the second $\pi/2$ pulse relative to the first and relative to the phase ϕ_a gained by the ion during the gap. Experimentally we do this by three different methods. For the measurement of spin coherence presented in this chapter the detuning from resonance of the laser pulses driving the $\pi/2$ carrier pulses is varied. For values of δ_s much smaller than the Rabi frequency of the carrier transition, the effect is very similar to that of varying ϕ_f and the treatment given above is valid. Hence as the relative frequency of the Raman laser beams is changed we observe oscillations in the spin population with period $1/\tau$, where τ is the time between the two $\pi/2$ pulses.

An alternative method is to fix the detuning δ_s and change the length of the gap between pulses (this method is similar to that used for the motional coherence experiments). The fringes observed have time period $2\pi/\delta_s$.

Finally, by using different synthesizers to drive the initial and final $\pi/2$ pulses, a chosen phase difference ϕ_f can be introduced between these two pulses. The synthesizers are referred to the same clock source to ensure ϕ_f is well-defined. Oscillations are observed in $P(\uparrow)$ with period 2π . This method is used for the experiments in chapters 7 and 9.

5.1.1 Decoherence.

Decoherence effects cause the amplitude of the oscillations in the Ramsey signal to be reduced. We mostly use an exponential decay model to deduce the decay time observed in the data. However this does not account for all types of decoherence. As a simple guide to possible decays, we first discuss two different types of noise which affect the coherence of the spin state.

Consider a single ion which starts in a superposition of the two spin states $|\uparrow\rangle$ and $|\downarrow\rangle$ at time $\tau = 0$. The phase ϕ_a acquired by the ion is given by the integral of the frequency splitting of the two states with respect to time. In our experiment, the frequency splitting is due to the magnetic field applied to the atom. Fluctuations in the magnetic field amplitude will cause a fluctuation in the frequency splitting of the two states. We can model this by writing the frequency splitting as a sum of a constant term ω_0 plus a noise parameter $\Delta(t)$. The phase acquired by the ion over time τ is thus

$$\phi_a = \omega_0 \tau + \int_0^\tau \Delta(t') dt' \quad (5.4)$$

The density matrix represents the ensemble average of the state over an infinite number of repetitions, hence the coherence of the density matrix has magnitude

$$C = |\langle e^{-i \int_0^\tau \Delta(t') dt'} \rangle| \quad (5.5)$$

where the angular brackets represent the ensemble average.

Noise with time period much shorter than the Ramsey gap time can have many forms. One simple model is that the noise is “white”, i.e. it has the average value $\langle \Delta(t') \rangle = 0$ and a two-time correlation function $\langle \Delta(t') \Delta(t'') \rangle = 2D\delta(t' - t'')$, where D is the diffusion coefficient. The mean and variance of the phase ϕ_a are then given by

$$\mu_\phi(\tau) = \overline{\phi_a} = \omega_0 \tau \quad (5.6)$$

$$\sigma_\phi^2(\tau) = \overline{\phi_a^2} - \overline{\phi_a}^2 = 2D\tau \quad (5.7)$$

Making the further assumption that the fluctuations are due to a large number of small and random effects, we can make use of the central limit theorem and assume that the fluctuations in the value of the phase ϕ_a are normally distributed. The coherence C can then be calculated by making use of the moment generating function for Gaussian distributed variables [75], which gives $C = e^{-D\tau}$. Thus in this model the amplitude of the Ramsey fringes decays exponentially as the gap time is increased.

The fluctuations of the frequency difference of the two spin states may also have a component with a time period which is long compared to the gap length between the $\pi/2$ pulses. This can be modelled by taking $\Delta(t')$ to be a constant value Δ for each experimental sequence. The magnitude of the coherence is then

$$C = |\langle e^{-i\Delta\tau} \rangle| = \left| \int_{-\infty}^{\infty} P(\Delta) d\Delta e^{-i\Delta\tau} \right| \quad (5.8)$$

where $P(\Delta)d\Delta$ is the probability that the detuning is between Δ and $\Delta + d\Delta$. The amplitude of the fringes observed in the Ramsey experiment is thus given by the Fourier transform as a function of time of the probability distribution $P(\Delta)$. This means a Lorentzian distributed noise variable will give exponential decay of the amplitude of the Ramsey fringes with time, whereas a Gaussian noise distribution will give a Gaussian decay with time.¹

In the analysis presented below we do not attempt to model noise in a rigorous way since the data are not sufficient to discriminate between different noise models. An exponential decay is fitted to the data in order to give an indication of the relevant timescale over which decoherence occurs.

5.1.2 Experimental results

The coherence time for the spins was determined using a Ramsey experiment. After preparing the state $|\downarrow\rangle$, a carrier $\pi/2$ pulse was applied to the ion using the Raman laser, which puts it into a superposition of spin states $\frac{1}{\sqrt{2}}(|\uparrow\rangle + |\downarrow\rangle)$. After a delay time τ , a second $\pi/2$ pulse is applied on the carrier transition. If the detuning $\delta_s \ll \Omega_R$, the probability of finding the ion spin up after the second $\pi/2$ pulse is

$$P(\uparrow) = \frac{1}{2} [1 + C \cos(\delta_s \tau)] \quad (5.9)$$

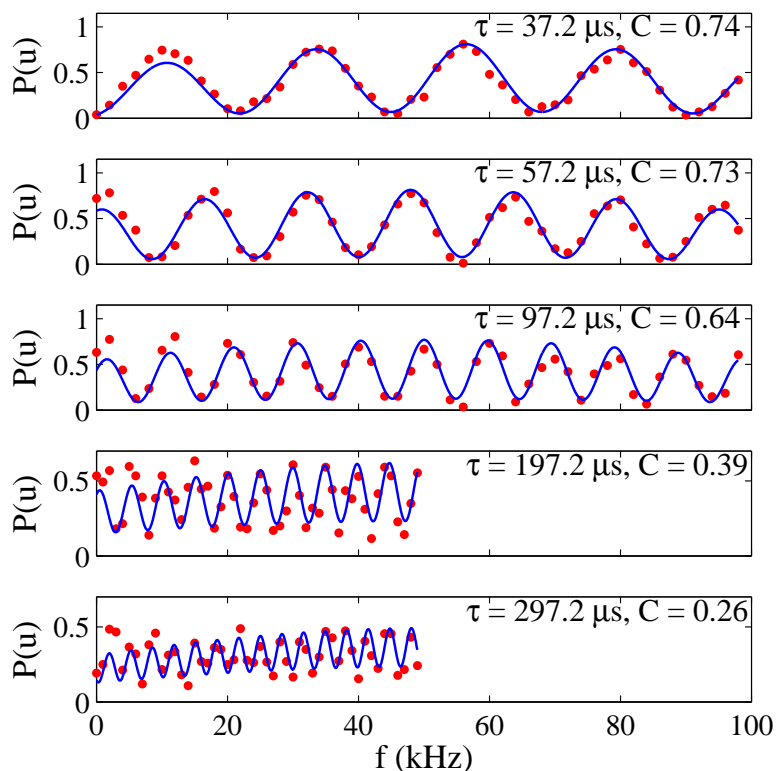


Figure 5.2: The probability $P(u) = P(\uparrow)$ of finding the ion spin up after a Ramsey pulse sequence versus the difference frequency of the Raman beams (used to give the $\pi/2$ pulses). For each data point, the experimental sequence was repeated 500 hundred times. $P(\uparrow)$ was then calculated from the fraction of times the ion fluoresced using the method of section 2.4.3. $f = (\delta_s + \omega_0)/2\pi$, where δ_s is the detuning of the difference frequency of the two Raman laser beams from the qubit resonance and ω_0 is the centre frequency of the fringe pattern. The data is fitted with the form of $P(\uparrow)$ given in equation 5.10, with the centre frequency ω_0 , the baseline B and the amplitude of the central fringe C allowed to float. The qubit transition frequency was measured to correspond to $f = 50$ kHz prior to carrying out these experiments, and 24 kHz two and a half hours after the final scan. For the data sets with delay times 197.2 μs and 297.2 μs a range of starting values for the centre frequency of the Ramsey fringe pattern were used in fitting the data. The amplitudes obtained from these fits were all within one standard error (~ 0.04) of the fitted amplitudes given in the plot.

The frequency of the carrier pulses was scanned in these experiments. The data from these scans is shown in figure 5.2. For these experiments δ_s was scanned over $2\pi \times 100$ kHz with $\Omega_R = 2\pi \times 41.7$ kHz, hence the condition $\delta_s \ll \Omega_R$ is not valid for the full range of the scan. In order to extract the amplitude of the fringes the data was fitted with

$$P(\uparrow) = B + [1 + C \cos(\delta_s(\tau + t_{\pi/2}))] \frac{\Omega_R^2}{\delta_s^2 + \Omega_R^2} \sin^2 \left(\frac{(\delta_s^2 + \Omega_R^2)^{1/2} t_{\pi/2}}{2} \right) \quad (5.10)$$

¹Experimental observations of such a Gaussian decoherence are described in [25]

where the detuning $\delta_s = 2\pi f - \omega_0$. The floated parameters were the centre frequency ω_0 , the baseline B and amplitude C of the central fringe. The fitted curves are shown in figure 5.2. A plot of the amplitude of the central fringe C as the gap time τ is increased is given in figure 5.3. The decoherence time was estimated by fitting an exponential decay curve

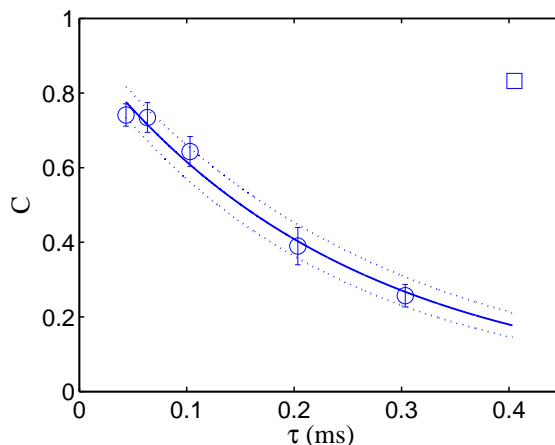


Figure 5.3: The amplitude of the Ramsey fringes for different gap times τ between $\pi/2$ carrier pulses. The amplitudes for a Ramsey sequence of two separated $\pi/2$ pulses on the carrier transition are represented by \circ . This data is fitted with an exponential decay, which gives a decoherence time of $245(22) \mu\text{s}$. The data point represented by a square is the fringe contrast after a spin-echo pulse sequence, with the initial and final $\pi/2$ pulses were separated by $400 \mu\text{s}$. This indicates that the phase decoherence of the spin state of our ion is mostly caused by fluctuations which are slow compared to the time taken for one experimental sequence.

$e^{-\tau/T}$ to the data, giving a decay time of $T = 245(22)\mu\text{s}$.

The most likely cause of decoherence of the spin state is fluctuations in the magnetic field at the ion [30]. In order to test whether these fluctuations are fast or slow compared to the experimental sequence, we performed a spin echo sequence by adding an additional π pulse on the carrier transition half way between the two Ramsey $\pi/2$ pulses. A data point from this spin-echo sequence is shown on figure 5.3. If a spin-echo pulse sequence is used, the coherence is maintained over much longer times. This indicates that the decoherence is mostly caused by fluctuations of the magnetic field which are slow compared to the $400 \mu\text{s}$ total gap time used in this experiment. The reduction of the contrast using a spin-echo sequence corresponds to a decoherence time of ~ 2.5 ms. In chapter 8, the density matrix of two ions after a spin-echo sequence with total length $240\mu\text{s}$ is deduced from experimental results. This has a 95% fidelity with a pure state, which may indicate that the coherence time is ~ 4.4 ms.

The r.m.s. amplitude of the fast fluctuations in the magnetic field which would give rise to the observed decay time of $245\mu\text{s}$ is $0.23(2)$ mG.

A spin-echo sequence is required to preserve coherence for the Schrödinger's cat and gate experiments described in chapters 7 and 9, where the ions are required to be in a coherent superposition of the spin states for longer than $100 \mu\text{s}$.

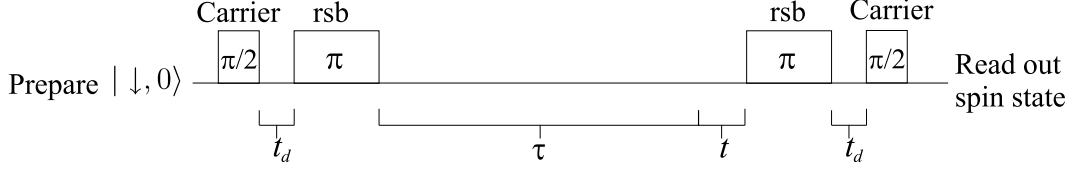


Figure 5.4: Pulse sequence used for the motional coherence experiments. In the gap between the red-sideband pulses the state of the ion is $\frac{1}{\sqrt{2}}|\downarrow\rangle (|0\rangle + |1\rangle)$. The minimum gap time between the $\pi/2$ carrier pulses and the red-sideband pulses is limited by the control unit which generates the pulse sequence. For the experiments presented in this chapter, $t_d = 13.6 \mu\text{s}$. The delay t is varied in order to change the phase of the laser pulses in the second half of the pulse sequence relative to the two initial pulses. The synthesizers producing the red sideband and carrier pulses are phase locked together.

5.2 Measurement of motional coherence

In section 4.3 of the previous chapter, π pulses on the sidebands were used to prepare the ion in Fock states of motion. We can create superpositions of motional states using sideband pulses of intermediate length or by setting up a superposition of spin states and subsequently applying a π pulse on the sideband. This allows us to study the decoherence rate of the motional states by performing a Ramsey experiment with a superposition of motional states. In order to distinguish motional decoherence from spin decoherence, we must prepare states of the form

$$|\psi\rangle = |\downarrow\rangle (\alpha |n\rangle + \beta |n'\rangle) \quad (5.11)$$

or the equivalent state with the spin state $|\uparrow\rangle$. α and β are the amplitudes of the two states in the superposition. The experiments presented here used $n = 0$ and $n' = 1$ and $\alpha \approx \beta \approx \frac{1}{\sqrt{2}}$. The sequence of pulses used in the experiment is shown in figure 5.4. The first carrier pulse puts the ion into an equal superposition of spin states. The ion is in this spin state for time t_d , which is the minimum time between programmed pulses in our experiment ($t_d = 13.6 \mu\text{s}$ for the experiments presented in this chapter). The π -pulse on the red-sideband transfers population from the $|\uparrow, 0\rangle$ state into $|\downarrow, 1\rangle$. In a perfect experiment, the state of the ion after time $\tau + t$ is

$$\frac{1}{\sqrt{2}} \left[|\downarrow, 0\rangle + e^{i\delta_s t_d} e^{i\delta_m(\tau+t)} |\downarrow, 1\rangle \right] \quad (5.12)$$

where δ_s is the detuning of the carrier $\pi/2$ pulse from resonance and δ_m is the detuning of the difference of the carrier and red-sideband pulses from the motional frequency. Ideally we would keep $\delta_s = 0$ but we include it to allow for the effect of magnetic field drift during the experiment. The synthesizers producing the carrier pulses and the sideband pulse are phase locked together, hence the final sequence of a π pulse on the red sideband, gap of length t_d , and $\pi/2$ carrier pulse put the ion into the state

$$|\psi_f\rangle = \frac{1}{2} \left[\left(1 + e^{2i\delta_s t_d} e^{i\delta_m(\tau+t)}\right) |\downarrow, 0\rangle + \left(-1 + e^{2i\delta_s t_d} e^{i\delta_m(\tau+t)}\right) |\uparrow, 0\rangle \right] \quad (5.13)$$

The probability of finding the ion in the spin state $|\uparrow\rangle$ after this sequence of pulses is therefore

$$P(\uparrow) = \frac{1}{2} [1 + \cos(2\delta_s t_d + \delta_m(\tau + t))] \quad (5.14)$$

In reality, decoherence processes randomise the phase between the two states in the superposition, hence the amplitude of the fringes observed is decreased. Decoherence of the motional state is caused by fluctuations in the electric potential, which might be due to fluctuations in the voltage applied to the electrodes, or by fluctuating patch potentials on the electrode surfaces [30].

In the experiments presented here, the delay time used was $\tau + t$, where t is scanned from $0 \rightarrow 500\mu\text{s}$. The experiment was set up with $\delta_s \approx 0$ and $\delta_m \simeq 2\pi \times 10\text{kHz} \ll \Omega_R$. $P(s)$ was measured and fitted with a sinusoidal function with floated period, amplitude, baseline and phase. The probabilities obtained are plotted against t for various delay times τ in figures 5.5 (812 kHz trap) and 5.7 (500 kHz trap). The fitted oscillation amplitudes are plotted against τ in figures 5.6 and 5.8.

For longer times, the experiments become increasingly difficult to perform due to instability of the apparatus over the period required to take one scan (~ 50 minutes for the $\tau = 49$ ms experiment). One problem in such experiments is that the trap frequency makes infrequent sudden changes. These can be seen in the $\tau = 49$ ms data shown in figure 5.9, where the trap frequency changed suddenly at $t = 190 \mu\text{s}$ from 8.2 kHz to 10.1 kHz. If this was due to a change in the end-cap voltage it would correspond to a change of 3.3 V, which seems unlikely. Another potential cause of such a shift is a change in a patch potential. It has been observed previously that there are some Calcium deposits on the trap electrodes. A shift in these deposits would change the surface potential of the electrodes. An estimate of the surface voltage change required was made by modelling the electrode potentials using CPO [76]. The modelled patch had length 0.25 mm, and extended around one of the r.f. electrodes. The patch was positioned at the closest position on the r.f. electrodes to trap centre. It was found that a patch of this size would require a change in voltage of 0.6 V. This is consistent with the work function of the materials involved. Equipment in the laboratory was switched off during the run, as this data was taken at the end of the day and left to run into the evening. This might have created some sort of instability which allowed such a patch to be displaced.

The data for experiments with a single ion in an 800 kHz trap indicate that the motional coherence time of the ion is $T_{800} \simeq 157(34)$ ms. In the 500 kHz trap, the coherence time is $T_{500} \simeq 76(30)$ ms. If this decoherence was all due to parametric heating, the heating rates would be 6.4 ± 1.4 quanta s^{-1} and 13.2 ± 5.1 quanta s^{-1} for the 800 and 500 kHz traps respectively. The 800 kHz trap value is reasonably consistent with the heating rate measurements presented in chapter 4.

The motional coherence time in the 800 kHz trap is longer than motional coherence times measured elsewhere [51, 25]. The trap used in the measurements made at NIST Boulder [51] was smaller than the one used here, hence, as in the case of the heating rates presented in chapter 4, their shorter coherence time can probably be assigned in part to the smaller distance from the centre of the trap to the electrode surfaces. The measurement made in Innsbruck [25] used a trap with similar dimensions to the one used here, and observed a motional coherence time of approximately 100 ms in a 1.5 MHz trap.

We can place an upper limit on the slow voltage fluctuations on the trap end caps using the measured decoherence rate. For this purpose we assume that the observed decoherence is caused by changes in the trap frequency due to slow fluctuations of the voltage on both end cap electrodes. This would dephase the motional states, but would not contribute to heating. If the voltage noise amplitude has a Lorentzian distribution, the r.m.s amplitude is given by $\delta U = \frac{2U\delta\omega_z}{\omega_z}$, where $\delta\omega_z = 1/T$. For the 812 kHz trap this gives $\delta U_{800} = 1.8(4)$ mV and for the 500 kHz trap $\delta U_{500} = 2.2(8)$ mV. Both these values

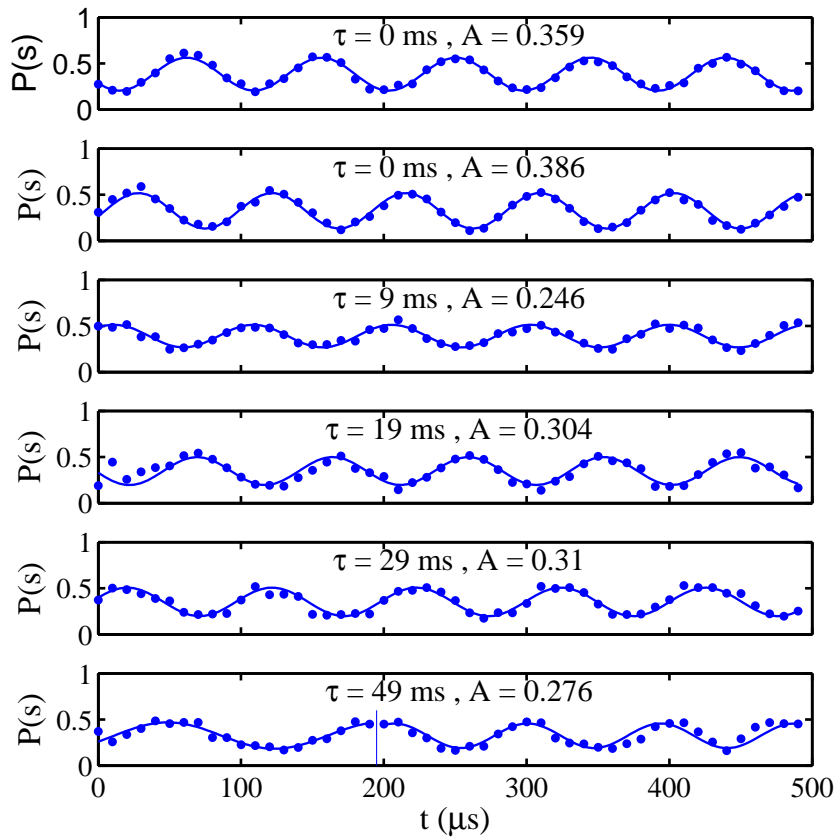


Figure 5.5: The probability of finding the ion shelved in motional coherence experiments. These experiments were all carried out in an 812 kHz trap. The pulse sequence used is shown in figure 5.4. Each data point is the result of 500 repeats of the pulse sequence. The data is fitted with sinusoidal curves, with the amplitude A , phase, baseline and frequency floated. The phase of the fringes for two experiments performed with equal values of τ is not the same. This could be due to changes in the detuning of the laser from the spin resonance due to magnetic field drift. Where it appeared that the frequency of the fringes changed during the experiment (eg. for the $\tau = 49$ ms data) the data was fitted with two sin curves and their amplitudes were averaged. The time at which the change occurs is indicated by a vertical line.

are upper limits, since we have neglected the contribution to the decoherence rate due to heating processes.

These would be consistent with the amplitude of noise on the end cap voltage being independent of the applied voltage. The specification for the EMCO octo-channel supply which supplies voltage to the end-caps is a peak-peak ripple voltage of 0.001 %. For the 700 V applied to the end-caps of our trap this corresponds to fluctuations of amplitude < 7 mV. The 500 kHz trap uses a voltage of $\simeq 270$ V applied to both end caps. This would mean that the voltage fluctuations specified by the manufacturer would have amplitude < 2.7 mV. Both of these values are consistent with the measurements we have made.

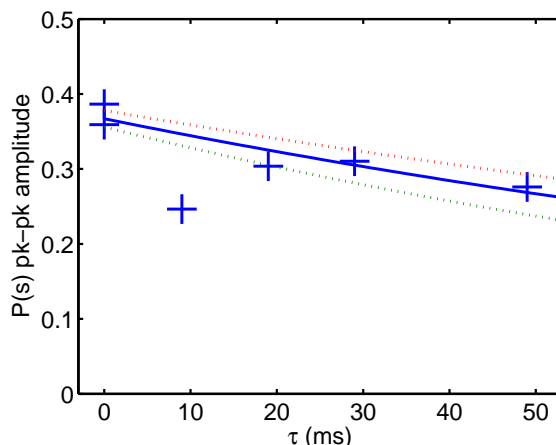


Figure 5.6: The amplitude of the sinusoidal variation of $P(s)$ with time plotted against gap time τ , for experiments performed using an 812 kHz trap. This amplitude is reduced by decoherence effects, which randomise the phase between the two states in the motional superposition. The data is fitted with an exponential decay which has a time constant of 157(34) ms.

5.3 Coherence during quantum manipulations

An additional source of decoherence during quantum manipulation of the ion is that which derives from the Raman beams themselves. A fundamental source is off-resonant scattering of photons on the 397 nm transition. Fluctuations of the intensity or phase of the laser light at the ion would also lead to imperfect operations, which would randomise the state which results.

In chapter 6 the results of scanning the duration of a carrier pulse applied to two ions are fitted with a product $P_1(\uparrow, t)P_2(\uparrow, t)$ of the probability of finding the spin up or down for each ion,

$$P_l(\uparrow, t) = \frac{1}{2} \left[1 - e^{-\frac{\Gamma t}{2}} \left\{ \cos \left(\sqrt{4\Omega_l^2 - \Gamma^2} t/2 \right) \right\} \right]$$

where $\Gamma \ll \Omega_l$, $l = 1, 2$. This formula can be derived by assuming phase damping at a rate Γ [77]. The same dephasing rate in a Ramsey experiment would result in coherences decaying with a time constant Γ . The decay rates obtained from fitting the data are between $\Gamma \simeq 3$ and 6 ms^{-1} , but are badly determined due to the correlation between the value of the readout levels and the decay parameter. Further experiments are required in order to get a more accurate estimate of the value of Γ at different laser powers. These may enable us to determine whether the damping is due to B-field fluctuations, or fluctuations in the intensity or phase of the Raman laser beams. A decay constant of 4 ms^{-1} would be consistent with the decoherence observed due to magnetic field fluctuations using the Ramsey experiment described in section 5.1.2.

5.3.1 Photon Scattering.

One source of decoherence in our system is photon scattering. During coherent manipulation of the ion's spin state, the Raman lasers off-resonantly scatter photons on the 397 nm

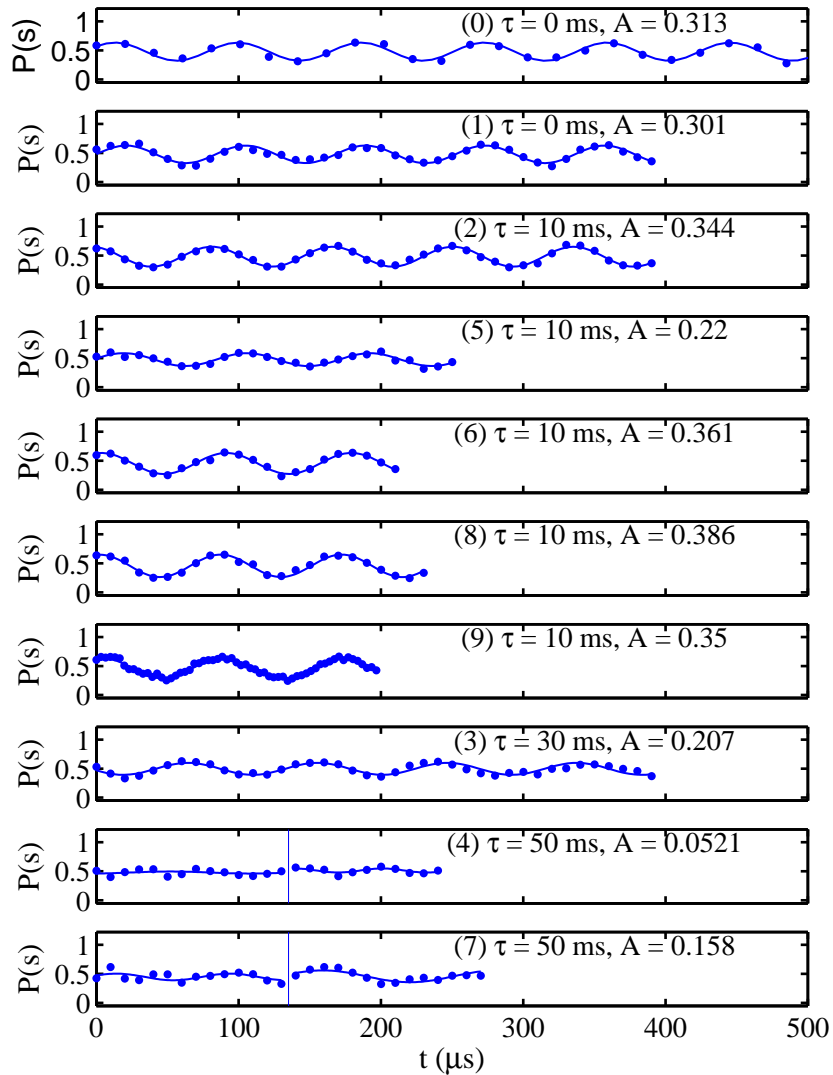


Figure 5.7: The probability of finding the ion shelved in motional coherence separated pulse experiments. These experiments were all carried out in a 500 kHz trap. The pulse sequence used is shown in figure 5.4. Each data point is the result of 500 repeats of the pulse sequence. The data is fitted with sinusoidal curves, with the amplitude A , phase, baseline and frequency floated. The data is presented in order of increasing delay time. The plots are numbered in the order in which they were performed. Where it appeared that the frequency of the fringes changed during the experiment (datasets (4) and (7), $\tau = 50$ ms) the data was fitted with two sin curves and their amplitudes were averaged (c.f. figure 5.9). The time at which this change of fit occurs is indicated by a vertical line.

transition. The relationship between photon scattering and loss of coherence is non-trivial for Raman scattering [49]. For the relatively modest detuning of 30 GHz employed in our experiments, most scattering events result in a complete loss of coherence, hence to first

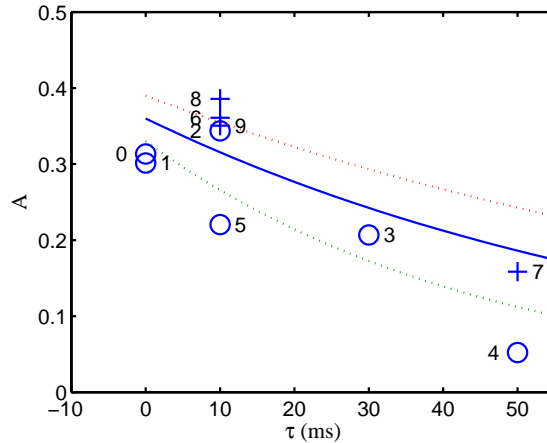


Figure 5.8: The amplitude of the sinusoidal variation of $P(s)$ with time plotted against gap time τ , for experiments performed using a 500 kHz trap. The data is numbered with the order in which the points were taken. After taking data point 5, the difference frequency of the Raman beams driving the red sideband transition was changed by 15 kHz as the magnetic field was observed to have changed. This may explain the low amplitude of the fringes for points 4 and 5 relative to points 2, 6, 7, 8. The data represented by + are data taken after this change was made. Points 1-3 and 6-8 of the data are fitted with an exponential decay curve (solid curve) which has a time constant of 76(30) ms. When points 4 and 5 are included this time constant becomes 53(18) ms.

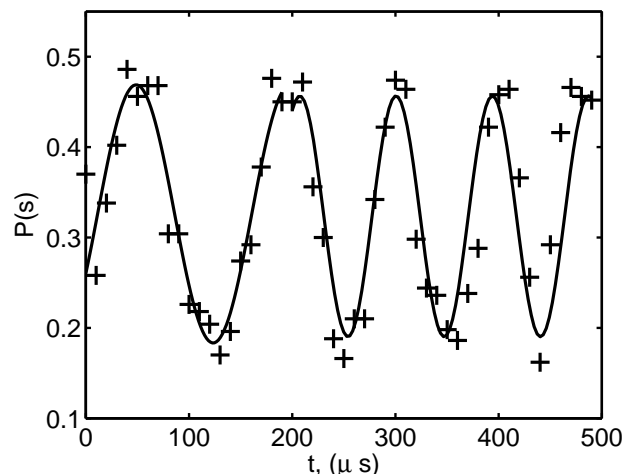


Figure 5.9: An example of fringes from a motional coherence separated pulse experiment taken with $\tau = 49$ ms (this is the same data as shown in figure 5.5). Each point represents the fraction of 500 repetitions in which the ion was shelved at the end of the sequence. The data is taken in order from $t = 0 \rightarrow 500 \mu\text{s}$. At $t \simeq 190 \mu\text{s}$ the phase and frequency of the fringes changes, which suggests that the trap frequency changed abruptly.

approximation the decoherence rate equals the scattering rate.

The photon scattering rate from the Raman beams was measured by preparing the spin state $|\downarrow\rangle$ (or for two ions $|\downarrow\downarrow\rangle$) and then turning on one of the Raman beams for time t_p . The state of the ion was then measured. This was repeated 500 times for a range of

values of t_p between 0 and 1 ms. Figure 5.10 shows the results of this type of experiment performed on two ions using laser beam powers of $P_{63} = 471 \mu\text{W}$ and $P_{\text{para}} = 188 \mu\text{W}$. The rate of photon scattering was modelled using rate equations for the $S_{1/2}$ and $P_{1/2}$

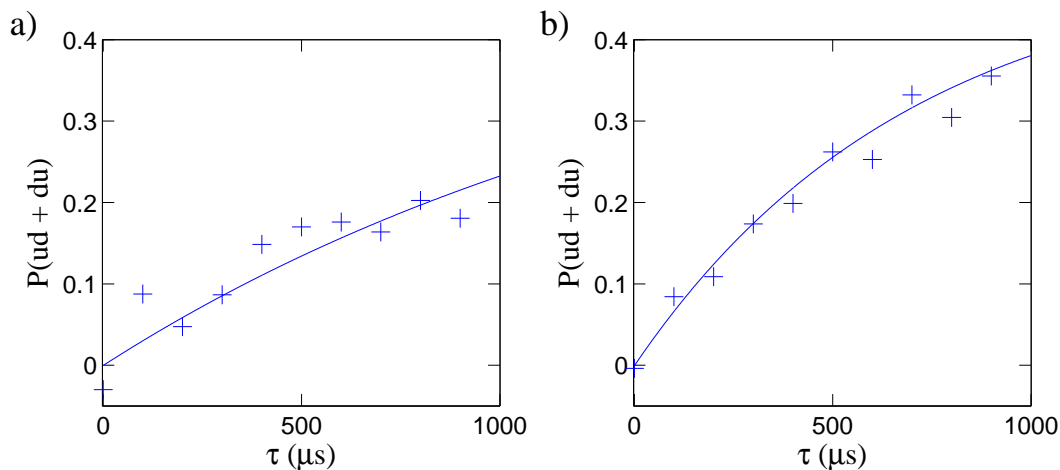


Figure 5.10: The effect of photon scattering on $P(\uparrow\downarrow + \downarrow\uparrow)$ for a) the Raman laser beam at 3° to the magnetic field and b) the Raman laser beam at 63° to the magnetic field. The solid curves were generated using a 4-level rate equations routine which models the $S_{1/2}$ and $P_{1/2}$ levels using intensities 0.07 Wmm^{-2} and 0.1 Wmm^{-2} for the 3° and 63° beams respectively. The photon scattering rates for the generated curves are $R_3 = 0.45 \text{ ms}^{-1}$ and $R_{63} = 0.67 \text{ ms}^{-1}$.

levels. This model does not take into account the branching ratio of 0.06 for the decay from the $P_{1/2} \rightarrow D_{3/2}$ level, however for low levels of scattering it should be able to give an indication of the scattering rate. The curves in the figures are not fitted, but were generated by inputting intensities $I_{63} = 0.1 \text{ Wmm}^{-2}$ and $I_3 = 0.07 \text{ Wmm}^{-2}$ into the model. The photon scattering rates obtained for these two curves were $R_{63} = 0.67 \text{ ms}^{-1}$ and $R_3 = 0.45 \text{ ms}^{-1}$.

The intensities of the two beams were independently estimated using the measured beam powers given above and measured spot sizes of $51 \times 37 \mu\text{m}^2$ and $69 \times 20 \mu\text{m}^2$ respectively. The spot sizes may have changed between the spot size measurement and the photon scattering experiment due to small changes in the optics used to align the laser beams. The 63° beam had a glass slide removed from its beam path between the spot size measurement and the photon scattering measurement. The intensities deduced from the powers and spot sizes were $I_{63} = 0.16 \text{ Wmm}^{-1}$ and $I_3 = 0.09 \text{ Wmm}^{-1}$. This is in reasonable agreement with the results deduced from the photon scattering rate. Taken together, these measurements imply that the broadband emission due to amplified spontaneous emission (ASE) in the diode laser is weak enough not to dominate the ion excitation at 30 GHz detuning.

The Raman laser powers used in these photon scattering experiments were higher than the typical laser powers used to drive carrier Rabi flopping, but the scattering rate is much lower than the decoherence rate estimated from carrier flopping. This indicates that the primary source of decoherence when driving transitions with the Raman laser is not due to photon scattering. In the gate experiments described in chapter 9, by contrast, we think that the major source of decoherence is due to photon scattering.

Chapter 6

Coherent Manipulation of Two Trapped Ions.

6.1 Interaction of two trapped ions with light

6.1.1 Modes of oscillation

If two ions are trapped in a three dimensional harmonic potential, they exhibit two modes of oscillation in each direction. In our experiments, we choose the trap parameters so that the confinement along the z -axis is weak compared to the radial directions. This means the ions form a linear crystal along the z -axis.

The two axial modes are the centre of mass (COM) mode, in which the ions oscillate in phase with each other, and the stretch (otherwise known as the “breathing”) mode, in which the two ions oscillate in antiphase. The position of each ion can be written in terms of the centre of mass z_c and the separation $d + 2z_s$

$$z_l = z_c + (-1)^l \left(\frac{d}{2} + z_s \right) \quad (6.1)$$

where l is the number of the ion under consideration and d is the equilibrium separation. z_c and z_s can be written in terms of the creation and annihilation operators of each mode as

$$z_c = \sqrt{\frac{\hbar}{4M\omega_c}} (\hat{a} + \hat{a}^\dagger) \quad (6.2)$$

$$z_s = \sqrt{\frac{\hbar}{4M\omega_s}} (\hat{b} + \hat{b}^\dagger) \quad (6.3)$$

where a^\dagger (a) and b^\dagger (b) are the creation (annihilation) operators for the centre of mass and stretch modes respectively. M is the mass of a single ion. The vibrational frequencies of the two modes are ω_c for the COM mode and $\omega_s = \sqrt{3}\omega_c$ for the stretch mode.

With the positions of the ions written in this form, the motional Hamiltonian is

$$\hat{H}_m = \hbar\omega_c(\hat{a}^\dagger\hat{a} + 1/2) + \hbar\omega_s(\hat{b}^\dagger\hat{b} + 1/2) \quad (6.4)$$

where the energy of the ions at their equilibrium positions has been omitted as it contributes only to a global phase.

6.1.2 Interaction with light.

The laser-ion interaction Hamiltonian for laser light interacting with two trapped ions is the sum of the Hamiltonian 3.9 for each ion, but with the motional matrix element $M_{n',n}$ modified to include the two modes. The Lamb-Dicke parameters of the two modes are defined as

$$\eta_c = \delta k z_c = 2k \sin(\theta/2) \sqrt{\frac{\hbar}{4M\omega_c}}, \quad \eta_s = \delta k z_s = 2k \sin(\theta/2) \sqrt{\frac{\hbar}{4M\omega_s}} \quad (6.5)$$

The matrix element for ion l is $\langle n' | \langle k' | e^{i\delta k z_l} | k \rangle | n \rangle$, where $|n\rangle$ are the Fock states of the COM mode and the $|k\rangle$ are the Fock states of the stretch mode. This can be written in terms of the Lamb-Dicke parameters as

$$M_{k',n',k,n} = \langle n' | e^{i\eta_c(\hat{a}e^{i\omega_c t} + \hat{a}^\dagger e^{-i\omega_c t})} | n \rangle \langle k' | e^{(-1)^l i\eta_s(\hat{b}e^{i\omega_s t} + \hat{b}^\dagger e^{-i\omega_s t})} | k \rangle \quad (6.6)$$

For radiation resonant with the carrier transition, the two ions evolve independently, hence the evolution of each ion is described by the operator $U(t, \delta)$ from equation 3.12, where for the l th ion, the phase of the light field is denoted by ϕ_l and the Rabi frequency of the interaction between the light field and the ion is Ω_l . Experimental implementation of carrier transitions is discussed in section 6.3.

In the Lamb-Dicke regime, terms of order η_c^2 , η_s^2 , $\eta_c\eta_s$ and higher can be neglected, and the Hamiltonian for the interaction between two ions and light becomes

$$\begin{aligned} \hat{H}_I &= \sum_{l=1}^2 \frac{\hbar\Omega_l}{2} e^{-i(\delta t - \phi_l)} |\downarrow_l\rangle \langle \uparrow_l| [|n, k\rangle \langle n, k| \\ &+ i\eta_c(\sqrt{n}|n-1, k\rangle \langle n, k| e^{i\omega_c t} + \sqrt{n+1}|n+1, k\rangle \langle n, k| e^{-i\omega_c t}) \\ &+ (-1)^l i\eta_s(\sqrt{k}|n, k-1\rangle \langle n, k| e^{i\omega_s t} + \sqrt{k+1}|n, k+1\rangle \langle n, k| e^{-i\omega_s t})] \\ &+ \text{h.c.} \end{aligned} \quad (6.7)$$

6.1.3 Sideband transitions

In this subsection I use the Hamiltonian of equation 6.7 to calculate the coherent dynamics when the ion is illuminated with radiation resonant with the red and blue sideband transitions. In order to simplify the discussion, the ions are assumed to be equally illuminated by the light. If only resonant terms are considered, the ions make transitions within the manifolds shown in figure 6.1. The resonant terms in the Hamiltonian for radiation resonant with the blue sideband of the COM mode are

$$\hat{H}_{c,\text{bsb}} = i\eta_c \sqrt{n+1} \frac{\hbar\Omega}{2} |n, k\rangle \langle n+1, k| \left[|\downarrow_1\rangle \langle \uparrow_1| e^{i\phi_1} + |\downarrow_2\rangle \langle \uparrow_2| e^{i\phi_2} \right] + \text{h.c.} \quad (6.8)$$

For an ion starting in the state $|\downarrow, n, k\rangle$, the ions stay in the manifold $(|\uparrow, n+2, k\rangle, |\uparrow, n+1, k\rangle, |\downarrow, n+1, k\rangle, |\downarrow, n, k\rangle)$. Using these states as the basis states, the Hamiltonian can be written in matrix form as

$$\hat{H}_{c,\text{bsb}} = i\eta_c \frac{\hbar\Omega}{2} \begin{pmatrix} 0 & -\sqrt{n+2}e^{i\phi_1} & -\sqrt{n+2}e^{i\phi_2} & 0 \\ \sqrt{n+2}e^{-i\phi_1} & 0 & 0 & -\sqrt{n+1}e^{i\phi_2} \\ \sqrt{n+2}e^{-i\phi_2} & 0 & 0 & -\sqrt{n+1}e^{i\phi_1} \\ 0 & \sqrt{n+1}e^{-i\phi_2} & \sqrt{n+1}e^{-i\phi_1} & 0 \end{pmatrix} \quad (6.9)$$

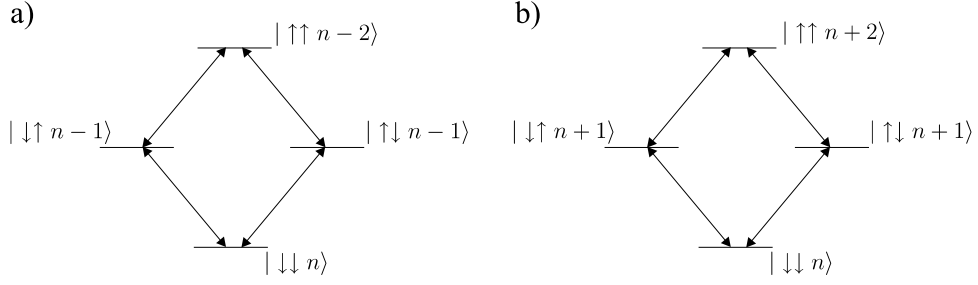


Figure 6.1: Levels involved in resonant transitions on a) the first red sideband and b) the first blue sideband for two ions initialised in the state $|\downarrow\downarrow, n\rangle$. In this figure, n can represent the vibrational quantum number for either the stretch or COM mode. In the Lamb-Dicke limit and rotating wave approximation, the state of the other mode is unchanged.

Since this Hamiltonian is time independent, the state of the system at time t can be found using the propagator $U_{c,\text{bsb}} = V e^{-iV^{-1}\hat{H}_{c,\text{bsb}}Vt/\hbar} V^{-1}$, where V is the matrix of normalised eigenvectors of $\hat{H}_{c,\text{bsb}}$. Solutions for the case of an ion starting in the $|\downarrow\downarrow, n\rangle$ state and excited on the red and blue sidebands of either mode are given in appendix B.

6.2 Cooling and Temperature diagnostics.

6.2.1 Cooling two ions.

To cool two ions we use the same methods as for a single ion, except that both modes of motion must be cooled. For the Doppler cooling stage, this has little impact because the width of the cooling transition is much larger than the spacing of the sidebands. In the red-detuned continuous Raman cooling we typically set the pump-probe difference frequency between the red sidebands of the two modes.

Pulsed Raman sideband cooling is then applied on the red sidebands for both the COM and stretch mode. The ion recoil due to the repumping pulse can heat either mode, so it is necessary to intersperse the cooling pulses for the two modes. In experiments, we typically use 5 pulses of cooling on each vibrational mode.

6.2.2 Temperature Diagnosis.

In order to deduce the mean vibrational excitation of one of the modes of motion, the method described in chapter 4 is used. The ions are optically pumped into the spin state $\downarrow\downarrow$, then the Raman laser beams are switched on for a time t_p . This is carried out for the red and blue sidebands, and the probabilities $P(\uparrow\uparrow)$, $P(\uparrow\downarrow) + P(\downarrow\uparrow)$ and $P(\downarrow\downarrow)$ of finding the ions in the spin states $\uparrow\uparrow$, $\uparrow\downarrow + \downarrow\uparrow$, or $\downarrow\downarrow$ after the pulses on each sideband are compared. The method of section 6.1.3 allows us to calculate the expected form of the wavefunction after time t_p , these are given in appendix B. The probabilities of finding both ions spin up after a pulse of length t_p are

$$P(\uparrow\uparrow, \bar{n}) = \sum_{n=0}^{\infty} P_n \frac{(n+1)(n+2)}{(2n+3)^2} \left[1 - \cos(\sqrt{2(2n+3)}\Omega t_p/2) \right]^2 \quad (6.10)$$

for a pulse on the blue sideband and

$$P(\uparrow\uparrow, \bar{n}) = \sum_{n=2}^{\infty} P_n \frac{n(n-1)}{(2n-1)^2} \left[1 - \cos(\sqrt{2(2n-1)}\Omega t_p/2) \right]^2 \quad (6.11)$$

for a pulse on the red sideband. $\Omega = \eta\Omega_R$ where η is the Lamb-Dicke parameter of the mode in question. An exact expression for the mean vibrational quantum number can be extracted from the ratio of $P(\uparrow\uparrow, \bar{n})$ for the red and blue sidebands

$$R = \frac{\sum_{n=2}^{\infty} P_n \frac{n(n-1)}{(2n-1)^2} \left[1 - \cos(\sqrt{2(2n-1)}\Omega t_p/2) \right]^2}{\sum_{n=0}^{\infty} P_n \frac{(n+1)(n+2)}{(2n+3)^2} \left[1 - \cos(\sqrt{2(2n+3)}\Omega t_p/2) \right]^2} \quad (6.12)$$

This expression can be simplified by replacing n in the numerator by $n+2$, and taking the sum from $0 \rightarrow \infty$. For a thermal state $P_n = \bar{n}^n / (\bar{n}+1)^{n+1}$ the ratio simplifies to

$$R = \left(\frac{\bar{n}^{n+2}}{(\bar{n}+1)^{n+3}} \right) \times \left(\frac{(\bar{n}+1)^{n+1}}{\bar{n}^n} \right) = \left(\frac{\bar{n}}{\bar{n}+1} \right)^2 \quad (6.13)$$

In practice, for $\bar{n} < 1$, the red-sideband signal becomes very small, hence the signal to noise ratio is also small. In order to increase the signal to noise ratio, we also use the $P(\uparrow\downarrow + \downarrow\uparrow)$ signal. The fraction of times that at least one ion is shelved gives a hybrid measurement of both $P(\uparrow\uparrow)$ and $P(\uparrow\downarrow + \downarrow\uparrow)$. With knowledge of the conditional probabilities $P(f|\uparrow)$ and $P(s|\downarrow)$ (section 2.4.3) it is possible to calculate the ratio of $(1 - P(ss))$ on each sideband for a given mean vibrational quantum number. The inverse cannot be done analytically, hence the NSolve function in Mathematica is used to solve for \bar{n} numerically.

Experimental results from a scan of the difference frequency of the Raman beams over the sidebands of both the stretch and COM modes after 4 ms of continuous sideband cooling and 5 pulse cycles of Raman sideband cooling on each mode are shown in figure 6.2. The pulsed cooling used 25 μs sideband pulses for the COM mode, and 40 μs sideband pulses for the stretch mode. Each data point corresponds to the 500 repeats of the experiment. The fraction of the times that the ions are shelved is converted into a probability $P(\uparrow\uparrow)$ using equation 2.17. The ratios R for each of the modes are $R_c = 0.08$ and $R_s = 0.09$, which correspond to mean vibrational quantum numbers of $\bar{n}_c = 0.40$ and $\bar{n}_s = 0.44$.

The two-ion cooling typically achieves mean vibrational quantum numbers of $\simeq 0.2$. This is not as cold as in the single ion experiments presented in chapter 4 in the 800kHz trap. This is due to two factors. First, the axial trap frequency required to keep the two ion crystal aligned along the trap axis is 500 kHz. This means that the sideband is closer to the carrier, hence off resonant excitation of the carrier is increased. Secondly, the repumping pulse on either mode heats the other. The gate implemented in experiments presented in chapter 9 does not require ground state cooling of the ion, but does require the ions to be in the Lamb-Dicke regime ($\eta^2(2\bar{n}+1) \ll 1$), which is comfortably satisfied for $\bar{n} \simeq 0.2$.

6.3 Carrier transitions with two ions.

If the two ions are driven on resonance with the carrier transition, the motional state of the ion does not change. The two ions evolve independently. If we assume that damping

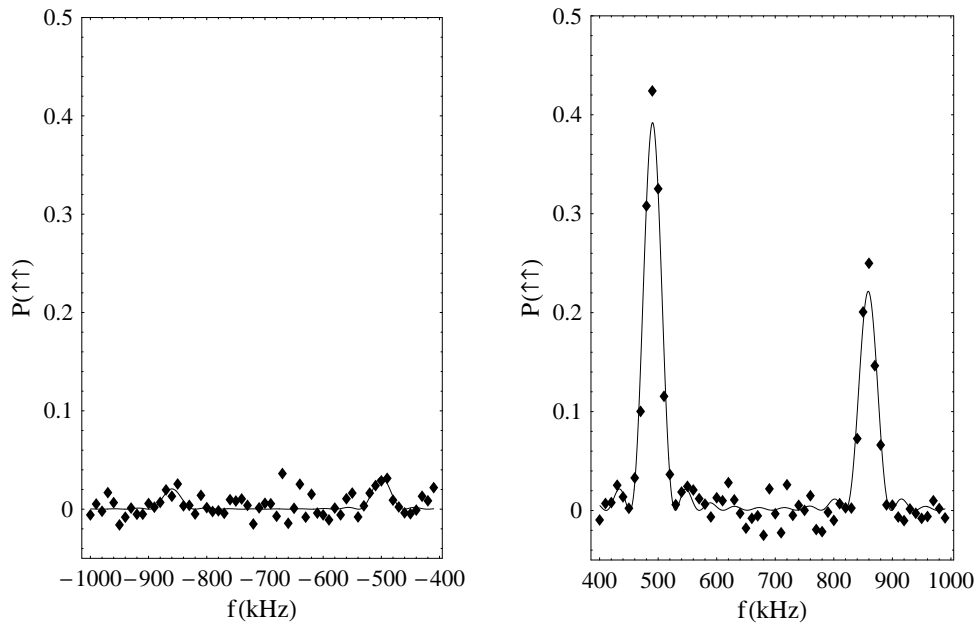


Figure 6.2: $P(\uparrow\uparrow)$ for a scan over the sidebands of the COM mode (centred at $\pm \simeq 500$ kHz) and the stretch mode (centred at $\pm \simeq 860$ kHz). For each point, $P(\uparrow\uparrow)$ was calculated using equation 2.17 from the measured fraction of times the ions were shelved out of 500 runs of the experiment. This data was obtained using 4 ms of continuous sideband cooling and 5 pulses per mode of the Raman sideband cooling. The Raman pulse length $t_p = 25 \mu\text{s}$, which is shorter than the sideband π time for either mode. The ratio of sideband heights give mean vibrational quantum numbers of $\bar{n}_c = 0.40$ and $\bar{n}_s = 0.44$ for the COM and stretch modes respectively.

takes the form of phase damping which occurs at a rate Γ , and that $\Gamma \ll \Omega$, then after preparing the state $|\downarrow\downarrow\rangle$, the probability of finding ion l in each spin state is

$$\begin{aligned} P_l(\uparrow, t) &= \frac{1}{2} \left(1 - e^{-\Gamma t/2} \left(\cos(\sqrt{4\Omega_l^2 - \Gamma^2 t/2}) \right) \right) \\ P_l(\downarrow, t) &= \frac{1}{2} \left(1 + e^{-\Gamma t/2} \left(\cos(\sqrt{4\Omega_l^2 - \Gamma^2 t/2}) \right) \right) \end{aligned} \quad (6.14)$$

As the ions are independent, the probability for finding the two ions in the states $|\uparrow\uparrow\rangle$, $|\uparrow\downarrow\rangle + |\downarrow\uparrow\rangle$ and $|\downarrow\downarrow\rangle$ are $P_1(\uparrow)P_2(\uparrow)$, $P_1(\uparrow)P_2(\downarrow) + P_1(\downarrow)P_2(\uparrow)$ and $P_1(\downarrow)P_2(\downarrow)$ respectively. The Rabi frequency Ω_l depends on the intensity of the radiation at the ion and on the motional matrix element given by

$$\begin{aligned} M_{n,k,n,k} &= \langle n | e^{i\eta_c(\hat{a}e^{i\omega_c t} + \hat{a}^\dagger e^{-i\omega_c t})} | n \rangle \langle k | e^{(-1)^l i\eta_s(\hat{b}e^{i\omega_s t} + \hat{b}^\dagger e^{-i\omega_s t})} | k \rangle \\ &= e^{-\eta_c^2/2} L_n^0(\eta_c^2) e^{-\eta_s^2/2} L_k^0(\eta_s^2) \end{aligned} \quad (6.15)$$

Experimental results for the probabilities $P(\uparrow\uparrow)$ and $P(\uparrow\downarrow + \downarrow\uparrow)$ when the difference frequency of the Raman laser beams is resonant with the carrier transition are shown in figures 6.3 and 6.4. The data is fitted with

$$P(\uparrow\uparrow) = \sum_{k=0}^{11} \sum_{n=0}^{11} P(n, k) P_1(\uparrow_{n,k}) P_2(\uparrow_{n,k}) \quad (6.16)$$

$$P(\uparrow\downarrow + \downarrow\uparrow) = \sum_{k=0}^{11} \sum_{n=0}^{11} P(n, k) [P_1(\uparrow_{n,k}) P_2(\downarrow_{n,k}) + P_1(\downarrow_{n,k}) P_2(\uparrow_{n,k})] \quad (6.17)$$

where $P_l((m_s)_{n,k})$ is given by equation 6.14 with $\Omega_l = M_{n,k,n,k} \Omega_l^{(0)}$. $\Omega_l^{(0)}$ is the bare Rabi frequency of the l th ion and $P(n, k)$ is a thermal population distribution over motional states, given by

$$P(n, k) = \frac{\bar{n}^n}{(\bar{n} + 1)^{n+1}} \frac{\bar{k}^k}{(\bar{k} + 1)^{k+1}} \quad (6.18)$$

As the ions were at mean vibrational quantum numbers of $\bar{n}, \bar{k} < 1$, the probability of finding them in states with n and k greater than 10 is very small, hence the sums in equation 6.16 were limited at $n, k = 11$ to save computing time. The fit to the data shown in figure 6.3 gives Rabi frequencies of $2\pi \times 66.6$ kHz and $2\pi \times 59.0$ kHz. This suggests that the ions are unequally illuminated by one or both of the Raman laser beams.

In order to make the tomography and gate experiments of chapters 8 and 9 easier to interpret, it is preferable to work with the ions equally illuminated. We can achieve this by tuning each of the Raman laser beams to resonance with the 397 nm transition, and observing the fluorescence from the ions on a CCD camera. In order to ensure that the CCD camera detects equal fluorescence from both ions if they are equally illuminated, the fluorescence from the ions when illuminated with 397 nm Doppler beam (which has a much larger spot size) is used as a comparison. The position of the Raman beams can be adjusted by moving optical elements in the beam path, until the detected fluorescence from each ion is the same. The data in figure 6.4 was taken after equalising the illumination of the ions. The fitted Rabi frequencies are $2\pi \times 46.8$ kHz and $2\pi \times 44.3$ kHz (the data in figures 6.3 and 6.4 were taken using different laser powers, which explains the difference in Rabi frequencies).

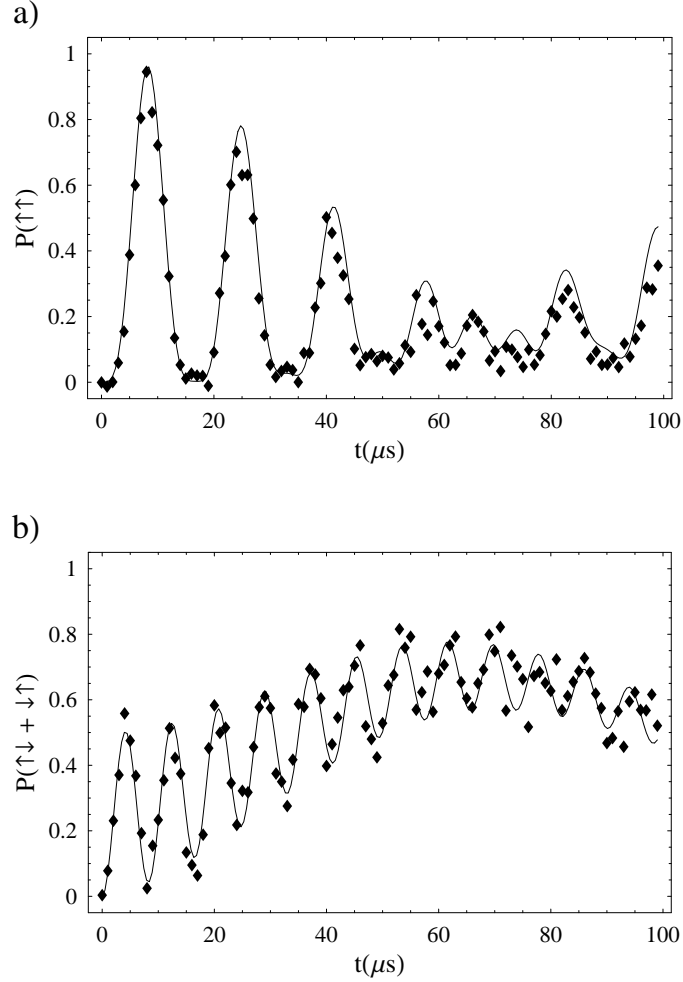


Figure 6.3: Rabi flopping on the carrier transition for two ions, with the ions unequally illuminated. Each data point is the result of 500 repeated experiments. The $P(\uparrow\uparrow)$ and $P(\uparrow\downarrow + \downarrow\uparrow)$ data was separately fitted with equation 6.16, using $\bar{n} = 0.5$ and $\bar{k} = 0.1$ obtained from sideband measurements. The average fitted values for the Rabi frequencies of the two ions are $2\pi \times 66.6$ kHz and $2\pi \times 59.0$ kHz respectively. The fitted values of Γ are 4.1 ms^{-1} from the fit to $P(\uparrow\uparrow)$ and 5.5 ms^{-1} for the fit to $P(\uparrow\downarrow + \downarrow\uparrow)$. These values are highly dependent on the value of the readout levels, which may be the origin of the discrepancy between these two values.

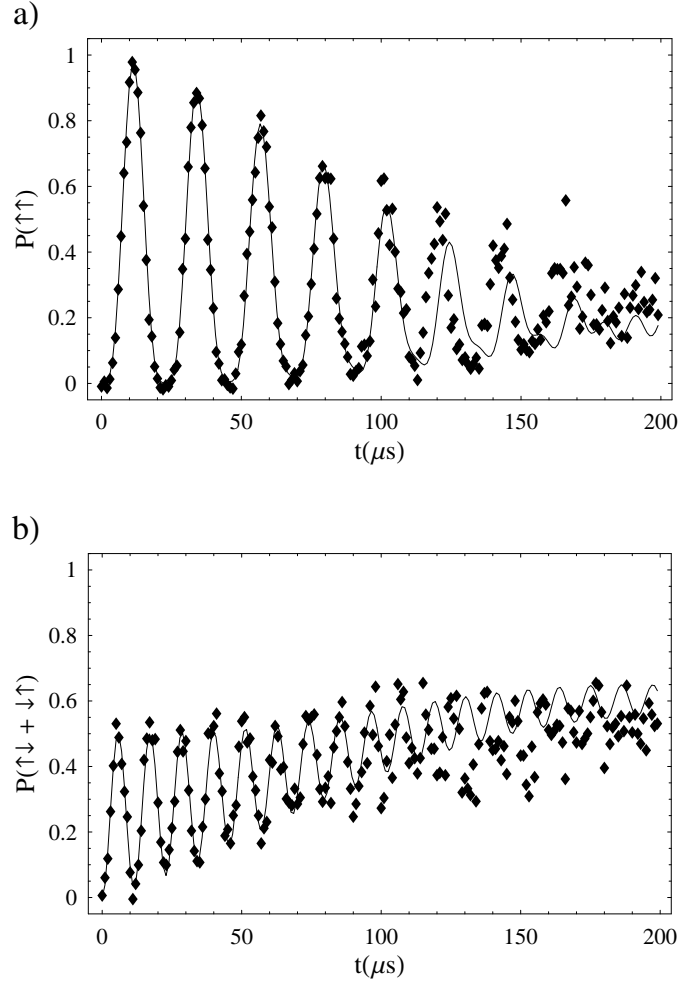


Figure 6.4: Rabi flopping on the carrier transition for two ions, after aligning the Raman beams so that both ions are equally illuminated. Each data point is the result of 500 repeated experiments. For $t = 0 \rightarrow 90 \mu\text{s}$, the $P(\uparrow\uparrow)$ and $P(\uparrow\downarrow + \downarrow\uparrow)$ data was separately fitted with equation 6.16, using $\bar{n} = 0.3$ and $\bar{k} = 0.3$ obtained from sideband measurements. The average fitted values for the Rabi frequencies of the two ions are $2\pi \times 46.8 \text{ kHz}$ and $2\pi \times 44.3 \text{ kHz}$ respectively. The fitted values of Γ are 2.7 ms^{-1} from the fit to $P(\uparrow\uparrow)$ and 4.6 ms^{-1} for the fit to $P(\uparrow\downarrow + \downarrow\uparrow)$. These values are highly dependent on the value of the readout levels, which may be the origin of the discrepancy between these two values. At $t \simeq 100 \mu\text{s}$ the frequency of the flops increases. This may be because of a change in the d.c. magnetic field such as to change the Zeeman splitting by 3 kHz (c.f. figure 2.3).

Chapter 7

Spin-Dependent Forces and Schrödinger's Cat.

This chapter describes the generation of “Schrödinger Cat” like states. In the Schrödinger’s Cat thought experiment, a cat is placed in a superposition of being dead and alive (correlated with a single radiative atom which is in a superposition of an excited and a ground state). This confounds our classical intuition. In the macroscopic world, we do not observe superposition states such as Schrödinger’s Cat. The experiments presented here explore the boundary between the classical and quantum regimes. We demonstrate superpositions of motional states of a trapped ion which are mesoscopic in the sense that the two motional states in the superposition are separated by a distance much larger than their individual wavepacket, and the energy excitation involved is much larger than the fundamental quantum of motional energy. The motional states are entangled with the spin of the ion, and span a large Hilbert space.

The states are generated by applying a force to the ion which has a direction dependent on the ion’s spin state. The force is provided by the optical dipole force in a laser standing wave described in section 3.2.3. By tuning the difference frequency ω of the two Raman beams, the force is made to oscillate close to resonance with the motional frequency ω_z of the trapped ion. In the Lamb-Dicke regime this can be considered as a spatially uniform oscillating force which drives the motion of the ion into Glauber or “coherent” states of the harmonic oscillator. In order to make larger motional states in our trap, we must drive the ion out of the Lamb-Dicke regime. In this case the dynamics becomes more complicated. We have studied this case numerically, and the experimental results were mostly found to be in agreement with the theory.

In addition to the interesting quantum states which are produced, these experiments provide much valuable information about the properties of the state-dependent force which is used. This state-dependent force is crucial to the implementation of the logic-gate between two ions which is presented in chapter 9.

The chapter begins with an introduction to coherent states and the forced harmonic oscillator. The behaviour of the ion’s motional wavepacket in the type of potential created by the standing wave is then described for an ion which is inside the Lamb-Dicke regime, and for an ion whose motional state is outside the Lamb-Dicke regime. The travelling-standing wave light field produced by our lasers is then described, and is related to the potential discussed in the previous section. In addition to the state-dependent force, components of this light field change the relative energy of the two spin states. This

is used to obtain a diagnostic of laser intensity. Finally, the experimental results are presented and analysed.

7.1 Introduction to coherent states

The coherent states of a harmonic oscillator are quantum mechanical states which oscillate in position and momentum (\hat{z} and \hat{p}) just like a classical particle, but the wavepacket has a fixed uncertainty in position and momentum [78]. In order that the expectation values of position and momentum follow the classical behaviour, the coherent states must satisfy

$$\langle \alpha | \hat{z} | \alpha \rangle = A \cos(\omega_z t), \quad \langle \alpha | \hat{p} | \alpha \rangle = -A\omega_z \sin(\omega_z t) \quad (7.1)$$

where A is a constant, ω_z is the frequency of the oscillator and $|\alpha\rangle$ represents a coherent state. Inspection of the quantum mechanical operators for position and momentum reveals that the eigenstates of the annihilation operator satisfy these equations. We will write the eigenstates of \hat{a} as $|\alpha\rangle$, with the corresponding complex eigenvalue α . The mean excitation number for such a state is given by

$$\langle \alpha | \hat{N} | \alpha \rangle = \langle \alpha | \hat{a}^\dagger \hat{a} | \alpha \rangle = |\alpha|^2 \quad (7.2)$$

and $A = 2\alpha z_0$ with $z_0 = (\hbar/2M\omega_z)^{1/2}$.

The Fock states can be generated by repeated application of the creation operator \hat{a}^\dagger on the ground state $|0\rangle$. This allows us to write the overlap between a coherent state and a Fock state as

$$\langle n | \alpha \rangle = \langle 0 | \frac{\hat{a}^n}{\sqrt{n!}} | \alpha \rangle = \langle 0 | \alpha \rangle \frac{\alpha^n}{\sqrt{n!}} \quad (7.3)$$

The normalisation condition is

$$\sum_{n=0}^{\infty} \langle \alpha | n \rangle \langle n | \alpha \rangle = 1 \quad (7.4)$$

hence we find that $\langle 0 | \alpha \rangle = \exp(-|\alpha|^2/2)$. Making use of this result, the coherent states can be written in the Fock state basis as

$$|\alpha\rangle = \sum_{n=0}^{\infty} |n\rangle \langle n | \alpha \rangle = e^{-|\alpha|^2/2} \sum_{n=0}^{\infty} \frac{\alpha^n}{\sqrt{n!}} \cdot |n\rangle \quad (7.5)$$

This is a convenient form to use when calculating the overlap of two coherent states $\langle \alpha |$ and $|\beta\rangle$, which gives the result

$$\langle \alpha | \beta \rangle = e^{-|\alpha|^2/2} e^{-|\beta|^2/2} e^{\alpha^* \beta} \quad (7.6)$$

7.2 The forced harmonic oscillator.

In the interaction picture, the Hamiltonian for a harmonic oscillator driven by a spatially uniform time-dependent force $\hbar f(t)/z_0$ is [79]

$$H_f(t) = \hbar f(t)(\hat{a}^\dagger e^{-i\omega_z t} + \hat{a} e^{i\omega_z t}) \quad (7.7)$$

The solution of the time dependent Schrödinger equation for this Hamiltonian can be most easily found by noting that the commutator of the Hamiltonian at different times is

$$[H_I(t_1), H_I(t_2)] = 2i\hbar^2 f(t_1)f(t_2) \sin(\omega_z(t_2 - t_1)) \quad . \quad (7.8)$$

This is a number, hence commutes with both \hat{a} and \hat{a}^\dagger . We can use this to write the evolution operator in time-ordered form as

$$\hat{U}(t) = e^{-\frac{i}{\hbar} \int_0^t H_I(t_1) dt_1} e^{-\frac{1}{2\hbar^2} \int_0^t dt_2 \int_0^{t_2} [H(t_2), H(t_1)] dt_1} \quad (7.9)$$

$$= D(\alpha(t)) e^{i\Phi(t)} \quad (7.10)$$

where $D(\alpha(t))$ is the displacement operator given by

$$D(\alpha(t)) = e^{\alpha(t)\hat{a}^\dagger + \alpha^*(t)\hat{a}} \quad (7.11)$$

where

$$\alpha(t) = \alpha(0) - i \int_0^t f(t_1) e^{-i\omega_z t_1} dt_1 \quad . \quad (7.12)$$

The action of the displacement operator $D(\alpha(t))$ on the annihilation operator \hat{a} is

$$D(\alpha(t))\hat{a}D^\dagger(\alpha(t)) = \hat{a} + \alpha(t) \quad . \quad (7.13)$$

This means that the effect on the coherent states (which are the eigenstates of \hat{a}) is to displace the state in phase space by $\alpha(t)$, with no change in the uncertainty of z and p . The trajectory $\alpha(t)$ is identical to the result for a classical harmonic oscillator driven by a time-dependent force which is independent of position.

The phase $\Phi(t)$ acquired by the state as it moves through phase space is given by

$$\Phi(t) = -i \int_0^t \left[f(t_1) \int_0^{t_1} f(t_2) \sin(\omega_z(t_2 - t_1)) dt_2 \right] dt_1 \quad (7.14)$$

which can be rewritten using equation 7.12 as

$$\Phi(t) = \frac{i}{2} \int_0^t \left[\frac{d\alpha}{dt_1} \alpha^* - \frac{d\alpha^*}{dt_1} \alpha \right] dt_1 \quad . \quad (7.15)$$

This form illustrates that the phase is given by the area enclosed in phase space as the wavepacket is displaced.

7.2.1 The oscillating force.

The combination of the harmonic trapping potential with the moving standing wave potential provided by our light fields (see section 7.3) results in the following motional Hamiltonian for an ion in the spin state m

$$\hat{H} = -\frac{\hat{p}^2}{2M} + \frac{1}{2}M\omega_z^2 z^2 + V(z, t) \quad (7.16)$$

where

$$V(z, t) = \hbar\Omega(\cos(\delta k z - \omega t + \phi_m)) \quad (7.17)$$

$$= \hbar\Omega [\cos(\delta k z) \cos(\omega t - \phi_m) + \sin(\delta k z) \sin(\omega t - \phi_m)] \quad . \quad (7.18)$$

In the interaction picture $z = z_0(\hat{a}e^{i\omega_z t} + \hat{a}^\dagger e^{-i\omega_z t})$. Therefore if $\omega \sim \omega_z$, then the first term in $V(z, t)$ contains no resonant parts since all powers in the expansion of $\cos(\delta k z)$ are even. It therefore only contributes an oscillating light shift, which will be discussed in section 7.3.3. The second term in $V(z, t)$ is the potential which produces the force on the ion. Expanding this term in powers of $\delta k z$, we find

$$\hbar f(t) = \hbar\Omega \sin(\delta k z) \sin(\omega t - \phi_m) = \hbar\Omega \left[\delta k z - \frac{(\delta k z)^3}{3!} + \dots \right] \sin(\omega t - \phi_m) \quad (7.19)$$

In the Lamb-Dicke regime $\delta k z \ll 1$, hence the higher order terms in this expression can be neglected. The force on the ion is therefore spatially independent.

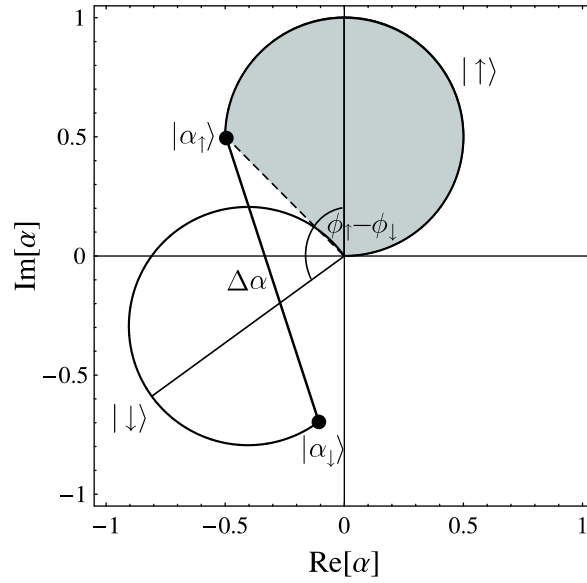


Figure 7.1: Phase space representation of the time evolution of α for both spin states driven by the oscillating state dependent force. The initial motional state is the ground state ($\alpha = 0$) and the ion is assumed to be in the Lamb-Dicke regime throughout its trajectory. The phase angle between the forces on the two states is $\phi_\uparrow - \phi_\downarrow$. The grey shaded area is the phase acquired by the state as it passes through phase space, which is given in equation 7.22. In our experiments we measure the spin state of the ion after a $\pi/2$ pulse. This does not produce a direct measurement of $|\alpha_\uparrow\rangle$ and $|\alpha_\downarrow\rangle$, but does give information about the separation of the two motional states $\Delta\alpha$.

In this case, we can make the substitution $f(t) = F_m \sin(\omega t - \phi_m)$, where $F_m = \eta\Omega$ and $\eta = \delta k z_0$ is the Lamb-Dicke parameter. The displacement of the state at time t is then found using equation 7.12 to be

$$\alpha(t) = -\frac{F_m}{\delta} e^{-i\phi_m} e^{-i\frac{\delta t}{2}} \sin\left(\frac{\delta t}{2}\right) + \frac{F_m}{(\delta + 2\omega_z)} e^{i\phi_m} e^{-i\frac{(\delta + 2\omega_z)t}{2}} \sin\left(\frac{(\delta + 2\omega_z)t}{2}\right) \quad (7.20)$$

$$\simeq -\frac{F_m}{\delta} e^{-i\phi_m} e^{-i\frac{\delta t}{2}} \sin\left(\frac{\delta t}{2}\right) \quad (7.21)$$

where $\delta = \omega - \omega_z$ and the second line is the result after making the rotating wave approximation. The trajectory of the coherent wavepacket in the interaction picture phase space

is thus a circle with diameter F_m/δ . This is shown in figure 7.1. The phase acquired by the motional state as it is pushed through phase space is found using equation 7.14 to be

$$\Phi(t) \simeq \frac{1}{4} \left(\frac{F_m}{\delta} \right)^2 (\sin(\delta t) - \delta t) \quad . \quad (7.22)$$

The motional wavepacket returns to its initial position after time $t_r = 2\pi/\delta$, when the ion has acquired a phase of

$$\Phi(t_r) = -\frac{\pi}{2} \left(\frac{F_m}{\delta} \right)^2 \quad . \quad (7.23)$$

For $\delta k z \sim 1$ and above, the higher order terms in equation 7.19 become important, and the force on the ion is no longer spatially uniform. This leads to a modification of the trajectory of the wavepacket through phase space, and squeezing. The Hamiltonian can be written in the number state basis as

$$\hat{H}_I = \sum_{n=0}^{\infty} \sum_{f=0}^{\infty} \frac{\hbar\Omega}{2} [(M_{f,n} + M_{f,n}^*) \cos(\omega t - \phi_m)] |f\rangle \langle n| \quad (7.24)$$

$$- (M_{f,n} - M_{f,n}^*) i \sin(\omega t - \phi_m) |f\rangle \langle n| \quad (7.25)$$

where the $M_{f,n}$ are the motional state matrix elements given by equation 3.7 in chapter 3 and the * indicates the complex conjugate. In the interaction picture with respect to the motional states, this Hamiltonian becomes

$$\hat{H}_I = \sum_{n=0}^{\infty} \sum_{f=0}^{\infty} \frac{\hbar\Omega}{2} [(M_{f,n} + M_{f,n}^*) \cos(\omega t - \phi_m)] |f\rangle \langle n| \quad (7.26)$$

$$- (M_{f,n} - M_{f,n}^*) i \sin(\omega t - \phi_m) e^{i(f-n)\omega_z t} |f\rangle \langle n| \quad . \quad (7.27)$$

For $\omega \sim \omega_z$, the near resonant terms are those for which $|f - n| = 1$.

In the case of the non-uniform force Schrödinger's equation cannot be solved analytically. A numerical simulation was performed by Dr. Matthew McDonnell. The simulation considered terms in the Hamiltonian with $|f - n| \leq 3$, and vibrational levels up to $n = 100$, which is a factor of ~ 4 higher than the highest n achieved in our experiments. A plot of the simulated trajectory of the centre of the wavepacket through phase space is given in figure 7.2 a), using a force which had $F_m/\delta = 5.6$, $\eta = 0.244$ and $\omega_z = 2\pi \times 537$ kHz. The trajectory is plotted up to time $t = 2\pi/\delta$, which is the time taken for the state to return to its starting position in the Lamb-Dicke case. It can be seen from the figure that the trajectory is no longer a circle. The maximum excursion of the centre of the wavepacket from the origin is reduced compared to the value obtained using the Lamb-Dicke theory, as is the time taken for the wavepacket to return to its original position. Empirical formulae for the maximum excursion α_{\max} and the return time t_r were found for $1 < F_m/\delta < 10$ to be

$$\alpha_{\max} = \frac{1}{\eta} (0.0768x^3 - 0.4554x^2 + 1.1352x - 0.0113) \quad (7.28)$$

$$t_r = \frac{2\pi}{\delta} \left(\frac{1}{1.18} \frac{\alpha_{\max}}{\alpha_0} + \frac{0.18}{1.18} \right) \quad (7.29)$$

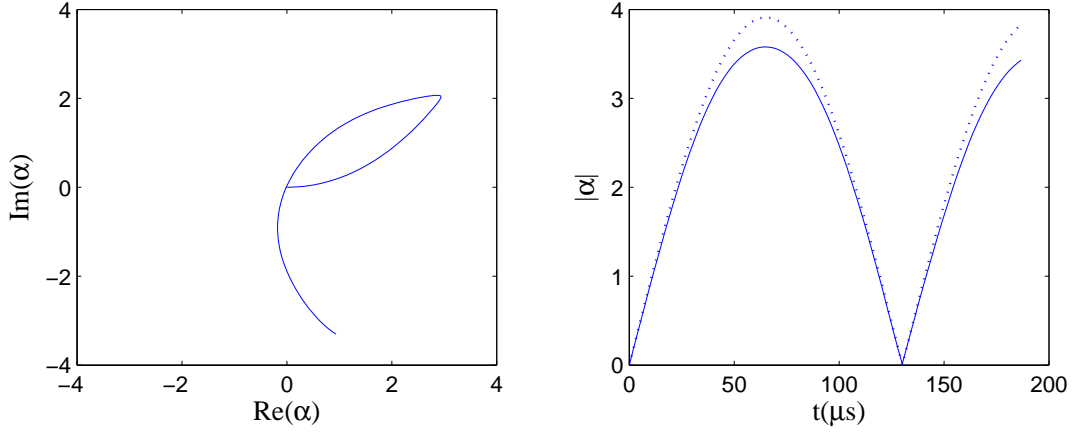


Figure 7.2: a) Phase space representation of the time evolution of the displacement of the centre of the motional state. $F_m/\delta = 5.6$ and $\eta = 0.244$. The displacement takes the ion outside the Lamb-Dicke regime, hence the force is not spatially uniform, hence the shape of the trajectory in phase space is very different from that shown in figure 7.1. The trajectory has been drawn for $\tau = 0 \rightarrow 2\pi/\delta$, which is the time taken for the state to return to its initial state in the Lamb-Dicke case. It can be seen that the time taken for the state to return to the initial state is reduced by the behaviour of the ion outside the Lamb-Dicke regime. b) The absolute value of the displacement from the origin as a function of time. The solid curve is the magnitude predicted from simulations of the system performed by numerically integrating Schrödinger's equation. The dotted line is the value of $|\alpha_{\text{eff}}|$ found from equation 7.30 using the value of δ_{eff} determined from the first minimum of the numerical simulation. It can be seen that for $|\alpha| < 2$ the two curves are similar.

where $x \equiv \eta\alpha_0$ and $\alpha_0 \equiv F_m/\delta$. The absolute value of the displacement of the wavepacket in phase space is shown in figure 7.2 b) for $\alpha_0 = 5.6$, $\delta = 2\pi \times 5.4$ kHz and $\eta = 0.244$. Also shown in 7.2 is $|\alpha_{\text{eff}}(t)|$, where

$$\alpha_{\text{eff}}(t) = \frac{\alpha_0 \delta}{\delta_{\text{eff}}} \sin\left(\frac{\delta_{\text{eff}} t}{2}\right) \quad (7.30)$$

where $2\pi/\delta_{\text{eff}}$ is the return time obtained from the numerically calculated result. It can be seen from the figure that the full calculation has roughly the form of equation 7.30 for $|\alpha_{\text{eff}}(t)|$, especially for $|\alpha| < 2$. In our experiments, we measure the interference of two wavepackets, which approximately goes as $e^{-|\alpha|^2}$. For $|\alpha| > 2$, $e^{-|\alpha|^2} < 0.02$, which is at the noise level of our data. For higher values of α_0 , the discrepancy between the numerical solution of Schrödinger's equation and $|\alpha_{\text{eff}}|$ occurs at lower displacements. We use $|\alpha_{\text{eff}}|$ to extract information from our data, but it is important to keep in mind the difference between this and the real result.

A useful representation of the motional wavepacket is the Wigner function. This is defined in terms of the density matrix ρ of the motional state as [80]

$$W(\alpha) = \frac{1}{\pi^2} \int \text{Tr}[\rho D(\lambda)] e^{\alpha\lambda^* - \alpha^*\lambda} d^2\lambda \quad (7.31)$$

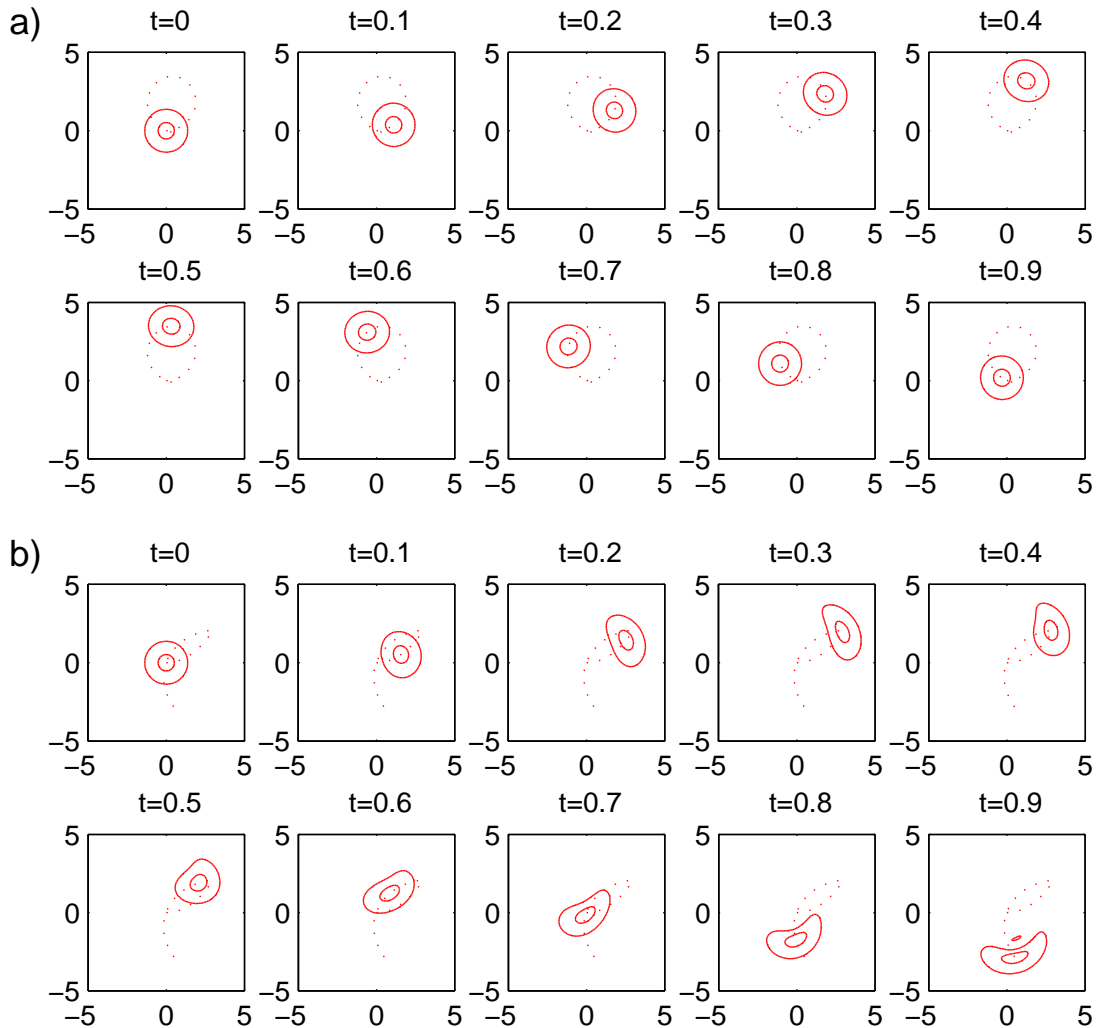


Figure 7.3: The evolution of the Wigner function of a motional state in the potential of equation 7.16. The solid curves are contours of the Wigner function, and the dotted curve indicates the trajectory of the centre of the wavepacket. a) $F_m/\delta = 3.75$, $\delta = 2\pi \times 5.4$ kHz, $\omega_z = 2\pi \times 3200$ kHz and $\eta = 0.1$. The ion starts in the ground state and stays in the Lamb-Dicke regime throughout its trajectory, hence the motional state is displaced around a circle but maintains its shape. The times are given in units of $2\pi/\delta$, which is the time taken for the motional wavepacket to return to its starting position. b) The evolution of the Wigner function for $F_m/\delta = 5.6$, $\delta = 2\pi \times 5.4$ kHz, $\omega_z = 2\pi \times 537$ kHz and $\eta = 0.244$. For these parameters the evolution in the potential of equation 7.16 takes the motional state outside the Lamb-Dicke regime. As a result, the state is squeezed, and the state returns to the origin in a reduced time.

where $D(\lambda)$ is the displacement operator. In order to derive the Wigner function from the numerical simulations, it is useful to express W in terms of the matrix elements of ρ in

the Fock state representation [80]

$$W(\alpha) = \frac{2}{\pi} e^{-2|\alpha|^2} \sum_{n \geq m} \sum_{m=0}^{\infty} (-1)^m (2 - \delta_{n,m}) \left(\frac{m!}{n!} \right)^{\frac{1}{2}} (2\alpha)^{n-m} L_m^{n-m}(4|\alpha|^2) \rho_{m,n} \quad (7.32)$$

where $\delta_{n,m}$ is a Kronecker delta function and $L_m^{n-m}(4|\alpha|^2)$ is a generalised Laguerre polynomial of order $n - m$.

The evolution of the Wigner function of the motional state with time is shown in figure 7.3 for $\alpha_0 = 3.75, \eta = 0.1$ and $\alpha_0 = 5.6, \eta = 0.244$. The value of δ in both cases was $2\pi \times 5.4$ kHz. The first set of parameters keeps the motional state in the Lamb-Dicke regime ($\max(\alpha_0\eta) = 0.375$), whereas for the second set $\max(\alpha_0\eta) = 1.4$. The figure shows that for the trajectory which takes the motional state outside the Lamb-Dicke regime the return time is reduced, and the shape of the wavepacket is squeezed throughout its trajectory. The amount of squeezing can affect our observations of the state as it returns to its original position.

7.3 Laser-ion interaction

7.3.1 Travelling-standing wave

The light field which we use to apply the state-dependent force is produced by the interference of the two Raman laser beams. The beams and their polarisations are described in chapter 2. The beam at 3° to the magnetic field is horizontally polarised, hence to a good degree of approximation it can be considered to have no π component. It has equal circular components σ^+, σ^- , with no phase difference between them.

The laser beam at 63° to the magnetic field is approximately linear in polarisation, with the angle between the polarisation vector and the vertical set using a waveplate. If this angle is non-zero, this beam contains a π component as well as equal amounts of both circular polarisation components. The phase difference between the two circular polarisations depends on the angle of the polarisation vector.

Four combinations of polarisations from the two beams give rise to transitions in our ion. The π light from the 63° beam combined with either circular polarisation from the 3° beam drives transitions between the spin states of the ion. Throughout this chapter, the Rabi frequency characterising the interaction of the ion with these $\pi - \sigma^+$ or $\pi - \sigma^-$ components is Ω_π .

Transitions between different motional states for spin \uparrow are driven by the σ^- polarisation components from both beams, whereas transitions between different motional states for spin \downarrow are driven by the two σ^+ polarisation components. The Rabi frequencies for these transitions are given by $M_{f,n}\Omega_\uparrow$ and $M_{f,n}\Omega_\downarrow$ for the \uparrow and \downarrow spin states respectively, where $M_{f,n}$ is the motional matrix element given in equation 3.7 and f, n are the vibrational quantum numbers of the two motional states between which the transition is being driven.

If the difference frequency of the two laser beams $\omega = 0$, the resulting interference pattern is a standing wave. The relative intensities and phases of the components of the standing wave are given by the relative intensities and phases of the three polarisation components of the 63° beam. In general, $\omega \neq 0$, which results in a travelling standing wave, which moves over the ion with phase velocity $\omega/\delta k \sim 0.2 \text{ ms}^{-1}$ for $\omega \sim 2\pi \times 500$ kHz. For comparison, the maximum velocity of an ion in the coherent state with $\alpha = 1$ in a 500 kHz trap is 0.05 ms^{-1} .

7.3.2 State-dependent force

The $\sigma^- - \sigma^+$ travelling standing wave interacts with an ion in spin state \downarrow and creates the potential

$$V(z, t) = \hbar\Omega_{\downarrow} \cos(\delta k z - \omega t + \phi_{\downarrow}) \quad (7.33)$$

where ϕ_{\downarrow} is the phase of the standing wave at the ion. The $\sigma^- - \sigma^-$ travelling standing wave will interact with an ion in the spin state \uparrow and produce the same potential, but with the replacements $\phi_{\downarrow} \rightarrow \phi_{\uparrow}$ and $\Omega_{\downarrow} \rightarrow \Omega_{\uparrow}$. The intensities of the two components of the light field are set close to equal in such a way that $\Omega_{\uparrow} = \Omega_{\downarrow}$ (see section 7.3.3) and therefore the major difference is the phase of the force on the ion. This ion thus sits in a potential which is of the same form as that described in section 7.2.1, with the relevant values of Ω and ϕ dependent on the spin state. The motion of an ion in either spin state will thus behave as a driven harmonic oscillator.

7.3.3 Light shifts

The Hamiltonian for the ion in the travelling standing wave light field includes terms which change the energy separation of the two qubit states. This results in a differential phase shift of one state relative to the other. In the Schrödinger's cat experiments presented later in this chapter, the ion is in a superposition of spin states throughout the time when the light field is on, hence the change in the relative phase will lead to modification in the populations when the states are recombined.

We will consider three types of light shift. The first is caused by the interaction of the ion with a single Raman beam. This can be cancelled experimentally, which leads to a small imbalance between the intensities of the σ^+ and σ^- components of the light field. The second light shift is due to the off resonant terms in the oscillating potential $V(z, t)$. This will be dominated by the zero order term in $\delta k z$. This produces an oscillating light shift which we find produces a small effect. The third light shift we will consider is due to off resonant driving of carrier transitions by the π component from the 63° beam and the circular polarisation components of the 3° beam.

Single beam light shifts. Each Raman laser beam is far detuned from resonance with the $S_{1/2} \rightarrow P_{1/2}$ transition, hence as shown in chapter 3 and appendix A, the upper level can be “adiabatically eliminated”. This results in the Hamiltonian of equation 3.5 in which the first two terms are the single beam light shifts. These are given by

$$\frac{|g_{13}|^2}{4\Delta} \text{ and } \frac{|g_{32}|^2}{4\Delta} \quad (7.34)$$

where $|g_{13}|$ ($|g_{32}|$) is the strength of the coupling between levels 1 ($|\downarrow\rangle$) and 3 (2 ($|\downarrow\rangle$) and 3) and $|\Delta|$ is the detuning of the Raman laser field from resonance with the $S_{1/2} \rightarrow P_{1/2}$ transition.

In order to simplify the analysis of the Schrödinger's cat experiments, we require the single beam light shifts to be equal for the two qubit states. In order to ensure that this is the case, we use the ion to detect any rotation of the spin state caused by each Raman beam acting on its own. This is done by introducing one of the Raman beams in a pulse in the first gap of a spin-echo sequence ($\pi/2, \pi, \pi/2$). The experiment is repeated 500 times, and the probability of finding the spin up at the end of the sequence is obtained. This is repeated as the duration of the pulse is scanned between 0 and 200 μs . If a significant

change in the population is observed, a half wave plate in the beam path is adjusted, and the scan is repeated. This is repeated until the population change is minimised. To speed up the optimisation of the waveplate angle, we commonly insert a fixed length pulse, and change the waveplate while observing the effect on the populations. When the minimisation has been achieved, a scanned pulse is then used to check that the phase produced by the fixed duration pulse was zero and not an integer multiple of 2π .

The change in population due to a single Raman beam is never zero owing to photon scattering mixing up the spin state. A check of the contribution due to photon scattering can be obtained by turning on the single laser beam in both halves of the spin echo. The phases acquired in both halves of the spin-echo should then cancel out, leaving a residual population change due to photon scattering.

In practice, equation 7.34 is not quite accurate due to the Zeeman splitting of the ground and excited states. Taking this Zeeman splitting into account, then for the 3° beam the ratio of the Rabi frequencies of the two circular polarisation components after cancellation of the light shifts is

$$\frac{\Omega_3^{\sigma^-}}{\Omega_3^{\sigma^+}} = \left(1 + \frac{8\omega_0}{3\Delta}\right)^{\frac{1}{2}} \quad (7.35)$$

where ω_0 is the frequency splitting of the two qubit states. The ratio ω_0/Δ is 1.6×10^{-4} , thus the light field will be linear to a good degree of approximation.

For the 63° beam, the situation is complicated by the presence of the π polarisation component. The differential light shift due to off-resonant driving of the single photon transitions is of order ω_0/Δ , hence can be cancelled by a small imbalance in the intensities of the two circular polarisation components. In addition, the π polarisation combines with the two circular polarisation components of the same beam to drive the spin-flip transition in the ground state. Since the two light fields are co-propagating, this will lead to a motion-independent light shift which increases the frequency separation of the qubit levels by

$$\frac{(\Omega_{63}^{\sigma^+} \Omega_{63}^{\pi})^2 + (\Omega_{63}^{\sigma^-} \Omega_{63}^{\pi})^2}{8\Delta^2\omega_0} \quad (7.36)$$

where Ω_{63}^{π} , $\Omega_{63}^{\sigma^+}$ and $\Omega_{63}^{\sigma^-}$ are the Rabi frequencies for the π , σ^+ and σ^- light respectively. The imbalance in the Rabi frequency of the two circular polarisation components required to cancel out this light shift is therefore given by

$$\frac{\Omega_{63}^{\sigma^-}}{\Omega_{63}^{\sigma^+}} = \left(\frac{1+r}{1-r}\right)^{\frac{1}{2}} \quad (7.37)$$

where $r = \Omega_{63}^{\pi 2}/2\omega_0\Delta$. In our experiments, $\Omega_{63}^{\pi} \sim 2\pi \times 100$ MHz, $\omega_0 \sim 2\pi \times 4.7$ MHz and $\Delta \sim 2\pi \times 30$ GHz, hence $\Omega_{63}^{\sigma^-}/\Omega_{63}^{\sigma^+} \sim 1.02$. The implication for the Schrödinger's cat experiments is that the force on the ion in the spin state $|\uparrow\rangle$ is larger by 2% than that on the spin state $|\downarrow\rangle$.

In the rest of the chapter, it will be assumed for simplicity that both Raman beams are linearly polarised, hence the forces on the two spin components will be assumed to be equal.

Off resonant terms in $V(z, t)$. The second light shift which we consider is that due to the off resonant terms in the potential $V(z, t)$, equation 7.18. The dominant contribution

is that of the $\cos(\delta k z)$ term, hence for small $\delta k z$ is independent of the position of the ion in the standing wave. The oscillating light shift causes the energy gap between the states to oscillate at the frequency ω . The shift in the energy gap between the states at time t is

$$\hbar\Delta_f = \hbar\Omega_R^\uparrow \cos(\omega t - \phi_\uparrow) - \hbar\Omega_R^\downarrow \cos(\omega t - \phi_\downarrow) \quad (7.38)$$

$$= 2\hbar\Omega_R \sin((\phi_\uparrow - \phi_\downarrow)/2) \sin(\omega t - (\phi_\uparrow + \phi_\downarrow)/2) \quad (7.39)$$

where $\Omega_R^\uparrow = \Omega_R^\downarrow = \Omega_R$. The relative phase of the two spin states is the integral with respect to time of this shift. The phase acquired will thus be zero if ωt is an integer multiple of 2π . If this is not the case, then this light shift may cause a problem because the value is likely to change from shot to shot, e.g. if the standing wave is displaced by movement of a mirror in one of the beam paths.

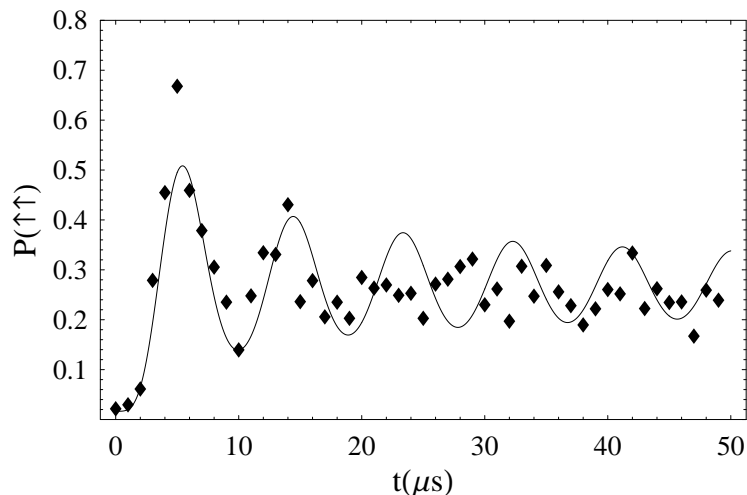


Figure 7.4: The probability of finding both spins up after inserting a Raman pulse of duration t_p in the first gap of a spin-echo sequence with the difference frequency of the Raman beams set to zero. Each experimental point is the result of 500 repeats of the experimental sequence. The fraction of times that both ions fluoresced at the end of the sequence was converted into a probability of finding the spins up using equation 2.17. The solid curve is fit to the data using equation 7.43. The mean phase of the σ^\pm standing waves was assumed to be completely random from shot to shot of the experiment. The floated parameters were the baseline and the Rabi frequency Ω_R . The fitted value of Ω_R was $2\pi \times 79$ kHz, which was lower than the value predicted from a carrier flopping experiment performed on the same day. The experiment and the theory show similar features, which indicates that this phase is not constant from shot to shot of the experiment, but the form of the decrease in amplitude of the oscillations in $P(\uparrow\uparrow)$ is different. The discrepancy in the fitted value of Ω_R and the form of the data suggests that when the experiment was performed, the mean phase of the two components of the light field was distributed around a mean value of $\arccos(79/112) \simeq \pi/4$ radians.

The effect of this light shift was tested experimentally in a two-ion experiment. A Raman pulse with $\omega = 0$ and duration t_p was inserted in the first gap of a spin-echo sequence. The sequence was repeated 500 times, and the probability of finding both spins up was obtained. Experiments were performed with the duration of the pulse set to 50

equally spaced values of t_p from $0 \rightarrow 49 \mu\text{s}$. The data is shown in figure 7.4. Assuming that the phase of the standing wave is constant over a single shot of the experiment, the relative phase between the two spin states is

$$\phi_f = \int_0^{t_p} \Delta_f dt = \int_0^{t_p} 2\Omega_R \sin(\Delta\phi/2) \sin(-\bar{\phi}) dt = -2\Omega_R \sin(\Delta\phi/2) \sin(\bar{\phi}) t_p \quad (7.40)$$

where $\bar{\phi} = (\phi_{\uparrow} + \phi_{\downarrow})/2$. The state of each ion just prior to the final $\pi/2$ pulse in the spin-echo sequence will therefore be

$$|\psi_f\rangle = \frac{1}{\sqrt{2}} \left[|\downarrow\rangle + e^{i\phi_f} |\uparrow\rangle \right] \quad (7.41)$$

In order to model the behaviour of the experiment, we assume that the mean phase $\bar{\phi}$ is completely random from shot to shot of the experiment. In this case the coherence element of the density matrix for each ion will be given by an ensemble average over a uniform distribution of $\bar{\phi}$,

$$C = \frac{1}{2\pi} \int_0^{2\pi} e^{i\phi_f} d\bar{\phi} \quad (7.42)$$

The probability of finding both ions spin up after the spin-echo sequence is

$$P(\uparrow\uparrow) = \frac{1}{4} [1 - C \cos(2\Omega_R \cos(\Delta\phi/2))]^2 \quad (7.43)$$

This form was fitted to the data in figure 7.4, with the value of Ω_R allowed to float and the value of $\Delta\phi$ fixed at the value measured using the Schrödinger's cat experiments presented later in the chapter. The fitted value of Ω_R was $2\pi \times 79$ kHz. The value of Ω_R calculated from the Rabi flopping rate on the carrier transition on the same day was $2\pi \times 112$ kHz. Though the simple model shows the same basic features as the experimental data, the modelled rate at which the amplitude of oscillations of $P(\uparrow\uparrow)$ decreases has a different form to the experimental data. This is probably due to the assumption of random phase. The discrepancy in the fitted value of Ω_R and in the form of the data suggest that when the experiment was performed, the mean phase of the two components of the light field was distributed around a mean value of $\arccos(79/112) \simeq \pi/4$ radians.

When the difference frequency ω of the Raman lasers is non zero, the phase difference introduced by Δ_f (equation 7.38) is

$$\frac{2\Omega_R}{\omega} \sin(\Delta\phi/2) (\cos(\omega t - \bar{\phi}) - \cos(\bar{\phi})) \quad (7.44)$$

The maximum value of this phase difference is $\frac{2\Omega_R}{\omega} \sin(\Delta\phi/2)$. In our experiments typical values are $\Omega_R = 2\pi \times 125$ kHz, $\omega \simeq 2\pi \times 535$ kHz and $\Delta\phi = \pi/2$ radians. Thus the maximum value of the phase shift introduced is 0.32 radians. If the mean phase of the two laser beams has a random value between $-\pi$ and π from shot to shot of the experiment, the fractional reduction in the contrast of the fringes (observed when $\omega t = \pi/2$) is 0.985. This is of a similar size to the noise in an experiment which is repeated 500 times. Tests were carried out at $\omega \sim \omega_z$ with the light field pulsed on for a series of pulse durations between 0 and 5 μs spaced by 0.2 μs . No evidence was found of oscillations in the population observed at the end of the sequence. We conclude that although this light shift will be

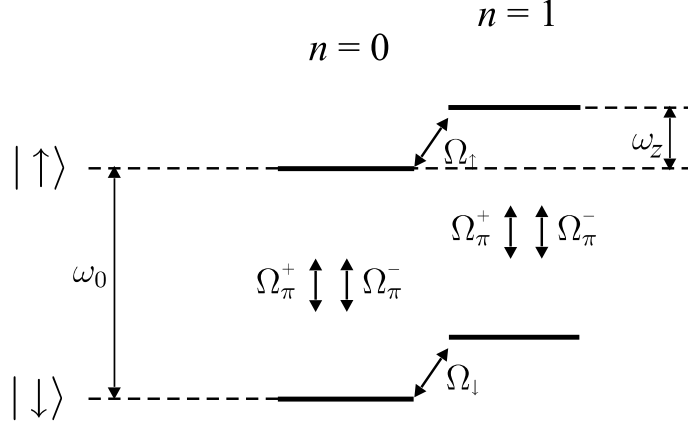


Figure 7.5: A schematic of the transitions driven by the combination of laser fields present when the light field is being used to drive the spin-dependent force. The difference frequency of the two Raman beams ω is close to the trap frequency ω_z . The frequency splitting of the two qubit states is ω_0 . The σ^+ (σ^-) components from each Raman beam couple motional states with spin \downarrow (\uparrow) with strength $M_{f,n}\Omega_{\downarrow}$ ($M_{f,n}\Omega_{\uparrow}$), where $M_{f,n}$ are the motional matrix elements given in equation 3.7. This gives rise to the state-dependent force. The π components of the beam at 63° to the magnetic field combine with the circular polarisation components of the beam at 3° to the magnetic field to off-resonantly drive spin-flip transitions. The Rabi frequencies for the driven transitions are Ω_{π}^+ Ω_{π}^- for the two circular components. The largest matrix element for these transitions is on the carrier transition, for which the components of the light field are off resonant by $\omega_0 + \omega$ and $\omega_0 - \omega$, which are both much larger than Ω_{π} . The main effect of these light fields is therefore a light shift which pushes the spin states apart in energy.

important in very precise experiments at small η , it is small enough in our Schrödinger's cat experiments to be negligible.

Off resonant driving of the carrier transition. The third light shift is due to the π polarisation component of the Raman laser beam at 63° to the magnetic field combined with the σ^+ and σ^- light from the beam at 3° to the magnetic field. The interaction arising from these components drives spin-flip transitions. Since the laser difference frequency is detuned far from resonance with the spin flip transition, the probability that the spin will flip is negligible, but the interaction does give rise to a light shift which pushes the energy of the qubit states apart. The light shift is greatest for the carrier transition, for which the Raman processes are detuned by $\omega_0 + \omega$ and $\omega_0 - \omega$.

For the carrier transition, the Hamiltonian describing the interaction of these polarisation components with the ion is found from equation 3.5 in chapter 3 to be

$$H_I = H_{\pi,\sigma^+} + H_{\pi,\sigma^-} \quad (7.45)$$

$$= -\hbar\Omega_{\pi} \cos(\delta kz - \omega t - \phi) [e^{i\omega_0 t} |\downarrow\rangle \langle\uparrow| + e^{-i\omega_0 t} |\uparrow\rangle \langle\downarrow|] \quad (7.46)$$

where Ω_{π} is the effective Rabi frequency which characterises the coupling between the two spin states and ϕ is the difference between the phases of the light in the two laser beams. For $\omega_0 \sim \omega$, the rotating wave approximation is not applicable.

In the limit that $\omega_0 + \omega, \omega_0 - \omega \gg |M_{m,n}|\Omega_{\pi}$, the light shift pushes the states $|\downarrow, n\rangle$

and $|\uparrow, m\rangle$ apart in energy by $\hbar\Delta_\pi$ where

$$\Delta_\pi(n, m) = \frac{|M_{m,n}|^2 \Omega_\pi^2}{2} \left[\frac{1}{\omega_0 + (m-n)\omega_z + \omega} + \frac{1}{\omega_0 + (m-n)\omega_z - \omega} \right] \quad (7.47)$$

Since $|M_{m,n}| \sim \eta^{|m-n|}$ and $\eta \sim 0.25$, the dominant effect in the shift of each level will be due to the carrier transition, and the qubit states of the vibrational level n are pushed apart by

$$\Delta_\pi(n) = \frac{|M_{n,n}|^2 \Omega_\pi^2}{2} \left[\frac{1}{\omega_0 + \omega} + \frac{1}{\omega_0 - \omega} \right] \quad (7.48)$$

In the experiments presented in this chapter, typical values are $\omega_0 \simeq 2\pi \times 4.7$ MHz, $\omega = \delta + \omega_z \simeq 2\pi \times 540$ kHz and $\Omega_c \simeq 2\pi \times 130$ kHz. Thus for an ion in the ground state, $\Delta_\pi \sim 2\pi \times 4$ kHz. For an ion in a higher vibrational state, the matrix element is smaller, and the light shift is reduced. In analysing the experimental results we extract Ω_π using

$$\Delta_\pi = \frac{\Omega_\pi^2}{2} \left[\frac{1}{\omega_0 + \omega} + \frac{1}{\omega_0 - \omega} \right] \quad (7.49)$$

Due to the weak dependence of $M_{n,n}$ on n , the difference between Ω_π obtained from this expression and equation 7.48 is $< 10\%$ in our experiments.

7.4 Creation of ‘‘Schrödinger’s Cat’’ states

A Schrödinger’s cat state is a superposition of two states far apart in Hilbert space. The state dependent force discussed above allows us to create large superpositions of motional states by entangling the spin state of the ion with the motional state. In our experiment

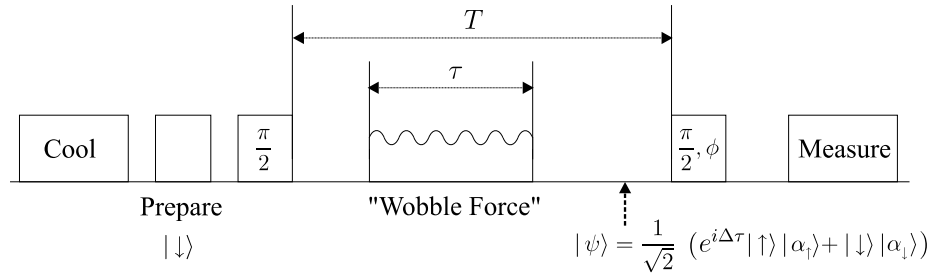


Figure 7.6: The pulse sequence used for the ‘‘Schrödinger Cat’’ experiments. The state-dependent force is sandwiched between two carrier $\pi/2$ pulses. The spin state after the second $\pi/2$ pulse is given in equation 7.52.

we create such states using the first four pulses of the sequence shown in figure 7.6. The ion is first cooled to the ground state, and optically pumped into the state $|\downarrow\rangle$. The first $\pi/2$ pulse puts the ion into an equal superposition of the two spin states. The state dependent force is then applied for time τ , which results in the creation of the state

$$|\psi\rangle = \frac{1}{\sqrt{2}} e^{i\Phi(\tau)} [e^{i\Delta_\pi\tau} |\uparrow\rangle |\alpha_1\rangle + |\downarrow\rangle |\alpha_1\rangle] \quad (7.50)$$

where $|\alpha_{\downarrow}\rangle$ ($|\alpha_{\uparrow}\rangle$) is the state of motion of population in the spin state $|\downarrow\rangle$ ($|\uparrow\rangle$), $\Phi(\tau)$ is the phase acquired by the displacement of the motional states in phase space, and Δ_{π} is the light shift due to off resonant excitation of the carrier transition described in section 7.3.3.

To diagnose the state of the ion after the force has been applied, we apply a second $\pi/2$ pulse and subsequently measure the spin state of the ion. The second $\pi/2$ pulse applies the rotation

$$R(\pi/2) = \frac{1}{\sqrt{2}} \begin{pmatrix} 1 & -e^{i\phi} \\ e^{-i\phi} & 1 \end{pmatrix} \quad (7.51)$$

where ϕ is the phase of this pulse relative to the initial $\pi/2$ pulse. The state of the ion after this pulse is then

$$|\psi_f\rangle = \frac{1}{2} e^{i\Phi(\tau)} \left[(e^{i\Delta_{\pi}\tau} |\alpha_{\uparrow}\rangle - e^{i\phi} |\alpha_{\downarrow}\rangle) |\uparrow\rangle + (e^{-i\phi} e^{i\Delta_{\pi}\tau} |\alpha_{\uparrow}\rangle + |\alpha_{\downarrow}\rangle) |\downarrow\rangle \right] \quad (7.52)$$

hence the probability of measuring spin up is

$$P(\uparrow) = \frac{1}{4} \sum_{n=0}^{\infty} \langle \phi_f | (|\uparrow\rangle |n\rangle \langle n| \langle \uparrow|) | \phi_f \rangle \quad (7.53)$$

$$= \frac{1}{4} \left(e^{-i\Delta_{\pi}\tau} \langle \alpha_{\uparrow} | - e^{-i\phi} \langle \alpha_{\downarrow} | \right) \left(e^{i\Delta_{\pi}\tau} |\alpha_{\uparrow}\rangle - e^{i\phi} |\alpha_{\downarrow}\rangle \right) \quad (7.54)$$

$$= \frac{1}{2} \left(1 - \text{Re} \left[\langle \alpha_{\uparrow} | \alpha_{\downarrow} \rangle e^{i(\phi - \Delta_{\pi}\tau)} \right] \right) \quad (7.55)$$

The overlap $\langle \alpha_{\uparrow} | \alpha_{\downarrow} \rangle$ can thus be determined experimentally by observing $P(\uparrow)$ as a function of ϕ and τ . The amplitude of the observed fringes gives $|\langle \alpha_{\uparrow} | \alpha_{\downarrow} \rangle|$, while a contribution to the phase of the observed fringes will be $\text{Arg}(\langle \alpha_{\uparrow} | \alpha_{\downarrow} \rangle)$. For motional states within the Lamb-Dicke regime, the overlap $\langle \alpha_{\uparrow} | \alpha_{\downarrow} \rangle$ can be found using equation 7.6 to be

$$\langle \alpha_{\uparrow} | \alpha_{\downarrow} \rangle = e^{-|\alpha(\tau)|^2(1-\cos(\Delta\phi))} e^{i|\alpha(\tau)|^2 \sin(\Delta\phi)} \quad (7.56)$$

where $|\alpha(\tau)|$ is the size of the coherent state produced by the force and $\Delta\phi = \phi_{\downarrow} - \phi_{\uparrow}$ is the relative phase of the two circular polarisation components in the standing wave. Hence

$$|\langle \alpha_{\uparrow} | \alpha_{\downarrow} \rangle| = e^{-|\alpha(\tau)|^2(1-\cos(\Delta\phi))} \quad (7.57)$$

$$\text{Arg}(\langle \alpha_{\uparrow} | \alpha_{\downarrow} \rangle) = |\alpha(\tau)|^2 \sin(\Delta\phi) \quad (7.58)$$

Outside the Lamb-Dicke regime, the motional states are not coherent states, and therefore these formulae are not appropriate. However the states are close to coherent ones and by making the substitution $\alpha \simeq \alpha_{\text{eff}}(\tau)$ from equation 7.30 they allow us to obtain useful information from our experimental data.

7.4.1 Effect of initial temperature on the observed signal.

In practice, the ion does not start in the ground state, but an incoherent mixture of states. If the mixture has a thermal distribution with mean vibrational quantum number \bar{n} , the ion starts in the Fock state $|n\rangle$ with probability $P_n = \bar{n}^n / (\bar{n} + 1)^{n+1}$.

The displacement operator $D(\alpha)$ applied to the Fock state $|n\rangle$ creates a displaced Fock state $|\alpha, n\rangle$ [81]. The overlap of two displaced Fock states $|\alpha_{\uparrow}, m\rangle$ and $|\alpha_{\downarrow}, n\rangle$ is

$$\langle \alpha_{\uparrow}, m | \alpha_{\downarrow}, n \rangle = \langle \alpha_{\uparrow} | \alpha_{\downarrow} \rangle \sqrt{\frac{m!}{n!}} (\alpha_{\uparrow}^* - \alpha_{\downarrow}^*)^{n-m} L_m^{n-m}((\alpha_{\uparrow} - \alpha_{\downarrow})(\alpha_{\uparrow}^* - \alpha_{\downarrow}^*)) \quad (7.59)$$

for $n \geq m$.

Consider an ion starting in the Fock state n . The state dependent force will displace the motional states for each spin state in different directions, creating two displaced Fock states. We will call these two motional states $|\alpha_{\uparrow}, n\rangle$ and $|\alpha_{\downarrow}, n\rangle$. The overlap of these two motional states is

$$\langle \alpha_{\uparrow}, n | \alpha_{\downarrow}, n \rangle = \langle \alpha_{\uparrow} | \alpha_{\downarrow} \rangle L_n^0((\alpha_{\uparrow} - \alpha_{\downarrow})(\alpha_{\uparrow}^* - \alpha_{\downarrow}^*)) \quad (7.60)$$

In the experiment, we observe the overlap of the two states over many repeated preparations. For a thermal distribution, the starting state of the ion is $|n\rangle$ with probability $P_n = \bar{n}^n / (\bar{n} + 1)^{n+1}$. The ensemble average of the motional state overlap is thus

$$\frac{\langle \alpha_{\uparrow} | \alpha_{\downarrow} \rangle}{\bar{n} + 1} \sum_{n=0}^{\infty} \frac{\bar{n}^n}{(\bar{n} + 1)^n} L_n^0((\alpha_{\uparrow} - \alpha_{\downarrow})(\alpha_{\uparrow}^* - \alpha_{\downarrow}^*)) \quad (7.61)$$

We can now make use of the identity $\sum_n \epsilon^n L_n^0(x) = (1 - \epsilon)^{-1} \exp[-\epsilon x / (1 - \epsilon)]$ [51] to write this expression as

$$\langle \alpha_{\uparrow} | \alpha_{\downarrow} \rangle e^{-\bar{n}(\alpha_{\uparrow} - \alpha_{\downarrow})(\alpha_{\uparrow}^* - \alpha_{\downarrow}^*)} \quad (7.62)$$

For the state dependent force described in section 7.3, we have $\alpha_{\uparrow} = \alpha_{\downarrow} e^{i\Delta\phi}$. The overlap then simplifies to

$$\langle \alpha_{\uparrow} | \alpha_{\downarrow} \rangle e^{-2\bar{n}|\alpha(\tau)|^2(1 - \cos(\Delta\phi))} \quad (7.63)$$

Note that this changes only the absolute value of the visibility of the fringes, it has no effect on the argument.

Using this result, we find using equation 7.57 that the amplitude of the observed fringes will be

$$A = e^{-(2\bar{n}+1)|\alpha(\tau)|^2(1 - \cos(\Delta\phi))} \quad (7.64)$$

7.5 Experimental results

Experiments were performed in both the 800 kHz and 500 kHz trap, using a range of detunings of the difference frequency of the Raman laser beams from the trap frequency. At each detuning, $P(\uparrow)$ was measured as a function of the phase of the second $\pi/2$ pulse ϕ for a range of τ . Figure 7.7 gives some examples of the data. The results from each scan of phase were fitted with a sine wave with floated baseline, amplitude, frequency and phase.

The amplitude and phase of the observed fringes gives us information about the *trajectory* of the two wavepackets through phase space. This allows us to obtain the magnitude and relative phase of the force on each spin state. The light shift contribution to the phase of the fringes and the rate of carrier Rabi flopping give a measure of the *intensity* of the light field. This can also be used to obtain the magnitude of the force on the ion. We use the two independently obtained values of the force parameter F_m to compare the measurements of the trajectory and intensity.

Experimental data was taken on several occasions. On each occasion, the temperature of the ion was measured, and preparatory experiments were used to determine parameters

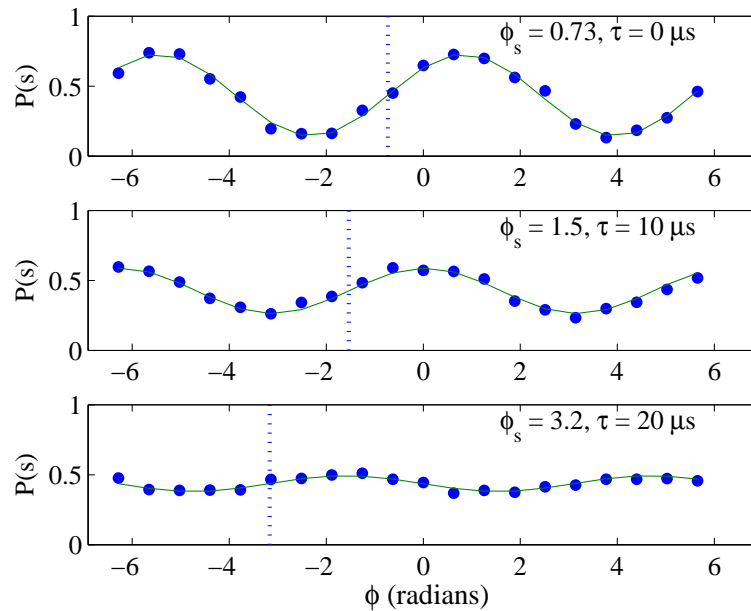


Figure 7.7: The variation in $P(s)$ with the phase of the second $\pi/2$ pulse in the Ramsey or spin-echo sequence. $P(s)$ is the fraction of times that the ion was shelved for 500 repeats of the experimental sequence. The data is fitted with a sine curve. As the duration τ of the spin-dependent force is increased, the phase and amplitude of the fringes changes, which allows us to determine the size of the coherent states produced and the angle between the state-dependent forces on each spin state. Since the function fitted to the raw data is periodic, the phase offset obtained from the fit and the phase introduced by the spin-dependent force may differ by integer numbers of 2π . In order to find the phase introduced, the starting value of the phase offset used for the fit was $\phi_{\text{off}}(0) + 2\pi\Delta_{\text{guess}}\tau$. The value of Δ_{guess} and the phase offset at $\tau = 0$ were chosen so that the fitted phase offsets varied smoothly for adjacent values of τ . The data shown here correspond to data points in figures 7.9 and 7.10

required to set up the Schrödinger's cat experiment. The first set of Schrödinger's cat experiments were performed in September 2004. A Ramsey pulse sequence was used. The range of parameters used in these experiments is shown in the upper half of table 7.1.

The experiment was performed with the axial vibrational frequency of the ion at close to 800 kHz and to 500 kHz. The trap frequency was measured to ± 0.5 kHz using an oscillating tickle voltage applied to one of the trap electrodes (as described in section 2.1.2 of chapter 2). ω was set by the difference frequency of the synthesizers used to drive the AOMs in the Raman beam paths. This frequency is thus known to an accuracy of a few Hz, therefore the uncertainty in the detuning δ is dominated by the uncertainty in the measured value of ω_z .

The frequency splitting of the qubit states ω_0 was determined by finding the Raman resonance of the carrier transition. This was done by preparing the ion in $|\downarrow\rangle$, then applying a fixed length probe pulse from the Raman laser. For a series of different values of the difference frequency of the Raman beams, the experimental sequence was repeated 500

times, and the population of spin \uparrow was obtained. The centre of the observed peak of the population $P(\uparrow)$ gives the qubit splitting. The Rabi frequency for carrier flopping Ω_c was then determined by resonantly driving Rabi flopping, and this was used to set the pulse lengths for the π and $\pi/2$ carrier pulses.

The power in the Raman beam at 3° to the magnetic field was set by choosing the drive power of the AOM. These laser beam powers were measured using a power meter. The ratio P of the power in 3° Raman beam during the spin-dependent force to the power used to drive carrier flops allows us to calculate the value of $\Omega_\pi = \sqrt{P}\Omega_c$ from the carrier flopping Rabi frequency.

For the September 2004 data the phase of the fringes observed is dependent not only on the light shift due to off-resonant carrier excitation, and on $\text{Arg}[\langle\alpha_\uparrow|\alpha_\downarrow\rangle]$, but also on the detuning of the carrier $\pi/2$ pulses from resonance. Though the magnetic field is stable enough to produce sinusoidal fringes as shown in figure 7.7, changes in the magnetic field over the time required to take the data shown in figure 7.8 mean the phase of the fringes does not give us any useful information.

Expt.	δ_{tickle} (kHz)	η	$ \alpha_A $	δ_{eff} (kHz)	t_r (μs)	B	$\Delta_\pi/(2\pi)$ (kHz)
1	-19.6	0.199	0.38	-18.5	54		
2	-9.6	0.199	0.74	-9.9	101		
3	-9.6	0.199	1.37	-9.3	108		
4	-10.2	0.255	1.34	-10.6	94		
5	-5.2	0.255	3.16	-5.8	172		
6	10.0	0.199	1.49	11.0	91	2.03	7.36
7	10.0	0.244	1.44	11.3	89	2.15	4.48
8	5.0	0.244	2.27	6.8	147	3.24	4.49
9	3.5	0.244	3.11	5.2	192	4.27	4.46
10	-5.5	0.245	1.88	6.3	160	2.72	4.27

Table 7.1: Experimental parameters and fitted results for Schrödinger's cat experiments. The first column is the reference number of the experiment, which corresponds to the numbers on the plots of the data (figures 7.8, 7.9 and 7.10). Experiments 1-5 were performed in September 2004 by inserting the state-dependent force between two Ramsey separated pulses. Experiments 6-10 were performed in July 2005 with the state-dependent force inserted in the first gap of a spin-echo sequence ($\pi/2, \pi, \pi/2$). δ_{tickle} is obtained by subtracting the measured trap frequency ω_z from the difference frequency of the two synthesizers in the beam paths of the two Raman beams. $|\alpha_A|$, δ_{eff} , t_r , B and $\Delta_\pi/(2\pi)$ were extracted by fitting the data with equations 7.68 and 7.69.

Since the data contains no information about the phase difference $\Delta\phi$ between the forces as an independent parameter, it was calculated using equation 2.12 from the angle between the polarisation vector and the vertical (β) obtained from the waveplate settings.

The angle $\beta = \pi/4$ ¹, therefore

$$\Delta\phi = 2 \arctan \left[\frac{1}{\cos(63^\circ) \tan(\pi/4)} \right] = 2.28 \text{ radians} \quad (7.65)$$

The angle of the polarisation vector also allows us to calculate the ratio of the power in the σ and π components of the Raman beam at 63° to the magnetic field from equations 2.13 and 2.14. For $\beta = \pi/4$,

$$\frac{I_{\sigma^+}^{63}}{I_{\pi}^{63}} = \frac{1}{2} \left(\cot^2(63^\circ) + \frac{\cot^2(\beta)}{\sin^2(63^\circ)} \right) = 0.76 \quad (7.66)$$

The force parameter F_m can therefore be calculated from the carrier flopping rate to be

$$F_m = \eta \sqrt{2} \sqrt{\frac{I_{\sigma^+}^{63}}{I_{\pi}^{63}}} \sqrt{P} \Omega_c \quad (7.67)$$

where the factor of $\sqrt{2}$ is the ratio of Clebsch-Gordan co-efficients for the $\Delta M_J = \pm 1$ and $\Delta M_J = 0$ transitions. For the September 2004 data, $P = 1$, thus we find $F_m = 1.29\eta\Omega_c$. This value was combined with the measured detuning to calculate the expected behaviour.

The amplitude of the fringes observed is plotted against the duration τ of the spin-dependent force in figure 7.8. We fit the data using

$$A = e^{-\gamma\tau} e^{-2|\alpha_A|^2 \sin^2\left(\frac{\delta_{\text{eff}}\tau}{2}\right)} \quad (7.68)$$

where γ , $|\alpha_A|$ and δ_{eff} are fitted parameters. We thus obtain three pieces of information. γ is a phenomenological decay constant. $|\alpha_A| = \sqrt{(\bar{n} + 1/2)}|\Delta\alpha|$ is a real number indicating the size of the relative excursion in phase space, c.f. figure 7.1 and equation 7.64, and δ_{eff} is an effective detuning which roughly accounts for the non-Lamb-Dicke limit behaviour as discussed in section 7.2.1. The fit parameters for the data taken in September 2004 are given in figure 7.8 and in table 7.1.

Schrödinger's cat experiments were also performed in July 2005. In these experiments the state-dependent force was applied in the first gap of a spin-echo pulse sequence. Experiments were again performed with the axial vibrational frequency of the ion close to 800 kHz and to 500 kHz. In order to create motional states with high vibrational quantum numbers n , the power in the Raman laser beam at 3° to the magnetic field was changed between the carrier $\pi/2$ and π pulses and the pulse used for the state-dependent force. The amplitude of the observed fringes is plotted against the duration of the spin-dependent force in figure 7.9. The amplitudes were again fitted using equation 7.68, with the values of γ , $|\alpha_A|$ and δ_{eff} allowed to float. The fit parameters are given in table 7.1.

Since a spin-echo pulse sequence was used to protect against magnetic field drift, the phase of the fringes is dependent only on the light shift due to off-resonant carrier excitation and $\text{Arg}(\langle\alpha_\uparrow|\alpha_\downarrow\rangle)$. The phase as a function of time was fitted with

$$\phi(\tau) = b + \Delta_\pi\tau + \text{Arg}(\langle\alpha_\uparrow|\alpha_\downarrow\rangle) \quad (7.69)$$

$$= b + \Delta_\pi\tau + B^2 \sin^2\left(\frac{\delta_{\text{eff}}\tau}{2}\right) \quad (7.70)$$

¹ Subsequently, we have discovered that this value is incorrect due to modification of the state of polarisation caused by a mirror placed after the $\lambda/2$ waveplate in the 63° beam path. The $\lambda/4$ waveplate after this mirror is used to make the polarisation linear, but at an angle which is not $\beta = \pi/4$. The analysis is self-consistent for $\beta \simeq 57^\circ$; however this angle cannot be checked, because the experimental setup has since changed.

where b is a phase offset, Δ_π is the light shift due to the off resonant driving of the carrier transition described in section 7.3.3, B^2 is the magnitude of $\text{Arg}(\langle\alpha_\uparrow|\alpha_\downarrow\rangle)$, and δ_{eff} is the effective detuning obtained from the fit to the amplitude of the fringes. The phases of the observed fringes are plotted against duration of the spin-dependent force τ in figure 7.10, along with the fit parameters B and Δ_π . The fitted value of Δ_π combined with the measured values of ω and ω_0 allow us to calculate Ω_π from equation 7.49, which can be compared with the value $\sqrt{P}\Omega_c$ calculated from the carrier flopping rate.

The fitted values of $|\alpha_A|$ and B enable us to derive $\Delta\phi$ and $|\alpha_{\text{max}}|$ as follows. In the Lamb-Dicke regime, the values of $|\alpha_A|^2$ and B^2 can be written in terms of $|\alpha|$ and $\Delta\phi$ using equations 7.64, 7.68, 7.58 and 7.70, we obtain

$$2|\alpha_A|^2 = (2\bar{n} + 1)|\alpha_{\text{max}}|^2(1 - \cos(\Delta\phi)) \quad . \quad (7.71)$$

$$B^2 = |\alpha_{\text{max}}|^2 \sin(\Delta\phi) \quad . \quad (7.72)$$

Solving for $|\alpha_{\text{max}}|$ and $\Delta\phi$ in terms of $|\alpha_A|$ and B gives

$$\Delta\phi = \arccos\left(\frac{1 - R^2}{1 + R^2}\right) \quad (7.73)$$

$$|\alpha_{\text{max}}|^2 = \frac{1}{4|\alpha_A|^2} (4|\alpha_A|^4 + B^4) \quad (7.74)$$

where $R = 2|\alpha_A|^2/(2\bar{n} + 1)B^2$. The values of $\Delta\phi$ calculated from the fitted parameters are given in table 7.2, rows 6 to 10.

The value of $\Delta\phi$ calculated by this method disagrees with the value derived from the expected polarisation for all the 2005 data, even when the motion was in the Lamb-Dicke regime where equations 7.73 and 7.74 are accurate. A further check is available, as follows. We use the obtained value of $\Delta\phi$ to calculate the relative intensities of the circular and π polarisation components of the 63° Raman beam. Using equations 7.65 and 7.66, the relative intensities can be written in terms of $\Delta\phi$ as

$$\frac{I_{\sigma^+}^{63}}{I_{\pi}^{63}} = \frac{1}{2} \cot^2(63^\circ) \left(1 + \tan^2\left(\frac{\Delta\phi}{2}\right)\right) = \frac{1}{2} \cot^2(63^\circ) \sec^2\left(\frac{\Delta\phi}{2}\right) \quad (7.75)$$

The force on the ion F_m can be calculated using Ω_π and the value of $\Delta\phi$ obtained using equation 7.67, see table 7.2, column 9.

An independent measure of the force is given by fitting the fringe amplitude as a function of time with a sum of Gaussians

$$A = \exp[-t^2/w^2] + r \exp[-(t - t_r)^2/w_2^2] \quad (7.76)$$

where

$$w = \frac{4/F_m}{\sqrt{(2\bar{n} + 1)(1 - \cos(\Delta\phi))}} \quad (7.77)$$

$$t_r = \frac{2\pi}{\delta} \left(\frac{1}{1.18} \frac{\alpha_{\text{max}}}{\alpha_0} + \frac{0.18}{1.18}\right) \quad (7.78)$$

$$w_2 \simeq w \quad (7.79)$$

and α_{max} was given by the empirical form from equation 7.28. An empirical form for w_2 as a function of w was found for $\Delta\phi = \pi$ and $\Delta\phi = 1$. For the range of parameters used

in our experiments this was found to be very close to $w_2 = w$ for all phase angles. This indicates that the squeezing as the motional wavepacket returns to the origin does not affect the fringes for the range of parameters explored by our experiments.

In fitting the data, $\Delta\phi$ was fixed at the values deduced from equation 7.73 and \bar{n} was fixed at the measured value, while F_m and δ were floated. Fitting this form makes it obvious that F_m is determined by the width of the peaks. The return time t_r determines the detuning δ . The fitted values are given in table 7.2, columns 10 and 11.

No.	δ_{tickle} (kHz)	\bar{n}	$\Omega_c/2\pi$ (kHz)	\sqrt{P}	$\Omega_\pi/2\pi$ (kHz)	$\Delta\phi$	$\Omega_\pi/2\pi$ (kHz)	F_m (kHz)	δ (kHz)	F_m (kHz)	α_{max}	$ \Delta\alpha_{\text{max}} $
1	-19.6	0.36	25.6	1	25.6	2.28		6.3				
2	-9.6	0.36	25.6	1	25.6	2.28		6.3	-9.7	5.3	0.5	1.0
3	-9.6	0.36	50.6	1	50.6	2.28		12.4	-9.1	10.6	1.1	1.9
4	-10.2	0.56	54.8	1	54.8	2.28		17.2	-10.4	11.5	1.0	1.9
5	-5.2	0.62	51.9	1	51.9	2.28		16.3	-5.1	13.5	2.2	3.9
6	10.0	0.04	107	1.41	151	1.57	185	26.6	10.2	22.2	1.9	2.6
7	10.0	0.07	96	1.45	139	1.34	145	23.0	10.1	24.0	2.0	2.5
8	5.0	0.07	96	1.45	139	1.41	145	23.7	5.3	22.5	3.1	4.0
9	3.5	0.07	96	1.45	139	1.50	145	24.6	3.4	22.9	4.0	5.4
10	-5.5	0.02	126	1.09	137	1.43	142	23.4	-5.2	18.0	2.7	3.5

Table 7.2: Results of the analysis of the Schrödinger's cat experiments. δ_{tickle} is the measured detuning of the force from the vibrational frequency of the ion deduced from the measured trap frequency and the synthesiser settings. \bar{n} is the mean vibrational quantum number of the ion, which is measured using scans over the red and blue sidebands as described in chapter 4. Ω_c is the Rabi frequency of the carrier flopping experiment. P is the ratio of the power in the 3° beam used for the force to that used for the carrier flopping rate measurement. This allows us to deduce a value for the carrier flopping rate at the beam powers used for the force, which is given in column 6 as Ω_π . For data sets 6 – 10, this value can be compared to the value obtained from the phase of the fringes as a function of the duration of the force, which is given in column 8. For data sets 1-5, the phase angle $\Delta\phi$ is deduced from the waveplate angles in the 63° beam (but see footnote 1). For data sets 6-10, the phase angle $\Delta\phi$ between the forces is deduced from the fits to the visibility and phase of the observed fringes as a function of time using equation 7.73. This is then combined with Ω_π to give an expected value for the force on the ions given that the phase difference between circular components in the 3° beam is zero (as would be expected from its horizontal polarisation). This value is given in column 9. An independent measure of δ and F_m is given by fitting equation 7.76 to the data. These deduced values (given in columns 12 and 13) allow us to calculate the maximum excursion of the ion in phase space α_{max} and the maximum separation of the orbits $\Delta\alpha$.

7.5.1 Discussion

The values of the Rabi flopping rate on the spin flip transition deduced from carrier flopping are consistent with the values calculated from the light shift Δ_π for most of the experimental data. This suggests that the carrier flopping diagnostic experiment gives an accurate indication of the laser intensity at the ion for the oscillating force part of the sequence. In particular, the frequency shift of the AOM appears not to have caused a beam alignment shift.

For the data taken in 2005, the phase difference between the two circular polarisation components of the standing wave could be inferred from the data (fringe amplitude *and* phase). The mean value measured in these experiments is 1.45(4). This is consistent with an independent measure of the beam polarisation made using crossed polarisers. Results 6 and 10 have a $\sim 20\%$ discrepancy between the value of F_m determined from Δ_π and from the visibility curve. For result 6, this discrepancy is also observed between Ω_π and $\sqrt{P}\Omega_c$. Using $\sqrt{P}\Omega_c$, the predicted value of F_m is 21.7 kHz, which is consistent with the value measured from the visibility curve.

For results 7-9, the value of F_m deduced from carrier flopping is consistent with the value determined from the visibility curve. Therefore we can predict with confidence that the maximum separation of our wavepackets achieved in these experiments is $\Delta\alpha = 5.4$. This corresponds to spatial separation of the two wavepackets of $2\Delta\alpha z_0 = 172$ nm. The largest motional states created had $|\alpha_{\max}| = 4$ and thus the mean vibrational excitation was 16. The motion here is well outside the Lamb-Dicke regime and the theory predicts substantial squeezing of the motional states.

For the data taken in 2004, the force F_m predicted from the carrier flopping data is $\sim 20\%$ higher than that determined from the fringe visibility by $\sim 20\%$. This is because the polarisation angle (and hence the proportion of the intensity in the π and σ components of the 63° light field) deduced from the waveplate settings is not the same as the polarisation angle of the light at the ion, due to a mirror in the beam path. The data is consistent for a polarisation angle of $\simeq 57^\circ$, however the experimental setup has changed since these results were taken, thus we have been unable to confirm this value.

7.5.2 Coherence of Schrödinger's Cat states.

In the previous section, a phenomenological decay parameter γ was introduced in order to account for processes which lead to a loss of coherence in the motional and spin degrees of freedom of the ion. Assuming that the two degrees of freedom decay independently, we can write

$$\gamma = \gamma_s + \gamma_m \quad (7.80)$$

where γ_s accounts for effects unrelated to the motional state, and γ_m is the motional decoherence rate. In the experiments presented in the previous section, the amplitude of the fringes measured after the force has been applied is normalised by dividing through by the amplitude of the fringes using a zero length force. This allows us to eliminate the effects of decoherence due to fluctuations in the magnetic field. In this case, the primary source of spin decoherence is thought to be photon scattering.

In order to estimate the photon scattering rate during the experiments presented above we can use the measured beam powers and the results of section 5.3.1. For beam powers of $P_{63} = 471 \mu\text{W}$ and $P_3 = 188 \mu\text{W}$ the photon scattering rates were $R_{63} = 0.67 \text{ ms}^{-1}$ and $R_3 = 0.45 \text{ ms}^{-1}$. The measured beam powers and deduced scattering rate γ_s for results 6-10 from table 7.2 are presented in table 7.3. If all the spin decoherence is assumed to be due to photon scattering, the motional decoherence rate can be found from $\gamma_m = \gamma - \gamma_s$, where γ is the fitted value from the visibility curves shown in figure 7.9. The results are shown in table 7.3.

Motional decoherence of superpositions of coherent states have been extensively studied by Turchette et. al. [51]. In the Schrödinger's cat states described in the previous section, the motional states in the superposition have the same energy. The relative phase of the

two states is therefore independent of the trap frequency. Any decoherence of the motional state during the gap will therefore be due to parametric heating. The fluctuating electric field which induces this heating is caused by fluctuating patch potentials or electrode voltage fluctuations. The electric field $E(t)$ is uniform over the region which is explored by the ion, and will give a spatially uniform force $z_0 e E(t) / \hbar$. The result will be displacement of both motional states in a given direction in phase space. The area enclosed by the motional states in phase space will therefore be different for each state in the superposition and a phase difference will be acquired. For a ‘cat’ state of given, fixed $|\Delta\alpha|$, the motional decoherence rate due to this dephasing is exponential, with a decay parameter which has the form [51, 74],

$$\gamma_m = \gamma_0 |\Delta\alpha|^2 \quad (7.81)$$

where γ_0 is the motional decoherence rate of a cat state with $|\Delta\alpha| = 1$. For a superposition of states which are being displaced as a function of time, the reduction in the fringe contrast after time t will be

$$C = \exp \left[-\gamma_s t - \gamma_0 \int_0^t |\Delta\alpha(t)|^2 dt \right] \quad (7.82)$$

For a superposition of states which are being continually displaced, the separation of the states at time t can be approximated by $|\Delta\alpha(t)| = |\Delta\alpha_{\max}| \sin(\delta_{\text{eff}} t / 2)$ (see equation 7.68). The reduction in the contrast of the fringes at time t is then

$$C = \exp \left[-\gamma_s t - \frac{\gamma_0 |\Delta\alpha_{\max}|^2 t}{2} \right] \quad (7.83)$$

and hence

$$\gamma_m = \gamma_0 \Delta\alpha_{\max}^2 / 2 \quad (7.84)$$

Table 7.3 gives values of γ_0 calculated from the values of γ_m and $|\Delta\alpha_{\max}|$ for data sets 6-10, and the deduced values of γ_0 . For our largest ‘cat’, run 9, the coherence time $2/\gamma_0 \Delta\alpha^2$ is thus deduced to be of order 200 μs .

7.6 Conclusions

We have demonstrated a travelling wave state-dependent force, and used it to create ‘Schrödinger’s cat’ like states involving entanglement of the spin state with mesoscopic motional states. The size of the motional states created has been inferred from the visibility and phase of interference fringes observed by measuring the spin state of the ion.

The largest motional state superpositions which we observe are mesoscopic in the sense that they have a spatial separation much larger than the wavepacket size. These are among the largest superpositions of motional states which have been experimentally realised in an ion trap. The coherence time of these states has been measured and the lifetimes found to be larger than lifetimes measured in other ion trap systems.

At low laser powers the force is small, and the motional states were observed to return to the origin after times $\sim 2\pi/\delta$. This is the behaviour predicted by the Schrödinger equation for an ion in the Lamb-Dicke regime.

In a later set of experiments, the force on the ion was increased in order to make the force and the motional excursion as large as possible. At high forces, the large excursions

No.	γ	P_{63}	P_3	γ_s	γ_m	$ \Delta\alpha_{\max} $	γ_0
	(ms^{-1})	(mW)	(mW)	(ms^{-1})	(ms^{-1})		(ms^{-1})
6	3.5	368	370	1.4	2.1	2.6	0.6
7	2.0	572	377	1.7	0.3	2.5	0.0
8	4.1	572	377	1.7	2.3	4.0	0.3
9	5.6	572	377	1.7	3.9	5.4	0.3
10	4.6	572	280	1.4	3.2	3.5	0.5

Table 7.3: Decoherence rates of Schrödinger cat states. The values of γ are obtained from the fitted visibility curve shown in figure 7.8. The measured beam powers are given, which allows calculation of the photon scattering rate γ_s by comparison with the experiments described in section 5.3.1 (there the powers and rates were $P_{63} = 471 \mu\text{W}$, $P_3 = 188 \mu\text{W}$ and $R_{63} = 0.67 \text{ ms}^{-1}$, $R_3 = 0.45 \text{ ms}^{-1}$). If photon scattering is the only form of spin decoherence present, then the motional decoherence rate is given by $\gamma_m = \gamma - \gamma_s$. γ_0 is the motional decoherence rate for a superposition of motional states with $\Delta\alpha = 1$. This is calculated from γ_m and $\Delta\alpha_{\max}$ using equation 7.84.

of the motional wavepackets in phase space mean that they are outside the Lamb-Dicke regime for part of their trajectory. This means that the force on the ion becomes spatially dependent, which results in the motional states returning to the origin after times $< 2\pi/\delta$, a reduced motional excursion, and squeezing. We experimentally observe the early return time, and use this and the modified trajectory to deduce the motion and the force on the ion.

In addition to exploring the motional state excitation, these experiments have also provided insights into the nature of the light field producing the state-dependent force. The size of the light shifts expected have been experimentally tested, and are consistent with the measured rate of carrier flopping. By combining the data from the visibility and phase of the observed interference fringes we are able to infer the beam polarisation, and this value has subsequently been confirmed by independent measurements. The overall consistency of the data indicates that the light field has been understood correctly.

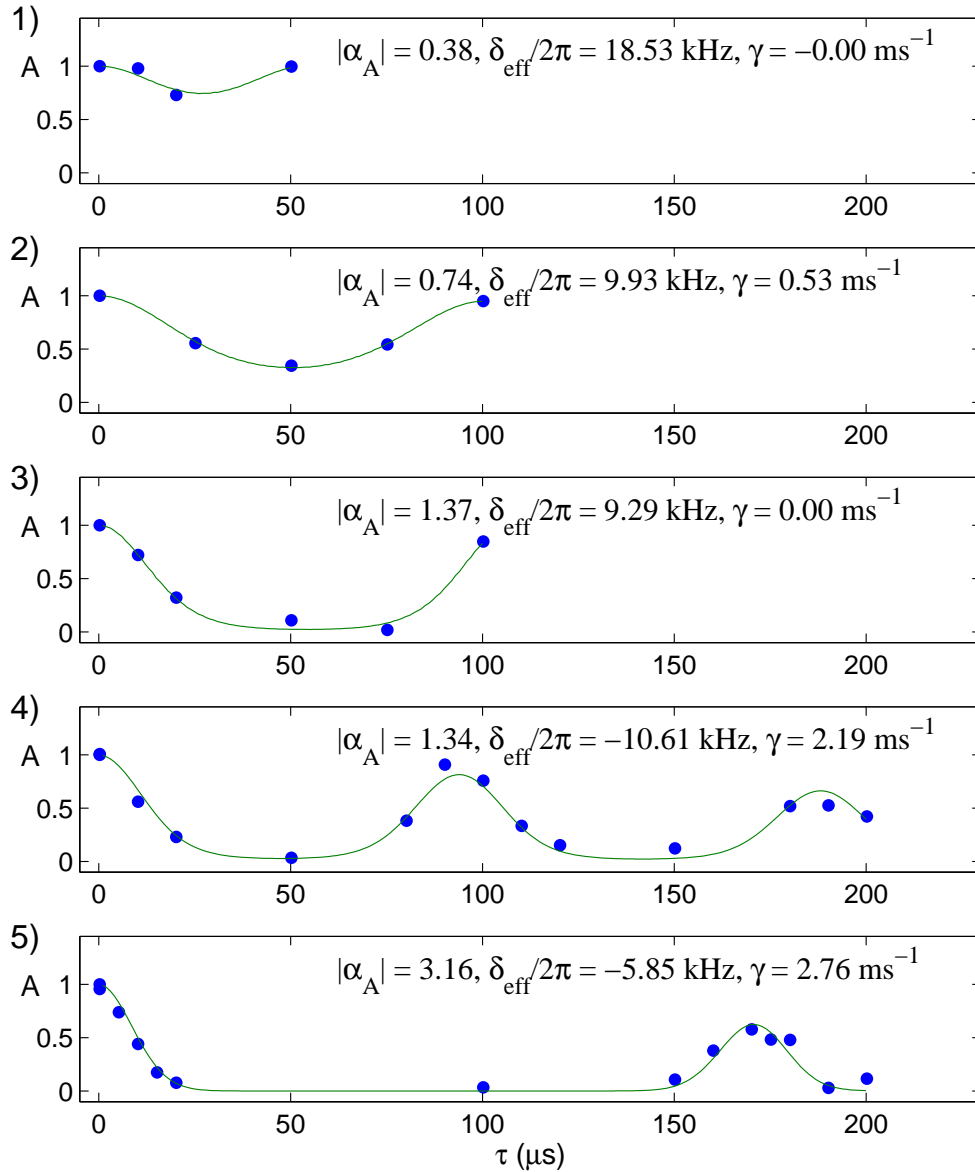


Figure 7.8: The amplitude of the fringes observed in Schrödinger's cat experiments, plotted against the duration of the pulse which generates the spin-dependent force. These results are obtained by fitting curves of the form $b + a \cos(\phi)$ to the oscillations of $P(\uparrow)$ as the phase of the second carrier $\pi/2$ pulse in the spin-echo sequence is scanned. The parameter $A = a/a_{\text{max}}$ is the normalised amplitude, where a_{max} is the amplitude of a control experiment with $\tau = 0$. The fitted curves are $A = \exp(-\gamma t) \exp(-2|\alpha_A|^2 \sin^2(\delta_{\text{eff}}\tau/2))$, γ is a phenomenological decay constant. $|\alpha_A|$ is a real number indicating the size of the relative excursion in phase space, c.f. figure 7.1, and δ_{eff} is an effective detuning which roughly accounts for non-Lamb-Dicke regime behaviour.

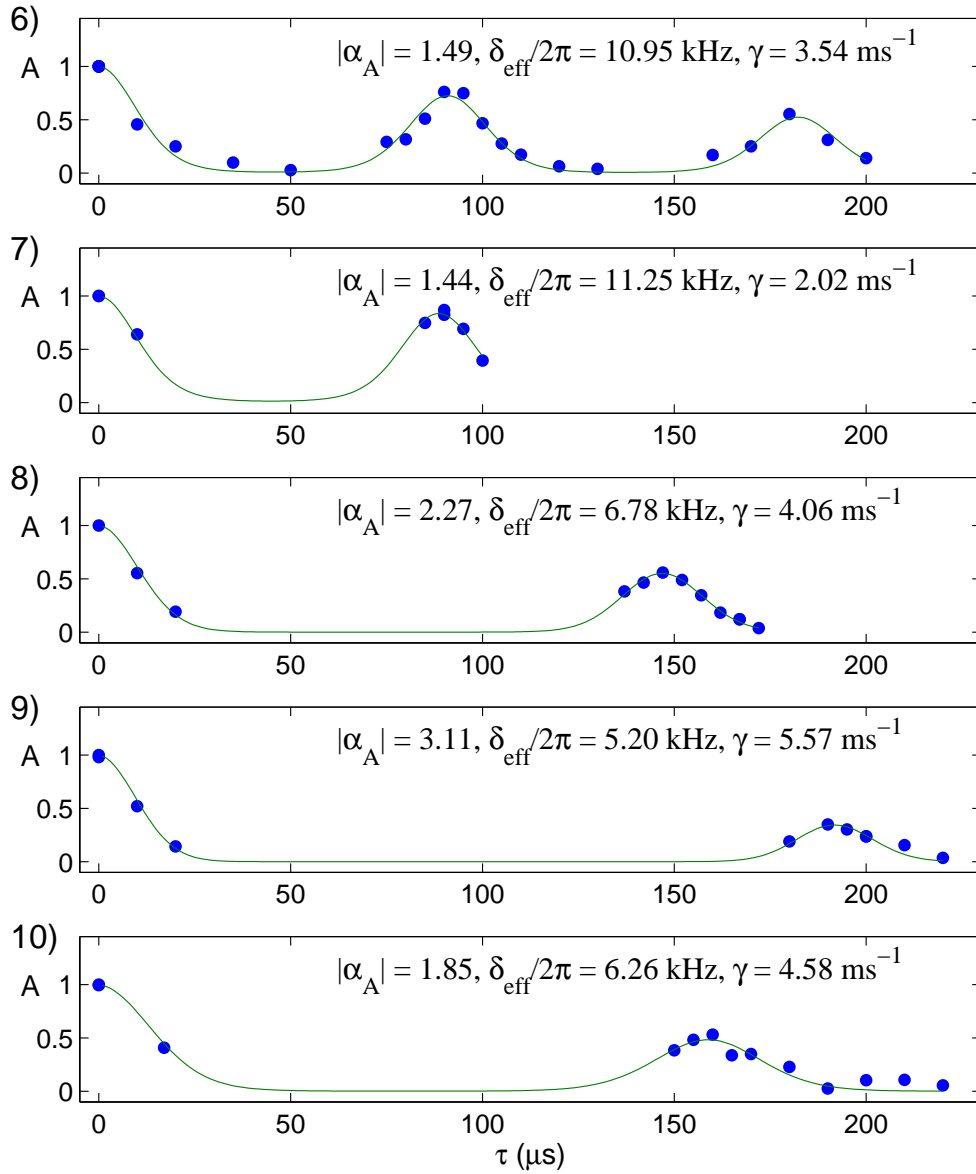


Figure 7.9: The amplitude of the fringes observed in Schrödinger's cat experiments, plotted against the duration of the pulse which generates the spin-dependent force. These results are obtained by fitting curves of the form $b+a \cos(\phi)$ to the oscillations of $P(\uparrow)$ as the phase of the second carrier $\pi/2$ pulse in the spin-echo sequence is scanned. The parameter $A = a/a_{\max}$ is the normalised amplitude, where a_{\max} is the amplitude of a control experiment with $\tau = 0$. The fitted curves are $A = \exp(-\gamma t) \exp(-2|\alpha_A|^2 \sin^2(\delta_{\text{eff}}\tau/2))$, $|\alpha_A|$ is a real number indicating the size of the relative excursion in phase space, c.f. figure 7.1, and δ_{eff} is an effective detuning which roughly accounts for non-Lamb-Dicke regime behaviour.

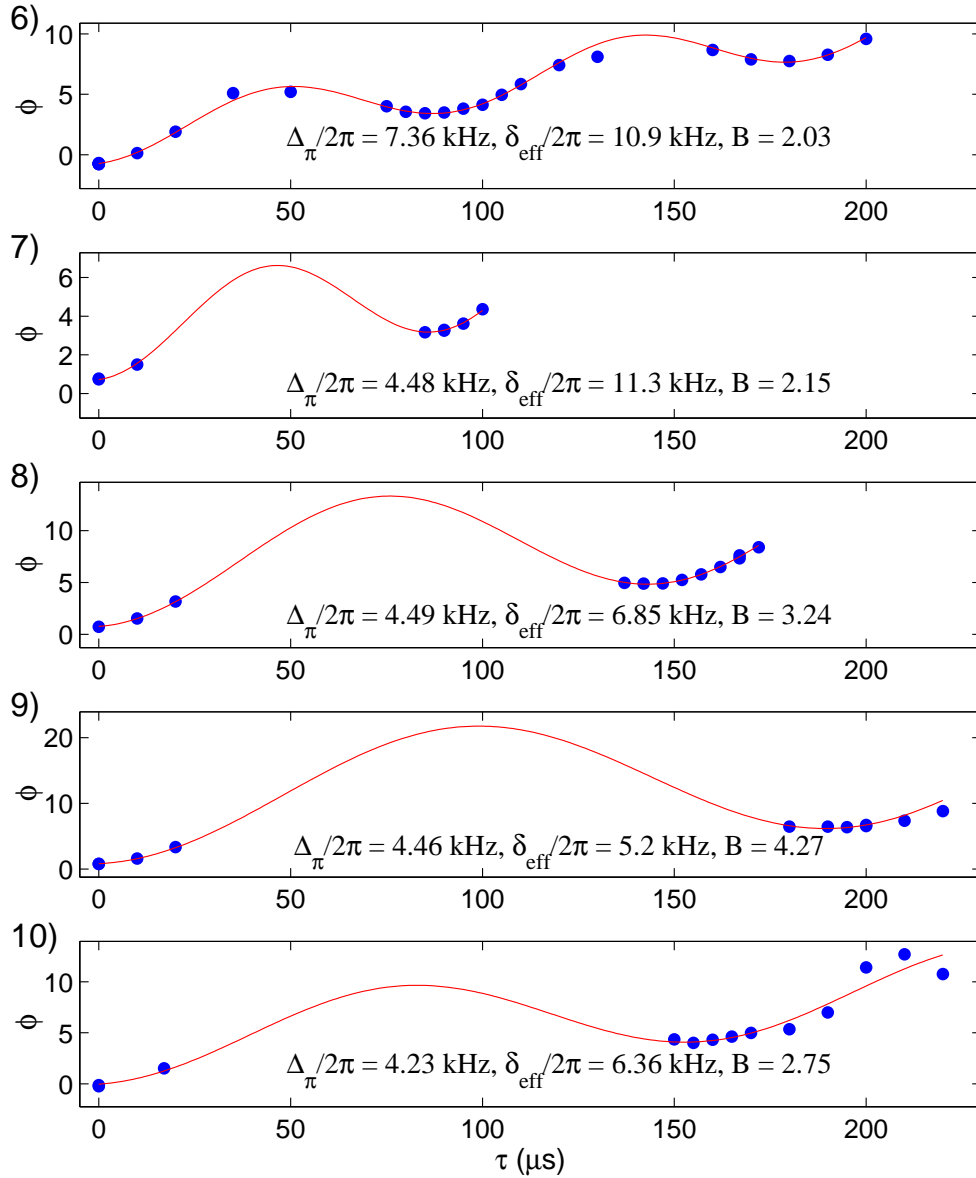


Figure 7.10: The phase offset of the fringe pattern observed as the phase of the second carrier $\pi/2$ pulse is varied relative to the first. The phase is plotted against the duration of the wobble pulse. The linear drift is caused by the light shift due to off-resonant driving of the carrier transition. The oscillation in the phase with the duration of the wobble pulse is due to the argument of $\langle \alpha_{\uparrow} | \alpha_{\downarrow} \rangle$. In order to find the phase, the starting value of the phase offset used to fit the observed fringes was given by $\phi_{\text{off}}(0) + 2\pi\Delta_{\text{guess}}\tau$. This ensures that the phase deduced is not out by an integer multiple of 2π . If the amplitude of the observed fringes was found to be less than 0.1, the phase of the fringes was considered to be uncertain, and this point was not used to fit the phase vs. τ . For the results shown in plot 10), the spin-echo sequence was carried out using the magnetic resonance coil.

Chapter 8

Spin state tomography.

In this chapter I discuss tomography, that is, complete experimental measurement of the spin state of trapped ions. In order to perform a full tomography of the spin state of two ions, we must be able to obtain values for all 16 of the density matrix elements. The method presented here is a partial tomography which is possible within the limitations of our current experiment. These are that we can currently only apply equal rotations to each qubit, and that we cannot distinguish $|\uparrow\downarrow\rangle$ from $|\downarrow\uparrow\rangle$. This results in only partial information about the density matrix being obtained. The method used an overcomplete set of measurements, which makes possible to diagnose drift in experimental parameters such as the magnetic field and the readout level.

The tomography method is demonstrated by applying it to example states which can be prepared from $|\downarrow\downarrow\rangle$ by pulses on the carrier transition. It will also be used in chapter 9 to reconstruct the density matrix of an entangled state.

8.1 Tomography

The density matrix for a two qubit system can be written in the general form

$$\hat{\rho} = \begin{pmatrix} w & p & q & r \\ p^* & x & s & t \\ q^* & s^* & y & u \\ r^* & t^* & u^* & z \end{pmatrix} \quad (8.1)$$

Since it must be normalized, this density matrix can be fully described by 15 independent real numbers, hence we need to measure 15 observables to extract this information. The 15 real numbers in the above density matrix are $w, x, y, p_R, p_I, q_R, q_I, t_R, t_I, u_R, u_I$ and s_R, s_I, r_R, r_I , where the subscripts R and I denote the real and imaginary parts of these parameters respectively. The density matrix must satisfy $\text{Tr}(\hat{\rho}) = 1$, hence $z = 1 - (w + x + y)$.

Tomography methods have been applied to two-qubit density matrices in a range of physical systems including photons [82] and trapped ions [40]. These have all made use of single-qubit addressing to apply rotations to each of the individual qubits. After each rotation the state of the qubits is measured. In our experiment, we can not apply rotations to individual qubits, therefore we only have access to restricted information about the density matrix.

8.1.1 Equal rotations applied to qubits

The tool available to us in the current experimental system is that we can drive Rabi flopping on the carrier transition of both ions simultaneously. The propagator for Rabi flopping of a single ion is given in equation 3.13 of chapter 3. Making the substitution $\theta = \Omega t$, this propagator takes the form of a rotation matrix

$$R^{(1)}(\theta, \phi) = \begin{pmatrix} \cos \frac{\theta}{2} & -ie^{i\phi} \sin \frac{\theta}{2} \\ -ie^{-i\phi} \sin \frac{\theta}{2} & \cos \frac{\theta}{2} \end{pmatrix} \quad (8.2)$$

The laser beams have equal intensity at each ion, so the same rotation is applied to each ion. The rotation matrix for the two ions is thus

$$R^{(2)}(\theta, \phi) = \begin{pmatrix} \cos^2 \frac{\theta}{2} & -ie^{i\phi} \sin \frac{\theta}{2} \cos \frac{\theta}{2} & ie^{i\phi} \sin \frac{\theta}{2} \cos \frac{\theta}{2} & -e^{2i\phi} \sin^2 \frac{\theta}{2} \\ ie^{-i\phi} \sin \frac{\theta}{2} \cos \frac{\theta}{2} & \cos^2 \frac{\theta}{2} & -\sin^2 \frac{\theta}{2} & ie^{i\phi} \sin \frac{\theta}{2} \cos \frac{\theta}{2} \\ ie^{-i\phi} \sin \frac{\theta}{2} \cos \frac{\theta}{2} & -\sin^2 \frac{\theta}{2} & \cos^2 \frac{\theta}{2} & ie^{i\phi} \sin \frac{\theta}{2} \cos \frac{\theta}{2} \\ -e^{-2i\phi} \sin^2 \frac{\theta}{2} & ie^{-i\phi} \sin \frac{\theta}{2} \cos \frac{\theta}{2} & ie^{-i\phi} \sin \frac{\theta}{2} \cos \frac{\theta}{2} & \cos^2 \frac{\theta}{2} \end{pmatrix} \quad (8.3)$$

The density matrix after this rotation has been applied is $\hat{\rho}_T(\theta, \phi) = R^{(2)}(\theta, \phi)\hat{\rho}R^{(2)\dagger}(\theta, \phi)$. The populations $P(\uparrow\uparrow)$, $P(\uparrow\downarrow)$ and $P(\downarrow\uparrow)$ give 3 independent pieces of information about $\hat{\rho}$ for each choice of θ and ϕ .

8.1.2 Available information.

We now ask what information is available to us using the rotation described by equation 8.3. Following the approach taken in [40], we write the density matrix as a superposition of mutually orthogonal Hermitian operators

$$\hat{\rho} = \sum_k \lambda_k \hat{O}_k \quad (8.4)$$

where the \hat{O}_k form a basis and obey the equation $\text{tr}(\hat{O}_k \hat{O}_j) = 4\delta_{kj}$. The coefficients λ_k are related to the expectation values of \hat{O}_k by $\lambda_k = \text{tr}(\hat{\rho} \hat{O}_k)/4$. A convenient set of operators is given by tensor products of the Pauli operators. Thus we can write the density matrix as

$$\hat{\rho} = \sum_{i,j=0}^3 c_{ij} \hat{\sigma}_i \otimes \hat{\sigma}_j \quad (8.5)$$

where the $\hat{\sigma}_i$ are given by \hat{I} , $\hat{\sigma}_x$, $\hat{\sigma}_y$, $\hat{\sigma}_z$ for $i = 0, 1, 2, 3$. The density matrix elements can be written in terms of the coefficients c_{ij} as

$$w = c_{00} + c_{03} + c_{30} + c_{33} \quad (8.6)$$

$$x = c_{00} - c_{03} + c_{30} - c_{33} \quad (8.7)$$

$$y = c_{00} + c_{03} - c_{30} - c_{33} \quad (8.8)$$

$$p = c_{01} + c_{31} + i(c_{02} + c_{32}) \quad (8.9)$$

$$q = c_{10} + c_{13} + i(c_{20} + c_{23}) \quad (8.10)$$

$$t = c_{10} - c_{13} + i(c_{20} - c_{23}) \quad (8.11)$$

$$u = c_{01} - c_{31} + i(c_{02} - c_{32}) \quad (8.12)$$

$$r = c_{11} - c_{22} + i(c_{12} + c_{21}) \quad (8.13)$$

$$s = c_{11} + c_{22} + i(c_{21} - c_{12}) \quad (8.14)$$

In order that $\text{tr}(\hat{\rho}) = 1$, we require $c_{00} = 1/4$.

The probabilities of finding the ions in each spin state after applying the rotation $R^{(2)}(\theta, \phi)$ are given by

$$P(\uparrow\uparrow) = a_{\uparrow\uparrow} + b_{\uparrow\uparrow} \cos(\phi) + c_{\uparrow\uparrow} \sin(\phi) + d_{\uparrow\uparrow} \cos(2\phi) + e_{\uparrow\uparrow} \sin(2\phi) \quad (8.15)$$

$$P(\uparrow\downarrow) = a_{\uparrow\downarrow} + b_{\uparrow\downarrow} \cos(\phi) + c_{\uparrow\downarrow} \sin(\phi) + d_{\uparrow\downarrow} \cos(2\phi) + e_{\uparrow\downarrow} \sin(2\phi) \quad (8.16)$$

$$P(\downarrow\uparrow) = a_{\downarrow\uparrow} + b_{\downarrow\uparrow} \cos(\phi) + c_{\downarrow\uparrow} \sin(\phi) + d_{\downarrow\uparrow} \cos(2\phi) + e_{\downarrow\uparrow} \sin(2\phi) \quad (8.17)$$

where a_i, b_i, c_i, d_i and e_i can be expressed in terms of the c_{ij} and θ as

$$a_{\uparrow\uparrow} = [1 + c_{11} + c_{22} + 2c_{33} + 4(c_{03} + c_{30}) \cos \theta - (c_{11} + c_{22} - 2c_{33}) \cos 2\theta]/4 \quad (8.18)$$

$$a_{\uparrow\downarrow} = [1 - c_{11} - c_{22} - 2c_{33} + 4(c_{30} - c_{03}) \cos \theta + (c_{11} + c_{22} - 2c_{33}) \cos 2\theta]/4 \quad (8.19)$$

$$a_{\downarrow\uparrow} = [1 - c_{11} - c_{22} - 2c_{33} + 4(c_{03} - c_{30}) \cos \theta + (c_{11} + c_{22} - 2c_{33}) \cos 2\theta]/4 \quad (8.20)$$

$$b_{\uparrow\uparrow} = -[2 \sin \theta (c_{02} + c_{20}) + \sin 2\theta (c_{23} + c_{32})]/2 \quad (8.21)$$

$$b_{\uparrow\downarrow} = [2 \sin \theta (c_{02} - c_{20}) + \sin 2\theta (c_{23} + c_{32})]/2 \quad (8.22)$$

$$b_{\downarrow\uparrow} = [2 \sin \theta (c_{20} - c_{02}) + \sin 2\theta (c_{23} + c_{32})]/2 \quad (8.23)$$

$$c_{\uparrow\uparrow} = [2 \sin \theta (c_{01} + c_{10}) + \sin 2\theta (c_{13} + c_{31})]/2 \quad (8.24)$$

$$c_{\uparrow\downarrow} = -[2 \sin \theta (c_{01} - c_{10}) + \sin 2\theta (c_{13} + c_{31})]/2 \quad (8.25)$$

$$c_{\downarrow\uparrow} = -[2 \sin \theta (c_{10} - c_{01}) + \sin 2\theta (c_{13} + c_{31})]/2 \quad (8.26)$$

$$d_{\uparrow\uparrow} = -d_{\uparrow\downarrow} = -d_{\downarrow\uparrow} = 2 \sin^2 \theta (-c_{11} + c_{22}) \quad (8.27)$$

$$e_{\uparrow\uparrow} = -e_{\uparrow\downarrow} = -e_{\downarrow\uparrow} = -2 \sin^2 \theta (c_{12} + c_{21}) \quad (8.28)$$

Inspection of these equations allows us to see that by choosing different values of θ and ϕ , 12 independent real numbers can be extracted from measurements of the populations $P(\uparrow\uparrow)$, $P(\uparrow\downarrow)$ and $P(\downarrow\uparrow)$. Three combinations of c_{ij} never appear in the equations. These are $c_{12} - c_{21}$, $c_{13} - c_{31}$ and $c_{23} - c_{32}$. This means that these 3 pieces of information about the density matrix are not available to a tomography method which applies the rotation $R^{(2)}(\theta, \phi)$ to the two qubits.

8.1.3 Indistinguishability of $\uparrow\downarrow$ and $\downarrow\uparrow$.

A further experimental constraint in our experiment is the inability to distinguish $P(\uparrow\downarrow)$ from $P(\downarrow\uparrow)$. This reduces the parts of equations 8.18 to 8.28 relating to the population in $\uparrow\downarrow$ and $\downarrow\uparrow$ to

$$a_{\uparrow\downarrow} + a_{\downarrow\uparrow} = 2[1 - c_{11} - c_{22} - 2c_{33} + (c_{11} + c_{22} - 2c_{33}) \cos 2\theta]/4 \quad (8.29)$$

$$b_{\uparrow\downarrow} + b_{\downarrow\uparrow} = \sin 2\theta (c_{23} + c_{32}) \quad (8.30)$$

$$c_{\uparrow\downarrow} + c_{\downarrow\uparrow} = -\sin 2\theta (c_{13} + c_{31}) \quad (8.31)$$

$$d_{\uparrow\uparrow} = -1/2(d_{\uparrow\downarrow} + d_{\downarrow\uparrow}) = 2 \sin^2 \theta (-c_{11} + c_{22}) \quad (8.32)$$

$$e_{\uparrow\uparrow} = -1/2(e_{\uparrow\downarrow} + e_{\downarrow\uparrow}) = -2 \sin^2 \theta (c_{12} + c_{21}) \quad (8.33)$$

hence it is not possible to extract $c_{10} - c_{01}$, $c_{20} - c_{02}$ and $c_{30} - c_{03}$ from our measurements. As a result our experiment can only determine 9 real numbers from the 15 which fully characterise the density matrix. The elements of 8.1 which can be extracted are w, z, r_R, r_I and s_R . We are also able to determine $x + y$, and the linear combinations $p + q, t + u$. This tomography method obtains no information about s_I .

8.2 Maximum likelihood estimation

Owing to experimental error, the density matrix $\hat{\rho}_T$ obtained from a set of measurements using the tomography described in the previous section is not necessarily positive definite. In order to obtain a density matrix which has this property from our data, we use a “maximum likelihood estimation” method [82]. We find the matrix $\hat{\rho}_R$ possessing the correct properties which minimizes the cost function

$$\sum_{i=1}^4 \sum_{j=1}^4 |(\hat{\rho}_R - \hat{\rho}_T)_{ij}|^2 \quad (8.34)$$

where $\hat{\rho}_T$ is the experimentally determined density matrix and $\hat{\rho}_R$ is a positive definite density matrix. The cost function was minimised using the Matlab `fminsearch` function.

In order to generate density matrices which are positive definite, we use the approach of James et. al. [82];

$$\hat{\rho}_R = \frac{\hat{T}^\dagger \hat{T}}{\text{Tr}\{\hat{T}^\dagger \hat{T}\}} \quad (8.35)$$

where \hat{T} is given by

$$\hat{T} = \begin{pmatrix} t_1 & 0 & 0 & 0 \\ t_5 + it_6 & t_2 & 0 & 0 \\ t_{11} + it_{12} & t_7 + it_8 & t_3 & 0 \\ t_{15} + it_{17} & t_{13} + it_{14} & t_9 + it_{10} & t_4 \end{pmatrix} \quad (8.36)$$

Any matrix which can be written in the form $\hat{G} = \hat{T}^\dagger \hat{T}$ is non-negative definite and Hermitian, therefore the normalizable form of equation 8.35 fulfils the mathematical requirement for density matrices. The tri-diagonal form is convenient because it is relatively simple to invert. This allows the starting point for the `fminsearch` function to be easily generated from the tomography result [82].

8.3 Experimental method.

It is possible to design a tomography method which uses a minimal number of measurements. Instead of taking this approach, we decided to use a method which produces redundant information, but is more robust against problematic experimental issues, such as drift of the readout levels and the magnetic field.

We make sets of measurements of the populations $P(\uparrow\uparrow)$ and $P(\uparrow\downarrow + \downarrow\uparrow)$ as a function of ϕ , with θ fixed. ϕ is typically scanned from $-\pi \rightarrow \pi$. Figure 8.1 gives a Bloch sphere representation of these sets of rotations which are applied to each qubit.

The choice of θ depends on experimental factors. Values for which $\sin \theta$, $\cos \theta$, $\sin 2\theta$ and $\cos 2\theta$ are close to zero give large errors in the density matrix elements for small errors in measurements. A further consideration is that one particular parameter may be important as a diagnostic. In this case θ should be chosen in order to get the maximum signal to noise ratio for the special parameter. In the experiments of chapter 9, $r = c_{11} - c_{22} + i(c_{12} + c_{21})$ is used as a diagnostic of the creation of the Bell state. The signal to noise on this parameter is maximised for $\theta = \pi/2$, hence we choose this value, despite this not giving as much information about other parameters. We choose the other value

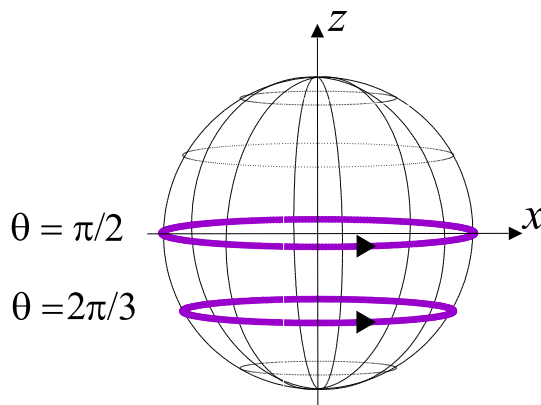


Figure 8.1: A Bloch sphere representation of the rotations applied to each qubit. The rotation shown is applied to each ion simultaneously. Two different values of θ are shown. For each θ the value of ϕ is scanned over a range of values between $-\pi$ and π . At each value of ϕ , the experiment is repeated a large number of times, and the fraction of times the ion fluoresces is measured. This is converted into a spin state measurement using the method of section 2.4.3. The populations as a function of ϕ are fitted with curves with a known sinusoidal dependence on ϕ , equations 8.15 to 8.17. This makes the method robust against drift in the readout levels, and the magnetic field.

of θ to be $\pi/3$ or $2\pi/3$. This choice of angle gives $\sin \theta = \sqrt{3}/2$, $\cos \theta = 1/2$, $\sin 2\theta = \sqrt{3}/2$ and $\cos 2\theta = -1/2$, hence this allows us to extract all of the 10 available real numbers (including one from normalisation).

8.3.1 Setting the correct pulse length.

Typical durations of carrier pulses for producing rotations with $\theta \sim \pi/2$ are $1 \rightarrow 2 \mu\text{s}$. In our initial experiments using sequences of carrier pulses, we experimentally determined the length of a carrier pulse by driving Rabi flopping on the carrier transition, and measuring the time taken for $P(ss)$ to reach a maximum. This was taken to be the π time, and smaller rotations were calculated as a fraction of this time.

In later work, we became aware that the pulse lengths set on the experimental computer were not equal to the time for which the ion (or ions) was illuminated by both of the Raman laser beams. The reason for this is the difference Δt in the times taken for the acoustic waves in the AOMs to travel from the transducers across each Raman beam. This results in one beam switching on and off more quickly than the other. The length of time for which the ion is addressed by both light fields is thus reduced by Δt .

In order to set pulse lengths accurately independent of the time offset, we use a diagnostic experiment which involves performing 6 consecutive identical pulses on the carrier transition. The length of these pulses is scanned between 0 and $\sim 5 \mu\text{s}$. The population after the pulses have been applied is measured by repeating the sequence 500 times. Example data for is shown in figure 8.2 a). In order to set a $\pi/2$ rotation, we note that $6 \times \pi/2 = 3\pi$, hence $6t_{\pi/2}$ is the time of the second peak in $P(\uparrow\uparrow)$. For the data shown in figure 8.2 a), $t_{\pi/2} = 12.0/6 = 2.0 \mu\text{s}$.

This method is very sensitive to the detuning of the radiation driving the carrier

transition from resonance. If the laser is detuned from resonance, the periods of dead time between pulses results in each pulse having a different relative phase. For short pulses, the dead time $6 \mu\text{s}$ is longer than the pulse length. The effects of detuning from resonance can be seen in data presented in figure 8.2 b), where the Raman difference frequency was found by a subsequent measurement to be detuned by 15 kHz from the carrier transition. This example was used to set up the tomography experiments which are described later in the chapter.

This method was used to set the lengths of both the analysis pulses used for tomography, and the carrier pulses which were used within experimental sequences (e.g. for a spin-echo sequence).

8.3.2 Determination of experimental rotation angle.

In order to deduce the rotations used for the tomography, the data from the 6 consecutive carrier pulse scan was fitted with

$$P(\uparrow\uparrow) = B + \frac{A}{4} [1 - e^{-6\gamma t_{\text{tot}} - \gamma t_{\text{gap}}} \cos(6\Omega_{R1}(t_p - \Delta t_p))] [1 - e^{-6\gamma t_{\text{tot}} - \gamma t_{\text{gap}}} \cos(6\Omega_{R2}(t_p - \Delta t_p))] \quad (8.37)$$

where $t_{\text{tot}} = t_{\text{gap}} + t_p$ is the total time of the pulse and the gap, Ω_{R1} and Ω_{R2} are the Rabi frequencies of each ion, t_p is the programmed length of each pulse and Δt_p is the difference between the programmed length of the pulse and the time for which the ions are illuminated. γ is a phenomenological decay constant which is taken to be the same during both the pulse and the gap since the decoherence is dominated by magnetic field fluctuations for these Raman beam powers. The values of $\Delta t_p, B, A, \gamma, \Omega_{R1}$ and Ω_{R2} were allowed to float. The six pulse method allows us to determine Δt_p with $6\times$ more accuracy than can be achieved using a single carrier pulse scan. The value of Δt_p was found to be between $\simeq 0.2 \mu\text{s}$ and $0.05\mu\text{s}$ for tomography experiments performed on 6 days over a 42 day period.

8.4 Application to easily prepared states.

The tomography method described above was tested by applying it to states which could be prepared with a single or no laser pulse. The fidelity with which the states were prepared was then calculated from the density matrices obtained from the tomography experiment using

$$F = \langle \psi | \hat{\rho}_R | \psi \rangle \quad (8.38)$$

where $|\psi\rangle$ is the state which we tried to prepare. The purity, defined as

$$P = \text{Tr}\{\hat{\rho}_R^2\} \quad (8.39)$$

was also calculated, which gives an indication of the amount of decoherence which was introduced in preparing the state. In some cases the density matrix $\hat{\rho}_R$ was compared with the density matrix of a general pure product state $|\psi_p\rangle$, which can be parameterised using the expression

$$|\psi_p\rangle = R^{(1)}(\theta_1, \phi_1) \otimes R^{(1)}(\theta_2, \phi_2) |\downarrow\downarrow\rangle \quad (8.40)$$

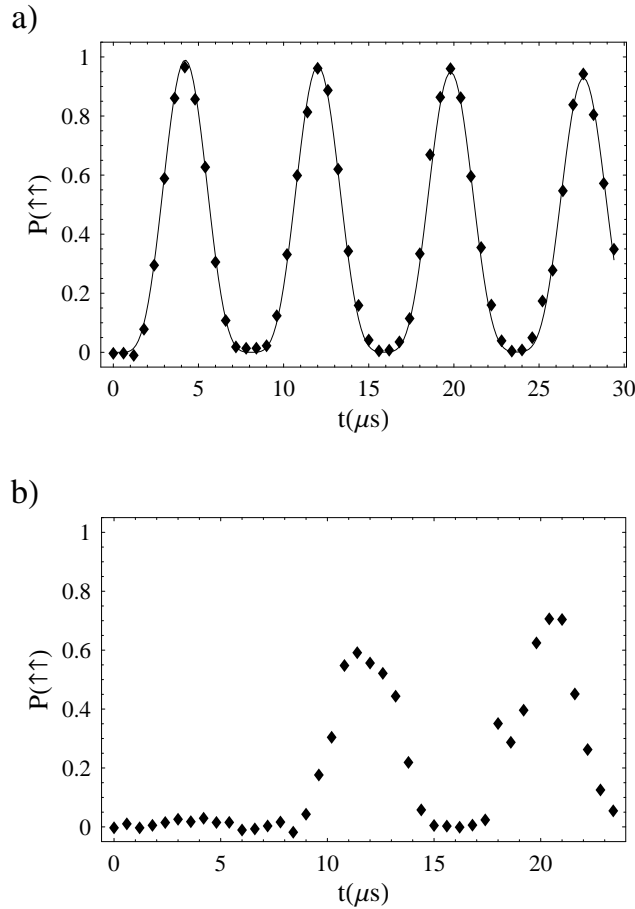


Figure 8.2: The result of six equal length pulses applied consecutively on the carrier transition. $t = 6t_p$, where t_p is the length of each pulse. a) Results from an experiment where the difference frequency of the Raman laser was exactly resonant with the carrier transition. t_p was scanned from $0 \rightarrow 4.9 \mu\text{s}$. The fitted curve is equation 8.37, with $\Delta t_p = 0.055(4) \mu\text{s}$ and $\Omega_R/2\pi = 128.3(2) \text{ kHz}$ for both ions. b) Results from an experiment performed on a different day with t_p scanned from $0 \rightarrow 3.9 \mu\text{s}$. The difference frequency of the Raman laser was 15 kHz detuned from the carrier resonance (deduced from a subsequent scan over the Raman resonance). This scan was used to set the pulse lengths from the positions of the maxima and minima as was done for the data shown in a), but it is much more difficult to analyse this data in order to extract Δt_p and Ω_R .

This was done in order to judge whether the operations which were being used to prepare the state were being performed correctly.

Prior to analysis of the states, a diagnostic six-pulse carrier scan was performed as explained in section 8.3.2. The data from this experiment is shown in figure 8.2 b). Unfortunately, it was not possible to extract useful information from this data because the magnetic field had shifted before starting the experiment. This means we must extract Ω_R and Δt_p from a single carrier pulse experiment, which increases the error on Δt_p , and hence on the rotation angles. The carrier flopping data which was used is shown in

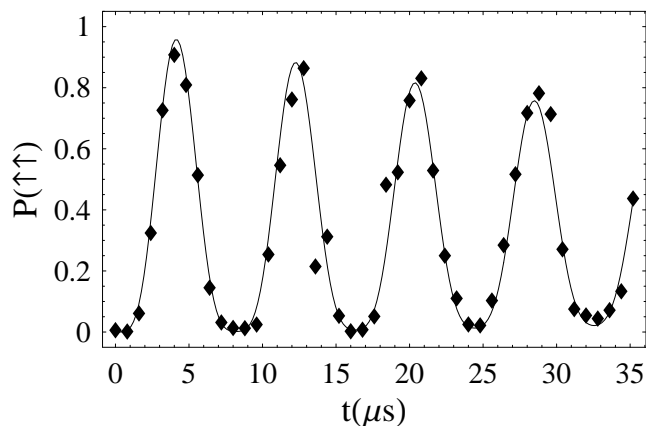


Figure 8.3: $P(\uparrow\uparrow)$ as a function of the time of pulse on the carrier transition. This data was used to determine the rotation angles used for the tomography experiments presented below. The horizontal axis gives the time duration of the pulse as programmed in to the computer. The data is fitted with the function in equation 8.37 with the factor 6 replaced by 1, which gives a Rabi frequency of $\Omega_R = 2\pi \times 123.2(6)$ kHz and a time offset for the pulse of $0.11(5)$ μs . The fit to the data allows the angles used in the tomography experiments to be determined from the times of pulses programmed in to the computer.

figure 8.3. This used a single Raman pulse with duration scanned from $0 \rightarrow 80$ μs (for times greater than 35 μs , the data is noisy). The value of the Rabi frequencies for both ions and the time offset obtained from the first 36 μs of data (shown in figure 8.3) were $\Omega_R/2\pi = 123.2(6)$ kHz and $\Delta t_p = 0.11(5)$ μs respectively. The two analysis pulses used had programmed lengths of 1.2 and 1.9 μs , hence we can deduce that the rotation angles were $\theta = 0.84(4)$ and $1.39(4)$ radians respectively.

The tomography was first applied to a state prepared by optical pumping, which should produce $|\downarrow\downarrow\rangle$. The results of the analysis pulse scans are shown in figure 8.4. The lack of oscillation as the phase is scanned indicates that all the coherences in the density matrix are zero. The density matrix obtained using the maximum likelihood method is shown in figure 8.5. The fidelity of producing the state $|\downarrow\downarrow\rangle$ is found to be 1, as is the purity of the state.

The tomography method was next used to analyse the state obtained after applying a π pulse on the carrier transition to the state $|\downarrow\downarrow\rangle$. This should produce $|\uparrow\uparrow\rangle$. The phase scans for the two different values of θ are shown in figure 8.6. The density matrix obtained using the maximum likelihood method is shown in figure 8.7. The fidelity with which the state $|\uparrow\uparrow\rangle$ was produced is 0.964. The purity of the state is 0.956. The overlap with the closest product state $|\psi_p\rangle$ to this density matrix is 0.97. $|\psi_p\rangle$ is the state produced by the rotations $\theta_1 = 1.05\pi$ and $\theta_2 = 1.00\pi$ radians. The difference between these two values of θ is not detectable by our tomography method, so must have been introduced by the maximum likelihood method. This would correspond to the difference in the populations $|x - y| = 0.024$. The values of ϕ_1 and ϕ_2 in equation 8.40 are badly determined as the coherence elements of the density matrix are close to zero.

The tomography method was also used to analyse the state obtained by applying a $\pi/2$ pulse on the carrier transition to a pair of ions starting in $|\downarrow\downarrow\rangle$. The state produced should be $|\phi_{\pi/2}\rangle = |\downarrow\downarrow\rangle + i|\downarrow\uparrow\rangle + i|\uparrow\downarrow\rangle - |\uparrow\uparrow\rangle$. The phase scans for the two different values of θ used

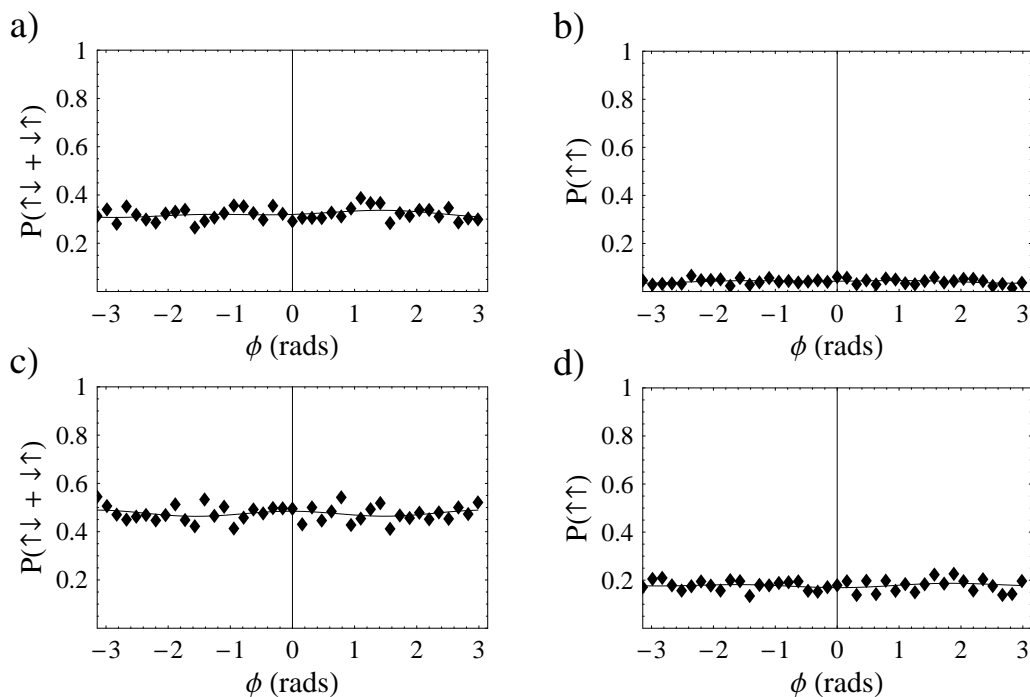


Figure 8.4: Phase scans used for state tomography of the spin state $|\downarrow\downarrow\rangle$ prepared by optical pumping. Plots a) and b) are the populations for a carrier pulse which had a programmed length of $1.2\ \mu\text{s}$, and c) and d) are the populations for a carrier pulse which had a programmed length of $1.9\ \mu\text{s}$. These correspond to rotations of $\theta = 0.84(4)$ (a) and b)) and $\theta = 1.39(4)$ radians (c) and d)). Each plotted point is the result of 500 repeated experimental sequences. The fraction of times the ions fluoresced at the end of the sequence was converted into spin state probabilities $P(\uparrow\uparrow)$ and $P(\uparrow\downarrow + \downarrow\uparrow)$ using equation 2.17. The data is fitted with equations 8.15 and 8.16, from which the density matrix was calculated.

for the tomography pulses are shown in figure 8.8. The density matrix ρ_R obtained using the maximum likelihood method is shown in figure 8.9. The fidelity with which the state $|\psi_{\pi/2}\rangle$ was prepared is 0.88. The purity of the state is 0.80. The pure product state closest to this density matrix is given by equation 8.40 with $\theta_1 = 0.455\pi$, $\phi_1 = 0.022\pi$, $\theta_2 = 0.545\pi$ and $\phi_2 = 0.022\pi$ radians. This state is produced with fidelity 0.89. As the tomography method fails to distinguish the two ions, the difference in values of θ can again be attributed to the use of the maximum likelihood method on the experimentally determined density matrix.

Finally, the tomography method was used to analyse the state obtained after a spin-echo sequence of pulses on the carrier transition, with the ions initialised in $|\downarrow\downarrow\rangle$. The state produced should be $|\downarrow\downarrow\rangle$. The phase scans for the two different values of θ used for the tomography pulses are shown in figure 8.10. The density matrix ρ_R obtained using the maximum likelihood method is shown in figure 8.11. The fidelity with which the state $|\downarrow\downarrow\rangle$ was prepared is 0.90. The purity of the density matrix is 0.91. The closest product state to ρ_R has rotations $\theta_1 = 1.89\pi$, $\phi_1 = 0.865\pi$, $\theta_2 = 1.89\pi$ and $\phi_2 = 0.864\pi$ radians. This state is produced with fidelity 0.95. This indicates that pulse length error may have

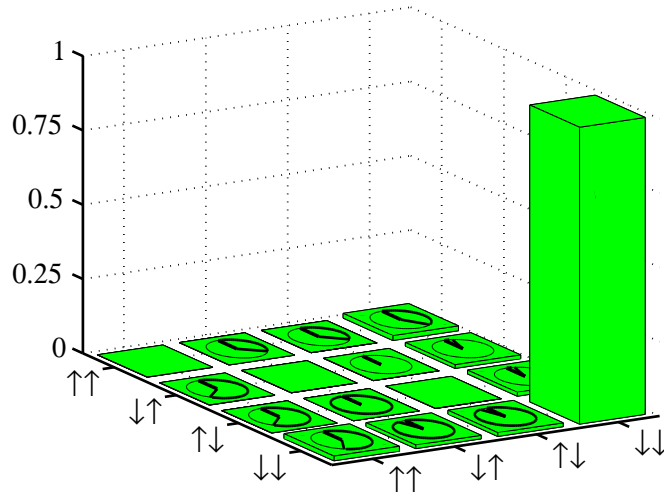


Figure 8.5: The density matrix obtained by tomography for the case of two ions prepared in $|\downarrow\downarrow\rangle$ by optical pumping. The height of each bar gives the absolute value of the density matrix element, the pie diagrams on the off-diagonal elements indicate their phase. The fidelity with which the intended state was produced is 1. The purity of this density matrix is also 1.

caused a 5% reduction in the fidelity owing to under rotation (note that if both qubits had rotations of 2.11π radians this would give the same density matrix). Using the results of the fit to the carrier flopping scan, we can deduce that the set pulse times of $1.9 \mu\text{s}$, $4.1 \mu\text{s}$ and $1.9 \mu\text{s}$ would produce a total rotation of 1.87π radians. Thus we gather that the spin-echo sequence was incorrectly set up.

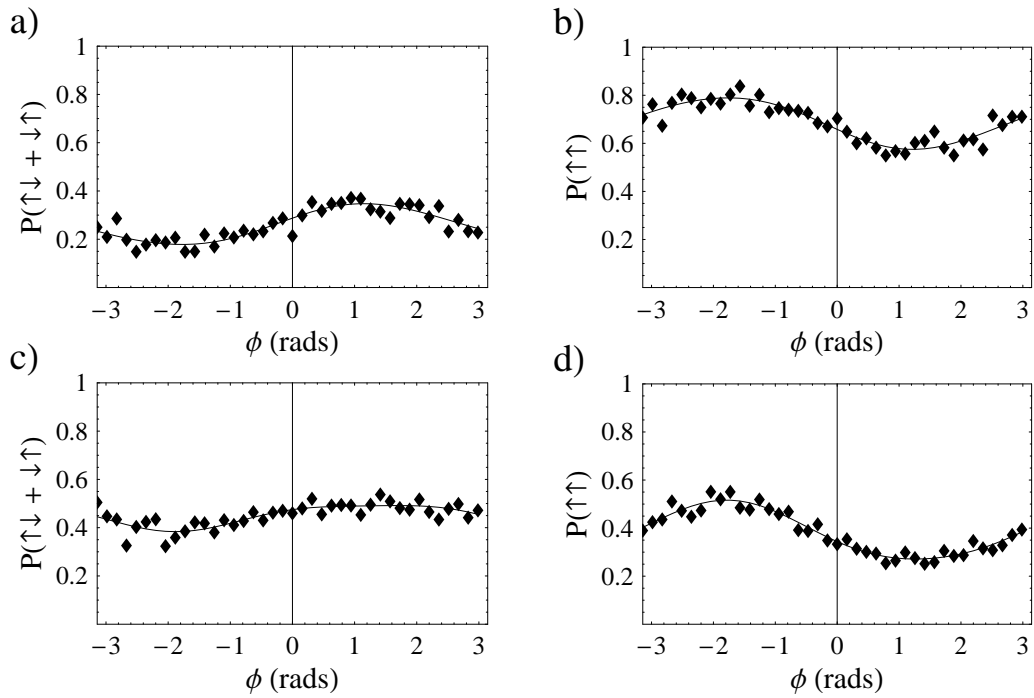


Figure 8.6: Phase scans used for state tomography of the spin state produced by applying a π pulse to the state $|\downarrow\downarrow\rangle$. Plots a) and b) were obtained with $\theta = 0.84(4)$ radians and plots c) and d) with $\theta = 1.39(4)$ radians. The data is fitted with equations 8.15 and 8.16, from which density matrix was calculated.

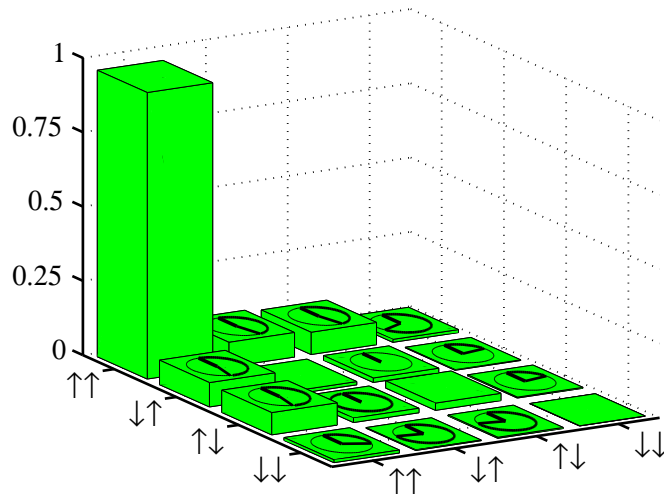


Figure 8.7: The density matrix obtained from state tomography for the state of the ion after a π pulse on the carrier transition is applied to the state $|\downarrow\downarrow\rangle$. A perfect π pulse would produce the state $|\uparrow\uparrow\rangle$. The fidelity with which this state was produced is 0.963. The purity of this density matrix is 0.95.

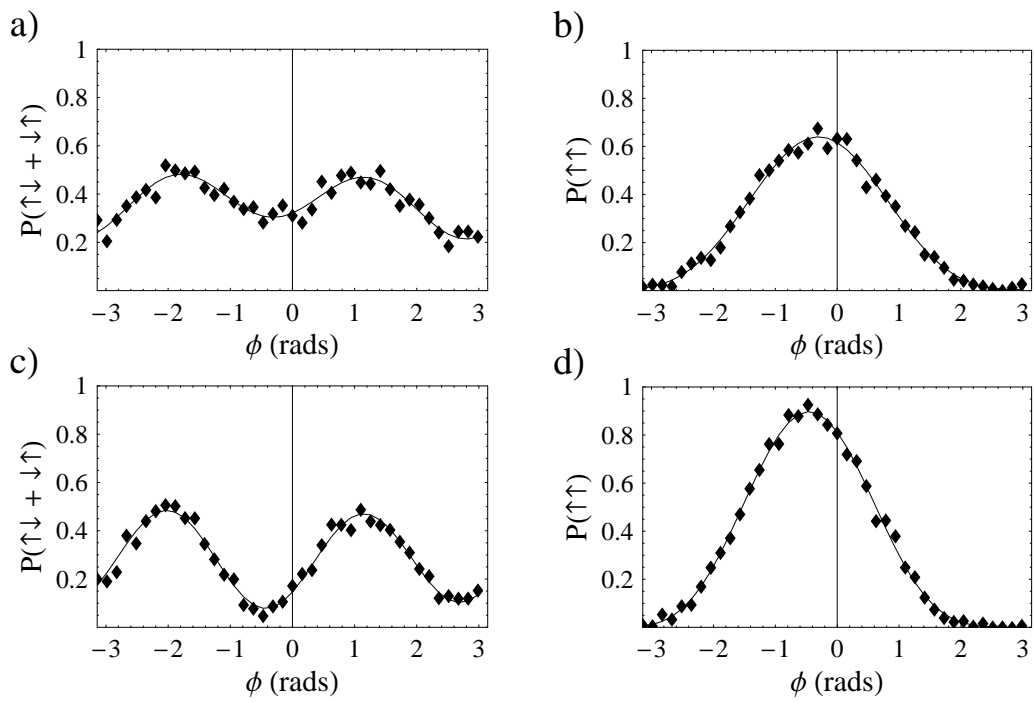


Figure 8.8: Phase scans used for state tomography of the spin state produced by applying a $\pi/2$ pulse to the state $|\downarrow\downarrow\rangle$. Plots a) and b) were obtained with $\theta = 0.84(4)$ radians and plots c) and d) with $\theta = 1.39(4)$ radians. The data is fitted with equations 8.15 and 8.16, from which density matrix was calculated.

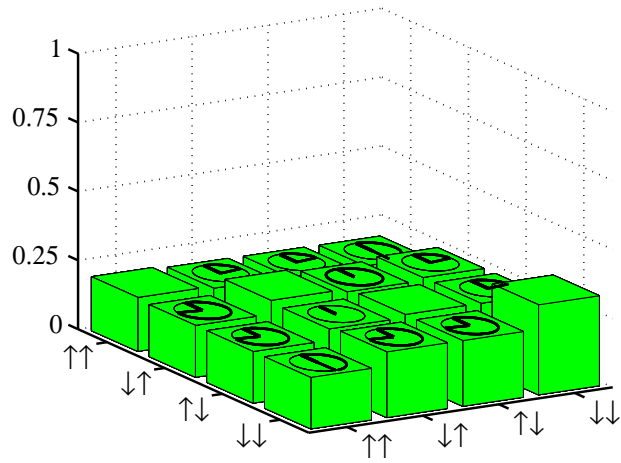


Figure 8.9: The density matrix obtained from state tomography for the state of the ion after a $\pi/2$ pulse on the carrier transition. A perfect $\pi/2$ pulse would produce the state $|\downarrow\downarrow\rangle + i|\downarrow\uparrow\rangle + i|\uparrow\downarrow\rangle - |\uparrow\uparrow\rangle$. The fidelity with which this state was produced is 0.88. The purity of this density matrix is 0.80. The pure product state closest to this density matrix is given by equation 8.40 with $\theta_1 = 0.466$, $\phi_1 = 0.02$, $\theta_2 = 0.544$ and $\phi_2 = 1.02 \pi$ radians. This is produced with fidelity 0.89.

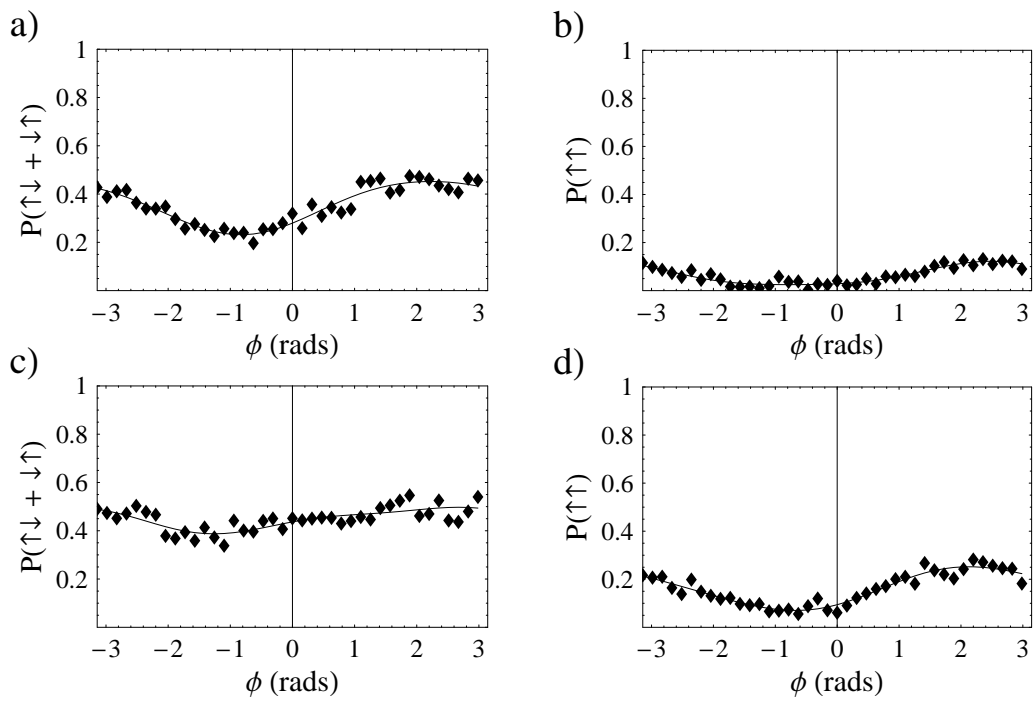


Figure 8.10: Phase scans used for state tomography of the spin state after a spin-echo sequence applied to the state $|\downarrow\downarrow\rangle$. Plots a) and b) were obtained with $\theta = 0.84(4)$ radians and plots c) and d) with $\theta = 1.39(4)$ radians. The data is fitted with equations 8.15 and 8.16, from which density matrix was calculated.

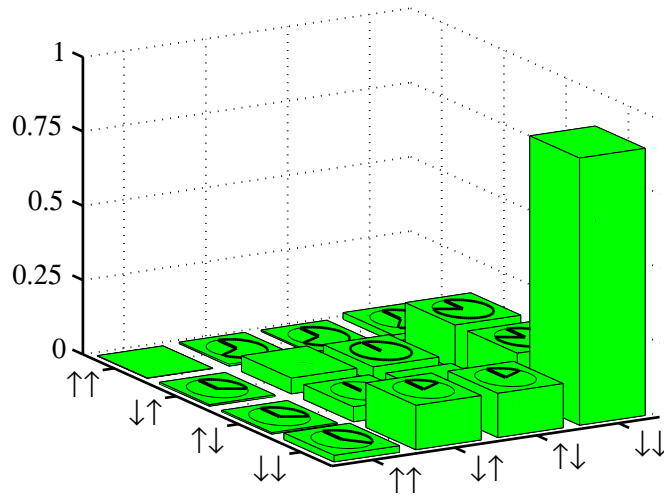


Figure 8.11: The density matrix obtained from state tomography for the state of the ion after a spin-echo sequence. A perfect spin-echo sequence would produce the state $|\downarrow\downarrow\rangle$. The fidelity with which this state was produced is 0.90. The purity of this density matrix is 0.91. The pure product state closest to this density matrix is given by equation 8.40 with $\theta_1 = 1.89$, $\phi_1 = 0.865$, $\theta_2 = 1.89$ and $\phi_2 = 0.864 \pi$ radians. The values of ϕ produced by fitting the pure state to the density matrix are likely to be badly determined as they depend on the values of the coherences, which in this case are small. The fidelity with which this state is produced is 0.95.

Chapter 9

Entanglement of spin qubits.

Single qubit and two-qubit logic gates form a universal set for quantum computation. Two-qubit gates generate entanglement of qubits, which is the fundamental resource on which all quantum algorithms are based. The implementation of a two-qubit gate is therefore of crucial importance for quantum computation. Entangled states are also of fundamental importance in quantum mechanics owing to their non-local properties [83, 84].

This chapter describes the implementation of a universal π -phase gate between two $^{40}\text{Ca}^+$ spin qubits, using the method devised and first demonstrated by Leibfried et. al. with Be^+ ions [23]. The basic idea of this phase gate was first proposed by Milburn and is a specific case of the more general formalism described by Milburn et. al. [85], Sørensen and Mølmer [86] and Wang et. al. [87]. The gate makes use of the optical dipole force which was described in chapter 7. It is implemented within a sequence of single-qubit rotations which result in the creation of a maximally entangled state. The density matrix of the entangled state is reconstructed using the partial tomography method described in chapter 8, from which we deduce the entanglement of formation of our qubits, and the fidelity with which the desired state is produced.

The π -phase gate applies the transformation

$$\hat{G} = \begin{pmatrix} 1 & 0 & 0 & 0 \\ 0 & i & 0 & 0 \\ 0 & 0 & i & 0 \\ 0 & 0 & 0 & 1 \end{pmatrix} \quad (9.1)$$

to the two qubits. This gate is equivalent to a universal controlled phase gate plus a single qubit $\pi/2$ rotation applied to each qubit.

The gate uses the state-dependent optical dipole force introduced in chapter 7, but now applied to a pair of ions. By setting the ion separation to an integer number of periods of the travelling standing wave, the same force is applied to the each ion if their spins are aligned. This means that only the COM mode of motion will be excited. If the spins are anti aligned, the forces are opposite, and both the stretch and COM modes will be excited. The excitation of the stretch mode of motion is resonantly enhanced by tuning the force frequency ω close to the stretch mode frequency ω_s .

The oscillating force on the stretch mode displaces the motional state around a circular path in phase space, as illustrated in figure 9.1. The displaced states involved gain a phase $\Phi_s(t)$. After time $2\pi/\delta$, where $\delta = \omega - \omega_s$, the motional wavepacket of the mode returns to its initial position in phase space, and the spin states are disentangled from the motional

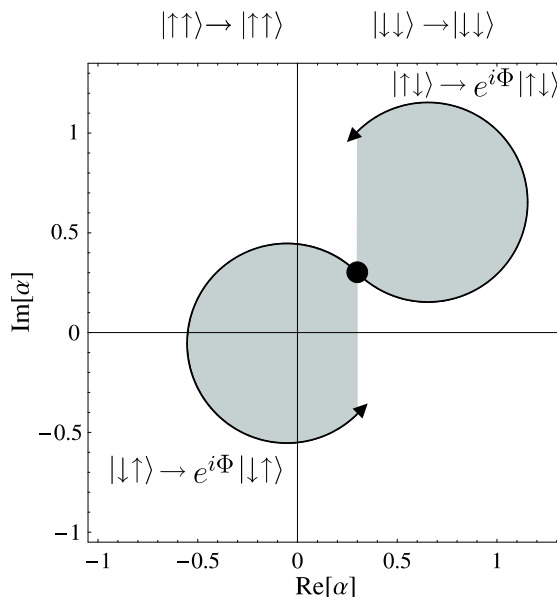


Figure 9.1: The displacement of the stretch mode in phase space under the influence of an oscillating force. The motional state components associated with the spin states $|\uparrow\downarrow\rangle$ and $|\downarrow\uparrow\rangle$ are driven by two forces of the same magnitude which are π out of phase. Both states acquire the same phase Φ because they enclose the same area in phase space and the sense of the trajectories are equal. The motional state components associated with $|\uparrow\uparrow\rangle$ and $|\downarrow\downarrow\rangle$ are not displaced by the force, hence these two states acquire no phase. The figure was copied from Leibfried et. al. [23]

state. The two spin states for which the motional mode was excited acquire a phase

$$\Phi_s(2\pi/\delta) = \frac{\pi}{2} \left(\frac{F_s}{\delta} \right)^2 \quad (9.2)$$

where $\hbar F_s \delta k$ is the force on the stretch mode. For $F_s/\delta = \sqrt{2m+1}$, where m is an integer, the phase acquired by the states $|\uparrow\downarrow\rangle$ and $|\downarrow\uparrow\rangle$ is $(2m+1)\pi/2$, hence the required operation \hat{G} is performed.

The Leibfried method [23] of implementing a two-qubit logic gate has several advantages over the original Cirac-Zoller [15] gate proposal. If the two modes of the ions are in the Lamb-Dicke regime, the motional wavepacket of the stretch mode will return to its original position in phase space after time $2\pi/\delta$ regardless of its initial position, orientation or shape. This makes the gate insensitive to the initial temperature of the ion (so long as the ions are in the Lamb-Dicke regime throughout the gate). Individual addressing of the ions with light is not required, which relaxes a stringent technical requirement of the Cirac-Zoller gate. Both of these advantages are shared by the Mølmer-Sørensen gate design [34, 24], which uses driving of both the red and blue sidebands of a spin flip transition in order to provide a state-dependent force similar to the one described here. In addition, the Leibfried gate has the advantage that the phase of the qubit after the gate is independent of the optical phase of the light producing the gate operation. This is not the case for the Mølmer-Sørensen proposal.

9.1 Implementation.

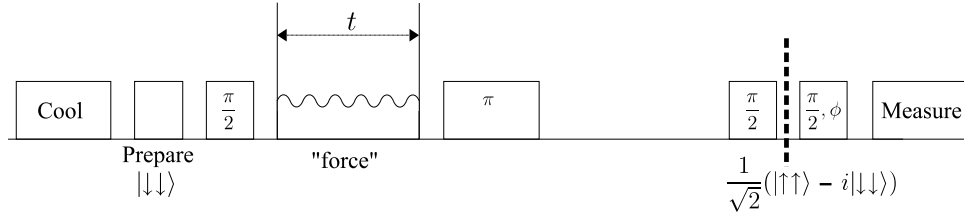


Figure 9.2: Pulse sequences used to create the maximally entangled state. The phase gate is applied in the first half of a spin echo sequence of carrier pulses. The carrier pulses are driven by the Raman laser. For $F_s/\delta = 1$ and $t = 2\pi/\delta$, the result is to produce the Bell state $|\psi\rangle = (|\uparrow\uparrow\rangle - i|\downarrow\downarrow\rangle)/\sqrt{2}$ at the time indicated by the dashed line.

Since the gate operation does not change the spin state populations of the ions, we cannot observe its effect directly by a spin-state measurement in the standard basis. To observe the accumulated phase, we apply the gate in the first gap of a spin-echo sequence as shown in figure 9.2. The initial $\pi/2$ pulse creates an equal superposition of $|\uparrow\uparrow\rangle$, $|\uparrow\downarrow\rangle$, $|\downarrow\uparrow\rangle$ and $|\downarrow\downarrow\rangle$. The gate is then applied, which in the ideal case creates the state

$$|\psi\rangle = \frac{1}{2} [|\uparrow\uparrow\rangle + i|\uparrow\downarrow\rangle + i|\downarrow\uparrow\rangle + |\downarrow\downarrow\rangle] \quad . \quad (9.3)$$

The final two pulses in the spin-echo sequence apply the rotation $R_2(3\pi/4, 0)$, which for a perfect experiment results in formation of the state

$$|\Psi\rangle = \frac{1}{\sqrt{2}} (|\uparrow\uparrow\rangle - i|\downarrow\downarrow\rangle) \quad . \quad (9.4)$$

This is a maximally entangled state.

In the experimental implementation of the gate, the spin state of the ions is given by the density matrix $\hat{\rho}$. In order to deduce how closely the state we create resembles $|\Psi\rangle$, we calculate the fidelity

$$F = \langle \Psi | \hat{\rho} | \Psi \rangle \quad . \quad (9.5)$$

Since $|\Psi\rangle$ has a simple form, this reduces to

$$F = \frac{1}{2} [P(\uparrow\uparrow) + P(\downarrow\downarrow) + 2|r| \cos(\theta_r)] \quad (9.6)$$

where $P(\uparrow\uparrow)$, $P(\downarrow\downarrow)$ are diagonal elements of the density matrix and $|r|$ and θ_r are the magnitude and argument of the coherence between $|\uparrow\uparrow\rangle$ and $|\downarrow\downarrow\rangle$.

9.2 State-dependent force on two ions.

The light field used to implement the phase gate is exactly the same as that used in chapter 7 to produce Schrödinger's cat states.

The generalisation of the state-dependent force terms of the Hamiltonian 3.17 to two ions is

$$\hat{H}_{\text{force}} = \hbar \sum_{l=1,2} \sum_{m_l=\uparrow,\downarrow} [-\eta\Omega_R^{m_l} \sin(\omega t - \phi_{m_l})z_l] |m_l\rangle \langle m_l| \quad (9.7)$$

where l is the number of the ion under consideration, m_l is the spin state of this ion, z_l is its position, and $\eta\Omega_R^{m_l}$ is the Rabi frequency of transitions between adjacent motional states for the spin state of ion l . To simplify this expression, we make the substitutions $z_1 = z_c - d/2 - z_s$ and $z_2 = z_c + d/2 + z_s$, where z_c is the position of the centre of mass, d is the equilibrium separation and z_s is the excursion from equilibrium of the separation of the ions. We can drop the terms which are associated with the equilibrium separation of the ions since they will only contribute to the global phase of the ions. If the intensities of the light fields are the same at each ion and the force on the spin state $|\uparrow\rangle$ is equal in magnitude to that on the state $|\downarrow\rangle$, the Hamiltonian simplifies to

$$\begin{aligned} \hat{H}_{\text{force}} &= 2\Omega_R [\sin(\omega t) |\uparrow\uparrow\rangle \langle\uparrow\uparrow| + \sin(\omega t + \Delta\phi) |\downarrow\downarrow\rangle \langle\downarrow\downarrow|] z_c \\ &+ 2\Omega_R \cos\left(\frac{\Delta\phi}{2}\right) \sin\left(\omega t + \frac{\Delta\phi}{2}\right) [|\uparrow\downarrow\rangle \langle\uparrow\downarrow| + |\downarrow\uparrow\rangle \langle\downarrow\uparrow|] z_c \\ &+ 2\Omega_R \sin\left(\frac{\Delta\phi}{2}\right) \cos\left(\omega t + \frac{\Delta\phi}{2}\right) [|\uparrow\downarrow\rangle \langle\uparrow\downarrow| - |\downarrow\uparrow\rangle \langle\downarrow\uparrow|] z_s \end{aligned} \quad (9.8)$$

where $\Omega_R = \Omega_R^{m_l}$ and $\Delta\phi$ is the phase difference between the force on the \uparrow and \downarrow spin state. The terms on the top line of this Hamiltonian produces an oscillating force on the COM mode for two ions in the spin states $|\uparrow\uparrow\rangle$ and $|\downarrow\downarrow\rangle$. The second line produces an oscillating force on the COM mode for spin states $|\uparrow\downarrow\rangle$ and $|\downarrow\uparrow\rangle$, and the third produces an oscillating force on the stretch mode for these spin states.

In order to implement the two-ion gate, we set the difference frequency of the Raman beams close to resonance with the stretch mode of the two ions. Since the stretch and COM mode are independent, we can treat the dynamics of each separately. First consider the stretch mode. Moving into the interaction picture with respect to its motional states and making the rotating wave approximation with respect to the motional frequencies, the Hamiltonian is

$$\hat{H}_{\text{force}} = 2\eta_s\Omega_R \sin\left(\frac{\Delta\phi}{2}\right) \left[\hat{b} e^{i\delta t + i\frac{\Delta\phi}{2}} + \hat{b}^\dagger e^{-i\delta t - i\frac{\Delta\phi}{2}} \right] (|\uparrow\downarrow\rangle \langle\uparrow\downarrow| - |\downarrow\uparrow\rangle \langle\downarrow\uparrow|) \quad (9.9)$$

where \hat{b} (\hat{b}^\dagger) is the annihilation (creation) operator for the stretch mode of motion, and $\delta = \omega - \omega_s$ is the detuning of the difference frequency of the Raman laser beams from the stretch mode vibrational frequency ω_s . The response of the stretch mode to this excitation is precisely as in chapter 7 section 7.2.1 (see figure 9.1).

9.2.1 Stretch mode excitation

The Hamiltonian in equation 9.9 gives an equal and opposite force on the stretch mode of motion for the spin states $|\uparrow\downarrow\rangle$ and $|\downarrow\uparrow\rangle$. The magnitude of this force is $F_s/\hbar\delta k$, where

$$F_s = 2\eta_s\Omega_R \sin\left(\frac{\Delta\phi}{2}\right) \quad (9.10)$$

A typical value for the centre of mass mode frequency is $\omega_c \simeq 2\pi \times 500$ kHz, hence the Lamb-Dicke parameter for the stretch mode of motion is $\eta_s = 0.136$. In all the experiments

$\alpha_0 = F_s/\delta$ was less than 3. This means that the treatment of the dynamics in the Lamb-Dicke limit is valid. The motion of the stretch mode under the influence of the Hamiltonian in equation 9.9 is thus to push the motional wavepacket around a circle in phase space with negligible distortion of its shape. The trajectory can be found from equation 7.12 to be

$$\alpha(t) = (-1)^u \frac{F_s}{\delta} e^{-i\frac{\delta t}{2}} \sin\left(\frac{\delta t}{2}\right) \quad (9.11)$$

where $u = 0$ ($u = 1$) for the state $|\downarrow\uparrow\rangle$ ($|\uparrow\downarrow\rangle$). The phase acquired is given by the area of the circle, $\Phi_s(t) = \Phi_{\uparrow\downarrow} = \Phi_{\downarrow\uparrow}$ where

$$\Phi_s(t) = \frac{1}{4} \left(\frac{F_s}{\delta}\right)^2 (\sin(\delta t) - \delta t) \quad (9.12)$$

9.2.2 Off-resonant COM mode excitation

Now consider the centre of mass terms in the Hamiltonian (equation 9.8). Since the radiation is far from resonance with this mode, we can not make the rotating wave approximation. In this case we find that $\alpha_c(t)$ is

$$\begin{aligned} \alpha_c(t) &= -\frac{\chi F_c}{\delta_c} e^{-i\phi_m} e^{-i\frac{\delta t}{2}} \sin\left(\frac{\delta t}{2}\right) \\ &+ \frac{\chi F_c}{g} e^{i\phi_m} e^{-i\frac{gt}{2}} \sin\left(\frac{gt}{2}\right) \end{aligned} \quad (9.13)$$

where $g = \delta_c + 2\omega_z$, $F_c = \eta_c \Omega_R$ is the force when the spin state of the ions is aligned and χ is a co-efficient which depends on the relative spin orientation of the two ions. From equation 9.8, $\chi = 1$ when the states are aligned and $\chi = \cos\left(\frac{\Delta\phi}{2}\right)$ when the states are anti-aligned.

In order to get an idea of the effects which occur due to COM mode excitation, consider the change in population of a spin state due to the displacement of the centre of mass mode. If the displacement of the centre of mass mode is at its maximum, the interference between the spin states will be at a minimum, due to the reduced overlap of the motional states. The fractional loss in interference is at most given by $e^{-2|\alpha_c(t)|^2}$. Typical values of experimental parameters for our experiments are $\omega_z = 2\pi \times 500$ kHz, $\delta = 2\pi \times 20$ kHz, $F_s = 2\pi \times 20$ kHz, hence $F_c = \eta_c F_s / \eta_s = 2\pi \times 26$ kHz and $\delta_c = 2\pi \times 386$ kHz. The minimum value of $e^{-2|\alpha_c(t)|^2}$ for these parameters is 0.99. This effect would be hard to notice in our experiments, where the shot noise is ~ 0.02 .

The phase acquired by displacement of the COM mode wavepacket can be found using equation 7.14 in chapter 7 to be

$$\Phi_c(t) = \frac{\chi^2 F_c^2}{2g\delta_c} \left[\omega_z t - \frac{\omega}{\delta_c} \sin(\delta_c t) + \frac{\omega}{g} \sin(gt) - \frac{\omega_z}{2\omega} \sin(2\omega t) \right] \quad (9.14)$$

For times greater than $2\pi/\delta_c$, the linear term in t dominates. In this regime, the difference in phases acquired by the anti-aligned spin states relative to the aligned spin states due to the centre of mass displacement is

$$\Delta\Phi_c(t) = -\frac{F_c^2 \omega_z t}{2g\delta_c} \sin^2\left(\frac{\Delta\phi}{2}\right) \quad (9.15)$$

Using the same values of ω_z , δ and F_s as previously and $\Delta\phi = \pi/2$, the phase difference acquired in a time $2\pi/\delta$ is $\Delta\Phi_c(2\pi/\delta) = 0.05$, which is 3% of the phase acquired by the anti-aligned states due to the stretch mode displacement.

In addition to the state-dependent force, the spin states of each ion will be light shifted due to interaction with the $\pi-\sigma^+$ and $\pi-\sigma^-$ components of the standing wave as described in section 7.3.3 of chapter 7. The size of this light shift is given in equation 7.47.

9.3 Experimental diagnostics.

Experimental requirements for implementing the gate described above are that the ion separation is an integer number of wavelengths, and that the power and detuning of the optical field producing the state-dependent force are set such that the phase acquired by the spin states $|\uparrow\downarrow\rangle$ and $|\downarrow\uparrow\rangle$ relative to $|\uparrow\uparrow\rangle$ and $|\downarrow\downarrow\rangle$ is $\pi/2$. In order to meet these requirements, a series of preparatory experiments are performed.

Throughout this chapter the polarisation of the beams is assumed to have been arranged such that any light shifts which arise from a single Raman beam cancel out. Prior to attempting entanglement experiments this is checked using the method described in section 7.3.3 of chapter 7.

9.3.1 Setting the correct ion separation.

In order that the state-dependent force does not excite the stretch mode for the states $|\uparrow\uparrow\rangle$ and $|\downarrow\downarrow\rangle$, the ions must be an integer number of wavelengths of the travelling standing wave apart. This also maximises the force exciting the stretch mode for the states $|\uparrow\downarrow\rangle$ and $|\downarrow\uparrow\rangle$. For a given trap frequency ω_z , the separation of the two ions is

$$d = \left(\frac{q^2}{2\pi\epsilon_0 M\omega_z^2} \right)^{\frac{1}{3}} \quad (9.16)$$

where M is the mass of a single ion. The Raman beam angles were measured by tracing the beam paths outside the trap. The angle between the Raman beams was found to be $59.8^\circ \pm 1^\circ$. The wavelength of the travelling standing wave is thus between 404 and 392 nm. A typical trap frequency is $2\pi \times 500$ kHz, hence for an angle between the beams of 59.8° , the separation between the ions corresponds to 22.3(4) wavelengths of the standing wave.

In order to set the ion separation to an integer number of wavelengths more precisely, we use the pulse sequence shown in figure 9.3. The ions are first cooled and prepared in the spin state $|\downarrow\downarrow\rangle$. A force resonant with one of the vibrational modes is then pulsed on for a time t_r . A probe pulse on a sideband of the same mode is then applied, and the probability of fluorescence is recorded.

The ratio of the fraction of times the ion fluoresced after probe pulses on the red and blue sideband is $R = P_f(\text{red})/P_f(\text{blue})$. Though this can be converted into a mean vibrational excitation, the application of the force to a thermal mixture puts the ion into a mixture of displaced Fock states [81]. This makes it non-trivial to calculate the mean vibrational quantum number from the ratio of sideband heights. For the purposes of deducing the correct ion separation, we do not attempt to quantify the mean vibrational quantum number. Instead, we simply observe the change in R as a function of the force duration. This gives an indication of how much effect the force is having. The separation

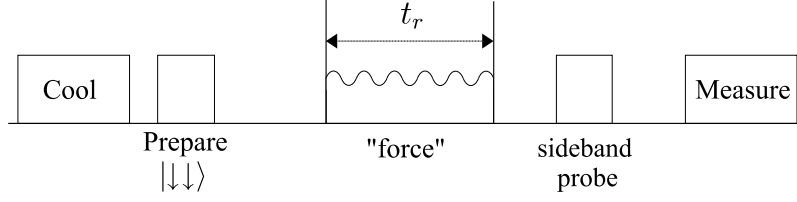


Figure 9.3: The pulse sequence used in the experiments which were performed in order to set the ion separation to an integer number of periods of the travelling standing wave. The ions are first cooled to the ground state of motion, then prepared in the state $|\downarrow\downarrow\rangle$ using optical pumping. A force resonant with one of the vibrational modes is then pulsed on for a time t_r . A sideband probe pulse is then applied to the same mode, and the state the ions is measured. Out of 500 repeats of this sequence, we record the fraction of times P_f that at least one ion fluoresced. This is repeated for probe pulses on both the red and blue sidebands. The ratio $R = P_f(\text{red})/P_f(\text{blue})$ gives an indication of the mode temperature.

of the two ions is adjusted by changing the d.c. endcap voltages. Figure 9.4 shows the change ΔR in the ratio of the sideband heights as a function of the trap frequency, for force durations t_r between 5 and 20 μs .

If the ions are an integer number of wavelengths of the travelling standing wave apart, the stretch mode will not be excited and the COM mode will be maximally excited. If the ions are an odd multiple of half a wavelength apart, the converse will be true. It can be seen from figure 9.4 that the trap frequency at which the stretch mode is not excited is 497(2) kHz. The ion separation at this trap frequency is 8.93 μm . If the number of periods of the standing wave between the ions is 22, we can deduce an angle between the two beams of 58.5(2) $^\circ$. If the number of periods of the standing wave between the ions is 23, the angle between the two beams is 61.5(2) $^\circ$. Both of these values are (just) consistent with the beam angle measurement. This means that we have an uncertainty in the Lamb-Dicke parameter of $\sim 5\%$.

9.3.2 Extracting the fidelity from experimental data.

We now turn to the diagnosis of the entangling experiment itself. At the end of the experimental sequence, we have a density matrix $\hat{\rho}$. In order to experimentally determine the fidelity of the density matrix with the state $|\Psi\rangle$ (equation 9.4) we must extract the populations $P(\uparrow\uparrow)$, $P(\uparrow\downarrow + \downarrow\uparrow)$ and the coherence matrix element r , see equation 9.6. The former are obtained by a simple measurement of the spin states of the ions. In order to determine r , we can use two different methods.

The first method is to measure the population of the spin states as a function of the duration of the oscillating force. The sequence used is that shown in figure 9.2, but without the final $(\pi/2, \phi)$ analysis pulse. If the force is close to resonant with the stretch mode the stretch motional states will be displaced around the trajectory $\alpha(t)$ (equation 9.11), while the COM mode will be displaced around a trajectory for which $|\alpha_c(t)| \ll |\alpha(t)|$. Since $\max(|\alpha_c(t)|)$ is small, we make the approximation that the centre of mass motional states do not change. In the absence of decoherence effects, the state of the ion after the application of the force is

$$|\psi_w\rangle = \frac{1}{2} \left[e^{2i\Delta\pi t} |\uparrow\uparrow\rangle |0\rangle + e^{i\Delta\pi t} e^{i\Phi(t)} (|\uparrow\downarrow\rangle |\alpha(t)\rangle + |\uparrow\downarrow\rangle |-\alpha(t)\rangle) + |\downarrow\downarrow\rangle |0\rangle \right] \quad (9.17)$$

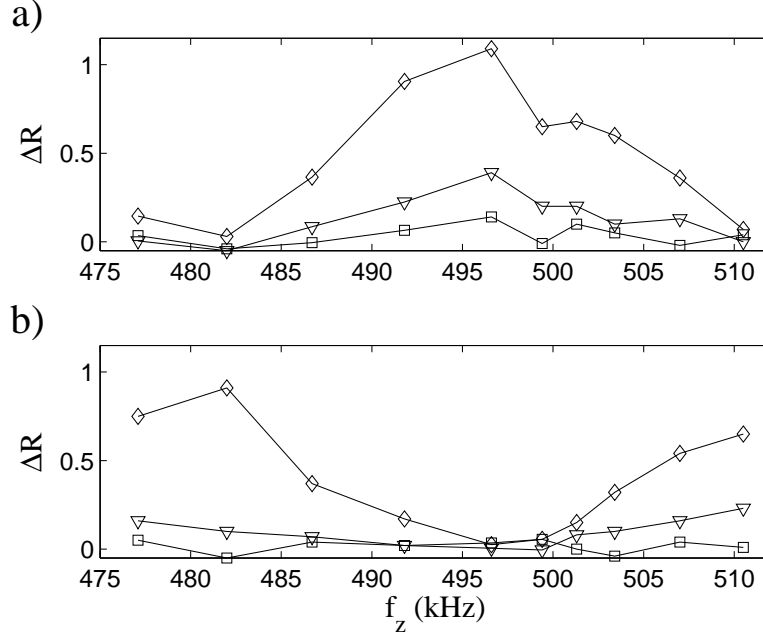


Figure 9.4: Experimentally determined values of the change in $R = P_f(\text{red})/P_f(\text{blue})$ after the state dependent force was applied to a vibrational mode for time t_r . The change ΔR is plotted as a function of the COM trap frequency for a) the COM mode and b) the stretch mode. The symbols \square , ∇ , \diamond indicate $t_r = 5, 10, 20 \mu\text{s}$.

where $\Phi(t) = \Phi_s(t) - \Delta\Phi_c(t)$ is the relative phase acquired as the motional states are displaced in phase space (given by equations 9.12 and 9.15) and Δ_π is the light shift due to off-resonant driving of the carrier transition.

We can model the evolution of the density matrix using a simple model of decoherence, which assumes that the coherences of the density matrix decay exponentially during the gate. The model assumes that each ion is affected independently by decoherence, hence the single qubit coherences decay at $e^{-\Gamma t}$ and the two-qubit coherences at $e^{-2\Gamma t}$.

The populations of the spin states at the end of the spin echo sequence are then

$$P(\uparrow\uparrow) = \frac{1}{4} + \frac{1}{8} e^{-2\Gamma t} \left[\cos(2\Delta_\pi t) + e^{-2|\alpha(t)|^2} \right] - \frac{1}{2} e^{-\Gamma t} e^{-\frac{|\alpha(t)|^2}{2}} \cos(\Phi(t)) \cos(\Delta_\pi t) \quad (9.18)$$

$$P(\uparrow\downarrow + \downarrow\uparrow) = \frac{1}{2} - \frac{1}{4} e^{-2\Gamma t} \left[\cos(2\Delta_\pi t) + e^{-2|\alpha(t)|^2} \right] \quad (9.19)$$

Using the same model for the evolution of the density matrix, we also obtain

$$r = \frac{1}{8} e^{-2\Gamma t} [\cos(2\Delta_\pi t) - 1] + \frac{i}{2} e^{-\Gamma t} e^{-|\alpha(t)|^2} \cos(\Delta_\pi t) \sin(\Phi(t)) \quad (9.20)$$

In order to obtain the fidelity, we first fit the experimentally obtained populations from the scan of the force duration using equations 9.18 and 9.19. The floated parameters are Γ , F_s and δ . The fit therefore gives information about all the experimental parameters. This also allows us to calculate r and thus the fidelity.

r can also be obtained by a more direct experimental method. A single carrier “analysis” pulse is applied as described in chapter 8, which performs the rotation $R_2(\theta, \phi)$. This is repeated for $-2\pi < \phi < 2\pi$, and we obtain the population after this pulse as a function of ϕ . The amplitude of the component of the oscillation in $P(\uparrow\downarrow + \downarrow\uparrow)$ which has frequency 2 is related to r by

$$A = 2 \sin^2(2\theta) |r| \cos(2\phi + \theta_r) \quad (9.21)$$

(this expression is determined from equations 8.32 and 8.33 of chapter 8, with $|r| \cos \theta_r = c_{11} - c_{22}$ and $|r| \sin \theta_r = c_{12} + c_{21}$).

In the initial attempts to create an entangled state, the phase ϕ of the analysis pulse relative to the rest of the sequence was not recorded. This means that the argument θ_r can not be obtained from the experimental data, but the magnitude $|r|$ can be. The result of this is that we cannot deduce the fidelity of producing the state $\Psi = (|\uparrow\uparrow\rangle - i|\downarrow\downarrow\rangle)/\sqrt{2}$ but can deduce the fidelity for producing the more general maximally entangled state $|\Psi_\kappa\rangle = (|\uparrow\uparrow\rangle - e^{i\kappa}|\downarrow\downarrow\rangle)/\sqrt{2}$ by maximising the fidelity with respect to the phase κ . The result is

$$F_\kappa = \frac{1}{2}(P(\uparrow\uparrow) + P(\downarrow\downarrow) + 2|r|) \quad (9.22)$$

In the absence of any information about the populations $P(\uparrow\uparrow)$ and $P(\downarrow\downarrow)$, the value of $|r|$ allows us to put a lower bound on the fidelity F_κ . We note that $|r|$ must satisfy $|r|^2 \leq P(\uparrow\uparrow)P(\downarrow\downarrow)$, thus $P(\uparrow\uparrow) \geq |r|^2/P(\downarrow\downarrow)$. Substituting this expression into equation 9.6 and minimising with respect to $P(\downarrow\downarrow)$, we find that the fidelity must satisfy $F \geq 2|r|$.

9.3.3 Cancellation of single qubit rotations

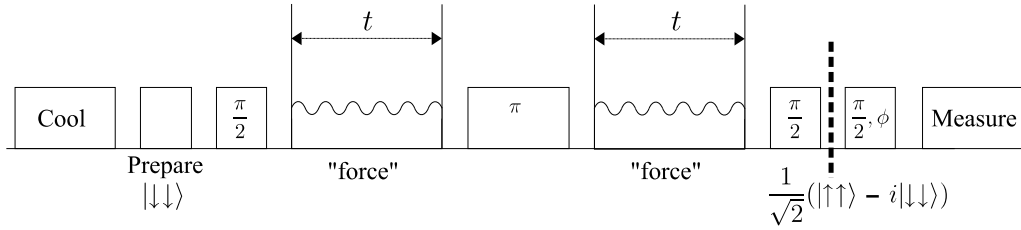


Figure 9.5: Modified pulse sequences used to create a maximally entangled state. The force pulse is applied in both gaps of the spin echo, and adds phase $\Phi(t)$ to $|\uparrow\downarrow\rangle$ and $|\downarrow\uparrow\rangle$ relative to the states $|\uparrow\uparrow\rangle$ and $|\downarrow\downarrow\rangle$ for each pulse. The relation between the force F_s and the detuning δ required for $\Phi(t) = \pi/4$ is $F_s/\delta = 1/\sqrt{2}$. The total phase acquired is then $\pi/2$. This method avoids the difficulty of having to choose a detuning δ for which the return time of the motional state coincides with the time taken for the single qubit phase to evolve by 2π . In the ideal case, the sequence produces the maximally entangled state $|\psi\rangle = (|\uparrow\uparrow\rangle - i|\downarrow\downarrow\rangle)/\sqrt{2}$.

In our experiments, diagnosing the correct laser power required to entangle ions is difficult due to the presence of the single qubit rotations caused by the light shift Δ_π . In order to produce an entangled state more reliably we use the pulse sequence shown in figure 9.5. The single force pulse is replaced by two separated pulses, one in each half of

the spin-echo sequence. As the spin state of the ions is flipped between each pulse from the state-dependent force, the phase acquired due to the light shift in both halves of the sequence cancels out (this also reduces the loss of coherence due to laser intensity drift). For a given detuning δ , the duration of each pulse is set to a multiple of $2\pi/\delta$. Thus the motional state completes a total of 2 loops in phase space, one in each half of the spin-echo sequence. This ensures that the two state-dependent force pulses do not have to be separated by a precise time gap in order to return the motional state to its initial position after the gate. If each pulse duration is a multiple of $2\pi/\delta$, and the spin-echo pulses are perfect, the probability of finding the ions in each spin state after the spin-echo sequence is

$$P(\uparrow\uparrow) = \frac{1}{4}(1 + e^{-4\Gamma t}) - \frac{1}{2}e^{-2\Gamma t}\cos(\Phi) \quad (9.23)$$

$$P(\uparrow\downarrow + \downarrow\uparrow) = \frac{1}{2}(1 - e^{-4\Gamma t}) \quad (9.24)$$

$$P(\downarrow\downarrow) = \frac{1}{4}(1 + e^{-4\Gamma t}) + \frac{1}{2}e^{-2\Gamma t}\cos(\Phi) \quad (9.25)$$

and the coherence between $|\uparrow\uparrow\rangle$ and $|\downarrow\downarrow\rangle$ is

$$r = \frac{i}{2}e^{-2\Gamma t}\sin(\Phi) \quad (9.26)$$

where Φ is the difference in phase acquired by the spin aligned and spin anti-aligned states during the displacement of the motional modes. In order that the combined effect of both pulses is to perform the rotation \hat{G} , we require $\Phi = \pi/2$. For two pulses, this means that we require $F_s/\delta = 1/\sqrt{2}$. In order to experimentally set the correct force, we performed a diagnostic experiment. The force duration was set to $2t_r = 4\pi/\delta$ for each of the pulses in the spin-echo sequence. The laser power was then adjusted so as to maximise $P(\uparrow\uparrow)$ (to be precise, the 3° Raman beam power was adjusted, and at each setting the experiment repeated 500 times so as to find $P(\uparrow\uparrow)$). For the correct value of the force, the population of $|\uparrow\uparrow\rangle$ at the end of the sequence is maximised at

$$P_{\max}(\uparrow\uparrow) = \frac{1}{4}(1 + e^{-8\Gamma t_r}) + \frac{1}{2}e^{-4\Gamma t_r} \quad (9.27)$$

The force duration was then set to $t_r = 2\pi/\delta$. For $\Gamma = 0$, the result is the production of the maximally entangled state.

9.4 Experimental results.

In order to implement the phase gate, recall that the force on the ion must be related to the detuning from the stretch mode of motion by $F_s/\delta = \sqrt{2m+1}$ with m integer, and the duration of the state-dependent force must be a multiple of $2\pi/\delta$. In order to set the detuning, we first measure the frequency of the COM vibrational mode ω_z to ± 0.5 kHz by applying a tickle voltage to one of the trap electrodes (this method is described in section 2.1.2 of chapter 2). The frequency of the stretch mode is $\omega_s = \sqrt{3}\omega_z$.

The frequency difference of the Raman beams is then set using the synthesizers which drive the AOMs in the beam path of each Raman beam. This frequency is stable to within a few Hz over the course of a day. The precision with which we know the detuning

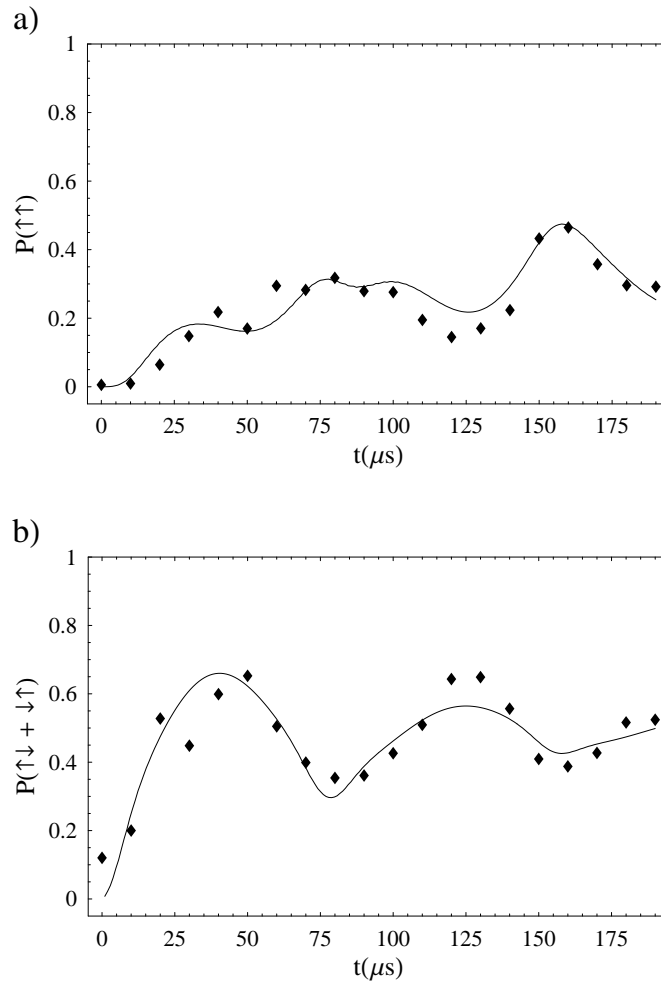


Figure 9.6: The probabilities a) $P(\uparrow\uparrow)$ and b) $P(\uparrow\downarrow + \downarrow\uparrow)$ as a function of the duration of a state-dependent force pulse applied in the first gap of a spin-echo sequence. Each data point was obtained from 500 repeats of the experimental sequence. The detuning of the force calculated from the measured value of the trap frequency and the difference frequency of the two Raman beams is $\delta = 2\pi \times 12.6$ kHz. The solid curves are a joint fit of equations 9.18 and 9.19 to the populations $P(\uparrow\uparrow)$ and $P(\uparrow\downarrow + \downarrow\uparrow)$. The floated parameters were the size of the force F_s on the stretch mode of motion, the detuning δ of the force from resonance, the phenomenological decay parameter Γ , and the phase difference $\Delta\phi$. The fit returned $F_s/\delta = 1.77$, $\delta = 2\pi \times 12.8$ kHz, $\Gamma = 5.4 \text{ ms}^{-1}$ and $\Delta\phi = 1.56$. From this information, we deduce a fidelity $F = 0.67$. The value of $P(\uparrow\downarrow + \downarrow\uparrow)$ at $t = 0$ is non-zero, which may indicate that the spin-echo pulse sequences were of inaccurate length. A further analysis was performed by fitting using a model which accounts for pulse length error. This returned a pulse length error close to zero and thus produced essentially the same results as the simpler theory.

δ is therefore ± 0.9 kHz, dominated by the error on the measurement of the COM mode frequency.

In order to determine the force on the ions, we first measured the intensity of the light fields at the ion by driving carrier flopping and obtaining the Rabi flopping rate Ω_c . In order to provide more intensity for the state-dependent force, the power in the Raman beam at 3° to the magnetic field was increased by a factor P relative to its value when driving carrier Rabi flopping. In order to find Ω_R , we use equation 7.66 from chapter 7

$$\Omega_R = \sqrt{2} \sqrt{\frac{I_{\sigma^+}^{63}}{I_{\pi}^{63}}} \sqrt{P} \Omega_c \quad (9.28)$$

where the ratio of intensities is given in equation 7.75. The force on the stretch mode can then be found from equation 9.10.

In our initial experiments, we used a single oscillating force pulse in the first gap of a spin-echo sequence. The trap frequency was measured to be $2\pi \times 495.6$ kHz, hence the stretch mode frequency is $\omega_s = 2\pi \times 858.4$ kHz. The qubit splitting was measured to be $\omega_0 = 2\pi \times 4800$ kHz. The mean vibrational quantum numbers of the COM and stretch motional modes were measured using the method of section 6.2.2, and found to be $\bar{n}_{\text{COM}} = 0.24(5)$ and $\bar{n}_{\text{str}} = 0.08(4)$.

A number of experiments were carried out at various δ , with data accumulated both as a function of force pulse duration t , and as a function of the phase ϕ of the further analysis pulse. The highest fidelity for production of the maximally entangled state was observed when the difference frequency of the Raman laser beams was set to $2\pi \times 871$ kHz, hence $\delta = 2\pi \times 12.6$ kHz.

An example of experimental data obtained from a scan of the duration of the force is shown in figure 9.6. The data was fitted using equations 9.18 and 9.19, with F_m/δ , δ , Γ and $\Delta\phi$ floated. The fitted values are $F_s/\delta = 1.77$, $\delta = 2\pi \times 12.8$ kHz, $\Gamma = 5.4 \text{ ms}^{-1}$ and $\Delta\phi = 1.56$. $(F_s/\delta)^2 = 3.1$. This indicates that the phase gate introduced a phase $\simeq 3\pi/2$ in the $\uparrow\downarrow$ and $\downarrow\uparrow$ states, rather than the minimum value of $\pi/2$ required to implement the gate.

Using the fitted parameters, we can calculate $P(\uparrow\uparrow) = 0.31$, $P(\downarrow\downarrow) = 0.39$ and $r = 0.01 + 0.31i$ at $t = 2\pi/\delta$. Thus the fidelity $F = 0.67$.

Figure 9.7 shows data for $P(\uparrow\downarrow + \downarrow\uparrow)$ as a function of the phase of the analysis pulse. This data was taken directly after the experimental data from the scan of the force duration which is shown in figure 9.6, using the same power and detuning. The duration of the force was $77 \mu\text{s}$. The analysis pulse duration was $t_{\text{set}} = 2\mu\text{s}$. A time scan on the carrier transition was performed on the same day, and fitted to obtain the pulse time offset and Rabi frequency. The fitted time offset was $t_{\text{off}} = 0.2 \mu\text{s}$ and the fitted Rabi frequency was $\Omega_c = 2\pi \times 128.5 \mu\text{s}$. The analysis pulse of $2 \mu\text{s}$ thus gives a rotation $\theta = \Omega_c(t_{\text{set}} - t_{\text{off}})/2 = 0.23\pi$. The amplitude of the oscillation in $P(\uparrow\downarrow + \downarrow\uparrow)$ with frequency 2 obtained from the fit to the data in figure 9.7 is 0.35, which indicates that $|r| = 0.36$. The maximum value of $|r|$ calculated from experimental data taken on the same day was 0.37. The fidelity is therefore $F_\kappa \geq 0.74$. This value is considerably higher than that obtained from the fitted parameters from the data from the scan of pulse duration.

In a second group of experiments, the two-pulse force method of section 9.3.3 was used to cancel out the single-qubit phase shifts. The mean vibrational number of the COM and stretch modes were found to be $\bar{n}_{\text{COM}} = 0.20(5)$ and $\bar{n}_{\text{str}} = 0.18(5)$ respectively. Preliminary experiments were used to determine the trap frequency required for the ions to be separated by an integer number of wavelengths. This was found to be $\omega_z = 2\pi \times$

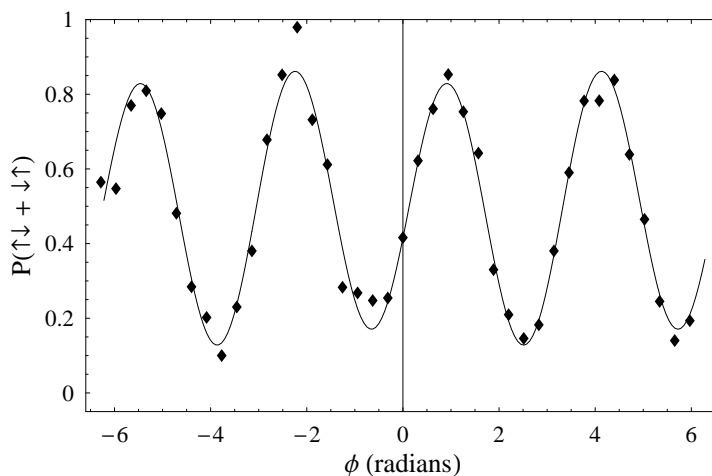


Figure 9.7: The probability of finding the spin states anti-aligned as a function of the phase of an analysis rotation pulse applied to the state produced at the end of the spin-echo sequence. The duration of the analysis pulse was $t = 2.0 \mu\text{s}$. The Rabi frequency and time offset were obtained by fitting the results of a carrier flopping experiment, giving $\Omega_c = 2\pi \times 128.5 \text{ kHz}$ and $0.2 \mu\text{s}$ respectively. The deduced rotation angle is thus $\theta = 0.46\pi$ radians. The amplitude of the oscillation at frequency 2 gives the magnitude of the density matrix element r , which is the coherence between $|\uparrow\uparrow\rangle$ and $|\downarrow\downarrow\rangle$. The data is fitted with $P(\uparrow\downarrow + \downarrow\uparrow) = b + a_1 \sin(W\phi + \phi_{\text{off}}) + a_2 \sin(2W\phi + \phi_{\text{off}})$, where b, a_1, a_2, W and ϕ_{off} were floated. The fitted value of a_2 is 0.35, which indicates that $|r| = 0.36$.

536.5 kHz, which implies that the angle between the two Raman beams is 59° . This trap frequency corresponds to a stretch mode frequency of $2\pi \times 929.2 \text{ kHz}$. The difference frequency of the Raman beams during the force was set to $2\pi \times 906.5 \text{ kHz}$, hence $\delta = 2\pi \times 22.7 \text{ kHz}$. Optimisation of the force on the ions was carried out using the method described above. That is, the duration of each state-dependent force pulse was set to $96 \mu\text{s}$ ¹, and the power in the laser beams was adjusted by changing the drive power of the 3° beam AOM. The maximum population achieved was $P_{\text{max}}(\uparrow\uparrow) = 0.54$. Using equation 9.27, this corresponds to $\Gamma = 3.9 \text{ ms}^{-1}$. Directly after performing this optimisation, we noticed that one of the readout lasers had drifted in frequency. Though this should not affect the optimal force used, it may affect the measured population and the deduced value of Γ .

The gate was then performed by setting the duration of the state-dependent force pulses to $t_r = 2\pi/\delta = 44 \mu\text{s}$. The carrier flopping Rabi frequency on the day in question was $\Omega_c = 2\pi \times 101(2) \text{ kHz}$. The ratio between the power in the 3° Raman beam used for the state-dependent force and for carrier flopping was measured to be $P = 1.6$. The values of the force calculated from equation 9.10 using values of $\Delta\phi$ between 1.34 and 1.56 (as measured in the Schrödinger's cat experiments of chapter 7) are in the range $2\pi \times 13.9 \text{ kHz}$ to $2\pi \times 17.5 \text{ kHz}$. If the force has been correctly optimised, $(F_s/\delta)^2 = 1/2$. This is the case for $\Delta\phi = 1.48$.

¹An experimental error was made, so the value used was not in fact $88 \mu\text{s}$ as would be expected from $4\pi/\delta$. This means that the deduced value of Γ is likely to be an overestimate.

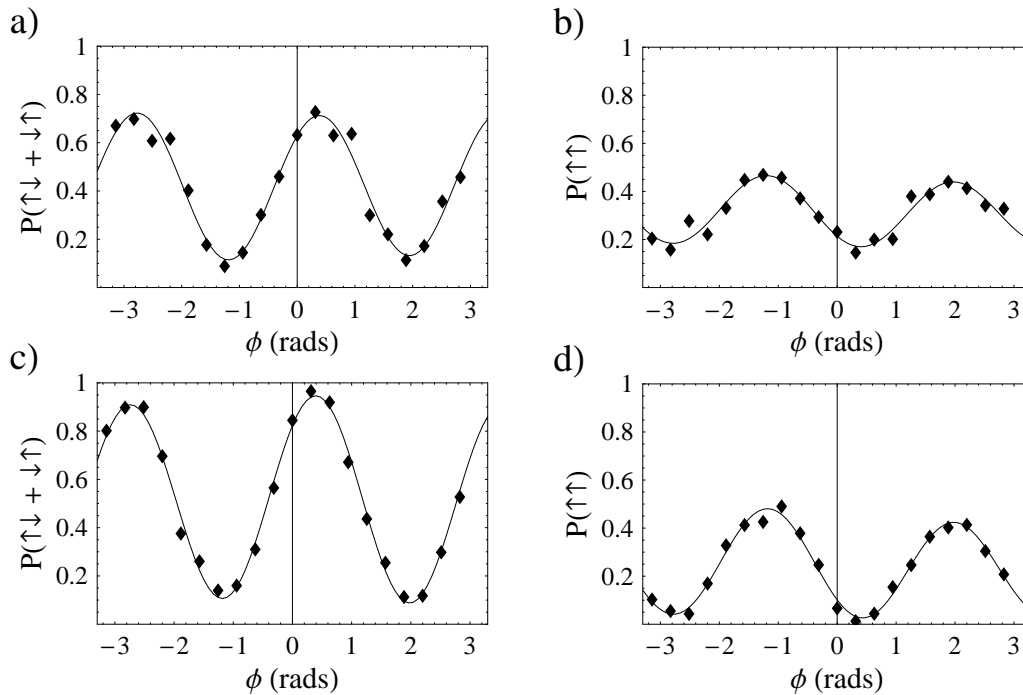


Figure 9.8: Populations as a function of the phase of the analysis pulse for the pulse sequence shown in figure 9.5. The programmed pulse lengths used were 3.4 and $2.8 \mu\text{s}$, which correspond to rotation angles of $\theta = 0.66\pi$ radians (plots a) and b)) and $\theta = 0.54\pi$ radians (plots c) and d)). The data is fitted with equations 8.15 and 8.16 from chapter 8, from which the elements of the density matrix were extracted. The high amplitude of variation with period π relative to all other components indicates that the coherence r is much larger than all other coherences. The zero value of the phase relative to the pulses producing the spin-echo sequence is probably not at $\phi = 0$, since this was not determined on the day in question. This doesn't affect the size of the density matrix elements determined from the tomography, but does mean that the phase of the off-diagonal elements can not be known.

The partial tomography method described in chapter 8 was used to extract information about the density matrix at the end of the spin-echo sequence. The results of the analysis pulses which were used to carry out tomography on the state are shown in figure 9.8. The programmed length of the tomography pulses were 3.4 and $2.8 \mu\text{s}$. On the same day, the Rabi frequency and time offset were calculated using 6 consecutive pulses driving Rabi flopping on the carrier transition, as described in section 8.3.2. The Rabi frequency and time offset were found to be $2\pi \times 101(2)$ kHz and $0.15(2) \mu\text{s}$ respectively. This Rabi frequency is the average of the Rabi frequency for each of the ions, which differed by 8% due to different intensities of the light at each ion. This is likely to lead to imperfection in the tomography as well as in the preparation of the entangled state. The programmed lengths of the tomography pulses correspond to rotation angles of $\theta = 0.66\pi$ and $\theta = 0.54\pi$ radians respectively. The results show a large amplitude of the oscillation with period π relative to that with period 2π . This indicates that the coherence r is the much larger than p , q , t , or u . The density matrix obtained using the maximum likelihood method is shown

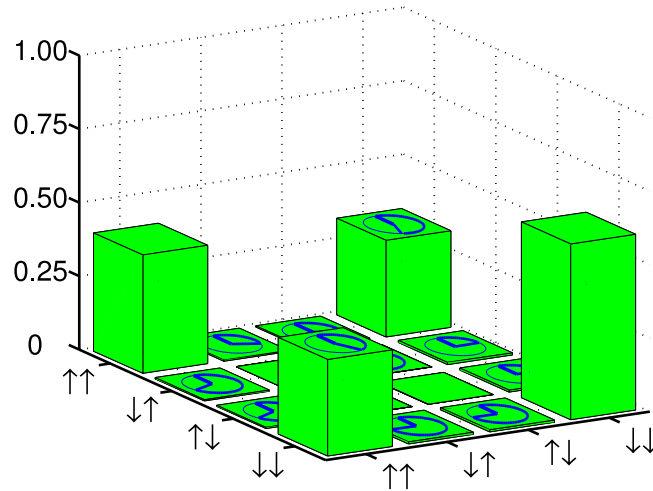


Figure 9.9: The density matrix of the state at the end of the pulse sequence shown in figure 9.5, determined using the tomography and maximum likelihood methods described in chapter 8. The fidelity of producing the Bell state $|\psi\rangle = (|\uparrow\uparrow\rangle + e^{i\kappa}|\downarrow\downarrow\rangle)$ is 0.83. The purity of the density matrix is found to be 0.74, and the entanglement of formation is 0.54.

in figure 9.9. Note the characteristic “castle” shape which shows that the population is almost all in $\uparrow\uparrow$ and $\downarrow\downarrow$, and there is a substantial coherence between them. The maximum fidelity with the general maximally entangled state $(|\uparrow\uparrow\rangle + e^{i\kappa}|\downarrow\downarrow\rangle)/\sqrt{2}$ is 0.83.

9.4.1 Measurement of Entanglement

In order to deduce the amount of entanglement in the state we have created, we use the experimentally determined density matrix of the two spins. From this density matrix, the value of the *entanglement of formation* can be extracted. This is a measure of entanglement which ranges between zero for a separable state to unity for a maximally entangled state.

For a pure state $|\psi\rangle$ of two quantum systems A and B , the entanglement is defined as the entropy of either of the two subsystems after tracing over the other system [88];

$$E(\psi) = -\text{Tr}(\hat{\rho}_A \log_2 \hat{\rho}_A) = -\text{Tr}(\hat{\rho}_B \log_2 \hat{\rho}_B) \quad (9.29)$$

where $\hat{\rho}_A$ is the partial trace of $|\psi\rangle\langle\psi|$ over subsystem B and vice versa. For a mixed state, the density matrix of the system can be decomposed into an ensemble of pure states $|\psi_i\rangle$ with probabilities p_i .

$$\hat{\rho} = \sum_i p_i |\psi_i\rangle\langle\psi_i| \quad (9.30)$$

There are many such decompositions. The entanglement of each decomposition is given by the average of the entanglements of each of the pure states $|\psi_i\rangle$. Since many decompositions exist, the entanglement of formation E is defined as the average entanglement minimised over all decompositions of the density matrix [89]:

$$E(\hat{\rho}) = \min \sum_i p_i E(\psi_i) \quad (9.31)$$

In general, explicit formulae for the entanglement of formation of mixed states do not exist. However for a two-qubit system an explicit formula for the entanglement of formation of a mixed state was found by W. K. Wootters [90]. He defines a spin-flipped density matrix

$$\tilde{\rho} = (\hat{\sigma}_y \otimes \hat{\sigma}_y) \hat{\rho}^T (\hat{\sigma}_y \otimes \hat{\sigma}_y) \quad (9.32)$$

For a separable pure state, the overlap of a spin-flipped state with the original state is zero, while for maximally entangled states, the overlap is 1. This means a measure of entanglement for pure states is this overlap

$$C(\psi) = |\langle \psi | \tilde{\psi} \rangle| \quad (9.33)$$

which is called the ‘‘concurrence’’. The equivalent expression for a mixed state is given by

$$C(\rho) = \max\{0, \lambda_1 - \lambda_2 - \lambda_3 - \lambda_4\} \quad (9.34)$$

where the λ_i 's are the positive square roots of the eigenvalues, in decreasing order, of the non-Hermitian matrix $\hat{\rho}\tilde{\rho}$. The entanglement of formation is then given by [90]

$$E(\hat{\rho}) = \varepsilon(C(\hat{\rho})) \quad (9.35)$$

where

$$\varepsilon(x) = -\frac{1 + \sqrt{1 - x^2}}{2} \log_2 \frac{1 + \sqrt{1 - x^2}}{2} - \frac{1 - \sqrt{1 - x^2}}{2} \log_2 \frac{1 - \sqrt{1 - x^2}}{2} . \quad (9.36)$$

The value of the entanglement of formation ranges between 0 for a separable state to 1 for a maximally entangled state. For the density matrix of the entangled state produced in our experiments, the entanglement of formation is 0.54.

9.5 Contributions to infidelity

In order to improve the gate operation, we need to understand the factors which contribute to infidelity. In our experiments, infidelity is caused mainly by decoherence during the gate, by imprecise setting of the lengths of carrier or state-dependent force pulses, and by unequal illumination of the two ions by the light field.

The measured powers of the 3° and 63° beams for the state-dependent force pulse were 290 μW and 560 μW respectively. From the results presented in chapter 5, the expected photon scattering rate for both beams is 1.46 ms^{-1} . Photon scattering produces decay of coherences which is well modelled by the phenomenological decay constant introduced in section 9.3.2. Using equations 9.23 to 9.26 and assuming the pulse lengths were perfect, the fidelity is given by

$$F = \frac{1}{4} [1 + e^{-4\Gamma t_r} + 2e^{-2\Gamma t_r}] \quad (9.37)$$

where $t_r = 2\pi/\delta = 44 \mu\text{s}$. For $\Gamma = 1.46 \text{ ms}^{-1}$, $F = 0.88$. This indicates that the major source of infidelity in our experiment is due to photon scattering. The value of Γ which would produce the observed fidelity of 83% is 2.2 ms^{-1} .

The contribution from motional decoherence can be estimated using the results of the single ion experiments in chapter 7. The maximum value of $\Delta\alpha$ for the stretch mode is $2 \times 1/\sqrt{2} = \sqrt{2}$ for the gate described above, hence from equation 7.84 we find that

$\gamma_m = \gamma_0$. Though a study has not been made of γ_0 for the stretch mode, we can get an estimate using a typical value of γ_0 from the Schrödinger's cat experiments, 0.3 ms^{-1} . Using this value, the measured fidelity is 86%. This extra contribution is therefore not enough to account for the value of Γ which gives the measured fidelity.

Other possible sources of infidelity are errors in pulse lengths used for the carrier pulses in the spin echo sequence, and in the length of the force pulse. We can estimate the infidelity due to imperfect carrier pulse lengths by assuming that each force pulse produced exactly the operation $\hat{G}^{1/2}$, where

$$\hat{G}^{1/2} = \begin{pmatrix} 1 & 0 & 0 & 0 \\ 0 & e^{i\frac{\pi}{4}} & 0 & 0 \\ 0 & 0 & e^{i\frac{\pi}{4}} & 0 \\ 0 & 0 & 0 & 1 \end{pmatrix}. \quad (9.38)$$

The ideal pulse sequence is $R^{(2)}(\pi/2, 0)\hat{G}^{1/2}R^{(2)}(\pi)\hat{G}^{1/2}R^{(2)}(\pi/2)$. Pulse length errors can be included by making the substitution $R^{(2)}(\theta) \rightarrow R^{(1)}(\theta_1, 0) \otimes R^{(1)}(\theta_2, 0)$, where θ_1 (θ_2) is the rotation applied to ion 1 (2). We expect the error in the pulse length to be $<0.05 \mu\text{s}$, which gives an infidelity of 1.8%.

Imbalance in the laser intensity at each ion during carrier rotations will also contribute to the infidelity. This was introduced by multiplying the rotation angles on each ion by $1 + \epsilon/2$ and $1 - \epsilon/2$ respectively, and replacing $\hat{G}^{1/2}$ with

$$\hat{G}^{1/2} = \begin{pmatrix} 1 & 0 & 0 & 0 \\ 0 & e^{i(1+\frac{\epsilon}{2})^2\frac{\pi}{4}} & 0 & 0 \\ 0 & 0 & e^{i(1-\frac{\epsilon}{2})^2\frac{\pi}{4}} & 0 \\ 0 & 0 & 0 & 1 \end{pmatrix} \quad (9.39)$$

where ϵ is the ratio of the Rabi frequency at each ion. For $\epsilon = 0.08$ (inferred from the fit to the data from Rabi flopping on the carrier transition), the contribution to the infidelity is 2.2%. This infidelity is dominated by the effect of the imperfect carrier rotations.

9.6 Conclusions

We have performed a quantum logic gate between two distinct qubits. The light shift due to the π component of the light field produced a single qubit phase which made it desirable to use two pulses of the state-dependent force to implement the gate, with a π carrier pulse inserted between them. In our experiments, this resulted in the creation of an entangled state with 83% fidelity. We expect that photon scattering contributes 12% to the infidelity, and that $\sim 2\%$ is due to decoherence of the motional state during the gate. A 2% contribution could be expected due to the observed imbalance in intensities of the light at each ion which was measured using a Rabi flopping experiment.

Chapter 10

Segmented Trap Design.

This chapter is a lengthy study concerned with the design of electrode structures optimized for separating ions from a single harmonic wells into two wells. The separation of ions is a crucial element of the “quantum CCD” architecture proposed by Kielpinski et. al. [31] for scaling up the ion trap system to many qubits.

We have written a comprehensive paper on this topic which has been accepted for publication in *The Journal of Quantum Information and Computation*, and is included in Appendix C.

The group has recently received a prototype trap built by S. Taylor and B. Brkic at the University of Liverpool, which is shown in figure 10.1. The electrode structure is closely related to some of the designs discussed in our paper. This trap is currently being tested for use in high vacuum.

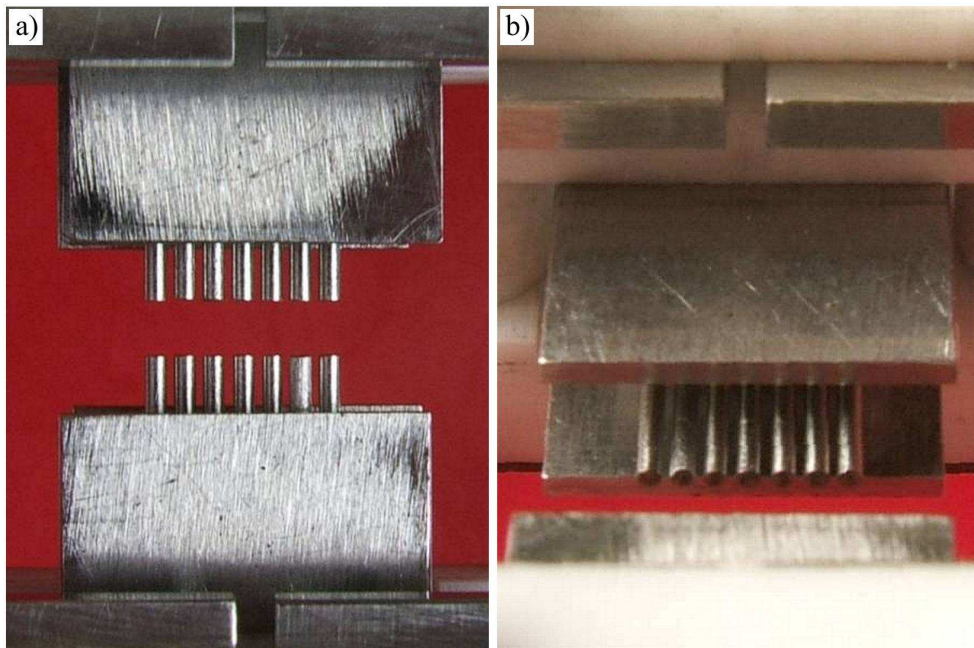


Figure 10.1: Two views of the trap built by S. Taylor and B. Brkic at the University of Liverpool, based on the designs discussed in Appendix C. The distance from the centre of the trap to the nearest electrode surface is 0.7 mm. The cylindrical d.c. electrodes have diameter 0.58 mm. The planar electrodes above and below the d.c. electrodes are r.f. electrodes, and the split planar electrode is a d.c. compensation electrode.

Chapter 11

Conclusion

This thesis described work towards development of a quantum information processor with trapped ions. The recent goal has been the realisation of a controlled phase gate between two ions. This was demonstrated, and used to create a maximally entangled state. In order to implement this gate, many diagnostic experiments were performed. These were mainly concerned with the quantum manipulation of one or two ions. Quantum states of motion such as Fock states and coherent states have been prepared, and also entangled states of the spin and motion of a single ion. The coherence times observed for such states are longer than equivalent results which have been measured previously.

In addition to experimental work, this thesis presents a theoretical investigation of the issues surrounding the fast separation of trapped ions. A range of electrode configurations are considered and compared, one of which has been manufactured and is expected to be used to trap ions in the near future.

The initial stage of the experiments concerned with manipulation of the motional state of a trapped ion is cooling to the ground state of motion. This is described in chapter 4. In our system, we find that three stages of cooling are required in order to prepare the ground state with high fidelity. The ion is first Doppler cooled, but this is insufficient to reach the Lamb-Dicke regime. Continuous sideband cooling is then used to reach $\bar{n} \simeq 0.4$. Pulsed sideband cooling is then used to prepare the ground state. Once the ion is in the Lamb-Dicke regime, a simple temperature diagnostic is available. This is described and is used to deduce the temperature of our ion. For a trapped ion with an axial vibrational frequency of 800 kHz we find that we can achieve 98% ground state preparation after optimisation of the cooling ($\bar{n} = 0.02$). We studied the heating rate from the ground state by inserting a delay between the end of the cooling and the temperature measurement. The measured heating rate was generally found to be less than 10 quanta s^{-1} , and could be as low as 2.5 quanta s^{-1} . This is the lowest value which has been observed in any ion trap. The small value can be ascribed in part to the relatively large size of our trap compared to others in which a heating rate has been measured. On a few occasions an anomalous heating rate > 30 quanta s^{-1} was observed.

The ground state of motion of the trapped ion is the Fock or number state $|0\rangle$ of the harmonic oscillator. The ability to prepare the ground state of motion with high fidelity allowed subsequent preparation of other Fock states. In these experiments we prepared the state $|1\rangle$ with $>91\%$ fidelity and the state $|2\rangle$ with $>88\%$ fidelity. Diagnosis of these states was performed by observing the rate of Rabi flopping on sideband transitions.

Decoherence limits the time over which manipulations of the motional and spin degrees of freedom can be carried out. Decoherence can occur due to interaction of the quantum

states with the environment. Chapter 5 describes a series of experiments which characterised the decoherence rate of a single trapped ion. A Ramsey experiment was used to measure the coherence times of an ion in a superposition of spin states. Decoherence of the superposition was found to occur on a typical timescale of $240 \mu\text{s}$, which is primarily due to magnetic field fluctuations which are slow compared to typical pulse times in our experiment. The ion can be protected against these slow fluctuations by use of a spin-echo sequence. This was used for much of the work presented in later chapters.

The decoherence rate of a superposition of motional states was studied at two different axial trap frequencies. For a single ion with an axial trap frequency of 800 kHz the motional coherence time was found to be 157 ms , which is the longest motional coherence time measured in an ion trap (again this can be ascribed to the large ion-electrode distance). In a 500 kHz trap the coherence time is found to be 76 ms .

The interaction of the ion with the Raman laser can also lead to decoherence of the spin and motional states. The coherence time for Rabi flopping on the carrier transition was found to be $\simeq 240 \mu\text{s}$, which is similar to that observed in the Ramsey spin experiment. This indicates that magnetic field fluctuations are the primary source of decoherence. A study of the photon scattering rate during illumination of two ions by the Raman laser beams was performed, and indicated that photon scattering would be a significant source of infidelity in the implementation of the two-qubit gate. For typical beam powers and detunings in our experiments, the photon scattering rate was $\sim 1.1 \text{ ms}^{-1}$.

In order to demonstrate the two-qubit gate, it is necessary to be able to prepare and manipulate quantum states of two ions. The cooling and preparation of the ground state of motion of two ions is described in chapter 6. The temperature diagnostic for two ions is performed by a similar method to that used for a single ion, but the interpretation of the signal is more complicated. Theoretical results for the spin state after application of radiation tuned to the blue sideband transition are presented, which allow us to deduce the final temperature of each mode of motion of the ions. Rabi flopping of the carrier transition is then demonstrated using two cold ions. If the laser beam does not equally illuminate both ions, we observe beating of the $P(\uparrow\uparrow)$ signal as a function of the Rabi flopping time. In order to simplify the gate implementation and diagnostics it is desirable for the ions to be equally illuminated. A method to do this was implemented, with the result that the Rabi frequency of each ion was equalised to better than 5%.

We used a state-dependent force to entangle the spin and motion, allowing us to implement the two-qubit gate. The state-dependent force was tested and demonstrated using a single trapped ion. The force was used to generate ‘‘Schrödinger’s Cat’’ entangled states of the spin and motion of the ion which are interesting in their own right. The motional states involved in the superposition were shown to be mesoscopic in the sense that both the separation of the motional wavepackets and the vibrational excitation involved were large. The largest state created had a separation $\Delta\alpha = 5.4$ and maximum mean excitation of $\bar{n} = 16$. The decoherence rate as the motional superpositions are displaced was determined, and assigned to contributions due to decoherence of the spin state superposition and of the motional states. The motional coherence times were again found to be much longer than those reported elsewhere for a similar size of state.

The single ion experiments also provided a useful insight into light shift effects due to the multiple polarisation components of the Raman laser beams. The π polarisation component in the 60° beam interacts with the σ components of the 3° Raman beam to off resonantly drive carrier transitions, producing a significant light shift effect. This effect allowed us to deduce the intensity of the different polarisation components in the light field

from the experimental results. The amplitude and phase of the overlap of the motional states was observed as a function of the duration of the state-dependent force, which allowed us to deduce the relative phase of the circular polarisation components of the light field. This was found to be significantly different to the experimentally set values from waveplate settings, which we subsequently found was due to rotation of the polarisation vector by a mirror in one of the Raman beam paths.

In order to provide better characterisation of the spin state of two ions, a method for tomography was developed. This method is described in chapter 8. Since experimental errors mean that the experimentally determined density matrix does not necessarily fulfil the condition of positivity, a maximum likelihood method is used to find the physical density matrix which most closely matches the data. In order to implement the tomography experimentally, we devised a method for ensuring that lengths of carrier pulses could be accurately set.

Two experimental limitations in our current setup mean that a full tomography cannot be performed. These are that we cannot address each ion individually, or read out the state of each ion individually. This restricts the available information about the density matrix of the ions. The experimental application of the tomography method to several easily created states is presented. This characterisation of the density matrix allows us to deduce useful information such as the purity and the fidelity with which the desired state is created.

The entanglement of two spin qubits using a universal two-qubit phase gate is described in chapter 9. The implementation led to the creation of a maximally entangled state with 83% fidelity. The tomography method described in chapter 8 was used to obtain information about the density matrix of the two ions. The entanglement of formation of this density matrix was found to be 0.54. The major sources of infidelity are discussed, and the major contribution is found to be from off-resonant scattering of photons while the Raman laser beams are on.

Chapter 10 is a major study into the design of traps for fast separation of trapped ions. We found that in order to optimally separate two ions in a single well potential into two separate wells, it is desirable to produce a strong d.c. octupole potential with an additional r.f. quadrupole. The problem is simplified by the introduction of two dimensionless parameters which characterise the axial and radial confinement at the electric field breakdown limit for any given design. The design considerations depend on the length scale at which the trap is designed to operate. For larger traps strong axial confinement is found to be harder to achieve than the necessary radial confinement required to keep the ions aligned along the axis of the trap. At smaller length scales the opposite is found to be true.

A range of different electrode configurations are described and analysed. The results show that in order to achieve fast separation of ions, planar trap geometries are particularly undesirable. One of the three layer trap designs has been built for our group by a research group in Liverpool, and is currently being prepared for testing.

11.1 Future plans and improvements.

Improving the speed and fidelity of the two-qubit gate is a significant short term goal. The speed of the gate can be increased by increasing the laser power. This also leads to an increase in the photon scattering rate such that the number of photons scattered per gate is unchanged. In order to maximise the force on the ion for a given laser intensity,

we plan to add an additional beam at 60° to the magnetic field, which would allow us to use a vertically polarised beam to implement the spin-dependent force. In addition, this would eliminate the π polarisation component of the light field during the force, which would avoid the current problems we have due to single-qubit rotations, and would result in fewer photons scattered per gate. The use of two beams on the same beam path would allow us to implement motion independent spin-flip transitions with the Raman laser. The high power of the laser means that these can be driven much faster than is possible with the magnetic field coil, and increases the robustness of the experiment against fluctuations in the magnetic field.

The fidelity of the gate is partly limited by photon scattering. In order to reduce this, we plan to increase the detuning of the Raman laser from resonance with the 397 nm transition. In order to maintain gate speed, it will therefore be necessary to increase the laser power. The scattering rate due to resonant ASE light has previously been measured using a blue laser diode [54] and found to be the dominant source of scattering at higher laser detunings. We plan to alleviate this problem using a solid etalon.

A multiple zone trap has been manufactured and is currently undergoing vacuum testing. This will be used to experimentally investigate issues surrounding the separation of ions. A further trap is currently being built at a much smaller scale, which will allow us to explore these issues further and enable investigation into the behaviour of ion heating this small scale. The development of stable voltage supplies which can be used to control the multiple voltages applied to the electrodes will form a core component of this work.

In the longer term, the aim is to implement error correction in an ion trap. This will require both the generation of multiple qubit entangled states and the separation of ions. The extension of the gate described in this thesis to larger numbers of ions produces states which are ideal for error correction demonstrations, and this will form a crucial part of these future experiments. The next few years should greatly clarify the promise of ion trap methods for quantum information processing.

Appendix A

Adiabatic elimination of the upper level

In the interaction picture of the internal Hamiltonian \hat{H}_S , a general state vector for the three level system is given by

$$|\psi\rangle = \sum_{i=1}^3 c_i |\phi_i\rangle \quad (\text{A.1})$$

where $|\phi_i\rangle$ is an eigenstate of \hat{H}_S . The time evolution of the c_i is given by the Hamiltonian in equation 3.4

$$\frac{dc_1}{dt} = -i \frac{g_{13}}{2} e^{-i\Delta t} e^{i\phi_1} c_3 \quad (\text{A.2})$$

$$\frac{dc_2}{dt} = -i \frac{g_{23}}{2} e^{-i(\Delta-\delta)t} e^{i\phi_2} c_3 \quad (\text{A.3})$$

$$\frac{dc_3}{dt} = -i \frac{g_{13}^*}{2} e^{i\Delta t} e^{-i\phi_1} c_1 + -i \frac{g_{23}^*}{2} e^{i(\Delta-\delta)t} e^{-i\phi_2} c_2 \quad (\text{A.4})$$

Integrating equation A.4 by parts gives

$$c_3 = -\frac{g_{13}^*}{2\Delta} e^{i\Delta t} e^{-i\phi_1} c_1 - \frac{g_{23}^*}{2(\Delta-\delta)} e^{i(\Delta-\delta)t} e^{-i\phi_2} c_2 + O(g^2/\Delta^2) \quad (\text{A.5})$$

where the detuning $\Delta \gg g$. If the ion starts in the ground state, the maximum probability for finding the ion in the state $|e_3\rangle$ at any time will be $\sim (g/\Delta)^2$, hence the rate of spontaneous emission from the level would be $\sim g^2\Gamma/\Delta^2$, where Γ is the natural width of the transition. Neglecting terms of order g^2/Δ^2 and higher, and substituting equation A.5 into equations A.2 and A.3 gives

$$\frac{dc_1}{dt} = -\frac{i|g_{13}|^2}{4\Delta} c_1 - \frac{ig_{13}g_{23}^*}{4(\Delta-\delta)} e^{-i\delta t} e^{-i(\phi_1-\phi_2)} c_2 \quad (\text{A.6})$$

$$\frac{dc_2}{dt} = -\frac{i|g_{23}|^2}{4(\Delta-\delta)} c_2 - \frac{ig_{23}g_{13}^*}{4(\Delta-\delta)} e^{i\delta t} e^{-i(\phi_2-\phi_1)} c_1 \quad (\text{A.7})$$

$$(\text{A.8})$$

For $\delta \ll \Delta$, these equations are the same as those generated by the two level Hamiltonian of equation 3.5. The rate at which coherent transitions are driven between the two levels

is of order g^2/Δ . This exceeds the spontaneous emission rate from the upper level by a factor Δ/Γ . In our experiments, $\Delta = 2\pi \times 30$ GHz, $\Gamma = 2\pi \times 22$ MHz. Thus the approximation that spontaneous emission can be neglected is good in this case.

Appendix B

Wavefunction for two ions driven on a motional sideband

The wavefunction for two ions starting in the state $|\downarrow\downarrow, n\rangle$ and driven for time t_p by light fields resonant with the red sideband is

$$\begin{aligned}
|\psi_r\rangle &= \pm e^{-i(\phi_1+\phi_2)} \frac{\sqrt{n(n-1)}}{2n-1} (1 - \cos(g_r\Omega t)) |\uparrow\uparrow, n-2\rangle \\
&\pm e^{-i\phi_2} \sqrt{\frac{n}{2(2n-1)}} \sin(g_r\Omega t) |\uparrow\downarrow, n-1\rangle + e^{-i\phi_1} \sqrt{\frac{n}{2(2n-1)}} \sin(g_r\Omega t) |\downarrow\uparrow, n-1\rangle \\
&+ \left[1 - \frac{n}{2n-1} [1 - \cos(g_r\Omega t)] \right] |\downarrow\downarrow, n\rangle
\end{aligned} \tag{B.1}$$

where the upper sign applies to the COM mode sideband and the lower sign to the stretch mode sideband. $g_r = \sqrt{(2n-1)}/2$. $\Omega = \eta_c\Omega$ for the COM mode and $\eta_s\Omega$ for the stretch mode. On resonance with the blue sideband, the wavefunction evolves as

$$\begin{aligned}
|\psi_b\rangle &= \pm e^{-i(\phi_1+\phi_2)} \frac{\sqrt{(n+1)(n+2)}}{2n+3} (1 - \cos(g_b\Omega t)) |\uparrow\uparrow, n+2\rangle \\
&\pm e^{-i\phi_2} \sqrt{\frac{n+1}{2(2n+3)}} \sin(g_b\Omega t) |\uparrow\downarrow, n+1\rangle + e^{-i\phi_1} \sqrt{\frac{n+1}{2(2n+3)}} \sin(g_b\Omega t) |\downarrow\uparrow, n+1\rangle \\
&+ \left[1 + \frac{n+1}{2n+3} [1 - \cos(g_b\Omega t)] \right] |\downarrow\downarrow, n\rangle
\end{aligned} \tag{B.2}$$

where again the upper sign applies to the COM mode and the lower sign to the stretch mode. $g_b = \sqrt{(2n+3)}/2$.

Appendix C

Electrode configurations for fast separation of trapped ions.

The following is a paper on electrode design which has been accepted for publication in The Journal of Quantum Information and Computation.

Bibliography

- [1] R. P. Feynman. Simulating physics with computers. *Int. J. Theor. Phys.*, 21:467–488, 1982.
- [2] R. P. Feynman. Quantum mechanical computers. *Found. Phys.*, 16:507–531, 1986.
- [3] D. Deutsch. Quantum computational networks. *Proc. Roy. Soc.*, 425(1868):73–90, 1989.
- [4] A. Barenco, C. H. Bennett, R. Cleve, D. P. DiVincenzo, N. Margolus, P. Shor, T. Sleator, J. A. Smolin, and H. Weinfurter. Elementary gates for quantum computation. *Phys. Rev. A*, 52(5), 1995.
- [5] T. Sleator and H. Weinfurter. Realizable universal quantum logic gates. *Phys. Rev. Lett.*, 74(4087), 1995.
- [6] P. W. Shor. Algorithms for quantum computation: Discrete logarithms and factoring. *Proc. 35th Annual Symposium of Foundations of Computer Science.*, 1994.
- [7] L. K. Grover. Quantum mechanics helps in searching for a needle in a haystack. *Phys. Rev. Lett.*, 79(2)(325), 1997.
- [8] A. M. Steane. A quantum computer needs only one universe. *Studies in History and Philosophy of Modern Physics*, 34:469–478, 2003.
- [9] R. Jozsa and N. Linden. On the role of entanglement in quantum computational speed-up. *quant-ph/0201143*, 2002.
- [10] A. Ekert and R. Jozsa. Entanglement-enhanced information processing. *Phil. Trans. R. Soc. Lond.*, 356:1769–1782, 1998.
- [11] A. M. Steane. Multiple particle interference and quantum error correction. *Proc. R. Soc. Lond. A*, 452:2551–2577, 1996.
- [12] A. R. Calderbank and P. W. Shor. Good quantum error-correcting codes exist. *Phys. Rev. A*, 54(1098), 1996.
- [13] D. P. DiVincenzo. The physical implementation of quantum computation. *Fortschr. Phys.*, 48:771–783, 2000.
- [14] M. A. Nielsen and I. L. Chuang. *Quantum Computation and Quantum Information*. Cambridge University Press, 2000.
- [15] J. I. Cirac and P. Zoller. Quantum computations with cold trapped ions. *Phys. Rev. Lett.*, 74:4091–4094, 1995.

- [16] J. I. Cirac and P. Zoller. A scalable quantum computer with ions in an array of microtraps. *Nature*, 404:579, 2000.
- [17] E. Knill, R. Laflamme, and G. J. Milburn. A scheme for efficient quantum computation with linear optics. *Nature*, 409(46), 2001.
- [18] J. Q. You and F. Nori. Superconducting circuits and quantum information. *Phys. Today*, 58(11)(42), 2005.
- [19] I. L. Chuang, L. M. K. Vandersypen, X. Zhou, D. W. Leung, and S. Lloyd. Experimental realization of a quantum algorithm. *Nature*, 393:143–146, 1998.
- [20] J. A. Jones, M. Mosca, and R. H. Hansen. Implementation of a quantum search algorithm on a quantum computer. *Nature*, 393:344–346, 1998.
- [21] S. L. Braunstein, C. M. Caves, R. Josza, N. Linden, S. Popescu, and R. Shack. Separability of very noisy mixed states and implications for nmr quantum computing. *Phys. Rev. Lett.*, 83(1054), 1999.
- [22] W. S. Warren. The usefulness of nmr quantum computing. *Science*, 277(1688), 1997.
- [23] D. Leibfried, B. DeMarco, V. Meyer, D. Lucas, M. Barrett, J. Britton, W. M. Itano, B. Jelenkovic, C. Langer, T. Rosenband, and D. J. Wineland. Experimental demonstration of a robust, high-fidelity geometric two ion-qubit phase gate. *Nature*, 422:412–415, 2003.
- [24] C. A. Sackett, D. Kielpinski, B. E. King, C. Langer, V. Meyer, C. J. Myatt, M. A. Rowe, Q. A. Turchette, W. M. Itano, D. J. Wineland, and C. R. Monroe. Experimental entanglement of four particles. *Nature*, 404:256–259, 2000.
- [25] F. Schmidt-Kaler, S. Gulde, M. Riebe, T. Deuschle, A. Kreuter, G. Lancaster, C. Becher, J. Eschner, H. Häffner, and R. Blatt. The coherence of qubits based on single ca ions. *J. Phys.*, B36:623, 2003.
- [26] O. Mandel, M. Greiner, A. Widera, T. Rom, T. W. Hansch, and I. Bloch. Controlled collisions for multi-particle entanglement of optically trapped atoms. *Nature*, 425:937, October 2003.
- [27] A. J. Berkley, H. Xu, R. C. Ramos, M. A. Gubrud, F. W. Strauch, P. R. Johnson, J. R. Anderson, A. J. Dragt, C. J. Lobb, and F. C. Wellstood. Entangled macroscopic quantum states in two superconducting qubits. *Science*, 300:1548–1550, 2003.
- [28] T. Yamamoto, Y. A. Pashkin, O. Astafiev, Y. Nakamura, and J. S. Tsai. Demonstration of conditional gate operation using superconducting charge qubits. *Nature*, 425:941, October 2003.
- [29] C. Langer, R. Ozeri, J.D. Jost, J. Chiaverini, B.L. DeMarco, A. Ben-Kish, R.B. Blakestad, J. Britton, D. Hume, W.M. Itano, D. Leibfried, R. Reichle, T. Rosenband, T. Schaetz, P.O. Schmidt, and D.J. Wineland. Long-lived qubit memory using atomic ions. *Phys. Rev. Lett.*, 95:419–439, 2005.
- [30] D.J. Wineland, C. Monroe, W.M. Itano, D. Leibfried, B.E. King, and D.M. Meekhof. Experimental issues in coherent quantum-state manipulation of trapped atomic ions. *J. Res. Natl. Inst. Stand. Technol.*, 103(3), 1998.

- [31] D. Kielpinski, C. Monroe, and D. Wineland. Architecture for a large-scale ion-trap quantum computer. *Nature*, 417:709–711, June 2002.
- [32] J. I. Cirac, P. Zoller, H. J. Kimble, and H. Mabuchi. Quantum state transfer and entanglement distribution among distant nodes in a quantum network. *Phys. Rev. Lett.*, 78(3221), 1997.
- [33] C. Monroe, D. M. Meekhof, B. E. King, S. R. Jefferts, W. M. Itano, and D. J. Wineland. Resolved-sideband raman cooling of a bound atom to the 3d zero-point energy. *Phys. Rev. Lett.*, 75(4011), 1995.
- [34] A. Sorensen and K. Molmer. Quantum computation with ions in thermal motion. *Phys. Rev. Lett.*, 82:1971–1974, 1999.
- [35] M. A. Rowe, D. Kielpinski, V. Meyer, C. A. Sackett, W. M. Itano, C. Monroe, and D. J. Wineland. Experimental violation of a bell’s inequality with efficient detection. *Nature*, 409:791–794, 2001.
- [36] M. A. Rowe, A. Ben-Kish, B. DeMarco, D. Leibfried, V. Meyer, J. Beall, J. Britton, J. Hughes, W. M. Itano, B. Jelenković, C. Langer, T. Rosenband, and D. J. Wineland. Transport of quantum states and separation of ions in a dual rf ion trap. *Quantum Information and Computation*, 2(4):257, 2002.
- [37] M. D. Barrett, J. Chiaverini, T. Schaetz, J. Britton, W. M. Itano and J. D. Jost, E. Knill, C. Langer, D. Leibfried, R. Ozeri, and D. J. Wineland. Deterministic quantum teleportation of atomic qubits. *Nature*, 429:737–739, 2004.
- [38] J. Chiaverini, D. Leibfried, T. Schaetz, M.D. Barrett, R.B. Blakestad, J. Britton, W. M. Itano, J. D. Jost, E. Knill, C. Langer, R. Ozeri, and D. J. Wineland. Realisation of quantum error correction. *Nature*, 432:602–605, 200.
- [39] D. Leibfried, E. Knill, S. Seidelin, J. Britton, R. B. Blakestad, J. Chiaverini, D. B. Hume, W. M. Itano, J. D. Jost, C. Langer, R. Ozeri, R. Reichle, and D. J. Wineland. Creation of a six-atom ‘schrodinger cat’ state. *Nature*, 438:639–642, 2005.
- [40] C. F. Roos, G. P. T. Lancaster, M. Riebe, H. Häffner, W. Hänsel, S. Gulde, C. Becher, J. Eschner, F. Schmidt-Kaler, and R. Blatt. Tomography of entangled massive particles. *quant-ph/0307210*, 2005.
- [41] M. Riebe, H. Häffner, C. F. Roos, W. Hänsel, J. Benhelm, G. P. T. Lancaster, T. W. Körber, C. Becher, F. Schmidt-Kaler, D. F. V. James, and R. Blatt. Deterministic quantum teleportation with atoms. *Nature*, 429:734–737, 2004.
- [42] H. Häffner, W. Hänsel, C. F. Roos, J. Benhelm, d. Chek-al kar, M. Chwalla, T. Körber, U. D. Rapol, M. Riebe, P. O. Schmidt, C. Becher, O. Guhne, W. Dur, and R. Blatt. Scalable multiparticle entanglement of trapped ions. *Nature*, 438:643–646, December 2005.
- [43] P. C. Haljan, P. J. Lee, K.-A. Brickman, M. Acton, L. Deslauriers, and C. Monroe. Entanglement of trapped-ion clock states. *quant-ph/0508123*, 2005.

- [44] S. Gulde, M. Riebe, G.P.T. Lancaster, C. Becher, J. Eschner, H. Hffner, F. Schmidt-Kaler, I.L. Chuang, and R. Blatt. Implementing the deutsch-jozsa algorithm on an ion-trap quantum computer. *Nature*, 421:48–50, 2003.
- [45] Implementation of Grover’s Quantum Search Algorithm in a Scalable System. K.-a. brickman and p. c. haljan and p. j. lee and m. acton and l. deslauriers, and c. monroe. *Phys. Rev. A*, 72(050306), 2005.
- [46] J. Chiaverini, J. Britton, D. Leibfried, E. Knill amd M.D. Barrett, R.B. Blakestad, W.M. Itano, J.D. Jost, C. Langer, R. Ozeri, T. Schaetz, and D.J. Wineland. Implementation of the semiclassical quantum fourier transform in a scalable system. *Science*, 308:997–1000, 2005.
- [47] J. Chiaverini, R.B. Blakestad, J. Britton, J.D. Jost, C. Langer, D. Leibfried, R. Ozeri, and D.J. Wineland. Planar electrode architecture for ion-trap quantum information processing. *Quantum Information and Computation*, 5:419–439, 2005.
- [48] D. Stick, W. K. Hensinger, S. Olmschenk, M. J. Madsen, K. Schwab, and C. Monroe. Ion trap in a semiconductor chip. *Nature Physics*, doi10.1038/nphys171, 2005.
- [49] R. Ozeri, C. Langer, J.D. Jost, B. DeMarco, A. Ben-Kish, R.B. Blakestad, J. Britton, J. Chiaverini, W.M. Itano, D. Hume, D. Leibfried, T. Rosenband, P.O. Schmidt, and D.J. Wineland. Hyperfine coherence in the presence of spontaneous photon scattering. *Phys. Rev. Lett.*, 95(030403), 2005.
- [50] C.R. Monroe, D.M. Meekhof, B.E. King, and D.J. Wineland. A “schrodinger’s cat” superposition state of an atom. *Science*, 272:1131–1136, 1996.
- [51] Q. A. Turchette, C. J. Myatt, B. E. King, C. A. Sackett, D. Kielpinski, W. M. Itano, C. Monroe, and D. J. Wineland. Decoherence and decay of motional quantum states of a trapped atom coupled to engineered reservoirs. *Phys. Rev. A*, 62(053807), 2000.
- [52] P. C. Haljan, K.A. Brickman, L. Deslauriers, P. J. Lee, and C. Monroe. Spin-dependent forces on trapped ions for phase-stable quantum gates and motional schrodinger cat states. *Phys. Rev. Lett.*, 94(153602), 2005.
- [53] S. Webster. *Raman Sideband Cooling and Coherent Manipulation of Trapped Ions*. DPhil thesis, Oxford University, 2005.
- [54] C. J. Donald. *Development of an Ion Trap Quantum Information Processor*. DPhil thesis, Oxford University, 2000.
- [55] P. K. Ghosh. *Ion Traps*. Clarendon Press, Oxford, 1995.
- [56] D. J. Wineland, C. Monroe, W. M. Itano, D. Leibfried, B. E. King, and D. M. Meekhof. Experimental issues in coherent quantum-state manipulation of trapped atomic ions. *J. Res. Natl. Inst. Stand. Technol.*, 103:259–328, 1998.
- [57] H. G. Dehmelt. Radiofrequency spectroscopy of stored ions. *Adv. At. Mol. Phys*, 3(53), 1967.
- [58] J. P. Stacey. *Stabilization and Control in a Linear Ion Trap*. DPhil thesis, Oxford University, 2003.

- [59] D. M. Lucas, A. Ramos, J. P. Home, M. J. McDonnell, S. Nakayama, J.-P. Stacey, S. C. Webster, D. N. Stacey, and A. M. Steane. Isotope-selective photoionization for calcium ion trapping. *Phys. Rev. A*, 69(012711), 2004.
- [60] M. D. McDonnell. *Two-photon Readout Methods for and Ion Trap Quantum Information Processor*. DPhil thesis, Oxford University, 2003.
- [61] D. A. Stevens. *The Quantum Manipulation of Ions*. DPhil thesis, Oxford University, 1999.
- [62] R. W. P. Drever, J. L. Hall, F. V. Kowalski, J. Hough, G. M. Ford, A. J. Munley, and H. Ward. Laser phase and frequency stabilization using an optical resonator. *appl. Phys. B*, 31:97–105, 1983.
- [63] B. Keitch. Transfer report. Technical report, Oxford University, 2004.
- [64] G. S. Smith. Proximity effects in systems of parallel conductors. *J. Appl. Phys.*, 43(5), May 1972.
- [65] M. J. McDonnell, J.-P. Stacey, S. C. Webster, J. P. Home, A. Ramos, D. M. Lucas, D. N. Stacey, and A. M. Steane. High-efficiency detection of a single quantum of angular momentum by suppression of optical pumping. *Phys. Rev. Lett.*, 93(153601), 2004.
- [66] A. M. Steane, C. F. Roos, D. Stevens, A. Mundt, D. Leibfried, F. Schmidt-Kaler, and R. Blatt. Speed of ion trap quantum information processors. *Phys. Rev. A*, 62(042305), 2000.
- [67] H. J. Metcalf and P. van der Straten. *Laser Cooling and Trapping*. Springer, 1999.
- [68] D. Leibfried, R. Blatt, C. Monroe, and D. Wineland. Quantum dynamics of single trapped ions. *Rev. Mod. Phys.*, 75:281, 2003.
- [69] Q. A. Turchette, D. Kielpinski, B. E. King, D. Leibfried, D. M. Meekhof, C. J. Myatt, M. A. Rowe, C. A. Sackett, C. S. Wood, W. M. Itano, C. Monroe, and D. J. Wineland. Heating of trapped ions from the quantum ground state. *Phys. Rev.*, A61:063418, 2000.
- [70] C. Roos, T. Zeiger, H. Rohde, H.C. Nagerl, J. Eschner, D. Leibfried, F. Schmidt-Kaler, and R. Blatt. Quantum state engineering on an optical transition and decoherence in a paul trap. *Phys. Rev. Lett.*, 83(4713), 1999.
- [71] L. Deslauriers, P. C. Haljan, P. J. Lee, K-A. Brickman, B. B. Blinov, M. J. Madsen, and C. Monroe. Zero-point cooling and low heating of trapped cd ions. *Phys. Rev. A*, 70(043408), 2004.
- [72] F. Diedrich, J. C. Bergquist, Wayne M. Itano, and D. J. Wineland. Laser cooling to the zero-point energy of motion. *Phys. Rev. Lett.*, 62(403), 1989.
- [73] R. G. DeVoe and C. Kurtseifer. Experimental study of anomalous heating and trap instabilities in a microscopic ^{137}Ba ion trap. *Phys. Rev. A*, 65(063407), 2002.

- [74] W. M. Itano, C. Monroe, D. M. Meekhof, D. Leibfried, B. E. King, and D. J. Wineland. Quantum harmonic oscillator state synthesis and analysis. *Proc. 1997 SPIE Conf.*, 2995:43–55, 1997.
- [75] M. L. Boas. *Mathematical Methods in the Physical Sciences*. J. Wiley and Sons, 1983.
- [76] CPO Ltd. Charged particle optics programs.
- [77] S. M. Barnett and P. M. Radmore. *Methods in Theoretical Quantum Optics*. Oxford Scientific, 2002.
- [78] M. O. Scully and M. S. Zubairy. *Quantum Optics*. Cambridge University Press., 1997.
- [79] F. Carruthers and M. M. Nieto. Coherent states and the forced quantum oscillator. *Am. J. Phys.*, 33:537–544, 1965.
- [80] M. Brune, S. Haroche, J. M. Raimond, L. Davidovich, and N. Zagury. Manipulations of photons in a cavity by dispersive atom-field coupling: Quantum-nondemolition measurements and generation of “schrodinger cat” states. *Phys. Rev. A*, 45(7), 1992.
- [81] A. Wunsche. Displaced fock states and their connection to quasiprobabilities. *J. Eur. Phys. Soc. B*, 3:359–383, 1991.
- [82] D. F. V. James, P. G. Kwiat, W. J. Munro, and A. G. White. Measurement of qubits. *Phys. Rev. A*, 64(052312), 2001.
- [83] J. S. Bell. On the einstein-podolsky-rosen paradox. *Physics*, 1:195–200, 1964.
- [84] J. S. Bell. *Speakable and unspeakable in quantum mechanics*. Cambridge University Press, 1987.
- [85] G. J. Milburn, S. Schnieder, and D. F. James. Ion trap quantum computing with warm ions. *Fortschritte der Physik*, 48:801–810, 2000.
- [86] A. Sørensen and K. Mølmer. Entanglement and quantum computation with ions in thermal motion. *Phys. Rev.*, A62(022311), July 2000.
- [87] X. Wang, A. Sørensen, and K. Mølmer. Multibit gates for quantum computing. *Phys. Rev. Lett.*, 86(17), 2001.
- [88] C. H. Bennet, H. J. Bernstein, S. Popescu, and B. Schumacher. Concentrating partial entanglement by local operations. *Phys. Rev. Lett.*, 53(2046), 1996.
- [89] C. H. Bennett, D. P. DiVicenzo, J. Smolin, and W. K. Wootters. Mixed-state entanglement and quantum error correction. *Phys. Rev. A*, 54(3824), 1996.
- [90] W. K. Wootters. Entanglement of formation of an arbitrary state of two qubits. *Phys. Rev. Lett.*, 80(10), 03 1998.